Amorphous carbon study on copper substrates applied to 3D metal printing

Ângela Elisa Crespi

Thèse de doctorat
NNT: 2022UPASP033

Amorphous Carbon Study on Copper Substrates Applied to 3D Metal Printing

Étude du Carbone Amorphe pour l'impression 3D du Cuivre

Thèse de doctorat de l'Université Paris-Saclay

École doctorale n° 572, Ondes et Matière (EDOM)
Spécialité de doctorat : Physique
Graduate School : Physique
Référent : Faculté des sciences d'Orsay

Thèse préparée dans l'unité de recherche, **Laboratoire de physique des gaz et des plasmas** (Université Paris-Saclay, CNRS), 91405, Orsay, France.
sous la direction de **Marie-Christine HUGON**, maitre de conférences, le co-encadrement de **Daniel LUNDIN** professeur, la co-supervision de **Albin EFFERNELLI** Ingénieur

Thèse présentée et soutenue à Paris Saclay, le 31mars 2022, par

Ângela Elisa CRESPI

Composition du Jury

Philippe LECOEUR Professeur, Université Paris-Saclay – C2N	Président du jury
Marie-Paule BESLAND D.R. Institut des Matériaux de Nantes – PCM	Rapporteur & Examinatrice
David HORWAT Professeur, Université de Lorraine – IJL	Rapporteur & Examinateur
Guillaume FRIBOURG Docteur- Schneider Electric – SE	Examinateur
Marie-Christine HUGON M.C. Université Paris-Saclay – LPGP	Directrice de thèse

université PARIS-SACLAY | ÉCOLE DOCTORALE Ondes et matière (EDOM)

Titre : Étude du carbone amorphe pour l'impression 3D du cuivre

Mots clés : Carbone amorphe, réflectance, cuivre, poudre, métal additive

Résumée : Le travail présenté dans cette thèse consiste en des expériences expérimentales et théoriques allant de domaines multidisciplinaires à l'amélioration de la réflectance du cuivre. La poudre de cuivre est utilisée comme matière première dans le processus d'impression 3D également appelé fusion laser sur lit de poudre ou fusion sélective par laser. Plus précisément, le lit de poudre signifie que le matériau en poudre est étalé en couches et fusionné pour former un nouvel objet. L'objectif principal de ce travail est de démontrer que les films à base de carbone amorphe déposés par pulvérisation cathodique magnétron sur des substrats en Cu sont une stratégie potentielle pour réduire l'apport énergétique de l'impression 3D utilisant un laser comme source d'énergie. L'ajout de carbone amorphe ne doit pas influencer les propriétés du Cu, comme la conductivité de la pièce produite. La première partie de cette thèse consiste à optimiser les propriétés du film à déposer sur le Cu. Deux films ont été déposés : des films de carbone a-C amorphe et des films carbone-métal a-C:SS amorphe (composé de 50% de métaux en acier inoxydable comme Fe, Ni, Cr et 50% de carbone). L'étape suivante a été de montrer que les films amorphes peuvent réduire la réflectance du substrat de cuivre jusqu'à 80% dans la longueur d'onde infrarouge. Cette réduction se produit en ajoutant les quantités minimales de matériau pour préserver les caractéristiques du cuivre. Ainsi, le choix du film se porte sur des films a-C ultra-minces. Ces films a-C réduisent drastiquement la réflectance due aux phénomènes d'interférence et aux pertes. Cette réduction a conduit à une diminution de 40% de l'apport d'énergie laser lors de l'utilisation de films a-C de 25 nm avec une fusion de qualité du Cu. Un autre sujet d'intérêt dans ce travail est la compréhension des mécanismes sur l'évacuation de charge d'une poudre de cuivre surtout lorsqu'on utilise un faisceau d'électrons comme source d'énergie. Plusieurs effets ont été observés lors du passage d'un courant à travers la poudre, le plus important étant une transition de l'état isolant à l'état conducteur pour des compressions et des polarisations spécifiques. On peut supposer que la transition dépend des charges électrostatiques, de l'effet de chauffage du micro-contact et de la taille des grains. La distribution des grains de petite taille soumise à de faibles courants (< 0,30 mA), a démontré que cette configuration est plus sensible à la compression et que la transition de l'état isolant à l'état conducteur est plus difficile à observer.

Title: Amorphous carbon study on copper substrates applied to 3D metal printing.

Keywords: amorphous carbon, reflectance, copper, powder, metal additive.

Abstract: This work present in this thesis consists of experimental and theoretical experiments ranging from multidisciplinary areas to improve the reflectance of copper. The Cu powder is used as feedstock in the 3D printing process also called Laser Powder Bed Fusion or Selective Laser Melting. Specifically, the powder bed process means that the powder material is spread in layers and fused to form a new object. The main objective of this work is to demonstrate that amorphous carbon-based films deposited by magnetron sputtering on Cu substrates are a potential strategy to reduce the energy input of 3D printing using a laser as a power source. The addition of amorphous carbon must not influence the properties of Cu, such as the conductivity of the printed object. The first part of this thesis consists of optimizing the properties of the film to be deposited on the Cu. Two films were deposited: amorphous a-C carbon films and amorphous a-C:SS carbon-metal films (composed of 50% stainless steel metals like Fe, Ni, Cr and, 50% of carbon). The deposition of these films is in the ballistic plasma regime. The next step demonstrated that amorphous films can reduce the reflectance of the copper substrate by up to 80% in the infrared wavelength. The reduction happens when adding the minimum quantities of material to preserve the Cu characteristics. Thus, the choice is a-C ultra-thin films. These films reduce the reflectance due to interference phenomena and losses. This reduction led to a 40% reduction in laser energy input when using 25 nm a-C films while maintaining a quality Cu weld. Another topic of interest in this work is the mechanisms of charges' evacuation mainly when using an electron beam as an energy source. Several effects were observed when passing a current through the powder, the most prominent is a transition from the insulator to the conducting state at specific compressions and polarizations. It can be assumed that the transition depends on the electrostatic charges, the micro-contact's heating effect, and the grain size. Smaller grain size distribution submitted to low currents (< 0.30 mA), demonstrated that the small powder in this configuration is more sensitive to compression and the transition insulator to a conductor is harder to observe.

A ma cousine « unique » au monde,
Karina

«A ship in harbor is safe, but that is not what ships are built for.»

— John A. Shedd

Acknowledgment

The investigations presented in this thesis are a result of fruitful teamwork and I owe my deepest gratitude to my co-workers for their commitment. The first person I would like to thank is my supervisor Marie-Christine Hugon an expert in plasma and thin films who trusted me and helped with everything I needed and gave me the freedom to explore different expertise in this thesis resulting in deposition on metal grains. I am very thankful for the corrections of the thesis, manuscripts (uncountable versions), abstracts. Her feedback point of view always focus on bringing improvements. I was her last PhD student before the retirement, I hope this work closed her carrier with a flourish. The second person I would like to thank is my co-supervisor, Prof. Daniel Lundin; It has been an honor for me to work with such a plasma expert and the most distinguished names in the community.

I must also mention Prof. Tiberiu Minea, who supervised me at the begging of this thesis and who came up with the elegant original idea of this work. Then I would like to express my heartfelt thanks to Prof. Jacques Robert, who patiently showed me how to understand the physics behind electromagnetic waves and optical topics as no one else could.

An exceptional thanks to the members of this thesis jury, composed of Marie-Paule Besland, David Horwat, Philippe Lecoeur, Guillaume Fribourg, Albin Effernelli, Daniel Lundin, and Marie-Christine Hugon for their interesting comments on this work.

To all the members of the Laboratoire de Physique des Gaz et des Plasmas LPGP, specially Charles Ballage, who solved numerous problems and gave brilliant ideas to create new experiments.. I must also mention Felipe Cemin who showed me the laboratory and explained all I know about Paris from his unique point of view; Felipe is always there when I need him. My colleagues, Ph.D. students of the TMP-DS team. Prof. Pierre Desesquelles, who helped me with calculations, and Michel Fleury, who found a simple and efficient solution for the electrical configuration of powder experiments. To Vinicius Antunes, which I could share the office for a while resulting in long (very long) discussions about everything. Adrien Revel for the games and barbecues, Benjamin Seznec for all the help with Clermont-Ferrand. The amazing intern I had the opportunity to have Selin Kaya. The administration staff composed by Thierry Devillers (merci pour tous les bons moments) Nicolas Dessaints as well the information technology service that could provide all the material to remote work very efficient during the COVID-19 quarantine and all the equipment for my hybrid defense presentation Marc Bisson and Michel Pascanu.

This work would not be possible without collaboration with several research partners. I am very grateful to José Alvarez from the laboratory Génie électrique et électronique de Paris Saclay (GeePS), for the productive discussions about Raman Spectroscopy and Resistivity analysis. Ian Vickridge from the Institut de nanosciences de Paris, INSP, Sorbonne Université for the Rutherford backscattered spectroscopy analysis so we could find out the metals in our samples (Bing!), Guillaume Nordet e Patrice Peyre from the Procédés et Ingénierie en Mécanique et Matériaux (PIMM) where I had the opportunity to prove the concept of this work welding the a-C copper samples; François Brisset and Jocelyn from the Institut de Chimie Moléculaire et des Matériaux d'Orsay (ICMMO) for several sections of copper metallography and the amazing images of scanning electron microscopy.

Un énorme merci beaucoup for laboratories and companies of the *AM-bition* project, which have contributed to France’s copper 3D printing process.

This thesis is part of the French fellowship called Convention Industrielle de Formation par la Recherche (CIFRE) N° 2018/0719; thanks to it, I could work with *AddUp Global solutions*; I have to acknowledge Albin Effernelli, Gilles Walrand, Benjamin Vayre, and Etienne Blanchet to all the support during these years to turn it possible the 3D printing with carbon. Furthermore, this research work was supported by LPGP, *Université Paris-Saclay*, *Conseil National de la Recherche Scientifique* (CNRS). My time in Paris was also an enriched cultural experience, evolution, and good memories. A special thanks to Carlos Figueroa and his team (Epipolé) from PGMAT at Universidade de Caxias do Sul, in Caxias do Sul, Brazil. Thanks to my Brazilian friends, who, after all these years of absence, still remember me and ask for news.

Finally, I would like to express my sincere thanks to Mari Moro Crespi and Egidio Crespi, mom and dad. They cheered with me in the good moments, endured three years without visits because of the pandemic time and understood my decision to fly far away from home (precisely 10.1 thousand kilometers) to do a Ph.D., believing the future could be different. To my aunt Inês Moro Baratto for her unmeasured enthusiasm during the presentation of the thesis and Miriam Moro who always supported me. I cannot end this without mentioning my cousin Karina Moro Baratto, the one who taught me that I had the capacity to do this PhD because she challenges herself every day, overcoming all the difficulties that show up along the way.

I am lucky to be among such talented people.

Thank you all.

General Summary

Preface

My thesis is part of the AMBITION PROJECT-FUI. This work studies the economic and technological viability of 3D printing using copper and precious metal as feedstock. Several university laboratories and companies collaborated on this project:

- Laboratoire de physique des gaz et des plasmas (LPGP);
- L'École nationale supérieure des arts et métiers Procédés - Ingénierie en Mécanique et Matériaux (PIMM);
- Université de Technologie de Belfort Montbéliard – Laboratoire des études et de recherche sur les matériaux, les procédés et les surfaces (LERMPS) ;
- Université Grenoble Alpes- Science pour la conception et optimisation (G-SCOP);
- L'institut Polytechnique de Grenoble -Science et Ingénierie des Matériaux et Procédés (SIMAP).

The partner companies are

- Add Up Global Solutions;
- Schneider Electric;
- Engineering Systems International Group (ESI);
- Varinor;
- (LIt Fluidisé Compagnie) LIFCO Industrie;
- Stellantis Group (for PSA group).

Throughout this project, I had the honor of working closely with partner companies thanks to the *CIFRE* fellowship (Convention Industrielle de Formation par la Recherche) regulated by l'Association Nationale de la Recherche et de la Technologie (ANRT). The project allowed enriching exchanges between the LPGP and the companies cited above. At LPGP, I was part of the Equipe Théorie et Modélisation des Plasmas - Décharges et Surfaces Group (TMP-DS). My work focused on plasma discharges for thin-film growth in close partnership with Add Up Global Solutions, specialized in 3D laser printing machines using metal as feedstock.

Outline

This thesis concerns the electrical and optical properties of carbon-based films and the electrical properties of copper (Cu) powder or metal additive (MA) with regard to increasing the efficiency of three-dimensional (3D) metal printing.

The rapid development of 3D metal printing technology demands optimizing the energy required during manufacturing processes. The main focus of the thesis is the 3D printing process called Laser powder bed fusion (LPBF), also known as *Selective Laser Melting* (SLM). A second method is mentioned, the electron beam powder bed fusion (EB-PBF), also known as selective electron beam melting or electron beam melting (EBM). In both methods, metallic Cu powder is delivered in layers to the fusion area and melted using an energy source (an electron beam or laser) to form a final piece. The metallic powder is fused or sintered within successive layers to form the final 3D object.

Cu and its alloys have high thermal and electrical conductivities. In the context of Cu printing by SLM, such features lead to deficient absorption, especially infrared (IR) radiation. Consequently, Cu reflects almost 100% of the near and far IR spectrum at room temperature. Printing machines usually use near-IR lasers wavelength ($\lambda = 1.06\ \mu m$). The low absorption of Cu necessitates a high-intensity laser to sufficiently penetrate the material, thereby ensuring a final quality piece. This thesis proposes the use of amorphous carbon-based thin films over copper as an original and simple method for increasing the efficiency of SLM. Such films absorb more laser radiation than copper due to their dark color and the complex refractive index. Fundamental research has evaluated the best optical and electronic properties of carbon-based films deposed by magnetron sputtering film to be applied in the SLM process.

Cu is one of the best conductors; when a metal is in granular form, however, conduction and electric charge evacuation are abruptly modified within the context of EB-PBF. The metallic powder used as feedstock in 3D printing accumulates electric charges, resulting in critical process failures. Therefore, observation of the Cu powder current flow is relevant to energy input and discharge of the grains in the 3D printing process.

The Challenges

High-quality Cu fusion during SLM requires different management of the laser energy. Cu has a high melting temperature (T_{Cu} = 1083 °C) and thermal conductivity (σ_{Cu} ~ 398 W/m K). When fusing Cu, the high T_{Cu} and σ_{Cu} result in the melting pool's rapid solidification and significant local thermal gradients. Such properties challenge the SLM process and require higher energies for homogeneous melting and solidification. Moreover, using an IR laser results in high reflectance of almost 100% of the incident light. Hence, a large amount of energy is usually involved in the fusion process due to the unique physical properties of Cu.

Adding other elements to the Cu matrix is an alternative strategy to facilitate the SLM process. However, other elements usually reduce Cu electrical conductivity. One example is phosphorous, which causes weld defects and conductive reduction. Amorphous carbon (a-C) thin and ultra-thin films, either pure or composed, are deposited only on the Cu's surface and not mixed in the matrix. The partial film of a-C limits the covered surface creating a multilayer system. The deposition is exposed to the laser, so it can leave the copper surface due to the effects of laser and Cu evaporation, avoiding Cu conductive reduction. Thus, one challenge is to use the a-C ultra-thin films deposited only in part of the Cu substrate to improve absorption during SLM without adversely affecting the properties of the Cu, such as conduction.

Finally, another challenge has been to control the electrical charges in the metallic powder used as a raw material in a 3D printing process. Understanding how a current flow influences the charging effects can prevent the smoking effect (displacement of loosened powder), improving the process's general quality.

Objectives

The objectives of the present thesis are as follows:

1) to explore the fundamental physical, electrical, and optical properties of thin a-C and composed a-C iron films deposited by direct current magnetron sputtering as a function of the target-to-substrate distance;

2) to identify the fundamental phenomena involved in the reduction of Cu reflectance when carbon-based films are added;

3) to determine the role of ultra-thin a-C films in interference when they are deposited on Cu substrates, and describe the interference phenomena for a double interface vacuum/a-C/Cu system in the studied spectrum;

4) to optimize the thickness of a carbon-based ultra-thin layer on the outermost surface of Cu powder to reduce the laser power required to melt Cu;

5) to investigate the flow of current and its effects on metallic Cu powder that are analogous to the behavior of the powder in the EB-PBF fusion process.

The following six chapters of this thesis address the objectives cited above. **Chapter 2** introduces the materials and the characterization techniques used in this work. **Chapter 3** discusses the results concerning the properties of the carbon films (objective (1)). **Chapter 4** is dedicated to the interferences of the a-C films on copper substrates (objectives (2), (3), respectively). **Chapter 5** describes the welding done using metallic powder and carbon (objective (4)). Finally, **Chapter 6** analyses the early phase of the metallic powder current flow study (objective (5)). The main results are summarized at the end of each chapter as well as in the **General Conclusions**. Open questions are outlined in the Perspectives section. The author's publications, and complementary contents are found in the **Appendices**. The **References** are arranged by order of appearance at the end of the manuscript.

CHAPTER I: Material's State-of-art

Chapter 1 introduces the state-of-art of amorphous carbon thin films and copper. Moreover, the chapter details the type of carbon used in this work, pure and composed films, and the copper used as substrates.

Summary

Abbreviations Chapter I

a-C	Amorphous carbon
B.C.	Before Christ
k	Boltzmann constant
V_B	Breaking down voltage
δ	Deep skin
DC	Direct current
d	Distance
n_e	Electron density
eV	Electron volts
E_g	Energy of band gap
A	Experimental constant of a given gas
B	Experimental constant of a given gas
T	Gas temperature
IR	Infrared
n_i	Ionization density
K	Kelvin
λ_{mpf}	Mean free path
Tm	Melting point of a given material
a-C:Me	Metal doped amorphous carbon
m	Molecular weight
n_n	Neutral's density
Pa	Pascal
h	Plank's constant
n_0	Plasma density
$F_{ionization}$	Plasma ionization fraction
p	Pressure
γ_{see}	Secondary electron emission
Ts	Substrate's temperature
USA	United States of America

1.1. Thin Films Background

Thin films are layers of a substance covering a bulk supporting material [1]. The thin film thickness ranges from a few atomic layers to a few micrometers. Such films grow by controlled deposition over a substrate. Thin films are also found in nature (leaves, butterfly wings, bubbles) [2,3]. The terminology used to describe these layers differs. It is often specific to a discipline or application [4,5]. The first thin films were deposited in 1852 and the plasma sputtering[I] was first studied by W.R. Grove. Nowadays, thin films are at the cutting edge of several fields [6].

Thin film materials are versatile because they present differences from bulk materials such as physical dimensions and large surface area to volume ratio. More importantly, the combination of the thin films and the bulk properties of the underlying material leads to enhanced chemical, mechanical or electrical properties [7,8]. The growing demand for layer structure and property optimization develops the use of many thin film systems. The pure metal films are ideal for conductive, decorative, and protective applications, for example, copper (Cu) for flexible electronics, thermal management, or antimicrobial film. Iron (Fe) improves protection against rusting. However, metals such as nickel (Ni) or chromium (Cr) and Fe are common in doped films to associate two or more material properties in one coating [9,10]. These combinations can combine, for example, conductivity and absorptivity in one layer [1].

Moreover, many applications employ the concept of *multilayers*. This concept combines several elemental or compound films presented above. As the name indicates, multilayer systems combine several layers of, for example, doped material and pure coating [11]. These systems can accumulate several layers, such as solar cells, anti-reflective coatings, or absorbing devices [12–14].

The ultra-thin films result from the last two decades of miniaturization in several areas. The term *ultra-thin film* describes nanometric layers of up to 100 nm [15]. For example, a soap bubble wall thickness is around 100 nm, and a graphene sheet has less than 1 nm [16]. It represents a single atomic plane of graphite [17]. The top and intermediate layers determine the properties of carbon film thickness below 10 nm. Few nanometer films demonstrate high hardness than thicker films [18].

The advantage of ultra-thin films is that minimal quantities of material can provide excellent properties modifications. Nowadays, biomedicine, electronics/optoelectronics, and catalysis utilize ultra-thin films [19,20]. The carbon films are the focus of this work. The variety of carbon films is attractive due to their unusual structure and properties. A rare combination of density, hardness, chemical inertness, and relative transparency makes such carbon film ideal for optical coatings. Other potential uses are cutting tools with low friction coating and a passivation diffusion barrier for electronic components. Besides, carbon films are good candidates to dope with a metal [21,22].

1.1.1. a-C Thin Films Deposition

The name *carbon* comes from the French “charbone”. “Carbo” from Latin means ‘charcoal.’ Ancient humans could not find carbon in nature; it was pretty much encountered in cinders[II], soot[III], and charcoal. Paradoxically, today carbon is harmful to the environment due to the abuse of gas emissions [23,24].

[I] To dislodge (atoms) from the surface of a material by collision with high energy. Definition from Merriam – Webster dictionary

[II] a partly burned coal capable of further consume itself without flame

[III] the fine powder consisting chiefly of carbon that colors smoke

A wide variety of both crystalline and amorphous structures are possible, thanks to the hybridization properties of the p and s orbital. The focus is on one of the simplest types: *a-C thin films* [20,25].

The amorphous carbon network does not present particular order [24]. However, the a-C films can present ordered atoms or molecules in the local scale [23,24]. Neighbor atoms can be ordered and define crystal structures. The carbon presents three hybridization sp, sp^2, and sp^3. The sp^2 is found in graphite-like arranged in trigonal planar shape forming three sigma (σ) and one π bonds. The volume of the arrangement sp^2 is around 6.68 $Å^3$ in Figure 1.1a. The sp^3 is characteristic of diamonds are arranged in a tetrahedral shape. The four valence electrons of carbon make σ bonds, the volume of sp^3 arrangement is 5.74 $Å^3$ (Figure 1.1b). The sp sites are not shown, but they can be present in amorphous carbon. The sp site forms linear σ and π bonds.

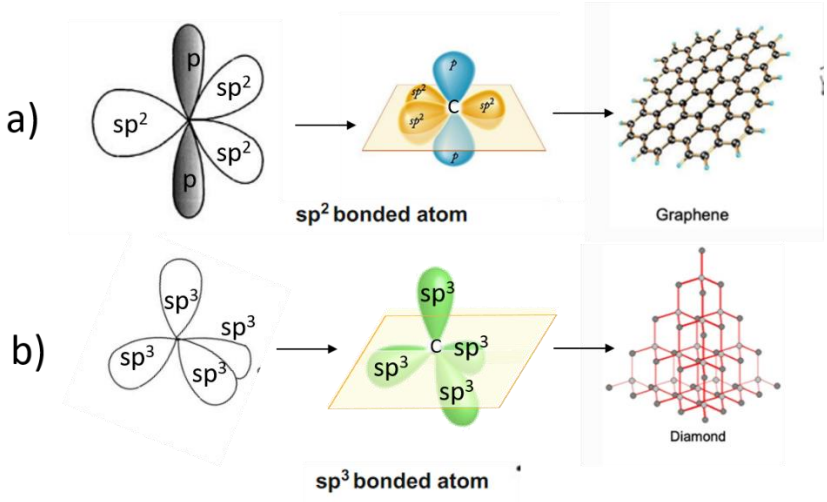

Figure 1.1: Typical representation of a) sp^2 in graphite sheet and b) sp^3 in diamond. Adapted from [26].

The DLC film's classification is shown in the diagram shown in Figure 1.2. Their properties depend beyond the hybridization's ratio to the presence or absence of hydrogen, and these films are classified accordingly [18,27]. The focus of this study is the non-hydrogenated amorphous carbon. The film which contains more sp^3 sites is the ta-C, the tetrahedral amorphous carbon. The a-C films contain mainly sp^2 hybridized sites. In the diagram of Figure 1.2 a-C is located on the left downside just above the graphite [28,29].

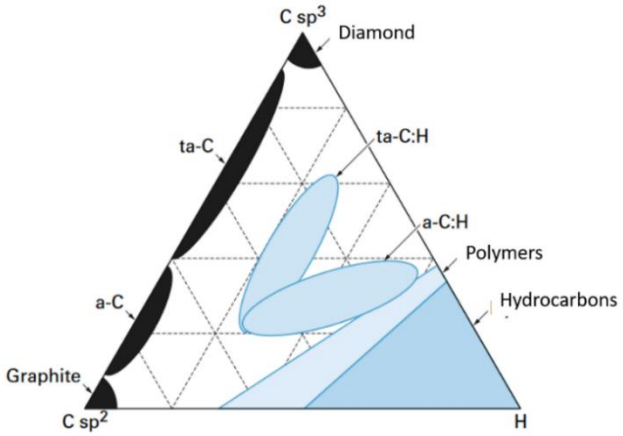

Figure 1.2: Ternary phase diagram of bonding for a-C films. The blue zones are hydrogenated and the black zones are non-hydrogenated carbon types. Adapted from [29].

1.1.2. Cold Plasma for Thin Film Deposition

The term "plasma" defined as partially or entirely ionized gases containing ions, electrons, and neutrals was first introduced in 1928 by Irving Langmuir. The most common plasma type used for thin film deposition is direct current (DC) glow discharges, generated by applying an electric field between two electrodes in a low-pressure gas chamber. In glow DC discharges, the predominant collisions are inelastic, involving electrons and gas atoms. The most crucial inelastic collision is the *electron impact ionization that* sustains the plasma. Some plasma processing, such as sputtering (which is further discussed in chapter 2) or etching, takes place in the glow discharge regime [20,30].

A crucial parameter to create plasma is the breaking down voltage (V_B). It represents the minimum voltage to transform an insulator, in this case, a gas or air, in a good conductor, the plasma. Free electrons can ionize some atoms by electron-impact ionization, producing electric currents, transforming the working gas into a glow discharge region. V_B is a function of the pressure distance (pd) product, where p is the working pressure and d is the distance between the cathode and the anode, according to Paschen's law, in equation (1.1) [31].

$$V_B = \frac{Bpd}{ln(Apd) - ln\left[\ln\left(1+\frac{1}{\gamma_{see}}\right)\right]} \quad (1.1)$$

Where γ_{see} is the secondary electron emission yield depending on the nature of electrodes and A and B are constants determined experimentally for a given gas [32]. A free electron is accelerated by the electric field and collides with a neutral atom. After these collisions, a fraction of the kinetic energy of the free electrons is transferred to the atom, releasing more free electrons called the first ionization potential [32,33]. Ions, neutrals, or photons impact the cathode surface leading to the ejection of free electrons, called *secondary electrons,* that define the secondary electron emission yield. These electrons are accelerated away from the cathode surface held at a negative potential to sustain the discharge by ionization of neutral gas by generating ions that bombard the cathode and release more secondary electrons [32].

The moving particles can travel a certain distance between two successive collisions in the plasma defined as the mean free path (λ_{mfp}). For low pressures, the species in the plasma have only a few collisions due to the large electron mean free path. The collision probability is low because most electrons reach the anode without colliding with gas atoms or molecules. They have kinetic energy but they do not have charges. On the other hand, at too high pressures (short λ_{mfp}), many elastic collisions prevent the electrons from reaching high enough energy for ionization resulting in the thermalized electrons. In conclusion, V_B increases to ignite plasma as «p» increases, the effect is equivalent if the distance «d» between the cathode-anode changes accordingly, following the product pd. [34–36].

The number of free electrons or charge carriers per unit volume defines the plasma density. The ion (n_i) and electron density (n_e) are similar due to a major principle of quasi-neutral. Thus $n_e \approx n_i = n_0$ where n_0 is the plasma density. Plasma usually differs according to the temperature of gas species and density. The plasma ionization fraction ($F_{ionization}$) depends on the neutral density (n_n) according to $F_{ionization} = n_e./(n_n + n_e)$.

The cold plasma is weakly ionized ($F_{ionization}$<0.01) and often out of equilibrium. The non-equilibrium characteristic is that electron temperature can be much higher than ions or neutral temperature [31]. Cold plasma is used for a large variety of applications, including in cancer treatment, sterilization, etching, and film deposition [14]. The cold plasma presents an electron density ranging from 10^{16} to 10^{19} m^{-3} [35].

On the other hand, *hot plasma* is completely ionized ($F_{ionization} \approx 1$) including the sun (and other stars), the Aurora Borealis [37,38]. The electron temperature in electron volts (eV)

is the amount of energy gained by an electron in the vacuum when it is accelerated across 1 volt (V) of electric potential equivalent to a temperature of 11600 K [33].

Thus, the glow DC discharges characteristic is the inelastic collisions involving electrons and atoms mainly the electron impact ionization that sustains the plasma. Hence glow discharges are suitable for plasma processing such as sputtering (further discussed in chapter 2) or etching.

1.1.3. Films Growth for a-C Thin Films

This section describes the atomic processes during the growth of a-C films in Physical Vapor Deposition (PVD). In PVD processes, heating (evaporation) or ion bombardment using plasma (sputtering) of a solid-state source material produces a vapor of the atoms that later form the film. These vapors are film-forming species that can be further ionized in the plasma (forming ion precursors). They also associate in the gas phase, forming molecules prior to their deposition onto the substrate [39].

The adsorbed species, called 'adatoms', move over the surface in a random movement process referred to as "adatom surface mobility" or "diffusivity". This phenomenon depends on deposition parameters such as plasma, the product pressure distance of electrodes, applied bias voltage, the temperature of the substrate, and kinetic energy of the arriving particles [40]. Experimental parameters such as the substrate temperature and plasma density are among the key variables affecting island nucleation and growth. When films are grown at low substrate temperature or high deposition rates, the adatoms do not have sufficient time to diffuse and find stable nuclei before the arrival of the newly deposited adatoms sticking on the surface [41,42].

Specifically for a-C, the bombardment energy changes the type of carbon in the film [42]. Three stages describe amorphous film growth. The definition used in this work is *a-C (a-C)*. The first is the collision state, where the plasma species collides with the sample surface. Mainly the implanted ions modify the structure causing other effects such as vibrations, diffusion means cluster formation as demonstrated in

Figure 1.3. On the one hand, low energy ions tend to stick on the surface and remain in their lower energy state sp^2, following the Volmer-Weber growth mode, i.e. island growth [41,43]. On the other hand, energetic atoms and ions can penetrate the surface and enter an interstitial site. The implanted ion modifies the film's local density, creating stress and compression in the local bonds [44,45].

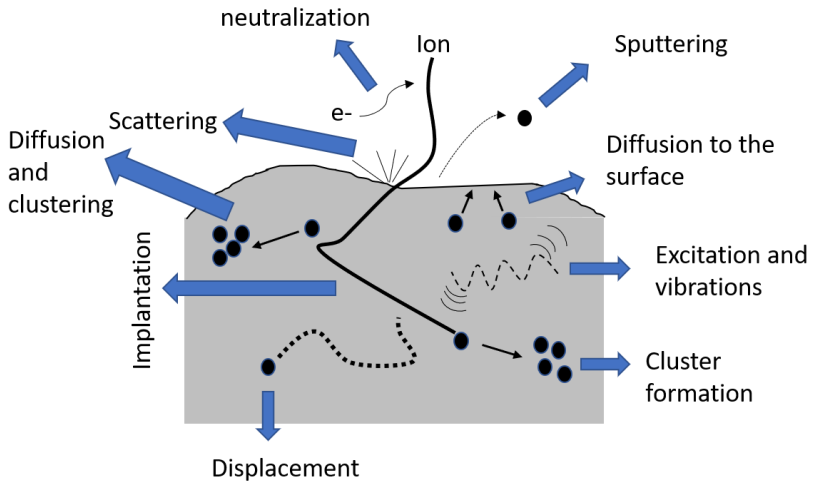

Figure 1.3: Implantation process in a-C films. Adapted from [44].

The second state is thermalization, where the excess energy dissipates in the film. Depending on the deposition conditions, the bond arrangements shift to an energetically

favorable hybridization. In general sp^3 becomes sp^2 in the amorphous film case[IV]. In the third state, the metastable structure relaxes by diffusion of compressed regions towards a free stress structure, leading to transitions of sp^3 (usually compressed) to a more favorable state the sp^2. Thus, if the particle bombardment has sufficient energy, the particles penetrate the film resulting in local densification; according to the new hybridizations, the bonds rearrange locally (the cluster formation indicates in

Figure 1.3) [44]. This results in volume disparity between the sp^2 and sp^3 bonding and shrinkage [46]. Consequently, the a-C properties and disorder degree depend on the species» energy during the deposition, which assesses its final hybridization and cluster size [47].

The a-C configuration and other carbon forms that contain sp^2 hybridization are present in Figure 1.4 a–c. The sp^2 orbital represented in Figure 1.4a, happens in graphite. The graphite constitutes connected plans of six folded rings (Figure 1.4b, the single planes are best known as graphene.

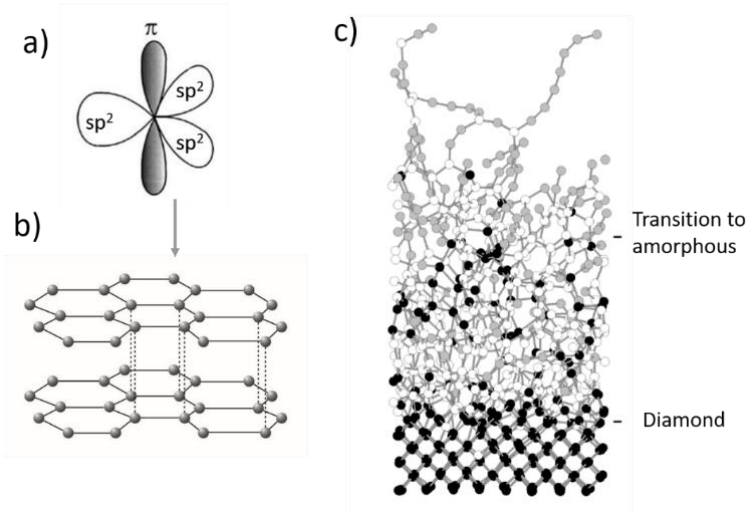

Figure 1.4: a) Schematic representation of sp2 orbitals consisting of three σ bonds in a trigonal planar arrangement and one π bond; b) Graphite planes type AA of six folded rings each atom in graphite consists of the arrangement in a); c)the diamond ordinate (black atoms) and the amorphous carbon structure of a deposited film. The gray and white atoms represent chains distorted odd fold coordinated rings. Adapted from [48,49].

The a-C properties and disorder degree depend on the energy of the ions during deposition, which assesses its final hybridization and cluster size as discussed in the section 1.1.3. The non-crystalline sputtered carbon can achieve densities such as 1.79 g/cm^3. The density depends on the film-forming species energy [18,46]. Non-crystalline or amorphous materials have an additional broadening contribution to the bond length and angle distribution [46,47]. In sp^2 coatings, the probability of clustering surges, and a variety of larger clusters can be formed by fusing double bonds and rings [50,51]. The formation of ta-C films has been modeled by an orthogonal tight-binding method in Figure 1.4 c. This simulation method is appropriate for the low-density surface region. The most remarkable feature is that the ordinate substrate becomes amorphous. The outermost layer of the film results in many sp bonded linear chains [18].

The addition of metal into the amorphous matrix improves mechanical and optical properties of the films [29]. The metal can be found in the interstices of the amorphous lattice, or forming carbides and crystalline phases, mainly influencing conductive sp^2 sites [52]. The insertion of metals can reduce stress and surface energy, for instance, the addition of Al and Fe [52]. Another interesting property is that the films become opaque. The mechanical properties

[IV] Introduced in section 1.1.1

are improved in terms of hardness and toughness. Metals turn the a-C films hydrophobic [29,53].

1.1.4. Thin Film Structure

Extensive studies on the relation between the microstructure of the layer deposited by PVD and the growth conditions have led to several structural zone models (SZM). The zones present the microstructure evolution as a function of the substrate temperature T and the material melting temperature T_m ratio. In Zone T (T/T_m <0.3), films deposited in the presence of modest energy ion bombardment do not present a smooth morphology with crystal sizes that are difficult to resolve. Some appear fibrous with sufficiently dense boundaries to yield good material properties in Zone 2 (0.3 <T/T_m<0.5), the adatom mobility increases (or surface diffusivity), resulting in columnar structure with void bands and smooth surfaces. The grain boundaries are nearly perpendicular to the film plane [54,55].

The substrate temperature is a determinant parameter in thin film growth and bulk diffusion. Therefore, bulk chemistry and diffusion tend to dominate at sufficiently high temperatures. On the contrary, the adatom mobility is low at low temperatures, leading to continued nucleation of grains. The second axis of the Thornton diagram is the Ar pressure. The collisional scattering effect has a much greater influence on the coating structure than the adatom mobility reduction associated with adsorbed inert gas species on the substrate surface, related to the pd parameter and the flux [56]. The sputtered atoms suffer collisions as the working pressure increases. The species energy in the working gas decreases the thermalization effect. The thermalized species tend to exhibit a porous fine-grained structure typical of Zone 1, even for high T/T_m. Low energy ion does not penetrate the surface, neutral atoms that mainly contribute to the growth (1–10 eV) [48,57].

Non-penetration ions (or atoms) can have enough energy to promote surface atomic diffusion. In a range of plasma energies of the bombardment species, which, does not cause defects in the bulk film. This energy is around the surface displacement energy on the surface and on the bulk [56].

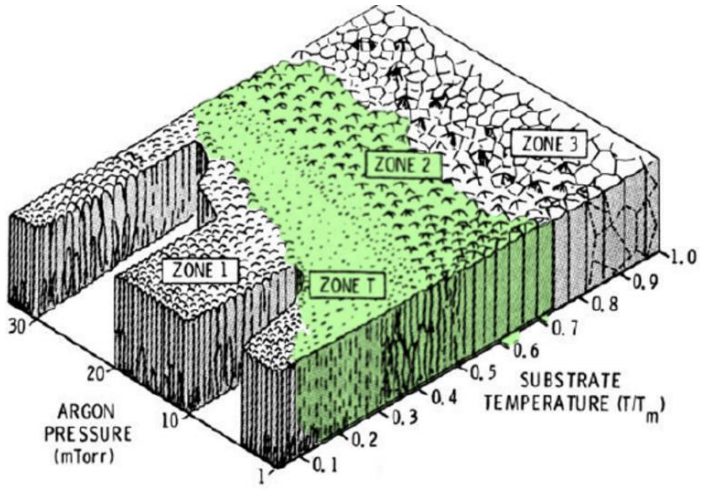

Figure 1.5: The Thornton diagram represents different microstructural zones classified as Zones:1, T, 2 and 3. The substrate temperature (T) and the material melting point (T_m) ratio and the argon pressure (mTorr) determine the structure of the material. The green zones are the zones of films deposited by magnetron sputtering process. Adapted from [54]

The presence of metals in the amorphous matrix, for example, dopants, or larger quantities of material in the case of compound films influence nucleation and cluster size. The larger clusters are obtained when adding metal into the amorphous matrix due to the higher

mobility of metal adatoms. The mobility catalyzes sp^2 ordered structure, the order of the bond is related to the length, and angle of carbon bonds [10].

1.2. Copper

Copper first used dates more than 10,000 years ago. In the Middle East, small decorative pendants and other items were discovered [58]. The earliest smelted artifacts known were made of copper. The alloy and its uses led to the Bronze Age, which began in the Middle East before 3000 B.C. Two of the best-known alloys contain Cu, brass (copper and zinc) and bronze (copper and tin), although hundreds of alloys containing Cu exist. Copper is a natural antibacterial agent; its use helps to prevent disease transmission during Sarcovid-19, an important issue nowadays [59]. It is soft, malleable, ductile, and an excellent conductor of heat and electricity, and it resists corrosion [60]. The red copper does eventually form oxides. The cupric oxide (CuO) can become dark. The most popular is the verdigris (green color) which contains several forms of copper acetate, present in the statue of liberty in New York USA, and the superb dome of the Palais Garnier in Paris France.

In 2021, the world refined copper consumption added up to more than 18 million tons only behind iron (Fe) and aluminum (Al) [61]. Copper is used in wiring (60 percent of use), plumbing, electronics, and building construction [58]. Copper is 100% recyclable metal. Nearly 80% of Cu mined in the Earth's crust to date is still in use. It is also present in the human body, helping absorb iron [62,63].

1.2.1. The reflected wavelength Copper Miniaturization

In the last decade, Cu has attracted much interest in nano-ranged devices. The demand for Cu devices miniaturization in several areas require attention. The bulk properties of copper can be completely modified for nano-range scale [64]. The main difficulty of copper is that electrical properties are size-dependent, resulting in poor electrical properties on such scale. The dependence on the size limits performance of sub-micrometer size wiring required by the downscale in present electronics. The continuous requirement for tiny devices with the lowest possible electrical resistance pushed the development of Cu processing.

The copper electrical performance is dependent on the microstructure and the chosen process to reduce scale [65]. For ultra-thin Si/Cu films, the high-power impulse magnetron sputtering (HiPIMS) process improves the main copper properties, such as crystal structure, microstructure and, grain morphology [30]. These properties are key parameters to the nanoscale conductivity. If the microstructure presents bigger grains, the conductivity is improved [66]. Grain boundaries act as barriers to the electron movement in the copper [65]. In addition, the copper oxides may have more impact on nano-Cu materials since the natural layer of CuO is around 3 nm [67]. More than films, several nano-components are used as Cu interconnections [68], foils [69], or granular metallic powder for applications in 3D metal printing [70].

1.2.2. Copper Powder

Additive manufacturing (AM) is the industrial production name for 3D printing, using a computer-controlled process that creates three-dimensional (3D) objects [71]. The AM includes several techniques that use powder as feedstock, including the laser powder bed fusion SLM described in Chapter 2 [72,73]. The metal powder used as feedstock is called either metal additive or metallic powder in this work [74]. The gas atomization process transforms Cu bulk into the metallic powder appropriate for AM feedstock [75].

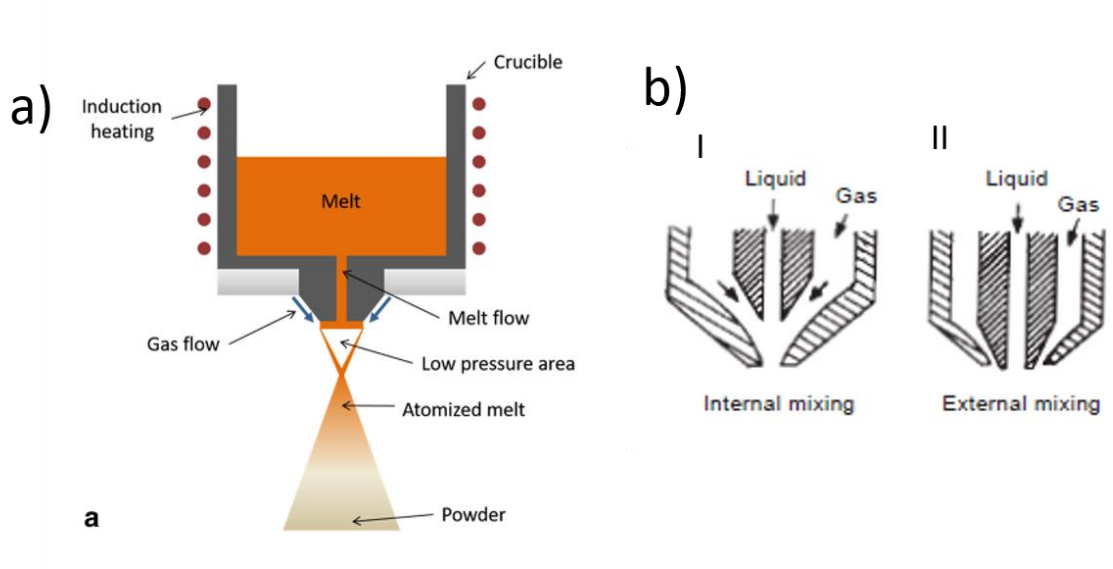

Figure 1.6:a) Schematic representation of gas atomization steps and b) the nozzle representation in two configurations: I) the gas and the melted metal are mixed inside the nozzle. II) the mixture happens outside the nozzle as in a) adapted from [75,76].

Figure 1.6a summarizes the atomization main steps. Pure Cu or Cu alloys are pre-alloyed in a graphite crucible and inductively melted at around 1450 °C. After, the molten material flows via a nozzle to a chamber, the vessel, within an inert atmosphere. Figure 1.6b demonstrates two configurations of the nozzle.

The gas jets, of around 12 bar pressure, atomize the melted Cu. The jets are equally inclined to the axis of the melt flow and intersect this axis at the point of geometric impact. The Cu solidifies very fast, up to 106 K/s in spherical format with a smooth surface [77]. The final metallic powder must have spherical particle sizes below 100 µm. For AM applications, the formation of spherical particle sizes below 100 µm requires an Ar flow of 360 m3/h flux [71]. The energetic efficiency of the method is poor (~3%) and expensive [71].

After atomization, air separation removes the fine particle fractions (d <10 µm). The tiny metallic powder is easier to melt and results in better surface finishing; thus, the most refined processes employ smaller powders. Bigger particles separation uses a 60 µm mesh sieve. The metallic powder feedstock is a mixture of different particles sizes, resulting in a Gaussian distribution, the small powders fill voids among bigger ones [78]. The most popular metallic powder distribution around 20–44 µm averaged at 30 µm [76].

1.3. The Materials Properties

This section focuses on a-C and copper (Cu) optical and electrical properties and how a-C films can contribute to the absorption of IR radiation due to copper. Also, the exceptionally high conduction of bulk Cu is discussed in the AM context.

1.3.1. Optical Properties

In several applications, reflectance and transmittance generate interferences or losses, in solar panels, laser cutting, and AM [79–81]. This section summarizes the mechanism of absorption for Cu, pure and composed carbon.

1.3.1.1. Copper

Metals generally present a bright silvery appearance when exposed to white light. This silvery appearance indicates that metals are highly reflective over the entire visible spectrum because the visible spectrum excites electrons into unoccupied energy states above the Fermi

energy. Figure 1.7a demonstrates that the excitation of the electron ΔE is equal to the photon's energy.

The reflected wavelength distribution determines the metal color. The copper and gold appear red-orange and yellow, respectively. Below λ=580 nm, copper absorbs around 60% more due to its orbital vacancies; the energy difference that provokes transitions of the two sub-shells (d and s) is small (2.7 eV). This energy is associated with photons having short wavelengths (λ> 580 nm). The little energy difference between the sub-shells is responsible for Cu absorption at short wavelengths. Higher wavelengths (λ>580 nm) reflect 98 % of all the incident light. The reflected wavelengths in the visible range lead to the characteristic Cu color, orange-red (λ =655 nm -750 nm) [67]. In contrast, silver has around the double 4.8 eV. However, an abnormally elevated absorption in molten copper around 580 nm is due to the natural absorption of copper in this range [82].

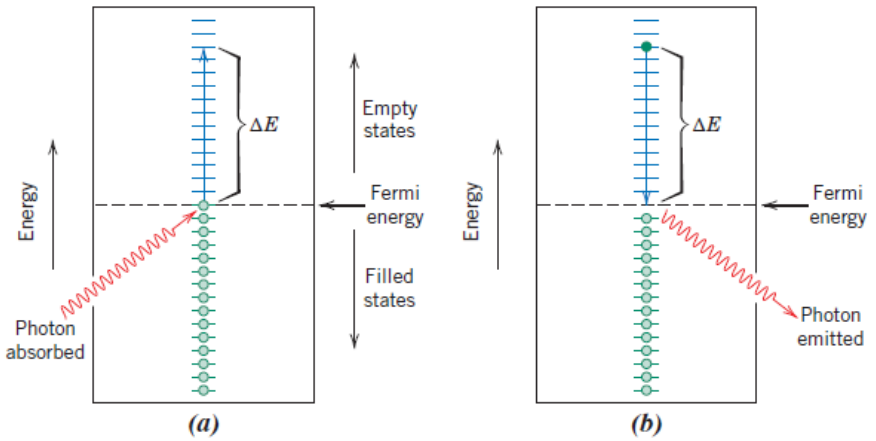

Figure 1.7: a*) Schematic representation of photon absorption for metallic materials in which an electron is excited into a higher-energy unoccupied state adapted from* [83].

At higher wavelengths, light penetration on Cu is only a few nanometers. One can calculate the penetration of light or the (deep skin) in nm (δ) according to the equation (1.2) [84] for Cu δ =5 nm at λ=1000 nm;

$$\delta = \sqrt{\frac{\rho}{\pi \times f \times \mu}} \qquad (1.2)$$

Where the absolute magnetic permeability is represented as $\mu = (\mu_0 \times \mu_r), \mu_0 = 4\pi \times 10^{-7}$ H/m, $\mu_r \sim 1$, f the frequency in Hz, ρ is the copper resistivity, μ_r and ρ can be found in [85,86].

The reflectance depends on temperature since absorption increases when the material gets hotter. However, the challenge of the AM process is to maintain Cu at its fusion point. The high thermal conductivity and reflection induce its rapid solidification [87].

1.3.1.2. Absorption of Carbon-Based Thin Films

It is pertinent to understand how carbon films can reduce reflectance through absorption. The necessary energy of excitation is related to the photon's frequency through equation (1.3). These excitations with the associated absorption can take place only if the photon energy is greater than that of the band gap's energy E_g – where, h= Planck constant, v= speed of light in a given medium. The result is a free electron in the conduction band and a hole in the valence band [88].

$$h \times v > E_g \qquad (1.3)$$

The disorder arrangement of a-C films has a multitude of optical band gaps, where the state density is low but not zero due to the distortions in the orbital sp^2, also called the pseudo-optical band gap [88,89]. The conduction band joins the valence band locally due to the sp^2 orbitals. The sizes of the pseudo-band gap depend on the mixture sp^2-sp^3 in the films. Films mainly composed of sp^3 sites are transparent and more resistive than sp^2 sites [90]. The optical properties of the a-C films are directly related to electronic transitions. The totality of the electronic transitions results in the photon's absorption [91].

The pseudo-band gap can be tailored over a wide range, from opaque graphite E_g= 0.0 eV to transparent diamond E_g= 5.5 eV. The amorphous films are between graphite and diamond depending on their orbitals. However, the measure of the pseudo-optical band gaps is not very reproducible due to the multitude of states [28]. Omskii *et al.* [92] describe the absorption of a-C deposited by magnetron sputtering using the dielectric function composed of an imaginary and real part (proportional to the complex refraction index) [28,93,94]. The imaginary part is the sum of the electronic transition dumping the electromagnetic waves. The graphite clusters significantly contribute to the absorption depending on their density [92]. The real part affects the velocity of a wave when it changes to a different medium.

1.3.1.3. Photon Absorption by Metal-Doped Amorphous Carbon

Metal-doped amorphous carbon films (a-C:Me) have a different absorption. The main difference between pure and composed materials is that the addition of an impurity creates other excitation states, the multi-steps. The multiple-step electron transitions facilitate the absorption within the band gap. In general, Fe, Cr, and Ni induce sp^2 clusters due to the relatively high mobility of the metallic adatoms. Indeed, these metals are very effective catalyzers, for instance, for carbon nanotubes [95,96].

1.3.2. Electrical Properties

This section resumes the electrical properties of a-C-based film and copper materials. In particular, for copper, the electrical properties are essential characteristics in this work.

1.3.2.1. Copper Bulk Conductivity

Copper's electrical conductivity is unique, and it is used as a reference scale to compare other materials. According to the International Annealed Copper Standard (IACS), the Cu's conductivity of 1913 is 100% of the scale [58]. This method rates the conductivity of any material. Good conductors present a greater ratio percentage. For example, the highest purity Cu produced today (99,999%) is 103% IACS (1.6723 μΩ cm) compared to the Cu conductivity in 1913 [87,97]. Only silver has a lower resistivity than copper 106% IACS (1.6206 μΩ cm) [98,99].

Cu presents an excellent intrinsic characteristic to transfer and conduct thermal energy. Cu heat conductivity is σ_{Cu} 398 W/m K (only silver and the diamond are above Cu heat conductivity). The good thermal transference makes this metal hard to melt. Due to this characteristic, copper is useful in a variety of applications, for example in pipes for hot fluids [99]. The Cu's fusion temperature is T_{Cu} = 1083°C [58].

Several factors affect Cu resistivity, temperature, dimensions, crystallography, and grain size. Heating copper reduces the conductivity to 38% IACS (4.537 μΩ cm) at 425°C [100,101]. Cu miniaturization also affects the conductivity, as discussed in the section 1.2.1. In particular, when dimensions reach the electron mean free path for electron-phonon collisions (39 nm for Cu), resistivity increases dramatically, even at room temperature [102]. In the case of thin films, grain size considerably affects the conduction of Cu [65]. The surface roughness, defects and, impurities such as oxygen are other factors that affect Cu conductivity [67,103].

1.3.2.2. Amorphous Carbon

The versatility of carbon bonds creates many structures, including a-C. In graphite, the bonds in the plane are crystalline, and the band gap in the sheets is negligible. The graphite thus conducts through π covalent bonds that allow electron mobility in the plan resulting in low resistivity. The resistivity among planes is higher because only Wan der Waals forces connect graphite planes. The resistivity from one sheet to another for pyrolytic graphite is 1000 μΩ/m - 3000 μΩ/m [104].

Carbon exhibits flexibility in the bond length. Figure 1.8 a – b shows that the length (d) of π bonds varies. The carbon-carbon bonds can stretch without changing their angles. The distance between the p orbitals measures the charge's transference [105]. Besides *stretching* bond lengths, a-C presents more than six-folded rings, resulting in dangling bonds and chains, as shown in Figure 1.4. As mentioned before, the conduction band joins the valence band locally due to the sp^2 orbitals; since the a-C contains different bond lengths and angles, the conduction band does not join the valence band, thus creating other states called the pseudo-band gap. In a-C, the size of the pseudo-band gap indicates the electrical properties and increases the overall resistivity of the film. The pseudo-band gaps can vary locally for non-crystalline carbon due to different density states and local order [23,92]. Chhowalla *et al.* [91] showed that the optical and electrical properties depend on sp^2 fractions. The resistivity of a-C can reach values in the range of MΩ cm [28,106].

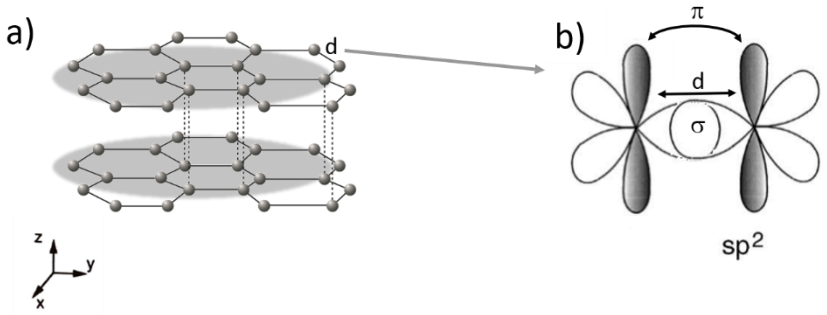

Figure 1.8: a) Demonstrative graphite planes conduction represented by the gray circles, b) two parallel p orbitals forming a π bond (axially symmetric) Adapted from [107].

1.3.2.3. Metal-Doped Amorphous Carbon

The addition of a metal (0–100 at. %) into the carbon matrix (a-C:Me) enhances conductivity. The electrical conductivity of a material is related to the capacity of electrons to move to the material. In general, metallic adatoms present higher surface mobility [108]. The metal can form carbides or be dispersed into the carbon matrix inducing sp^2 sites when the electron mobility increases due to metallic adatoms, for example, Fe, Au, W. The metal creates conductive paths when the concentration of the metal is high enough to establish contact [109]. In addition, the energy of the pseudo-optical band gap decreases when a metal is in the film [95,110,111]. This discussion links with the principle mentioned in section 1.3.1.

1.4. 3D Metal Printing of Copper

Copper and its alloys have high thermal and electrical conductivity, leading to poor absorption of the infrared spectrum at room temperature [112]. Laser radiation requires high laser power intensities to reach a deep penetration welding process *i.e.*, deep melting. The energy is transmitted to the metal additive through photons of the laser beam [113]. This thesis focuses on selective laser melting (SLM) or laser powder bed fusion (LPBF), as shown in Figure 1.9. This printing process builds 3D objects by fusing successive layers of metallic powder [114,115]. The metallic grains form a melt pool when the laser fuses the grain in

selected layer areas. After the weld material solidifies, the printing continues. Hence another cycle starts, and a new powder layer is spread and melted. After welding one layer, the 3D printing object height increases several µm. The thickness of the layer varies according to the process and the building object. The printing stops when the piece is finished [116]. Homogeneous powder bed and energy management result in quality 3D printed objects. A final part results in good mechanical and electrical properties when free of porous and defects [117,118].

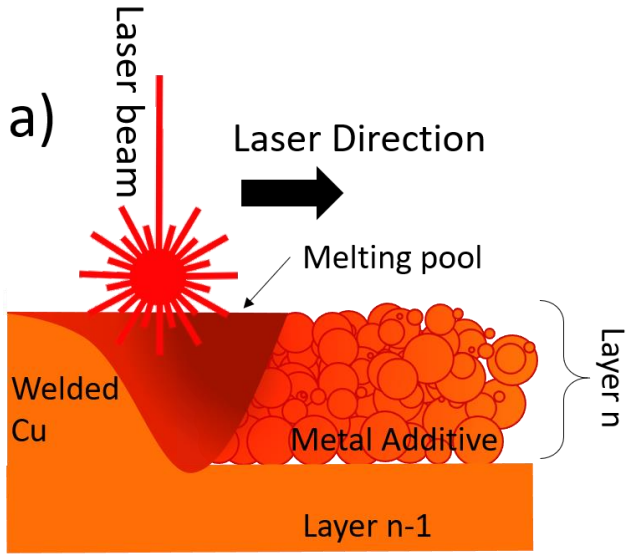

Figure 1.9: Melting pool mechanism of an additive manufacturing process using laser as the source; when the laser scans the powder bed, the metal additive melts, forming a new layer of the printed object [113].

One of the main problems is the low absorption of Cu in the IR range, the same typical laser installed on commercial 3D printing machines. The copper's low absorption of infrared radiation significantly rises at the phase transition from solid to liquid due to powder heating before the printing. By increasing the powder temperature from 25 °C to 1085 °C, pure copper absorption increases from 4.89% to 16.10% [113,119].

Pure Cu welding is difficult due to limited absorption, around 5% of the input power at infrared (IR) range λ= 1000 nm -1100 nm some strategies have been proposed to improve the absorption efficiency [120,121]. The development of Cu laser welding includes finding newly optimized parameters for IR laser, modifying or combining different energy sources, and adding another material in the metallic powder [122]. Colopi *et al.* [123] reported the range of acceptable SLM parameters for IR lasers without the occurrence of detectable defects in the printed part using a laser spot of 78 µm. It is worth mentioning that recent works have attained pure Cu pieces employing 400 W in SLM (spot of 70 µm, *i.e.* a power density of 103 kW mm^{-2} reaching 95% of final part relative density[V] [122,124]. Other approaches are green (526 nm) or blue diodes due to the naturally higher absorption of Cu in lower wavelengths, particularly around λ=580 nm (more detail are in chapter 4 and the section 1.3.1.1). Consequently, green laser use has arisen due to the higher natural absorption of copper in the green spectrum. Recently, blue diode lasers have been mentioned in the literature for Cu, showing promising results [125]. Zediker *et al.* [124] claim that 450 nm wavelength is highly absorbed by copper around 65% against around 5% from IR lasers. Hybrid sources using two or combined lasers

[V] Relative density: is the ratio between the density (mass of a unit volume) of SLM printed part and the density of a reference Cu material.

.

are also reported. Hess *et al.* improved the absorptivity of the copper welding process using combined green (532 nm) and infrared (1064 nm) lasers [126,127]. Another solution is the use of an electron beam. Cu-printed objects present satisfactory properties, when printed using an electron beam to melt the metallic powder [128]. Finally, adding a different material in copper is a sensible strategy since the minimum addition of other elements can easily penalize copper properties, mainly conduction. The addition of dark thin films using plasma, in particular, has become an alternative methodology to improve copper's absorption [129–131]. A complementary alternative is to study how current flows in the metallic during the 3D printing process.

1.5. Influence of the Powder Shape in 3D Metal Printing

The spreadability is the ability of granular media to spread over an area [132]. When the metallic powder presents a bad spreadability, in 3D metal printing, the layers are heterogeneously distributed, as demonstrated in Figure 1.10 a–b.

In the literature, powder spreadability depends on several surface-contact forces. Some inter-particle adhesions are Van der Waals forces (attraction between the particles at a certain distance), electrostatic charges, capillary (tension due to the presence of a liquid), or even friction between the beads. The poor spreadability tends to form powder agglomerates, as in Figure 1.10b. For small-size powder distributions, the inter-particle force becomes more important than the gravity: the cohesive powders [128]. The powder mass is not sufficient to overpass this cohesion. The closer these bodies come together, the more critical these forces become. The magnitude of the Van der Waals force influence is greater. Gravity is larger than the cohesion in bigger distributions (50–110µm), reducing these forces' importance [78].

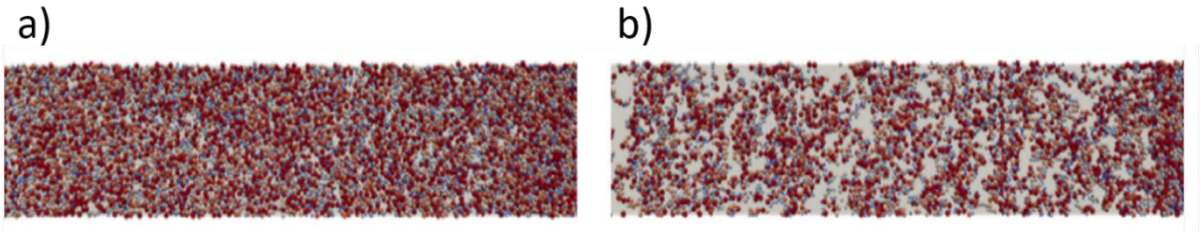

Figure 1.10: Numerical simulations of the layer topography view using 20–44 µm distribution of Ti6Al4V. a) The homogeneity of a non-cohesive powder and b) a cohesive powder. The images represent the spreading homogeneity after two layers each layer of 44 µm thickness. Adapted from [133].

The adhesive interaction forces between particles can easily vary by several orders of magnitude for a given material combination. Meier *et al.*[133] illustrate numerically for Ti_6Al_4V that the more cohesive powders required thicker layers to end up with a homogeneous covering [134–136].

It is essential to remember that a powder bed size distribution composition of a powder mixture is a key factor for spreadability. The compactness of bigger powder is lower, leading to more porosities and more melting difficulties [132]. Although to achieve the most efficient packing, different powder's sizes are mixed up. An efficient mixture prevents voids, so the smaller particles fill the interstices of the larger particles [78,128]. The most popular size distribution nowadays is 20 µm - 45 µm.

The electrical properties are important. The main point of dealing with electrical conduction *in granular media is to understand how it behaves*. Contrary to bulk materials, the resistance of metallic granular is not simple and varies from one configuration (spread) to another, sometimes by more than one (or several) order of magnitude [135]. It also depends on the electrical history of the system, and the state of compaction [137].

1.6. Main Objective

The main objective of this thesis is to create an efficient dark thin film using carbon to enhance absorption on Cu substrates without harming Cu resistivity. To achieve this objective amorphous carbon films deposited by DCMS were studied to determine the best film's properties. Optimize the addition of carbonaceous film to preserve the electrical properties of Cu used as substrates. Reduce the energy used in the SLM 3D printing process by decreasing the reflected light and intensifying Cu's absorption. Understand the electrical properties of the powder media used as feedstock in 3D printing.

CHAPTER II: Material Processing Techniques

To understand the experimental work carried out in this study the main material processing techniques are here described. The multidisciplinary character of this work creates the possibilities of using several techniques from plasma physics to 3D metal printing.

Summary

Abbreviations Chapter II

AM	Additive manufacturing
a-C:SS	Amorphous carbon stainless steel films
(a.u.)	Arbitrary units
NS	Areal density
M	Atomic mass
Z	Atomic number
N_a	Avogadro's number
CaF_2	Calcium fluoride
CAD	computer aid designed
$\frac{d\sigma}{d\Omega}$	Cross-section of the detector in RBS
I	Current
ρ_d	Density (g/cm^3)
$\vec{V}_{E/B}$	Drift velocity of particles
$\vec{E}$	Electric field (vector)
EBSD	Electron backscatter diffraction
ESD	Energy Dispersive X-ray Spectroscopy
Ho	Holmium
LPBF	Laser powder bed fusion
$\vec{B}$	Magnetic field (vector)
MA	Metal Additive
Nd	Neodime
OIM	Orientation Imaging Microscopy
Pa	Pascal
$\sum_i$	Peak integral area of element (i)
s	Probe spacing
ρ	Resistivity
RBS	Rutherford Backscattering Spectrometry
Sm	Samarium
SEM	Scanning electron microscopy
$\Delta\Omega$	Solid angle
S(E)	Sputtering Yield
SS	Stainless steel
Sr	Steradians
TSD	Target to substrate distance
U	Uranium
XRD	X-ray diffraction
Yb	Yterbium
YAG	Yttrium aluminum garnet

2.1 Chapter Introduction

This chapter describes the main techniques used in this work. The direct current sputtering used for thin films deposition, the infrared laser used in 3D printing machines (SLM). Later, a description of the principles of the *ex situ* characterization techniques.

2.2 Techniques

This section describes the thin film deposition by magnetron sputtering, the infrared laser, and the 3D printing process.

2.2.1 Magnetron Sputtering- Plasma for Thin Coatings

The magnetron sputtering is used to deposit carbon over different copper substrates. The copper substrates include copper films deposed by magnetron sputtering over Si. The technique was used to deposit carbon films. The carbon films can improve the absorption of IR light for applications as metal 3D printing.

2.2.1.1 Sputtering System

A common way of depositing thin films is by plasma deposition. The method used to create a plasma discharge is *the magnetron sputtering*. The deposition chamber consists of a cathode, represented by the target in Figure 2.1 and an anode (usually the grounded chamber walls) enclosed in an evacuated vacuum chamber. The power source is a direct current (DC) power supply. A sketch describing this typical setup is seen in Figure 2.1.

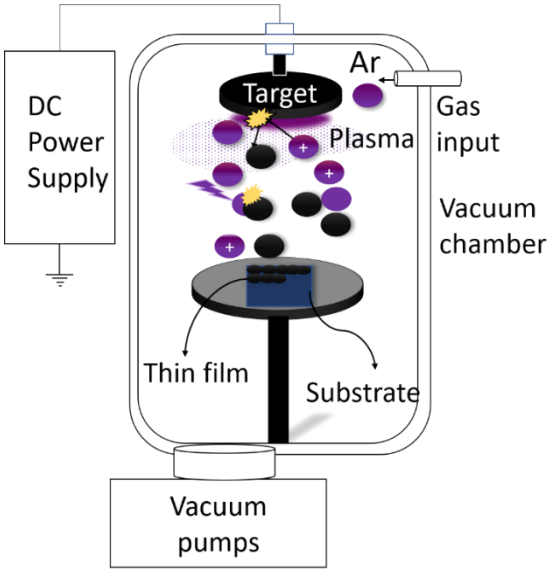

Figure 2.1: Illustration of a sputtering system for thin film deposition [138].

The plasma[VI] physics of the discharge concerning a magnetron sputtering is briefly introduced in this section while the generalities on cold plasma are given in Chapter 1 in the section 1.1.2.

2.2.1.2 Plasma physics

The working gas into the chamber serves as the medium where the electrical discharge is initiated and sustained. The glow is visible between the cathode and the anode by applying a few hundred volts to the cathode [7]. The plasma ignition starts with free electrons from background radiation or thermal energy, as discussed in Chapter 1.

[VI] A partially ionized gas composed of neutrals, ions and electrons. Often called a cold plasma [32,33],

The resulting electrons gain energy from the external applied electric field, and the most energetics sustain the plasma via ionization collisions with the neutral gas species. On the other hand, positive ions (Ar^+) are accelerated towards the cathode (also called target) and bombard it. This bombardment interaction releases among other particles, the secondary electrons. The cascade of ionizing collisions ultimately results in a large current causing the gas to break down [139]. The current density becomes more evenly distributed over the entire cathode surface, reaching the abnormal glow region by increasing the externally applied electric power. Plasma processing, such as sputtering and etching, occurs in a plasma density in the range from 10^{15} m^{-3} to 10^{19} m^{-3} [7,140].

The sputtering is a process where the cathode material leaves the solid as a vapor due to the impinging positive ions accelerated from the plasma [141]. The incoming ion breaks up the atom's bonds in the target, and the outcome is highly dependent on the material properties and ion energy. Therefore, it is meaningful to introduce the concept of sputtering yield, S(E), the number of sputtered atoms per incident particle. This is one of the factors that influence the deposition rate. For the most commonly used materials (such as Cu, Ti and, C), S(E) is around 0.5–2.5. More specifically, Cu has an S(E) of 2.5 atoms/ion for impinging Ar ions at energies of 500 eV, classified as an easy material to sputter. Carbon, for example, has a much lower S(E), less than one carbon atom/ion imping in the same energy. [142].

2.2.1.3 The Magnetron Discharge

In a classical DC sputtering process, electrons are accelerated over the cathode sheath and move with high velocity towards the anode. The electric field between the electrodes defines the electron trajectory, usually randomized by collision with the other gaseous species. However, by applying an external magnetic trap using permanent magnets behind the cathode, the electron trajectory is confined in the vicinity of the target and, consequently, increases their probability of ionizing gas atoms, thus plasma can be created in low operation pressure [139]. This magnetic trap prevents electron diffusion (loss) to the wall/anode. The ionization is very effective close to the target, where the magnetic field is the highest.

The reason for the magnetron confining the plasma is the magnetic field ($\vec{B}$) configuration combined with an electric field ($\vec{E}$) as shown in Figure 2.2a–b. Several configurations of magnets confine the electrons. For example, the magnets are placed with one pole positioned at the central axis of a circular magnetron, and the second pole placed in a ring configuration around the outer edge [138]. One of the disadvantages of these early sources was that both poles had the same magnetic strength, trapping the electrons too effectively in the near-cathode region in a closed-loop type of pattern, the so-called balanced magnetron. It effectively traps the electrons in a torus above the circular target.

On the contrary, the magnetron allows the plasma to diffuse away from the target surface. The magnetic field configuration of the unbalanced magnetron is displayed in Figure 2.2a. It will enable some electrons to escape from the confining $\vec{E}\times\vec{B}$ field that leads to a better transport of charged particles to use the substrate [143,144]. The point where $\vec{E}\times\vec{B}$ is perpendicular is the zone where the plasma is the densest due to the drift velocity of particles ($\vec{V}_{E/B}$) pointing in the azimuthal direction, which is normal to the plane formed by $\vec{E}$ (pointing towards the target) and $\vec{B}$ (parallel to it). Thus, the erosion of the target is particularly effective below this zone [138]. This results in a racetrack in the target represented in Figure 2.2a by bold curved zones. Further details of the magnetron deposition process and the related plasma physics can be found elsewhere [138,139,145–147].

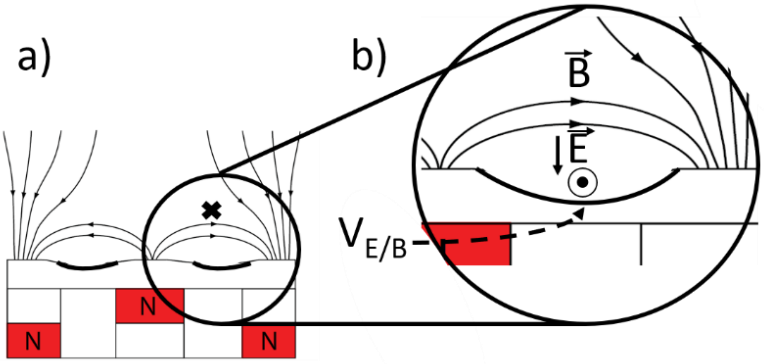

Figure 2.2: Schematic drawing of a cross-section of an unbalanced magnetron, displaying the magnetic field lines as only partially closed loops. The electrons can easily escape and travel towards the substrate region above the target surface. The "X" represents the point where $\vec{E}\times\vec{B}$ is perpendicular, as indicated in b) $\vec{E}$ points to the target, $\vec{B}$ is parallel to the racetracks below this point and $\vec{V}_{E/B}$ is perpendicular to $\vec{E}\times\vec{B}$ leaving the paper in the azimuthal direction. Adapted from [138].

2.2.2 The Custom-built Equipment

The custom-built chamber used in this work is displayed in Figure 2.3 a–c named Toccata. The principal setup is in Figure 2.3a. The deposition system was equipped with a carbon target (99.99% purity) clamped to a 1 in. top-mounted water-cooled magnetron (1) located in the main chamber (2). The system contains two pumps (3)- (4) and full-range gauges (5). A direct current power supply was used in all the depositions of this study (6). A load-lock chamber (7) was employed for sample transferring by utilizing the vertical arm facing the target (8) (Figure 2.3b). A movable sample holder (9) transports the sample to the deposition sample holder under the magnetron (10) displayed in Figure 2.3c. The films were grown using Ar (99.997% purity). The detailed diagram of the magnetron sputtering equipment is in appendix B.

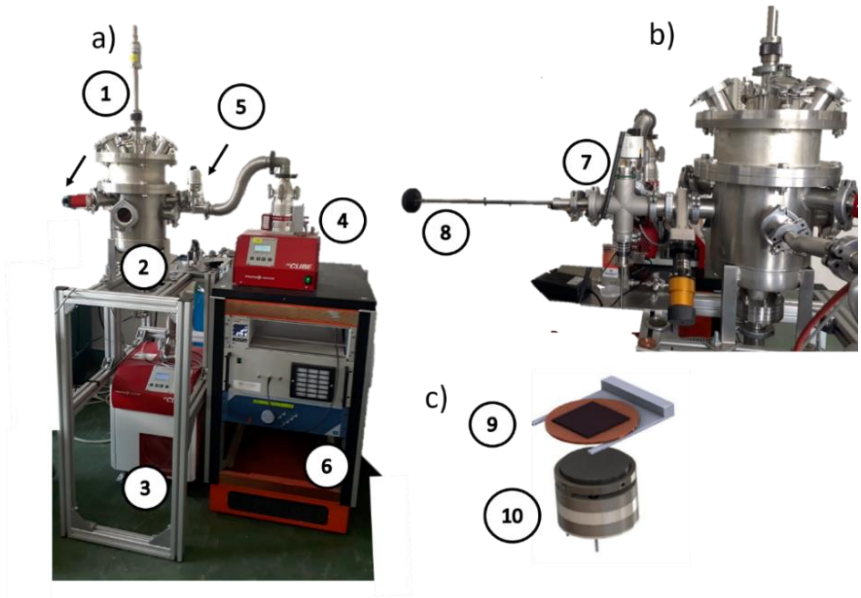

Figure 2.3: Magnetron sputtering deposition system utilized during this study. The system is located at the LPGP laboratory. It consists of a) (1) Magnetron target inserted into the (2) main chamber, a vacuum pumping system of (3) the main chamber, and (4) the load lock. It furthermore consists of (5) pressure controllers indicated by the arrows and (6) DC power supply. b) (7) load lock, (8) movable sample holder on a vertical arm. c) (9) movable sample holder and (10) fixed sample holder.

2.2.3 The Infrared Laser

This work employs a solid-state thin-disk laser. Solid-state lasers contain an active medium that consists of dopants such as Cr, Ni, Ti, or Co, or rare-earth ions (Nd, Ho, Sm, Yb) in a crystalline matrix (e.g. yttrium aluminum garnet: YAG) or amorphous material (glass). In the active medium, the population inversion and the photons of laser light are created. The concentration of dopants varies from 0.01 to 5%. These materials are called by the name of the dopant followed by their host structure, all in abbreviated form Yb:YAG, i.e. YAG doped with ytterbium (Yb) [148,149].

German universities the thin-disk lasers scalable to high output power. The first material used in this technology was the Yb:YAG. This combination has significant benefits: The laser does not present oscillations that extract energy from the system or absorption in the exciting estate and so on [150]. The core concept behind thin-disk lasers is the geometry and the heat sink. The pumped[VII] radiation is imaged onto the disk using a collimator and a parabolic mirror, creating a multiple pumped beam (Figure 2.4a). In this way, the crystal absorbs 90% of the pump power (Yb:YAG), resulting in a homogeneous appropriate power density [150,151].

Another feature is that one of the flat faces of the thin-disk crystal is coupled with a heat sink, as demonstrated in (Figure 2.4b). This face minimizes the transversal temperature gradient (thermal aberration is a problem in this laser type) and the phase distortion transversal to the direction of the beam propagation[150,152].

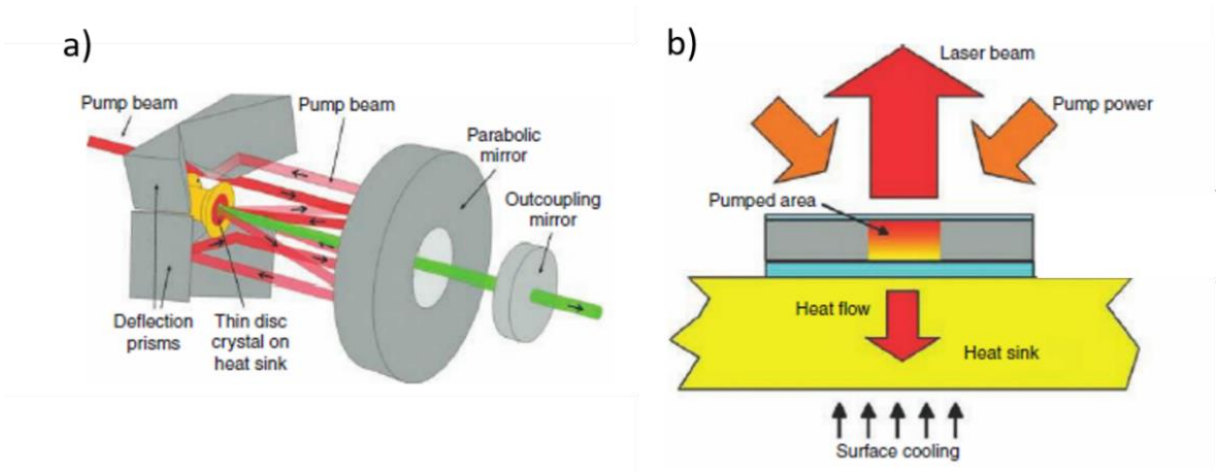

Figure 2.4: a) Design of thin-disk laser; b) the cross-section of the active thin-disk crystal in a heat sink. Adapted from [150].

A Gaussian function describes the intensity distribution of laser sources. This Gaussian profile generates inhomogeneous intensities on the laser spot. The laser spot is the delimited area of the laser beam indicating the beam diameter, as shown in Figure 2.5 a–b. [153]. Since uniform spatial laser beam profiles are required in laser applications, material processing, or lithography. The beam shape is the process of irradiance distribution. Complex lens configurations can modify the beam from Gaussian (Figure 2.5a) to flat-top, as seen in Figure 2.5b. A refractive, diffractive, and even absorptive element can generate a top hat or flat-top, where the wave reaching a target is homogeneous [153]. The complete mechanism of shaping is described elsewhere [154,155].

[VII] In lasers: to excite (atoms or molecules) especially so as to cause emission of coherent monochromatic electromagnetic radiation. From [370]

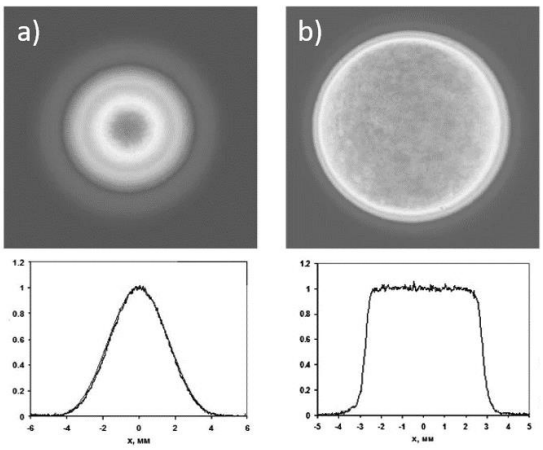

Figure 2.5: Comparison of spatial and signal intensities for a) Gaussian spot and b) flat-top spot for a Nd:YAG laser. Adapted from [153].

The laser used in this work was a Yb:YAG top-hat thin disk (λ= 1.03 µm) to imitate the SLM process on a laboratory scale. The setup is displayed in Figure 2.6 and is located at Procédés et Ingénierie en Mécanique et Matériaux (PIMM) laboratory in Paris. The equipment contains a sample holder (1), controlled Ar protective atmosphere composed of a hut (2) and flow valves (3) a conveyor belt (4) to transport the sample during the welding. The laser (5), a camera recording 8-10 k frames per second and a filter of 840 nm (6), the mirror is at 30° from the laser, the camera is pointed to the mirror. A high-speed camera Photron – Crysta PI-5WP coupled with an objective type Questar[VIII] (5) were used to record the *in-situ* welding and melt pools. A diode of 815 nm synchronized with the camera's acquisition illuminated the samples. The sample holder has 1-2° of inclination to avoid direct reflectance in the laser fiber. More details on the flat-top lasers can be found elsewhere [151,156,157].

In addition, reflectance measurement employed the laser (5) and an integrating sphere coupled 3 mm above the focal length. The laser power used in the measurements was 60 W.

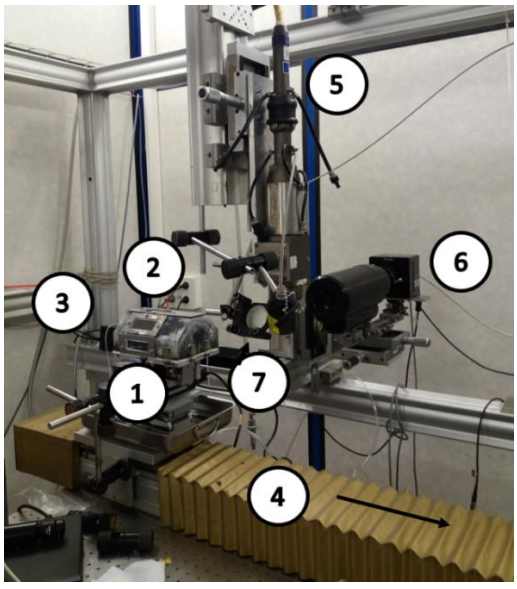

Figure 2.6: Infrared laser bench composed of (1) a sample holder, (2) a steel hut, (3) argon valves, (4) a conveyor belt, (5) a laser, (6) a camera and filter (7), and mirror to the camera at PIMM laboratory.

[VIII] It is a telescope with mirrors whose design has been studied and optimized to focus on short distances, more at [371]

2.2.4 The Laser Powder Bed Fusion Process

Additive manufacturing (AM) is a technology that changed the advanced development process [158]. The most remarkable advantage of AM is the design freedom. It builds complex parts, which had earlier required multiple processes. The main AM methods are powder bed fusion, material binder jetting, and directed energy deposition [71,159]. The present work focuses on powder bed fusion powered by a laser. Also, the last chapter of the manuscript tackles one of the aspects of the electron beam powder fusion, introduced in the section 2.3.1. The principle behind this technique is to create complex parts using computer aid design (CAD) specialized software [160]. The metal powder or metal additive (MA) is the feedstock to build a final piece. Successive thin layers are fused to create the three-dimensional (3D) object, previously projected in the CAD. The resulting object usually has a lower weight and novel design than ones done using metallurgy [161]. Other advantages of AM are summarized in Figure 2.7.

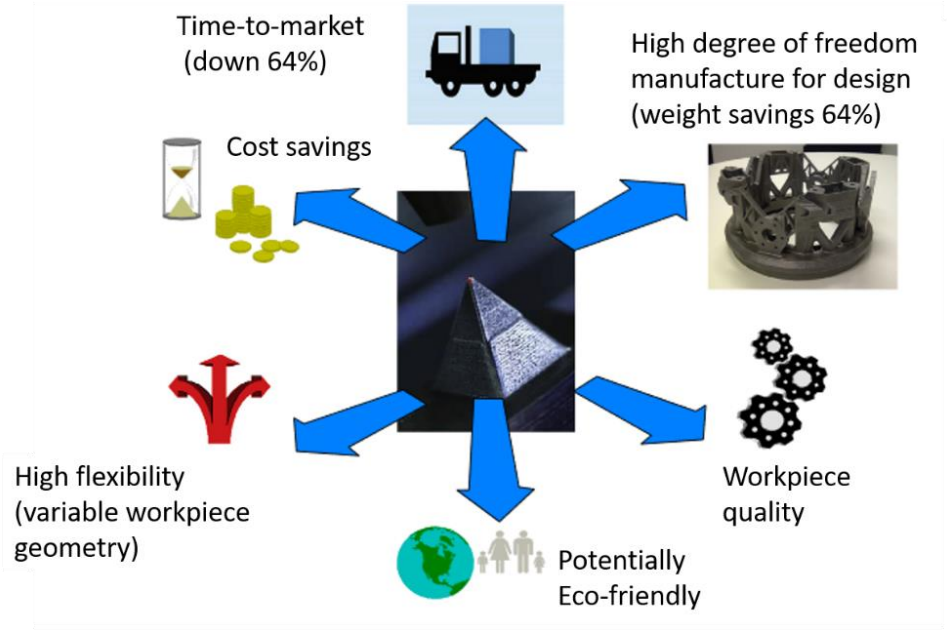

Figure 2.7: Schematic overview summarizing the advantages of additive manufacturing compared to classical metallurgical processes from [158]. *The data is from* [162].

Yap et al. [163] described the principle of SLM represented in Figure 2.8 a–b. The printing machines have two or three containers operating in atmospheric pressure or primary vacuum (100 -10^{-1} Pa).

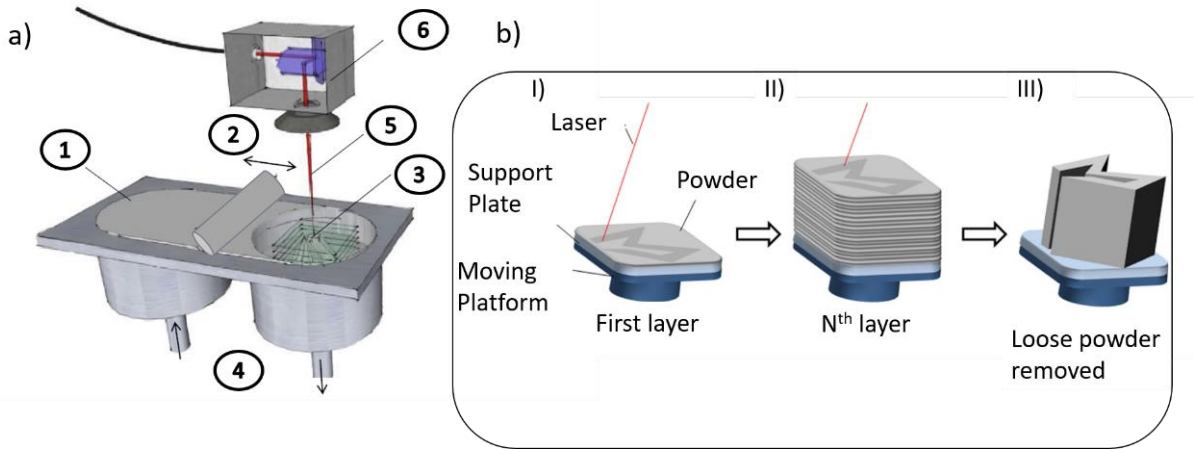

Figure 2.8: Representative scheme of SLM metal printing machine adapted from [163,164].

The feedstock is a reservoir (1) full of MA; a roller (or other mechanisms) (2) transports a precise quantity of MA to a support plate in the fusion zone (3). The layer of a chosen thickness is transported to the zone (3). According to the fabrication progress, the printed part grows, the MA is consumed from the container (1). The fused layer grows in the support plate (3). The bottom of containers (1) and (2) regulates their height (4) as the printed part is formed, so they are at the same level, and the roller can transport a new layer to the fusion zone. If a third container exists, it is as a collector, not represented in the scheme of Figure 2.8a. The principle is to heat the powder and melt only selected parts determined by the CAD project. Figure 2.7b state I) shows the fusion of the first layer. The new layer has to join the previously solidified layer without pores or cracks. Numerous parameters optimize the melting, such as scanning speed, hatch spacing[IX], spot[X], MA diameter distribution, and layer thickness [163]. This requires a laser (5) capable of producing a high-power density beam. The beam shape is typically Gaussian, or top-hat-shaped. After repeating this cycle several times, i.e. melting several layers, the part is ready. The final part is inside the MA in the format of a layer. This powder is compacted or sintered as presented in Figure 2.7b state II). A post-process step involving abrasive blasting removes the MA as displayed in Figure 2.7b. state III) [163,165]. Post heat treatments can be done for stress reduction or infiltration to eliminate pores [163,166].

When the laser melts the powder, a melt pool is created, a localized point where the Cu powder is liquid [167]. The melt pool lifetime is the period that the melted particles stay in the liquid state. The melt pool characteristic as dimensions, temperature, and duration dependents on the laser power and speed [167]. The melt pool duration increases at higher laser power and slow laser scanning speed [168]. The material properties play a role in the melting pool duration and temperature gradients. Cu melt pool is oval and tends to solidify faster than other materials. Other characteristics of the melt pool can be found elsewhere [167,169].

One drawback is that the fraction of laser power absorbed changes when the metal is molten. The absorption of laser power is greater for molten metal than solid metal. The reason is that clouds of vaporized metal can eventually form plasma above the melting pool. These clouds prevent energy from reaching the fusion zone. The pressure of the metal vapor's rapid expansion and superheated gases can create a depression in the molten pool trapping gases and further enhance absorption, causing a so-called keyhole formation [170]. This is often caused because the laser operates using higher power than necessary due to the poor absorption in the infrared range (1030 nm) [115].

SLM can print a wide range of materials, such as Ti, Ni, Fe, as well as ceramics, in atmospheric pressure, an advantage compared to conventional techniques used in metallurgy [171]. However, SLM printing is readily carried out for some materials, such as the most popular titanium alloy, Ti-6Al-4V it is still a challenge for Cu [115,172].

[IX] Distance between two welding tracks
[X] The area illuminated by a laser

2.3 Materials Characterization Techniques

The characterization techniques used in this thesis work are listed in Table 2.1 with corresponding references for the interested reader. The most used techniques are briefly described below.

Table 2.1: Characterization techniques utilized in this thesis work.

Technique	Equipment	Objective	Reference
Raman spectroscopy	Witech alpha300 R	Composition	[173]
X-ray diffraction	Bruker D8 ADVANCE Plus,	Crystallinity	[174]
Optical profilometer	Bruker GT contour	Roughness/thickness	[175]
Mechanical profilometer	Dektak	Roughness/thickness	
Electron Back Scattering Diffraction	Zeiss axio imager M2	Crystalline grains	[176]
Scanning electron microscope *	ZEISS Sigma HD	Thickness/topography	[177]
Optical microscope	Leica	Topography	[177]
Rutherford backscattering spectroscopy		Composition of high z elements	[178]
Nuclear reaction analysis		Composition of low z elements	[179]
Image treatment	Image J	Topographical analysis/measurements	[180]
Resistivity (four-point probe) *	Keithley	Composition/electrical properties	[181]
Ellipsometry	Horiba Jobin Yvon	Optical constants	[182]
Spectrometry Vis- IR*	PerkinElmer lambda35	Reflectivity	[183]
The Branly technique*	LPGP's homemade equipment	MA's behavior under a current flow	[184]

*Techniques described below

2.3.1 The Branly's Cohéreur

This technique is mainly described from a historical point of view since it is not yet entirely established nor commonly used. In 1890 Edouard Branly observed that electromagnetic radio waves could freely travel in open space. The discovery was possible because they observed the conductivity of iron dust. The iron dust was studied using the *cohéreur*[XI] apparatus consisting of a glass tube and two electrodes. The iron dust was between the electrodes, and its compression force was adjustable, as shown in Figure 2.9. The granular media *modifies its conductivity* in the presence of an electromagnetic field [185–187]. Several theories have come out about how the grains behave [185,188]. Some theories assert that grains form dipoles or electrostatic forces, inducing forming a conductive path [189,190]. He found out that the conductive path could easily end by a small shock in the *cohéreur*. To end the conductive path, they created a tool called 'the frappeur' or the striker represented in Figure 2.9. The main discovery was that a radio wave travels through the material in atmospheric pressure. Their findings developed communication using antennas. In 1900 – 1901 Guthe *et al.* [191] conducted more complex experiments to understand granular media conduction. Guthe's circuit used lower frequencies than in Branly's experiments. He employed more precise equipments such as millimeter[XII], galvanometer and an interrupter.

[XI] From Latin a synonym of bond or stick.
[XII] an instrument for measuring electric current in milliamperes.

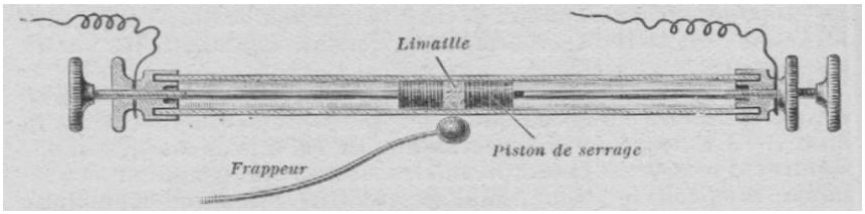

Figure 2.9: Original descriptive scheme of the apparatus used by Edouard Branly in 1888. A glass tube contains metal filings slightly compressed between two conductive plates (piston de serrage) using iron dust (limaille) and a striker (frappeur) (the compression force is adjustable). Adapted from Branly's manuscript [192].

This work proposes a different aim for the *cohéreur* to study the current flow in the metal additive, *3D printing*. Several similarities between the *cohéreur of 1888* and the one developed at the LPGP can be observed [192]. The detailed representation of the experimental setup and the circuit is presented in Chapter 6 were done in a plastic cohéreur to avoid wall conduction the 'LPGP *cohéreur'*.

The experimental setup shown in Figure 2.10 was built to the current flow in the MA. It is composed of an Arbitrary Waveform Generator (1) coupled with a direct current (DC) power supply (0–65 V) (2). Two probes registered voltage on an oscilloscope (3), the input V_1 (4) and output V_2 (5). A variable calibrated resistance R (6) is connected to the output MA crucible the 'V_3' (7)

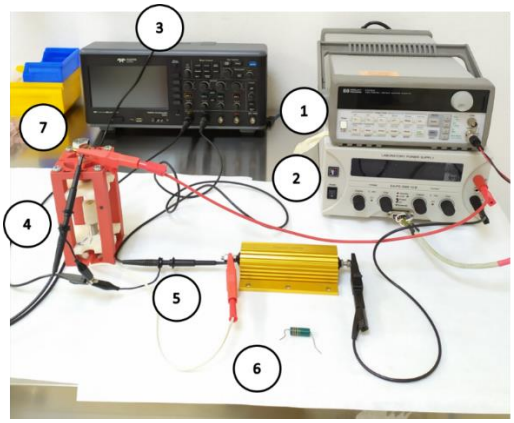

Figure 2.10: Description of the circuit used in this thesis: (1) function generator, (2) direct current (DC) power supply (0-65 V), (3) oscilloscope, voltage probes measuring (4) probe V1 and (5) Probe V2, (6) calibrated resistances 470 and 330k ohms, (7) powder support V_3.

2.3.2 Scanning Electron Microscopy

The simplicity of Scanning Electron Microscopy (SEM), where little sample preparation is required. The capability of producing high-resolution images makes this technique popular in industry and university. SEM can distinguish features in the order of tens of nm. As microscopes are developed, the magnitude decreases. The SEM uses electrons to form an image. A beam of electrons produced at the top of the microscope scan the sample surface. For example, a sharp point material is held in several negative kilovolts generating a strong field that emit electrons (the electron gun known as field emission gun (FEG)) near the anode. The electron beam follows a vertical path through the column of the microscope.

Once the electron beam hits the sample, it generates several emissions types, which contain different information. After the surface scan, the signals are detected and amplified. Important information is the magnification imaging and chemical analysis. Secondary electrons topographical images of the sample surface can readily be obtained. Furthermore, cross-

sectional images can be obtained by cleaving Si samples or cutting Cu plates[XIII]. Backscattered electrons generate contrasts varying according to their chemical weight. More than that, Auger electrons, X-rays and, photons can be emitted. The emission of characteristic X-rays brings the information about chemical elements present in the material [193]. SEM images were done at the *Institut de Chimie Moléculaire et des Matériaux d'Orsay* (ICMMO) and at Centre de nanosciences et de nanotechnologies (C2N).

Energy-dispersive X-ray spectrometry (EDS) employed a ZEISS Sigma HD EDS SAMx operating at 15 kV for chemical information also used for topography and cross-section images. This microscope also operates in backscattering mode, equipped with an electron backscatter diffraction (EBSD) system and a NORDIF CD detector. The software for quantifying the grains' orientation was the OIM™. Optical images were also taken with a Zeiss axio imager M2. Also, a Thermo Scientific Verios G4 HP (1 kV) was employed.

The cross-sections were polished using Cu standard metallography procedures (SiC foil grit 2,000) until active oxide polishing suspension 0.25 µm colloidal silica. Samples were electropolished, to produce a smooth surface and reveal crystallography grain of Cu welding by immersion as an anode in an electrolytic bath using a Struers LectroPol 5 with a 'D1'eletrolytic commercial solution for 12 s at the *ICMMO* laboratory.

2.3.3 Four Points Probe Technique

Electrical resistivity (ρ) measurements using the four-point probe technique is a standard routine for measuring the electrical resistivity of thin layers [181]. The simplest measurement setup consists of four small electrodes, equally spaced aligned in a straight line. The four points are placed over the thin film surface. The points might touch the film, and a substrate of higher resistance might be used to avoid misleading the resulting resistance.

A constant and low electric current is injected through the two outer contacts, while the voltage drop between the two inner contacts is measured with a high impedance voltmeter. In order to obtain the electrical resistivity, one needs to consider the geometry and the shape of the object at which the electric current is flowing. In the case of a thin film, one assumes an infinite 2D object, where electric current is supposed to flow cylindrically from the metal electrode [181]. Moreover, the film thickness (z) should be known and much smaller compared to the probe spacing (s) ($s \approx 1$ mm). Thus, the film ρ is given by the equation (2.1):

$$\rho = \frac{\pi}{ln\,2}\frac{V}{I}z \qquad (2.1)$$

where 'V' is the voltage, 'I' is the current and 'z' is the thickness.

2.3.4 Optical Spectrometry

Optical spectrometry analyzes the interaction of the material with light across a spectrum. In particular, optical spectroscopy was used to obtain the reflected incident radiation. The reflected intensity is composed of the specular reflectance when the light is reflected at an angle equal and opposite to the incident radiation (satisfying *Snell's law*) resulting in a mirror-like surface. And the diffusive radiation, when the radiation is scattered over a wide range of angles exhibiting a cosine response to the incident radiation results in an opaque surface. Optical spectrometry can also measure the quantity of absorbed light and the transmitted light of materials.

To measure reflectance, the integrating sphere of the equipment is calibrated with a Spectralon®. After the calibration, the sample is inserted into a sample holder. The sample position is normal or near-normal (8°) to the beam. The reflected radiation is collected by the

[XIII] In general, other materials than copper have standard metallography preparation for cross-section imaging.

sphere, which offers 180-degree field of collection. The detectors lie at another point on the inside tangent of the sphere and collect radiation. All the light that is not absorbed or transmitted is reflected (for transparent or very thin materials).

The measurement covers the near-infrared to the near-ultraviolet range. Deuterium, hydrogen, xenon, and tungsten are examples of lamps that emit wavelengths in different ranges and are commonly used in spectrometers.

A double-beam spectrometer is used in this study. A beam splitter separates the beam from a deuterium lamp into two channels. Approximately 50% of the source-emitted energy goes to the sample, and 50% to the reference, as indicated in Figure 2.11. The use of the dual-beam compensates instabilities inherent to all spectrometers [194]. The sample and reference beams are recombined at the phototube or photoelectric cell – the detector. The detectors compare the magnitude and phase of sample and reference signals. The complete optical path can be found elsewhere [195].

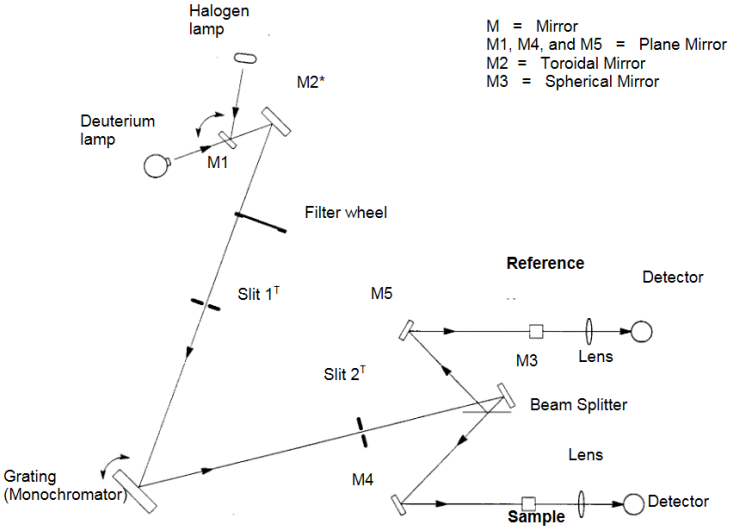

Figure 2.11: Schematic representation of a double beam optical spectrometer. Adapted from [195].

The reflectance of the films was measured using an integrating sphere calibrated with a Spectralon SRS99 PerkinElmer Lambda 35 UV-Vis spectrometer from 400 nm to 1000 nm (bandwidth of 2 nm) using two-sample holders. Near normal incidence,8° from the beam was employed for the samples deposited over a copper film and, normal incident beam for copper foils and MA, the diffusive reflectance. The Cu powder was analyzed using a PerkinElmer Lambda 950 until λ=2000 nm done at the *Laboratoire de génie électrique et électronique de Paris GeePs*. All measurements were repeated at least twice per sample in different surface sites.

2.3.5 Rutherford Backscattering Spectroscopy

Film composition and areal density were determined by Rutherford backscattering spectrometry (RBS) employing a 1.8 MeV $4He^{+}$ beam. The following equation was used to find the heavy elements in the sample. The reference and the sample peak ration are obtained from the equation (2.2) and (2.3):

$$\sum_{Bi} = \left(\frac{N°atoms}{cm^2}\right)_{Bi} \times \left(\frac{d\sigma}{d\Omega_{Bi}}\right) \times \Delta\Omega \times \text{dose} \qquad (2.2)$$

$$\sum_{Fe} = \left(\frac{N°atoms}{cm^2}\right)_{Fe} \times \left(\frac{d\sigma}{d\Omega_{Fe}}\right) \times \Delta\Omega \times \text{dose} \qquad (2.3)$$

One can consider that the cross-section is proportional to the square of the element atomic number (Z) as in equation

$$\frac{d\sigma}{d\Omega} \propto Z^2 \tag{2.4}$$

The final equation used to calculate the areal density of the sample is:

$$\left(\frac{N°atoms}{cm^2}\right)_{Fe} = \frac{\sum Fe}{\sum Bi}\left(\frac{N°atoms}{cm^2}\right)_{Bi} \times \frac{{Z_{Bi}}^2}{{Z_{Fe}}^2} \tag{2.5}$$

Where

$\sum_{Bi}$= integral peak area of the Bismuth used as reference;

$\sum_{Fe}$= integral peak area of the sample peak of representing the iron;

$\Delta\Omega$= Solid angle in steradians (sr);

$\frac{d\sigma}{d\Omega}$ = Cross-section (sr/cm ^{2});

Dose = the number of incident particles (μC).

The areas used in the calculation are present in Figure 2.12 a–b. The reference sample used is the bismuth implanted in Si is presented in Figure 2.12a. A representative sample composed of amorphous carbon stainless steel a-C:SS is presented in Figure 2.12b.

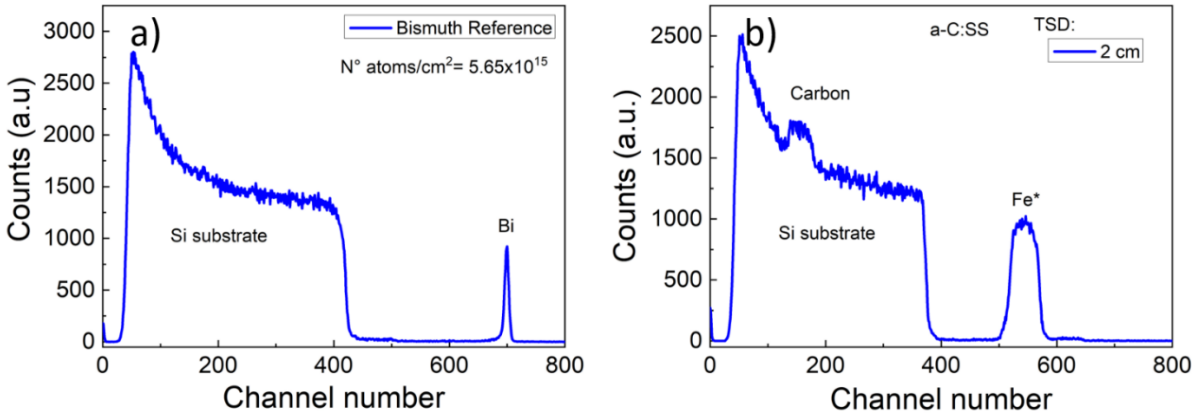

Figure 2.12: Rutherford backscattered Spectrometry (RBS) of a) the bismuth reference and b) the a-C:SS sample deposited at TSD:2 cm presenting the peak of carbon and Fe representing the metals of stainless steel.*

The complete set of samples is presented in chapter 3.

2.3.6 Nuclear Reaction Analysis

Nuclear reaction analysis (NRA) using a 950 keV deuteron beam was used to determine carbon quantity in the films. The equations used for NRA are displayed below, to find the ratio of the reference of oxygen and the sample carbon peak. First the reference is observed in energy of 850 keV (2.6):

$$\sum_{O^{16}} = \left(\frac{N°atoms}{cm^2}\right)_{O^{16}} \times \left(\frac{d\sigma}{d\Omega_{O^{16}}}\right) \times \Delta\Omega \times \text{dose} \tag{2.6}$$

Then the sample is analyzed using 970 keV:

$$\sum_{C^{12}} = \left(\frac{N°atoms}{cm^2}\right)_{C^{12}} \times \left(\frac{d\sigma}{d\Omega_{C^{12}}}\right) \times \Delta\Omega \times \text{dose} \tag{2.7}$$

The ratio of the cross-sections is $\frac{1}{5.56}$ as displayed below

$$\frac{\sum_{C^{12}}}{\sum_{O^{16}}} = \frac{\left(\frac{N°atoms}{cm^2}\right)_{O^{16}}}{\left(\frac{N°atoms}{cm^2}\right)_{C^{12}}} \times \frac{\left(\frac{d\sigma}{d\Omega O^{16}}\right)}{\left(\frac{d\sigma}{d\Omega_C}\right)} = \frac{1}{5.56}\frac{\left(\frac{N°atoms}{cm^2}\right)_{O^{16}}}{\left(\frac{N°atoms}{cm^2}\right)_{C^{12}}} \quad (2.8)$$

The areal density of carbon was calculated using the following equation:

$$\left(\frac{N°atoms}{cm^2}\right)_{C^{12}} = \frac{1}{5.56} \times \frac{\sum_C}{\sum_{O^{16}}} \times \left(\frac{N°atoms}{cm^2}\right)_{O^{16}} \quad (2.9)$$

Where $\sum_C$ is the integral peak area of carbon peak 1 and $\sum_{O^{16}}$is the integral area of the oxygen peak 1 reference.

The reference is presented in Figure 2.13a. The sample of amorphous carbon a-C deposited at Target to Substrate Distance (TSD)=2 cm is demonstrated in Figure 2.13b.

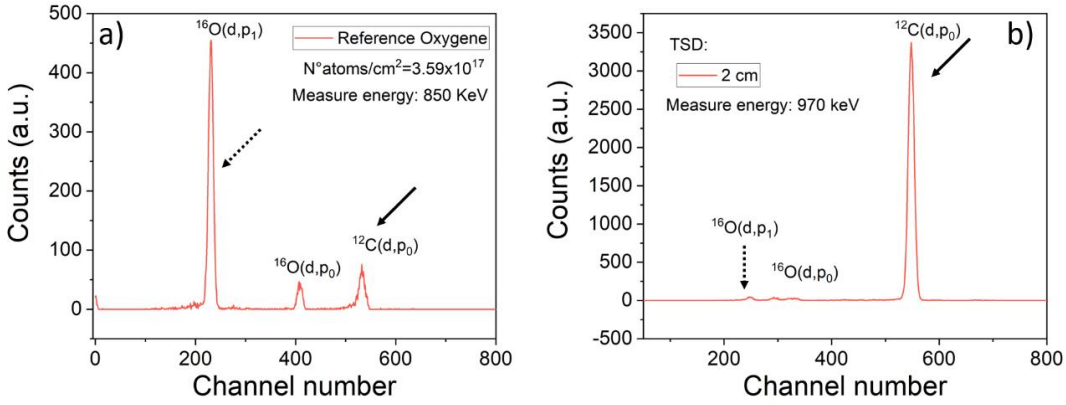

Figure 2.13: Nuclear reaction analysis (NRA) of a) the oxygen reference and b) the a-C sample deposited at TSD:2 cm.

The density (ρ_d) of the deposited thin film was obtained by measuring the areal atomic density NS in $\frac{N°atomos}{cm^2}$ by Rutherford backscattering spectrometry (RBS) and nuclear reaction and the thicknesses (z) were measured independently using SEM or optical profilometer [138].

$$\rho_d = \frac{NS_C \times M_C + NS_{Fe} \times M_{Fe}}{z} \times \frac{1}{N_A} \quad (2.8)$$

where M is the atomic mass for each element indicate in its indices and N_A is Avogadro's number as indicated in equation (2.8). RBS and NRA analyses were done at the *Institut de nanosciences de Paris, INSP, Sorbonne Université.*

2.4 Extra Parameters

Thickness measurements were performed with an optical profilometer (Bruker Contour GT-K) at five points covered from the deposition area (step measurement mode). The squared Si surface had points homogeneously distributed. The standard deviation obtained from the homogeneity tests is 20%. The optical images of the MA were done with a LEICA M165C IC80HD. The roughness was measured using the Bruker profilometer.

Raman spectroscopy measurements utilized a Witech alpha300 R at 532 nm wavelength magnification 20 X resolution 4 cm−1 9 mW for the structure of the film. Profilometry was used for surface roughness and thickness Bruker Dektak Stylus Profilometer 6M, and a mechanical profilometer Bruker Contour GT-K Vision 64.

One can find the techniques described in this chapter are essential to understand the objective of this work, although some of them appear more in specific chapters than others.

Precisely, in chapter 3, most materials characterization are mentioned as Four-point probe, RBS, NRA, Raman, profilometry, etc. Chapter 4 displays the reflectance measurements done with optical spectroscopy for different substrate and, a-C thicknesses. Chapter 5 presents SEM images of the laser welding. Finally, chapter 6 details Branly coherer's results using different Cu powder distribution size.

CHAPTER III: Physical Properties of Carbon Films

This chapter describes two sets of coatings deposited as a function of the target-to-substrate distance (TSD). Amorphous stainless-steel carbon (a-C:SS) and pure amorphous carbon (a-C) films were studied in TSDs, varying from 2 to 10 cm. The analysis of relevant film properties, such as topography, carbon hybridization, structure, density, and resistivity, are demonstrated in this chapter. The differences between the films grown at different distances from the cathode are discussed concerning the plasma process conditions.

Summary

Abbreviations Chapter III

AISI	American Iron and Steel Institute
a-C	Amorphous carbon
a-C:Fe	Amorphous carbon doped with iron
(a.u)	Arbitrary units
sp^3	Carbon hybridization, typical of diamond
sp^2	Carbon typical in graphite
σ_{coll}	Cross-section of neutral-neutral collisions
DLC	Diamond-like carbon
L_a	Graphite cluster size
In.	Inches
I	Intensity
λ_{mfp}	Mean free path
NC graphite	Nanocrystalline graphite
Pa	Pascal
P(z)	Probabilities for elastic collisions versus the thickness z
R	Reflectance
ρ	Resistivity
RBS	Rutherford Backscattered Spectrometry
SS	Stainless steel
sccm	Standard Cubic Centimeters per Minute
TSD	Target to substrate distance
ta-C	Tetrahedral amorphous carbon
I_D/I_G	The intensity of band D and G obtained in Raman Spectroscopy
z	Thickness
W	Watts
η_{gas}	Working gas density
XRD	X-ray diffraction

3.1 Chapter Introduction

The deposition of carbon coatings obtained by direct magnetron sputtering demonstrates the versatility of cold plasma processes for thin film. Among the vast carbon types, amorphous, stable allotropic forms and composites can be attained as thin films using plasma. The resulting arrangement depends on the plasma and substrate conditions [196].

A metal inserted in carbon (a-C:Me) enhances the composite conductivity [108,197]. Due to the metallic adatoms' relatively high mobility, a metal atom can bond to form carbides dispersed into the carbon host structure. Examples of metal are Fe, Ni, and Cr [108,109]. Grischke *et al.* [198] showed that a metal distribution within the DLC matrix is not homogeneous. The metal atoms form nano-clusters of carbides or metal atoms. Metals can create a carbide phase and the catalytic sp^2 structures [95]. In the case of iron-doped amorphous carbon films (a-C:Fe) (2% at.), the resistivity is one order of magnitude lower than pure a-C [199,200]. The choice of using metals from stainless steel (SS) (Cr, Ni, and Fe) noted SS hereafter includes cost and the enhancement of optical constants and resistivity of the deposited carbon-based films.

This thesis studied amorphous stainless-steel carbon (a-C:SS) and pure amorphous carbon (a-C) properties in different TSD from 2 cm to 10 cm. Once the fundamental film properties have been established, the objective is to find the best film properties as a function of TSD to the continuity for this work.

3.2 Methodology

3.2.1 Experimental Conditions

Carbon-based films were deposited onto Si (100) substrates using magnetron sputtering described in Chapter 2. The substrate sizes were 22 mm^2-62 mm^2 with a Si resistivity of ρ_{Si} = 10–14 Ω cm. Before film deposition, each Si substrate was cleaned in acetone and isopropanol using an ultrasonic bath for 30 min in each substance and then loaded into the grounded sample holder. Once the samples were loaded, the main chamber. The chamber is locked and pumped to a base pressure below 3×10^{-3} Pa. The chamber was then filled with argon (Ar) (99.997% purity). The working pressure was 0.5 Pa (3 sccm of Ar). The film deposition employed a DC source constant power at 55 W ± 2 W for all the samples of this thesis.

For the deposition of a-C:SS films, a stainless-steel ring, composition AISI 316 (1 in. external diameter, 2 mm thickness), was positioned around the edge of the carbon target to produce a mixed sputtering. The ring target composition is given in Table 3.1.

Table 3.1: Composition of the ring target used for a-C:SS depositions

Stainless Steel Composition	Composition wt. (%)
Ni	8-14
Cr	16.5-20
Mn	<2
Mo	2-3.5
Fe	60.5-73.5

All films were deposited at room temperature (*i.e.*, without additional heating to the substrate). All parameters described above for a-C and a-C:SS depositions were maintained for all the samples. The variable is the position of the sample holder to the target, referred to as a target to substrate distance (TSD). The TSD of 2,3,5 cm and 10 cm were tested in this series. The TSD length is demonstrated in Figure 3.1. The TSD values present an incertitude of ±5 mm.

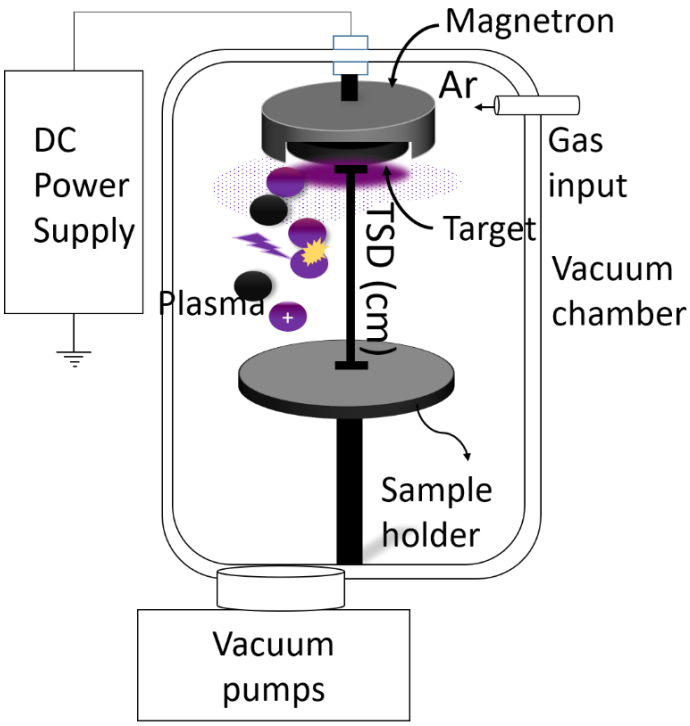

Figure 3.1: Schematic representation of the experimental setup's frontal view and the deposition the target-to-substrate distance (TSD).

The deposition rates for each TSD are summarized in Figure 3.2. The rate decreased significantly in both cases with increasing TSD (up to 95% for a-C and a-C:SS films). Note that the deposition rate for a-C:SS films is averaged 57% higher than pure C, mainly due to the higher sputter yield of iron[XIV] when sputtering the stainless steel ring target [56]. Furthermore, the deposition rate of both a-C and a-C:SS decreases with $1/TSD^2$, as expected for an approximately conical emission of the material from the sputtering target.

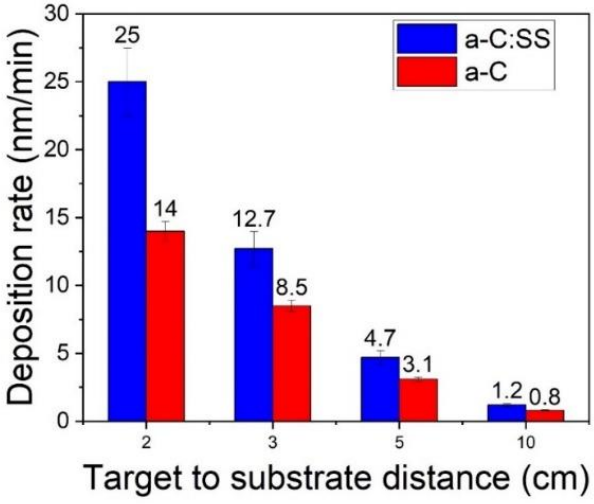

Figure 3.2: The graph indicates the average deposition rate at different TSD for a-C and a-C:SS films were grown using DCMS in Ar at 0.5 Pa and 55 W average power.

The thickness of the carbon-based films were maintained at 150 nm ± 30 nm by adjusting the deposition time.

[XIV] The deposition rate of AISI 316 was approximated to Fe data due to its quantity in the composition

3.2.2 The Effect of the Target to Substrate Distance on the Material Flux.

The plasma species interact with the substrate to create a film whose properties depend on the deposition conditions. All the properties studied in this chapter are reported as a function of TSD. Before addressing the film properties, it is instructive to discuss how the choice of TSD influences the flux of material arriving at the substrate. The energy of the film-forming flux is a key factor influencing the microstructure, affecting adsorption and other elementary processes during thin film growth [36,55,201].

The mean-free path (λ_{mfp}) of the sputtered species depends on the cross-section of elastic neutral-neutral collisions (σ_{coll}) and the working gas density during deposition (η) represented by Figure 3.3. A typical σ_{coll} from Phelps *et al.* [35] is assumed $2x10^{-19}m^2$ for argon at room temperature.

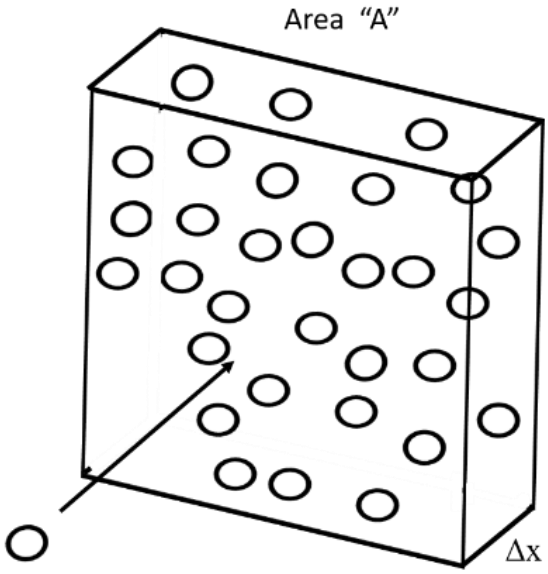

Figure 3.3: Representation of neutral-neutral collisions. The scheme indicates a neutral approaching a volume containing a gas in a slab Δx and cross-section area A. Adapted from [34]

Considering the elastic collision, the mean free path (λ_{mfp}) can be estimated by equation (3.1):

$$\lambda_{mfp} = \frac{1}{\eta_{gas} \times \sigma_{coll}} \tag{3.1}$$

The argon density (η_{Ar}) is $2.4 \times 10^{20} m^{-3}$. at 1 Pa and at 300 K. It scales linearly with pressure, so at the working pressure of this work 0.5 Pa[XV] it is $1.2 \times 10^{20} m^{-3}$ [30,31,36]. The $\lambda_{mfp}$is around 4 cm for the deposition parameter of this thesis.

The probability of having an elastic collision ($P(z)$) can thereby be calculated for any distance 'z' from the target using Eq. (3.2), λ_{mfp} can be estimated using Eq. (3.2)[36].

$$P(z) = 1 - e^{\left(\frac{-(z)}{\lambda_{mfp}}\right)} \tag{3.2}$$

All the $P(z)$ values are given in Table 3.2, calculated using the typical λ_{mfp}= 4 cm. For a TSD of 10 cm, it is seen that almost all sputtered neutrals undergo at least one collision with the Ar working gas *en route* to the substrate. However, only about half of the sputtered population collides with the working gas if the substrate is close to the target, TSD = 2 cm

[XV] One might consider pressure measurement errors due to the gauge position in the chamber, contamination [372]

[202]. This means that particles with typical sputter energies of a few eV will retain that energy when arriving at the substrate located at 2 cm [203].

From Monte Carlo simulations of sputtered species in DCMS, one can estimate the expected particle velocities depending on TSD. For example, studies on Ti in Ar show that the peak of the velocity distribution of sputtered Ti changes from about 2000-2600 m/s at 1 cm to close to thermalized at 5 cm (a few hundred m/s) at a working gas pressure of 0.4 Pa [202]. No significant velocity reduction is expected beyond that distance since the particles are already essentially thermalized.

Note that scattering on argon is not only slowing down the sputtered species. It also changes the flight direction and thereby reduces the flux of precursors to the substrate, which is directly linked to the deposition rate. The further the substrate from the target, the larger the number of sputtered species lost at the (lateral) walls.

Table 3.2: Estimation of the probabilities for elastic collisions $P(z)$ of sputtered particles for a mean free path of 4 cm using 0.5 Pa of Ar for the sputtered thin films.

TSD (cm)	$P(z)$ (%)
2	38
3	51
5	70
10	91

3.3 Analysis of Film Properties as a Function of TSD

3.3.1 Microstructure and Composition

Figure 3.4 shows the topography SEM images of the deposited carbon-based[XVI] thin films. Generally, the morphology is affected when decreasing TSD. The films present almost the same continuous morphology. For a-C, the surface is typically compact. At TSD = 5 cm, one can notice only sparse multiple protruding round shapes, mainly for a-C:SS shown in Figure 3.4 e-f.

At TSD = 10 cm, both films present a granular morphology Figure 3.4g and h. The measurements of the topography width of these features revealed that a-C:SS contains bigger structures. For a-C, the topography grains are averaged 17.5 nm ± 5 nm. Meanwhile, these structures are larger, around 40 nm ± 14 nm for a-C: SS. These granular structures are found in a-C:Me film, such as Ni and Cr [204–206]. Similar structures using DLC with tungsten deposited by cathodic arc reported that as the surface protuberance increased, the tungsten percentage went from 50% to 85% wt. [53,205,207].

The film structure follows the general model proposed by Thornton [208]. After the initial nucleation, the films deposited close to the cathode present a smooth surface characteristic of Zone T (see chapter 1). Films deposited far from the cathode exhibit a two-phase structure composed of voids and denser zones, as shown in Figure 3.4g and h Column with a characteristic diameter connects fine zones of low density (inter-columnar phase) for low temperature deposition [54,56].

[XVI] Refers to a-C and a-C:SS.

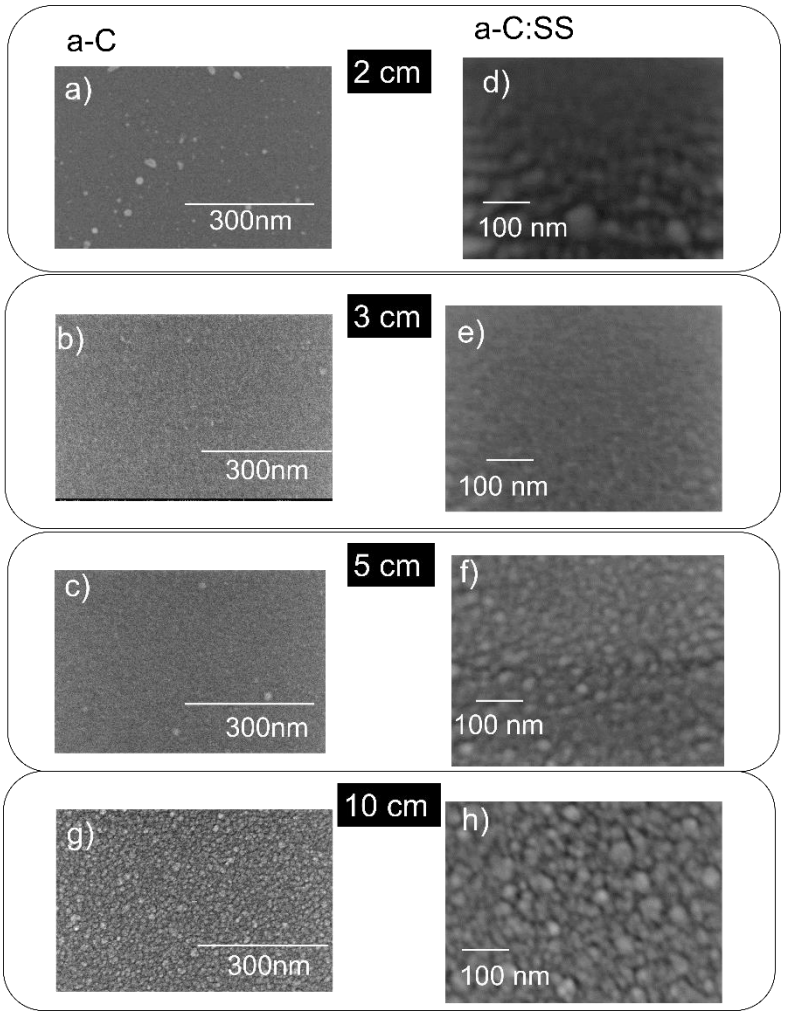

Figure 3.4: SEM topography micrographs of a-C films (left column) and a-C:SS (right column) deposited at TSD 2,3,5 cm and 10 cm. Note the different magnification between a-C and a-C:SS films.

The two-phase structure indicates anisotropy in the physical properties of the deposit [28]. Two zones are clearer for samples deposited at TSD = 10 cm. Figure 3.5 revealed the grainy columnar structure of the composed film a-C:SS deposited at TSD = 10 cm. Similar microstructures were found for amorphous metal films deposited by the electron beam evaporation [209].

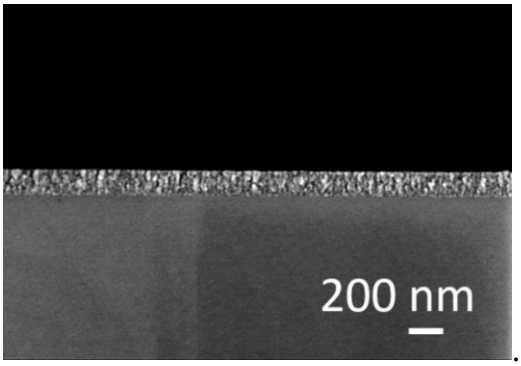

Figure 3.5: Cross-section of a-C:SS films at TSD = 10 cm.

Rutherford Backscattered Spectrometry (RBS) spectra show the influence TSD in the film composition presented in Figure 3.6 a–b.

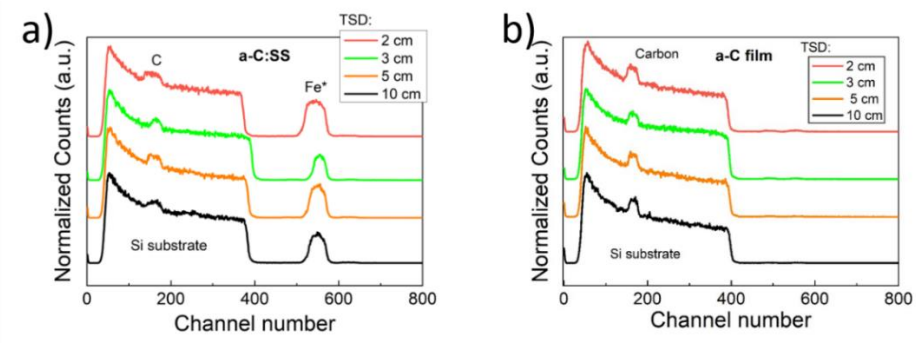

Figure 3.6: RBS spectrum of all TSD for a) a-C:SS and b) a-C. The peak of Fe may contain other metals from the SS target. Si substrate presents a thicker peak due to its thickness compared to one of the deposited films.*

One can notice that RBS identified three peaks for a-C:SS in Figure 3.6a, the Si used as a substrate (wide peak), the carbon, and some metals of the stainless steel (SS), while only the Si and C peak are observed in Figure 3.6b. The Fe* peak mainly comprises Fe, Ni, and Cr [210]. The RBS spectra demonstrated that stainless-steel composition was practically constant within the films. EDS analysis further confirms the presence of other metals than Fe in the film. The RBS of pure AISI316 can be found elsewhere [211]. One can notice that Figure 3.7 presents stainless steel metals. The main element detected was Fe with traces of Ni, Cr and O [212].

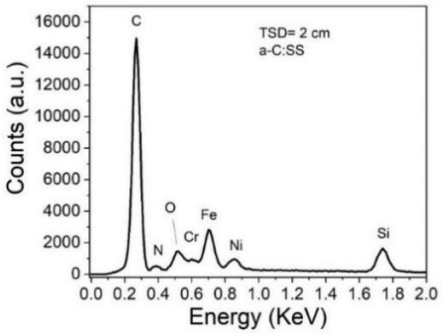

Figure 3.7: Representative EDS analysis of a-C:SS at TSD=2 cm.

The carbon contents in the films were analyzed using NRA to improve the resolution of lower atomic number elements contained in the films. The NRA spectra are presented in Figure 3.8 a–b. The RBS in Figure 3.6a and the NRA carbon peak in Figure 3.8a reveal the ratio of metals and carbon in a-C:SS. This film presents 50% at. of Fe with traces of Cr, Ni, and O and 50% at. of carbon for all analyzed samples. The small oxygen peak appears attributed to the oxidation of the stainless steel for higher TSD > 3 cm. The quantity of SS metals in the film is high, so a-C:SS films are a composition of amorphous carbon and metals. In contrast, the NRA confirms the presence of only carbon in the a-C shown in Figure 3.8b.

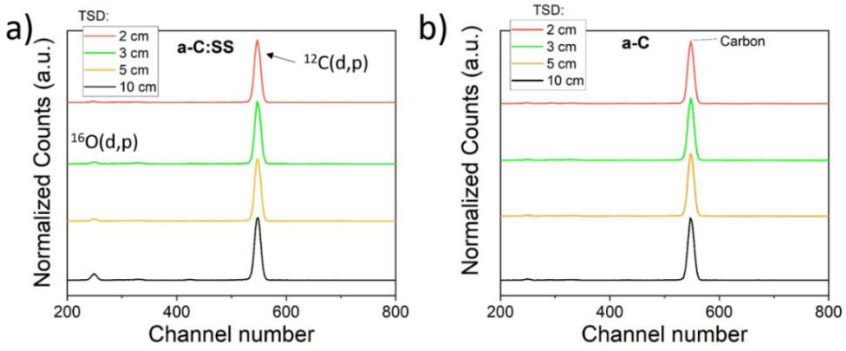

Figure 3.8: NRA Spectra of a) a-C:SS and c) a-C for carbon peak.

Figure 3.9 displays the density calculated from RBS and NRA spectra. The highest density is found in both samples at the smallest TSD = 2 cm. As a general tendency, a higher density is observed at 2 cm. After 3 cm for a-C:SS density barely varies with TSD. The density of 2 cm is 1.42 g/cm^3 for a-C and, 2.8 g/cm^3 for a-C:SS. Beyond 3 cm, thin film density is constant at around 1 g/cm^3 for a-C and 2.2 g/cm^3 for a-C:SS.

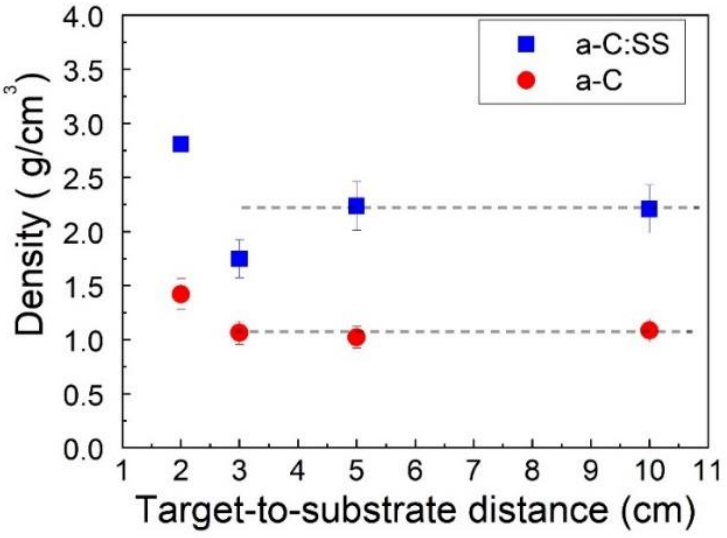

Figure 3.9: Film density comparison of a-C and a-C:SS. The dashed lines guide the eyes in the film density comparison.

The evolution of the density is attributed to the mean-free path. In small TSD, such as 2 cm, carbon species impact the surface up to several electron volts. The higher energy of imping electrons increases the adatom mobility and can densify the film structure. The reduction in the film's density at higher TSD can be attributed to the lower energy of the material flux [29,213,214]. The material flux corroborates the film's observed morphology which contains voids among the columns mainly identified at TSD= 10 cm. Considering the mean free path calculated in the section 3.2.1. The morphology presenting voids happens in distances >> λ_{mfp} (4 cm) the atoms reaching the substrate are largely thermalized due to elastic collisions [215].

The internal structural arrangement of the material was analyzed with Raman spectroscopy and X-ray diffraction (XRD) as a function of TSD. On the one hand, XRD did not detect any crystalline peak. Thus, the analysis is not shown in this manuscript. On the other hand, Raman spectroscopy of the deposited samples demonstrated the characteristic G and D bands of carbon, the I_D/I_G ratio calculation as Figure 3.10 a–b.

The characteristic of Highly Oriented Pyrolytic Graphite (HOPG) Raman bands is the G band at the precise position of 1581 cm^{-1} while the D band does not appear [216,217]. When the G band shifts from the HOPG position and the D band appears they indicate that the carbon is amorphous due to its structural characteristics as the presence of aliphatic chains as discussed in Chapter 1 in the section 1.1.4 [51,107,217]. The D band's shape depends on the cluster size, bonds in chains or odd folded rings, and carbon hybridization's ratio sp^2/sp^3 [29,216,218].

In Figure 3.10a, one can notice that the G band for a-C:SS deposited at TSD = 2 cm is at 1560 cm^{-1}, while for other TSDs G band position shifts to around 1547 cm^{-1}, the D band is at 1371 cm^{-1}. In Figure 3.10b, the bands for a-C films are demonstrated. The G band position is constant at 1541 cm^{-1}, meanwhile, the D band is at 1355 cm^{-1}. Note that the G and D bands are in lower positions for a-C compared to a-C:SS films. The I_D/I_G gradually decreases with TSD accordingly.

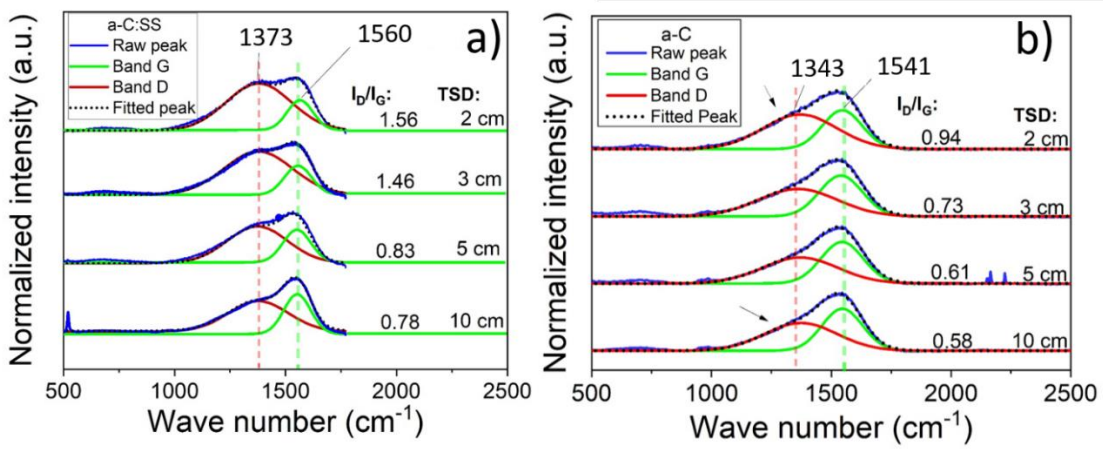

Figure 3.10: Raman microscopy of a) a-C and b) a-C:SS the vertical dashed lines indicate the band positions. The values indicated in the graphs are for TSD =2 cm.

One possible interpretation of a-C films Raman spectroscopy is the stages of carbon amorphization summarized in Figure 3.11[216].

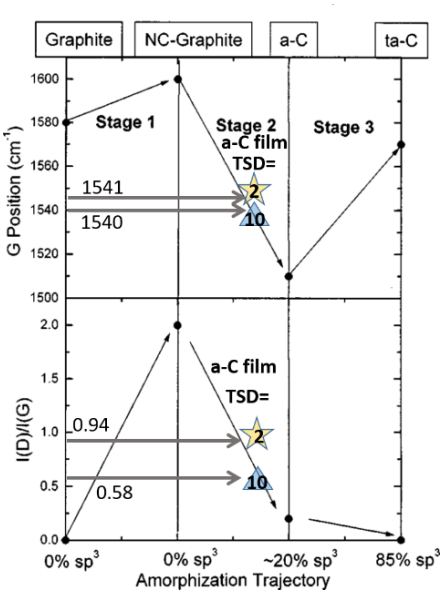

Figure 3.11: Three stage amorphization trajectory: G position and I_D/I_G ratio. The yellow star represents TSD =2 cm, and the blue triangle represents 10 cm. Adapted: [216].

The three-stage model shows how the carbon varies according to the G and I_D/I_G position versus the sp^3 (%). The diagram describes the 'amorphization path' from stage one, a perfect, infinite graphite sheet to stage three demonstrating the amorphous tetrahedral amorphous carbon (ta-C) containing 85% of sp^3 sites. Regarding the G position and the I_D/I_G, one can tell where the material is in the diagram of Figure 3.11. Stage one shows the progression of graphite to nanocrystalline graphite (NC- graphite). On stage 1, the D band appears [219]. Stage 2 represents the amorphization of NC-graphite into amorphous structures. In these stages, the film can present clusters and defects such as distortions and different bond lengths [216,219].

According to Ferrari *et al.* in stage 2 [216], I_D/I_G is proportional to the size of sp^2 domains or clusters in the films according to equation (3.3):

$$\frac{I_D}{I_G} = BL_a{}^2 \tag{3.3}$$

where B is a constant dependent on the excitation energy used in the Raman analysis and L_a is the graphite cluster size (or in-plane correlation length) [204,216]. Lastly, stage 3 is when the films increase sp^3 content, and the G position shifts to a higher position.

The a-C films of this work are in stage 2, as shown in Figure 3.11. Structure disorder slightly increases with TSD [29,216,220]. The samples deposited at TSD= 2 cm (star) and 10 cm (triangle) are indicated in the diagram [221]. Equation (3.3) shows that the sp^2 cluster decreases with TSD for the a-C samples. The films grown at 10 cm have smaller cluster sizes than those deposited at 2 cm [222].

Overall for a-C:SS films contain larger clusters than pure a-C films. The cluster size is consistent with the G peak shifts to higher wavenumbers and a higher intensity of the D band peak [216]. The larger clusters corroborate the metal catalyzes sp^2 sites in the amorphous matrix [9,53,204,223].

Amorphous carbon films were expected due to the relatively low energy involved in these depositions. The absence of biasing or heating the substrate leads carbon to be deposited with little energies (1–3 eV) [145].

3.3.2 Electrical Properties as a Function of TSD

Figure 3.12 shows the resistivity of the deposited a-C and a-C:SS films. The resistivity increases with TSD. The a-C films deposited at TSD = 2 cm and 3 cm have an average resistivity of 2.5×10^5 μΩ cm, see Figure 3.12 (red squares). This value agrees rather well with sputtered films deposited under similar conditions [104,224]. The measured value of resistivity for a-C at TSD= 5 cm and 10 cm is higher since the resistivity values were out of the used equipment range. So, it was not possible to measure the effective value of the film's resistivity.

On the other hand, the resistivity of the a-C:SS films is significantly lower for all studied TSD values. For the a-C:SS films at TSD = 2 cm, the resistivity is 1.3×10^3 μΩ cm, and at TSD =10 cm it is 3×10^4 μΩ cm

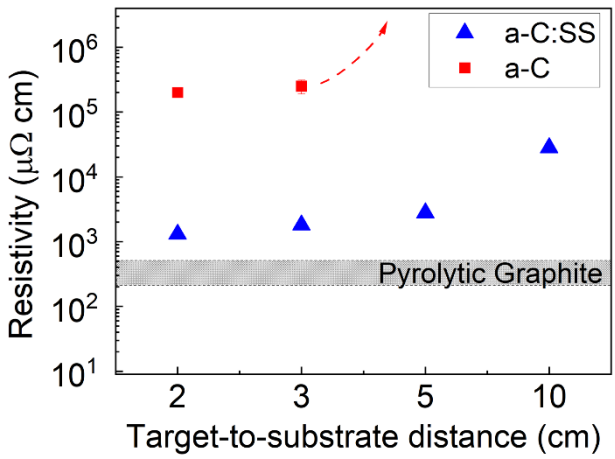

Figure 3.12: Resistivity of a-C and a-C:SS as a function of TSD.

The a-C:SS presents a reduction by two orders of magnitude at TSD = 2 cm compared to a-C due to the lower bulk resistivity of iron of 10.1 μΩ (0.04% of the a-C resistivity) [199]. The a-C:SS presents a reduction by two orders of magnitude at TSD = 2 cm compared to a-C (Figure 3.12). The reduction can be attributed to the addition of a metal in the carbon matrix that generally modifies the grain/cluster size [209,225,226]. According to the literature, metals like iron catalyzes sp^2 clusters, the composed films contain clusters with better conductivity [205]. One also has to consider the quantity of alloy in the film composition, the current can create paths through metal atoms reducing the resistivity [227,228]. Solovyev *et al.* [204]

reported similar resistivity for a-C:Ni. Amorphous carbon film containing 50% at. of Ni, deposited by pulse magnetron sputtering at a working pressure of 0.3 Pa presented 2.2 $\times 10^3$ μOhm cm applying a bias high-voltage pulse to the substrate (-3 kV). This resistivity is similar to the a-C:SS deposited at TSD= 2 cm and 3 cm deposited in this work.

A key factor for the observed resistivity trend as a function of TSD is the film structural changes and density. The plasma deposition process is dynamic and defines the final carbon structure, as mentioned in chapter 1. The sample deposited at 2 cm is denser than those deposited at higher distances, as shown in Figure 3.9. It presents a more compact morphology and a larger sp2 cluster. The features of samples deposited at TSD = 2 result from more energetic species during the deposition favoring the electrical properties [54,229]. The λ_{mfp} is 4 cm, hence at TSD =2, the sample is under a ballistic regimen during deposition. On the contrary, at TSD = 10 cm, results in thermalized atoms due to collisions. The structure at TSD =10 cm follows the model of Thornton *et al.* [54]. The thermalized species during deposition are responsible for the granular structure, not interesting for resistivity[45]

The comparably low film resistivity observed for the a-C:SS/Si samples can be further optimized by tailoring the film thickness, as shown in Figure 3.13.

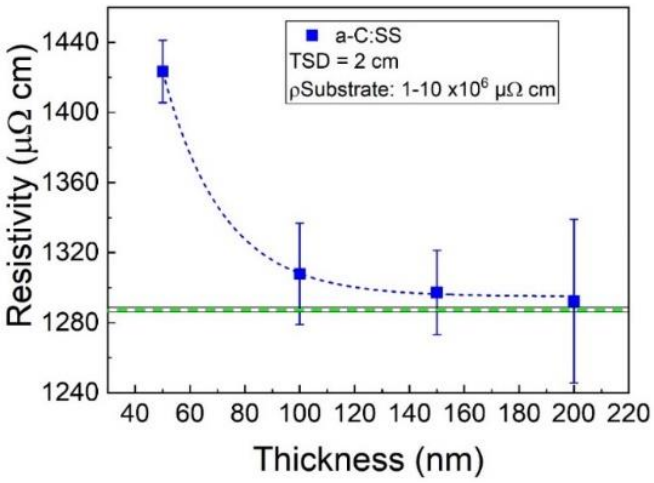

Figure 3.13: Thickness dependence of a-C:SS electrical resistivity deposited at TSD = 2 cm

Basically, exponential decay of the resistivity is observed, as the film thickness increases. At around a film thickness of 100 nm, the resistivity approaches 1280 μΩ cm, which is in the range of reported resistivity values for amorphous graphite and other amorphous metal composed films a-C:Me [110,197,204,230].

The observed trends agree with thin films' cluster size and scale nucleation. In general, the resistivity continuously decreases with an increase in the coating thickness, and should be constant for thick sputtered films [28,231]. Temperature and density enhance localized sp^2 states for the a-C coatings [28,216,231]. Another effect is the electron mobility inside ultra-thin films. The limited movement of electrons in low thicknesses increases the resistivity. According to this effect, as the thickness increases, the resistivity reduces [232].

3.4 Conclusion

The amorphous carbon-based microstructure film's properties vary as a function of TSD. The variation is due to the plasma the species interaction with the substrate during the deposition. The a-C and a-C:SS films deposited closer to the cathode are denser with smooth

morphology. On the contrary, the sample deposited at TSD = 10 cm shows a granular morphology with voids due to thermalization and scattering on the plasma species.

XRD indicated amorphous films and, the Raman Spectroscopy confirms that the films are composed mainly of amorphous sp^2 sites with clusters that can contain NC graphite. The film resistivity increases with TSD. The higher resistivity is due to the grainy morphology, the lower density, and the amorphous character at higher TSDs. The films deposited at TSD=2 cm and 3 cm presented the lowest resistivity of the series for a-C and a-C:SS. The main difference between the films is the incorporation of about 50% at. of stainless-steel metals such as (Cr, Ni and, Fe) in the amorphous matrix. The a-C:SS films resistivity at TSD =2 cm is 1.3×10^3 μΩ cm and for a-C films deposited under the same conditions is 1.3×10^5 μΩ cm. The metal composed film presents a resistivity reduction by up to two orders of magnitude. The amorphous films deposited close to the target using DCMS show the best morphology, density, and resistivity in this work set. Consequently, the samples deposited at TSD = 2 cm and 3 cm are used for the next step of this work.

CHAPTER IV: Reflectance of Amorphous Films on Cu substrates

Chapter IV studies the optical properties of the samples deposited close to the target. The main optical experiments on amorphous carbon films are described over Cu films, copper foils, and copper powder.

Summary

Abbreviations Chapter IV

μ	Absolute magnetic permeability
R_a	Arithmetic average height
λ_i	Characteristic wavelength in a medium
R_{exp}	Experimental Reflectance
n_i	Extinction coefficient
f	Frequency
IR	Infrared
LPBF	Laser Powder Bed Fusion
μ_r	Magnetic permeability
MA	Metal additive
MR_{exp}	Minimum experimental reflectance
Mz	Minimum reflectance without loses
MR_{th}	Minimum theoretical reflectance
NC graphite	Nanocrystalline graphite
δ	Penetration of the light intensity of good conductors
d	Penetration of the light intensity in semi-conductors
χ^2	Probability density function-statistical significance of the data
Ref.	Reference
R	Reflectance
n_r	Refractive index
ρ	Resistivity
sccm	Standard Cubic Centimeters per Minute
TSD	Target to substrate distance
R_{th}	Theoretical Reflectance
UV	Ultraviolet
μ_0	Vacuum permeability
λ	Wavelength

4.1. Chapter Introduction

The ability of ultra-thin film to reduce the reflectance can effectively improve the energetic performance of SLM. In general, copper demands extra energy for melting when an IR laser provides the power [233]. Three concepts inspire this work, the strong absorption of lossy ultra-thin film over a metal [234], the carbon nanotubes deposited between 10 nm and 100 nm [235], and infused materials [236]. The concept of infusion means, for example, the carbon infused into the metal using high currents, such as carbon steel [237]. The three concepts have one thing in common: the addition of minimal quantities of material. For example, small amounts of carbon in the copper (Cu) matrix can potentially improve electrical properties [236,238]. The innovative research on lossy coatings over metal substrates shows an efficient strategy to decrease reflectance [234,239]. The strong absorption of light in ultra-thin film coatings is of great interest due to little extra material added in RF, terahertz [240] mid-infrared, [241], near-infrared [242,243], and visible [244–246]. Ultra-thin films of metal, carbon nanotubes, graphene, and conductive polymers simultaneously exhibit high mechanical flexibility, low cost, and good optical properties [235,247,248].

Carbon films in minimal quantities can accomplish the task of absorbing further reflected laser energy with minimum or no modifications to the substrate in copper 3D printing [122,233]. The novelty is using ultra-thin films over metal additive (MA) or Cu powder, the feedstock of 3D metal printing. This work employs amorphous carbon, a simple and eco-friendly solution that reduces reflection on a broad spectrum [245,246]. The advantage of controlling carbon electric and optical properties is that they depend on the characteristics of sp^2 orbital bonds, such as bond angles, length, clusters, and the addition of metals like Fe, Ni and W [53,94,249].

The objective is to demonstrate that ultra-thin carbon-based film can reduce the reflectance of copper substrates. The analysis of reflectance reduction involved different thicknesses a-C and a-C:SS films over Si/Cu films, foils, and MA.

4.2. Methodology

The method describes the reflectance measurement of amorphous carbon over different copper substrates. At first, the description of pure copper is clarified.

4.2.1. The Copper Reflectance

The pure copper reflectance is 55% below λ= 580 nm (UV-green light), while beyond λ= 650 nm (red – IR), Cu reflects 98% of the incident light. Copper absorbs ultraviolet and visible energy below 580 nm due to the electronic structure of orbitals resulting in its red color [67]. Figure 4.1 shows the reflectance of copper foils, films, and MA. Copper film reflectance increases in a ramp until it reaches a maximal reflectance at λ = 1000 nm. The metal additive progression of reflectance as a function of the wavelength is valid. However, the absolute values are not displayed since the sample was encapsulated for safety reasons, as demonstrated Figure 4.6. Copper foil presents a similar trend. Hence, the substrate is the reference of maximal reflection. The Cu film deposited by DCMS surface is mirror-like reflective, so a near-normal incident beam (8°) was employed in the reflectance measurements, and normal incident for copper foils and Cu powder due to their opaque aspect.

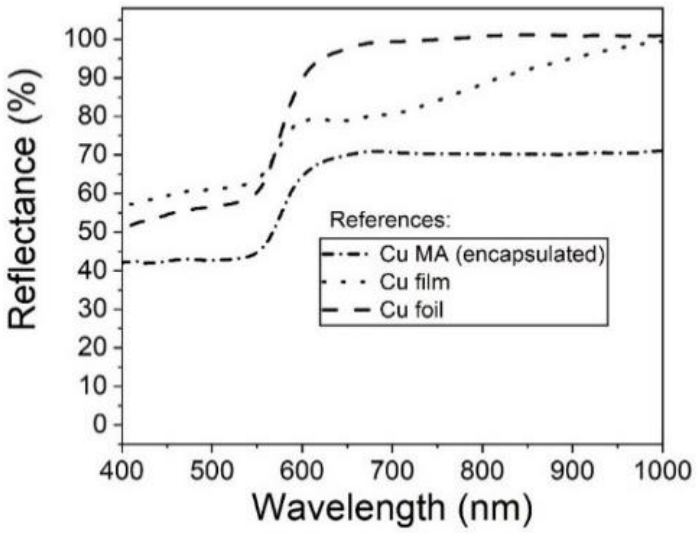

Figure 4.1: The reflectance of the substrate reference used in the work.

4.2.2. Copper Films

The first set of samples presented is the copper films coated with amorphous carbon or amorphous carbon iron films deposited in two steps as described below.

4.2.2.1. Copper Films – Substrates

The copper films were deposited over Si (100) (ρ Si =10–14 Ωcm). The samples of around 22–65 mm^2 were placed in an industrial reactor called A650, typical in several laboratories and industries in France. The reactor contains a turbo-molecular pump that evacuates the main chamber to a base pressure below 3×10^{-4} Pa, and a copper target (99.99% purity) clamped to a 6 in. top-mounted water-cooled magnetron. The target-to-substrate distance was fixed at 13.5 cm. The copper films were grown using argon (99.997% purity) as a working gas at 0.5 Pa (50 sccm). The thickness of the films was 200 nm ± 20 nm. The DC voltage applied to the magnetron was constant at 300 V -60 W±20 W). The resistivity of the copper films was around 5 μΩ cm (Cu bulk 1.67 μΩ.cm), which agrees with previous studies for deposited Cu thin films [65]. Cu films are used because they are shiny surfaces when newly deposited. The steps of depositions are described in Figure 4.2 a–b.

4.2.2.2. Amorphous Films Deposition

The copper films were transferred to a smaller chamber for carbon-based[XVII] thin film deposition (section 3.2). The depositions were carried out using a DCMS facility. The power applied to the target was 50 W ± 10 W. All films were deposited at room temperature, at 0.5 Pa (3 sccm of argon). Based on the properties of chapter 3, highlighting the fastest deposition rates, the samples were placed close to the cathode at TSD=2 cm and 3 cm. This chapter compares the a-C and a-C:SS to an arbitrary thickness value of 150 nm. After, the a-C thickness varies from 14 to 400 nm to demonstrate the influence of the film thickness over copper with minor roughness Ra =5 nm. This set of Si/Cu films is represented in Figure 4.2 c. and is later compared to commercial copper foils.

[XVII] It refers to a-C and a-C:SS

Figure 4.2: Schematic representation of the sandwich-like samples using a) Silicon as substrate; b) 200 nm of copper films were deposited using DCMS, and lastly, c) carbon-based films were deposited over the Si/Cu films.

4.2.3. Copper Foils

The second substrate is 110 µm thick flexible copper foils. The foils are easier to handle than Cu powder employed in 3D printing processes. In addition, their thickness of 110 µm is comparable to the larger diameter of the Cu powder distribution of 45–106 µm. The larger diameter is the hardest bead to fuse, and the copper foils are in the same thickness range represented in Figure 4.3a. Also, the carbon-based films were deposited on the flexible copper foils are illustrated in Figure 4.3b. The carbon films were deposited in the same conditions described in section 4.2.2.2 at TSD =2 cm.

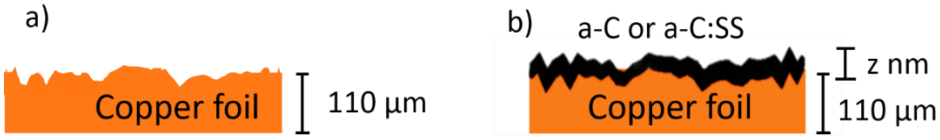

Figure 4.3: Schematic representation of a) pure copper foils of 110µm and b) coated carbon-based thickness (z).

The thicknesses of the film (*z*) were separated in groups according to the trend of their reflectance. The film thickness (*z*) varied from 3 nm to 150 nm according to the deposition rate calculated in chapter 3, section 3.2. The carbon-based thickness was varied, on copper foils as summarized in Table 4.1. The group 1 is called *flash depositions.* The deposition duration takes up to 120 s resulting in a thin and ultra-thin film.

Table 4.1: Summary of experimental deposition of carbon-based thin film over Cu foils

Thickness (*z*) (nm)			
Group 1		Group 2	Group 3
a-C	a-C:SS	a-C	a-C
4	4	42	150[XVIII]
14	8	50	-
18	17	70	-
21[XIX]	-	-	-
30	25	100	-

The thickness of the amorphous carbon films was measured on crystalline Si as described in the section 3.2 and on Si/Cu films as previously mentioned in section 4.2.2. This procedure was systematic, mainly because the Cu foil surface roughness (*Ra*=400 ±50 nm) is larger than the a-C thickness. The copper foil's topography aspects are presented in Figure 4.4 a–b. The good agreement between both thickness measurements (on Si and Si/Cu films) indicates conformal growth. The thickness values are an average of 5 points distributed in the surface, the homogeneity tests. The points were distributed over the squared Si surface deposited in the same condition. The standard deviation obtained is ± 20%.

[XVIII] The initial thickness for comparison of a-C and a-C:SS.
[XIX] Used only for a-C films.

In 3D printing, adding any material to the MA can harm the final printed part, including carbides or any iron composite [130,233]. So, only a minimal quantity of pure a-C films was deposited, discussed in detail in chapter 5. Thus, this chapter discusses the film's growth in its early stages.

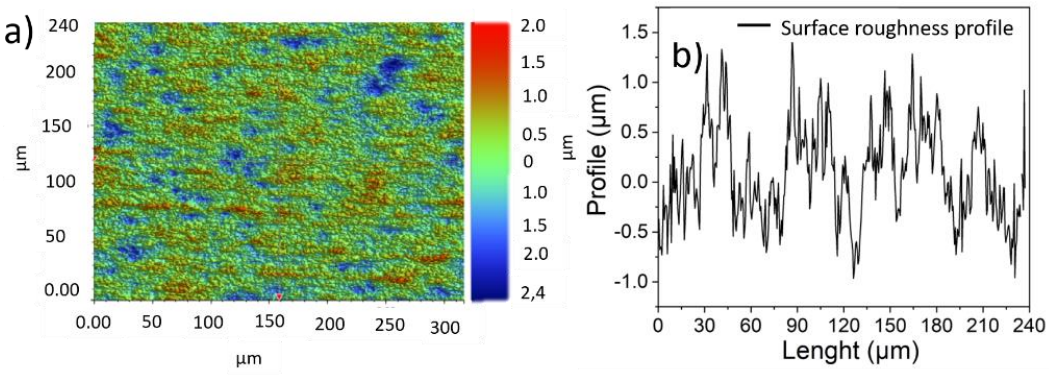

Figure 4.4: Roughness of the copper foils a) Topography surface and b) Roughness profile.

In the early stages of growth, the cluster formation and their coalescence are longer than the regular growth, in general, within the first nanometers of the film growth [57]. According to Thornton [55], the first step of the film growing involves the precursors' transport to the substrate. The second step consists of their adsorption onto the substrate surface and the beginning of the growth. Since the carbon deposit was at room temperature, a little amount of adatoms has mobility on the surface of the growing coating. The consequence is that initial nuclei tend to grow in the direction of the available coating flux, following the substrate geometry [250]. The coalescence stage can affect the sample of 4 nm a-C, the first sample of group 1. However, the experimental measurements for film thicknesses beyond 14 nm a-C films on Si demonstrate a linear growth, as shown in Figure 4.5. The thickness measurements employed the optical profilometer (contactless with 1 angstrom resolution). Local substrate defects can cause preferential nucleation or enhanced shadowing effects resulting in crystallites formation [54,56]. Such effects cannot be excluded from the sample's growth. More about the a-C growth mechanism can be found elsewhere [57,251,252]

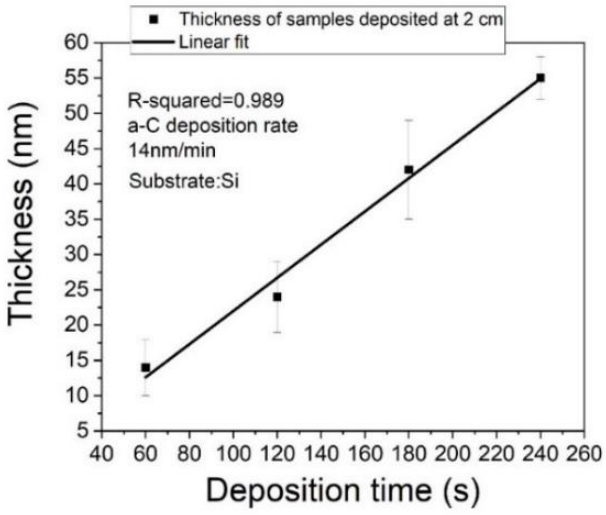

Figure 4.5: Experimental measurements of the a-C thickness on Si versus the deposition time.

For the set of samples using copper foils coated with pure a-C films, a multilayers calculation based on Maxwell's equations was developed to understand the reflectance of this set of samples discussed in the section 4.3.4 Appendix 4A.

4.2.4. Metal Additive

The Cu powder was wrapped for safety reasons. The Cu powder was previously covered in a glass shell consisting of a sandwich-like glass slide/Cu powder-Cu tape/glass slide. First, the powder was glued in Cu tape. Later the tape was encapsulated using a 3 mm glass slide at the bottom and a 1 mm glass slide at the top, in a sandwich-like format. The Cu powder was sealed using glue on both sides. The granulometry particle distribution is 45–106 µm. Add Up Metal Solutions supplied the Cu powder. The seal is a protective measure for handling the powder in any measuring instrument as represented in Figure 4.6a. The carbon deposition was done in the previously described conditions at TSD = 2 cm before the upper slide was fixed, as demonstrated in Figure 4.6b. Two thicknesses were deposited in different samples, 30 nm and 150 nm.

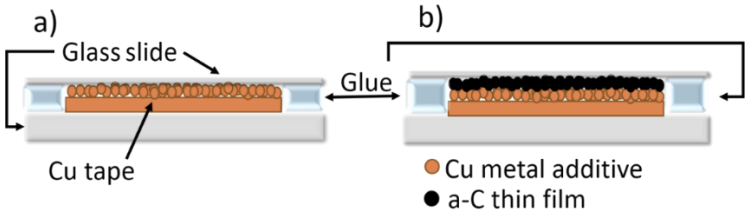

Figure 4.6: Encapsulated copper metal additive (powder) for reflectance measurements for a) Pure Cu powder; b) coated with a-C films.

4.2.5. Samples Summary

The first comparison involves thicker a-C and a-C:SS films compared with the group 1 range of thicknesses. For the next step of this work, the a-C film choice instead of a-C:SS is due to the addition of metals in a-C:SS since every element added over Cu can be considered an impurity. The addition of other metals in Cu MA can increase the electrical resistivity of the final printed object [253]. Thus, group 2 and Cu powder only analyze a-C films. A summary of the samples employed in this chapter is schematically represented in Figure 4.7.

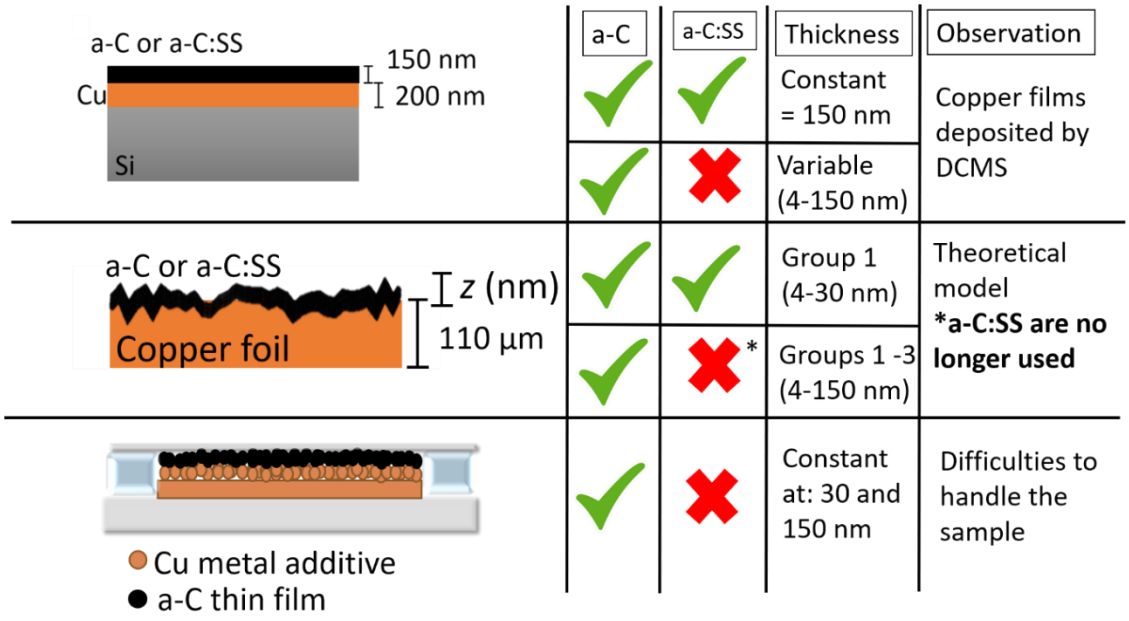

Figure 4.7: The summary of the three sets of samples displays the thickness of the substrate, the type and the main observations of each set.

Once all the methodology is clarified, the next step is to analyze the first set of samples. This chapter examined the reflectance from the near-ultraviolet (UV) to the near-infrared range

(IR). The spectrum is divided in three zones, the near UV around 450 nm -500 nm the visible range (500 nm-700 nm) near IR range (700 nm-1000 nm) to facilitate comprehension.

4.3. Results and Discussions

In brief, this chapter presents the experimental reflectance of a-C and a-C:SS films.

4.3.1. Comparison of Thicker a-C and a-C:SS on Copper Films

The reflectance of 150 nm of a-C and a-C:SS films deposited onto copper films are presented in Figure 4.8 a–b. The carbon-based films deposited at TSD= 2 cm and 3 cm result in marginal differences. Thus, increasing TSD by 1 cm the reflectance does not change, supporting Chapter 3 observations about the films' properties. The a-C:SS reflectance presents a slight variation in Figure 4.8 a. A minor increase can be observed around λ=700 nm. Despite a similar behavior of the films, a-C shows more protuberant regions observed in Figure 4.8b. Around λ=550 nm a soft lump is observed at the near-infrared λ= 900 nm (the dashed lines Figure 4.8b). The a-C film follows the trends of Si/Cu films in the visible range, which is not quite the same for a-C:SS.

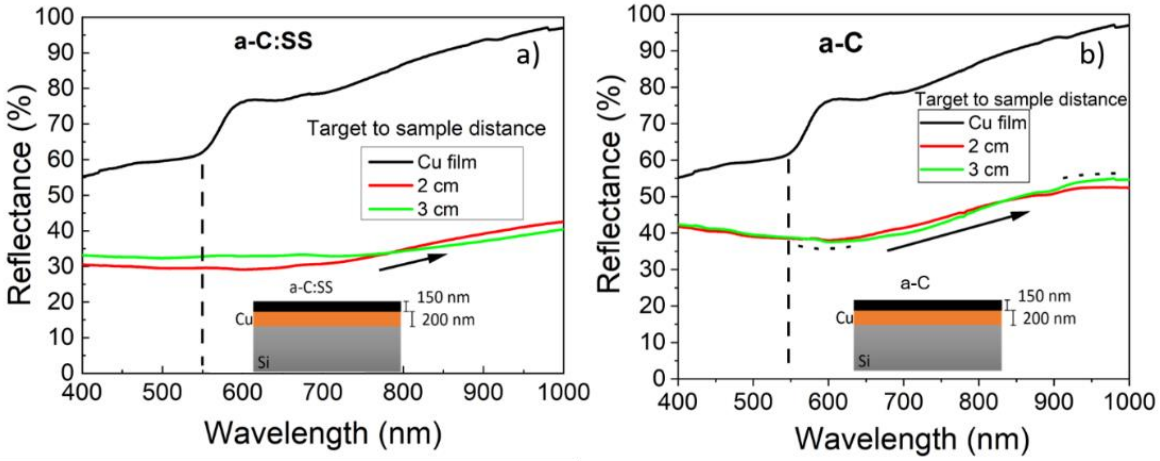

Figure 4.8: Reflectance (8° incidence) of a) a-C:SS and b) a-C deposited at TSD=2 and 3 cm. The arrow is to guide the reader. The dotted lines indicated inflection points. The inset shows the sample cross-section.

The comparison of a-C and a-C:SS on copper films is displayed in Figure 4.9. The macro surface of the samples can be seen on the right-hand side of Figure 4.9. The visual aspect does not significantly change between a-C/Cu and a-C:SS/Cu. The addition of carbon-based thin films darkens the color of the entire surface, as expected.

One can see that the reflectance behavior is similar to both materials in the entire broadband spectrum. In contrast, the reflectance of the samples with a-C:SS absorbs 10% more than a-C/Cu samples in all the spectrum. In the near – IR range, a-C:SS reflects 40% while a-C reflects 50%.

The optical properties of the films are attributed to the film composition [91]. The slight decrease in reflectance observed and its lower resistivity described in chapter 3 confirms that a-C:SS absorbs more due to the addition of 50% of stainless steel. Iron is the main metal in stainless steel composition found in the samples. The absorption coefficient of iron is higher than for sputtered a-C. The iron bulk's extinction coefficient (n_i) reaches around 4.0 in the infrared [254,255]. Craig *et al.* [110] reported several improvements on a-C:H/stainless-steel/Cu multilayers, the metal-rich component layer absorbs light and, the metal-free a-C:H acts as a front surface anti-reflection layer. The local density states (cluster) correspond to the

better optical absorption presented in Figure 4.9. These observations rather well Chapter 3 analyses.

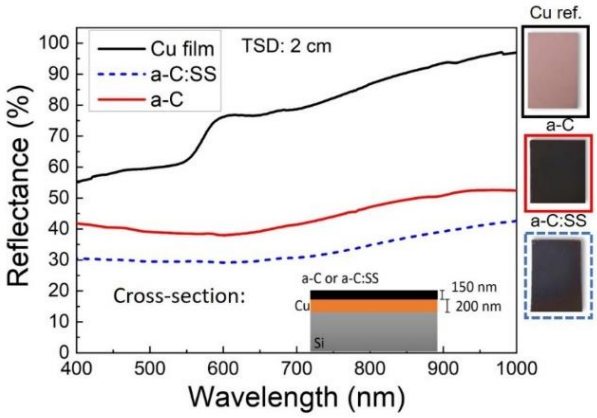

Figure 4.9: Near-normal incident (8°) reflectance of 150 nm a-C and a-C:SS thin films on deposited Cu film previously deposited on Si substrates. In the inset, the schematic representation of the cross-section samples carbon-based/Si/Cu films, the Cu and carbon-based thicknesses. The macro topographic surface of the samples is on the right-handed side.

The next step compares a-C and a-C:SS over copper foils for thin and ultra-thin films.

4.3.2. Comparison of a-C and a-C:SS Flash Deposition on Copper Foil

The *flash depositions' visual* surface aspect is displayed in Figure 4.10 a–c. The Cu surfaces change color as carbon-based film thickness (z) increases (the group 1 range). Both a-C and a-C:SS exhibit tawny to dark brown hues at equivalent thicknesses. Furthermore, metallic blue color is observed with 25 nm carbon-based films on the sample. Kats *et al.* [234] found blue hues depositing germanium over silver using Si as substrates at the same thicknesses range.

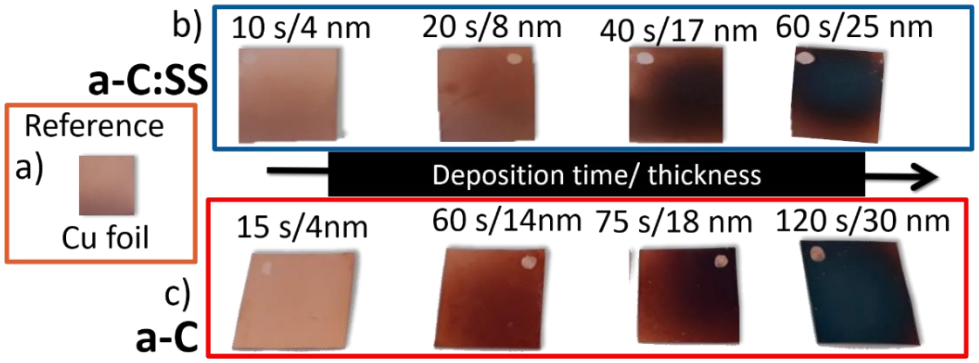

Figure 4.10: a) Reference copper foil aspect without film; b) foils coated with a-C:SS and c) a-C several thicknesses.

The Group 1 experimental reflectance is summarized in Figure 4.11. The ultra-thin carbon-based film drastically affects Cu reflectance. Globally, R_{exp} decays as the ultra-thin film's thicknesses increase for λ> 560 nm. Instead, for λ <560 nm R_{exp} has a constant behavior at around 25 ± 6% and 29 ± 7% for a-C and a-C:SS respectively. Thin films follow the Cu foil reference evolution with the wavelength, even if the R_{exp} decreases. When the films reach 25–30 nm another behavior is observed. The reflectance drops in the visible range reaching low values such as 13% at 650 nm for a-C and 19% in the same wavelength for a-C:SS. Towards the IR range, the reflectance grows. One can notice that 25–30 nm of a-C reduces around 50% of the Cu reflectance at λ=1000 nm. The samples that presented metallic blue hues substantially reduced the reflectance.

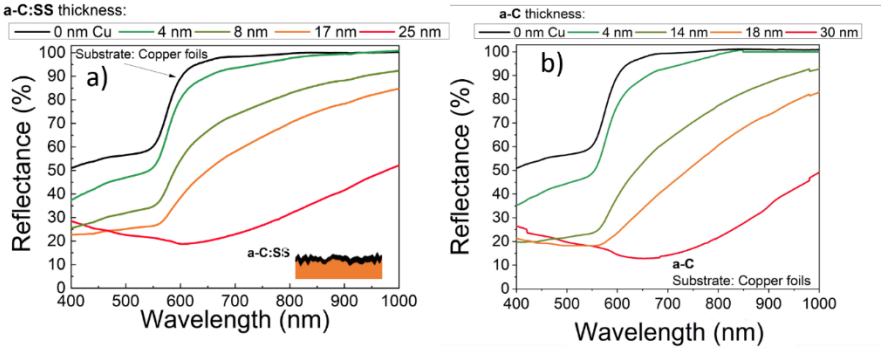

Figure 4.11: Comparison of a) a-C:SS and b) a-C ultra-thin films of group 1 on copper foils substrate at normal incidence.

One can notice that ultra-thin films reduce the reflectance more than thickener films represented in Figure 4.9. The next step is to analyze more thicknesses of *Group 2* to understand these phenomena. As mentioned in the section 4.2.3, pure a-C is preferable since minor addition of extra material is desired. Tran *et al.* [233] reported that 3D metal printing using pure materials results in final parts with lower defects, with higher density. In the case of pure carbon, the low probabilities of bonding with Cu can reduce the drawbacks in the final parts [237,256]. So the chosen film is pure a-C for the next part of this work [233,234].

4.3.3. The Reflectance as a Function of the Wavelength for a-C

This section presents the reflectance as a function of the wavelength of copper films and foils. The thickness varies to understand the different behaviors of light in different thicknesses and wavelengths.

4.3.3.1. The Deposition of a-C Films on Copper Films

This section presents thin and ultra-thin a-C films deposited on Si/Cu films of several thicknesses as displayed in Figure 4.12 a–b. Beyond λ= 580 nm, a gradual reduction in the reflectance is noticed for 14 nm-28 nm a-C thickness, still following the reference Cu film (black line). For slightly thicker films such as 58 nm and 42 nm, a drastic reflectance change occurs in Si/Cu films. The transition towards a strong absorption is produced for film thicknesses between 28 nm - 42 nm. Reflectance change is confirmed by the sample of 56 nm displayed in Figure 4.12a. Unexpectedly, increasing further the thickness of the films (z = 56 nm to 100 nm), the reflectance increases as shown in Figure 4.12b. For thicker films between 100 nm and 400 nm, the reflectance marginally decreases around 50% to 40% at λ=1000 nm. Considering the thickness versus the reflectance drop, thin and ultra-thin samples present more expressive reflectance reduction than thicker films in Figure 4.12b. One can conclude that thicker films are not as effective as thin and ultra-thin films to reduce reflectance.

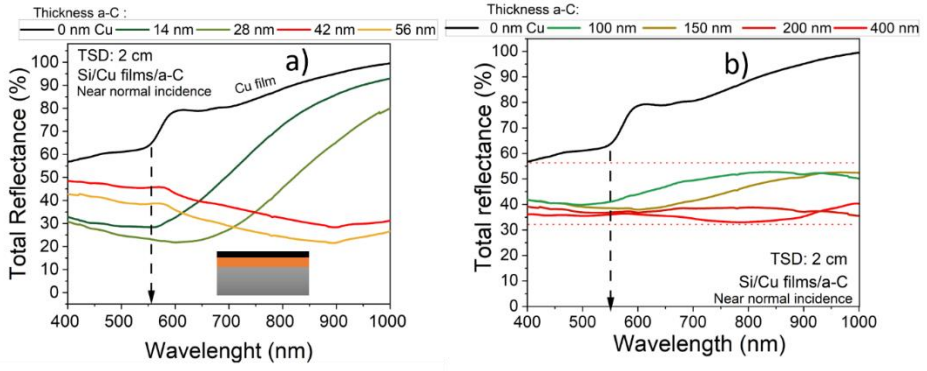

Figure 4.12: Experimental reflectance (R_{exp}) at near-normal incidence of a-C on copper films deposited over Si (0 nm Cu refers to the copper films) for thicknesses a) up to 56 nm, b) up to 400 nm.

The following section analyzes copper foil substrates. The maximum thickness present is 150 nm based on the previous results obtained. It is worth mentioning that for SLM minimum deposition time and thickness are preferable to be ultra-thin. However, a question arises concerning the optimum value of the deposited layer.

4.3.3.2. The Deposition of a-C Films on Copper Foils

The samples are divided in three groups[XX] presented in Figure 4.13 a–c. In general the λ = 580 nm remains the range where the reflectance change, corroborating the copper film comportment [257].

The reflectance decreases for the samples of Group 1 when increasing the thickness as shown in Figure 4.13a. The reflectance substantially reduces for 30 nm a-C as analyzed in the section 4.3.2. In Figure 4.13b group 2 indicates a transitory behavior. The reflectance behavior change as the thickness increases in group 2. The reflectance increases when the thickness grows from 50 nm to 70 nm. One can notice that for the 50 nm sample R_{exp} is ~20% at λ=750 nm and for 70 nm is ~40% at the same wavelength ≈750 nm). The 100 nm sample confirms the trend. Group 2 demonstrates that between 50 nm and 70 nm of a-C film R_{exp} upturns along the spectrum. Similar behavior is observed for Si/Cu films. For thicker samples, R_{exp} increases with the thickness accordingly in the range demonstrate in Figure 4.13b.

Finally, Group 3 tended to be constant. For 150 nm R_{exp} = 45% at λ=1000 nm. By increasing a-C thickness from z = 100 nm to 150 nm, R_{exp} alteration is minimal. Further, the R_{exp} flattens for thicker films [258]. In other words, for thicker films (z> 150 nm), the reflectance is constant at around 35–45% in the analyzed spectrum [258].

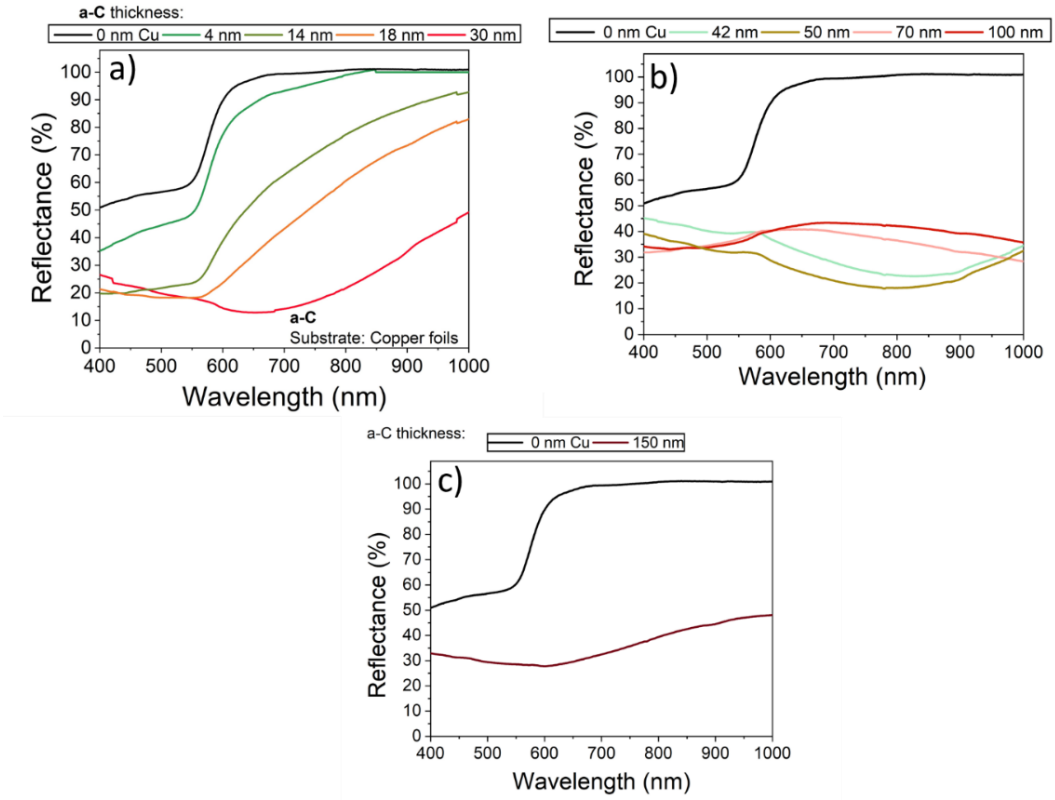

Figure 4.13: Experimental reflectance (R_{exp}) of a-C films on copper foils at normal incidence of 400 nm -1000 nm spectrum for thicknesses of a) Group 1 up to 30 nm (the 0 nm Cu refers to the copper foils), b) Group 2, 40 nm-100 nm, and c) Group 3, 150 nm

[XX] Detailed in the methodology section.

4.3.3.3. The Metal Additive Reflectance

The reflection measurement of metal additive is shown in Figure 4.14a–f. The power without treatment is presented in Figure 4.14 a – c. The visual of the Cu powder seems opaque classical Cu color in Figure 4.14b. On the contrary, the grains present a mirror-like reflectance in the magnified image in Figure 4.14c. In Figure 4.14d – f. 150 nm a-C film is added to the copper powder. In Figure 4.14e and f darker brown color is perceived.

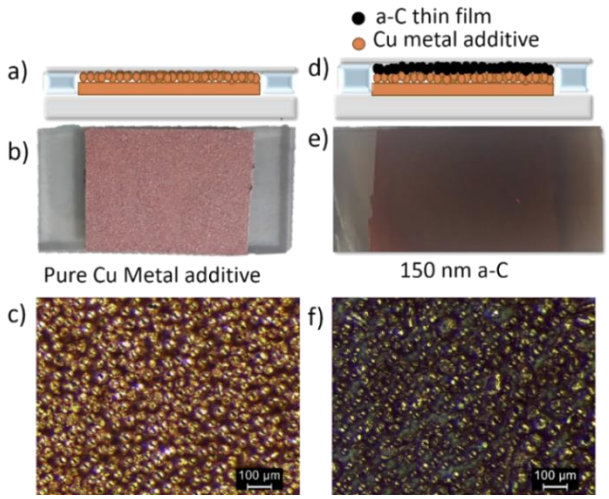

Figure 4.14: Wrapped copper powder and its native oxides of distributions 45–106 µm, a) schematic cross-section of pure powder, topographic view of the b) macro powder fixed in a tape (around 6cm^2) and c) Optical microscopy of 100 X magnification of the as-received Cu powder. The analogous to 150 nm a-C film are represented in d) e) and f).

The reflectance values on the y-axis are not displayed in Figure 4.15 to avoid mistakes in the interpretation, considering the glass in front of the powder. However, as the copper reference and the sample were both wrapped the relative variation in the reflection is valid. The larger spectrum confirmed that the reduction of R_{exp} reaches 2000 nm (2µm). The variation is observed in two wavelengths as indicated in position 1) at λ= 1000 nm and position 2) at λ= 2000 nm in Figure 4.15. For 150 nm a-C at position 1) the reflection presents a variation of 50%. For 30 nm a-C, the variation is about 17%. The position 2) the addition of 150 nm a-C films results in a reflectance variation of 27%. When reducing the film to 30 nm a-C becomes negligible.

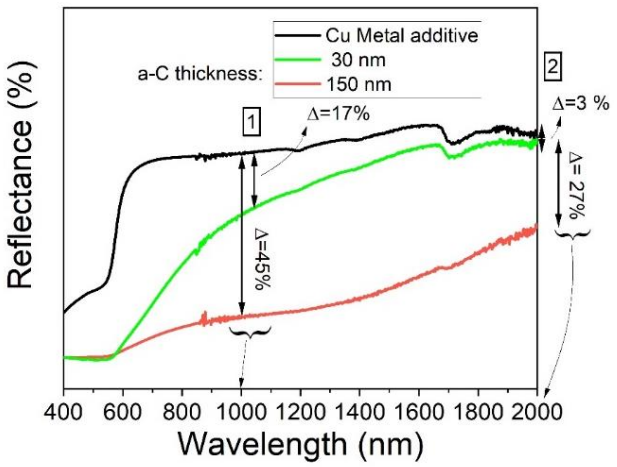

Figure 4.15: Normal incident beam reflectance for encapsulated powder samples of 30 nm and 150 nm, the variation is observed due to the encapsulation at two wavelengths, 1) 1000 nm, and 2) 2000 nm.

Due to the glass in front of the powder comparison with another sample is not precise. However, the 150 nm a-C variation for Cu powder corroborates copper foils and film. For 30 nm, Cu powder reflectance is comparable to the a-C over copper films. For foils, the reflectance variation is around 50%. The reflectance variation for 30 nm over the sphere can increase dispersion, the 20% standard deviation of the layer can cause significant variation in the reflectance. One can speculate that the Cu film and the beads present the same reflectance type (specular). More analyses in the deposition over spherical substrates are yet to study although the analysis done at two laboratories, corroborates the analyses made at the GeePs and LPGP for both samples. The 150 nm sample analysis done at LPGP and GeePs is in appendix 4C.

4.3.4. Multilayer Calculations

Multilayer calculations employed boundary conditions and Maxwell's equations to calculate the *reflectance power* or the theoretical reflectance (R_{th}). The model considers plane waves propagating in uniform media and perfectly flat interfaces [259,260]. The layers consist of vacuum, carbon and copper. The (R_{th}) was calculated by varying the a-C thickness (z) from 0 nm to 300 nm at constant wavelengths: 450, 650, 850, and 1000 nm. The equation (4A.25) represents the meaning of R_{th} in appendix 4A [261]. The input data consists of a complex refraction index corresponding to the material layer (a-C or Cu). The choice of the complex refractive index and other details are discussed in *Section 4.3.5*.

Similarly, Bludov *et al.* [262] reported models using electromagnetic waves interactions with carbon layers, precisely sheets of graphene at arbitrary angles of incidence. The abbreviations R_{th} and R_{exp} are employed to distinguish theoretical and experimental reflectance, respectively. The complete model and analytical calculations can be found in appendix 4A. The model is compared to the results obtained for Cu foils and copper films covered with an ultra-thin carbon layer. The model did not use Cu powder as a substrate. Powder samples were enveloped to guarantee safety when working and transporting powder samples.

4.3.5. The Reflectance as a Function of a-C Thickness

The theoretical and experimental reflectance over Cu foils as a function of a-C thicknesses are summarized in Figure 4.19a – d. The reflectance varies following a sinusoidal shape as the thickness increases at a constant wavelength. The wave-shaped reveals a maximum and a minimum reflectance point. The experimental minimum reflectance thickness, 'MR_{exp}' expressed in (nm), is the focus of the analysis considering the objective of reducing the Cu reflectance.

In general, *ultra-thin a-C film* over Cu foils sharply decreases the reflectance with the thickness until reaching the MR_{exp}. The a-C MR_{exp} increases more than 2.5 times, as a function of wavelength from $z \approx 25$ nm at $\lambda = 450$ nm to $z \approx 65$ nm at 1000 nm.

In constant wavelengths is clear to observe that continuously increasing the a-C film thicknesses beyond MR_{exp}, the reflectance grows, this corresponds to the *group 2* thicknesses in subsection 4.3.3. For thicker films (> 150 nm), the reflectance is constant at $\approx 30 \pm 10\%$ for all the wavelengths. These findings corroborate the observation of copper films in previous subsections.

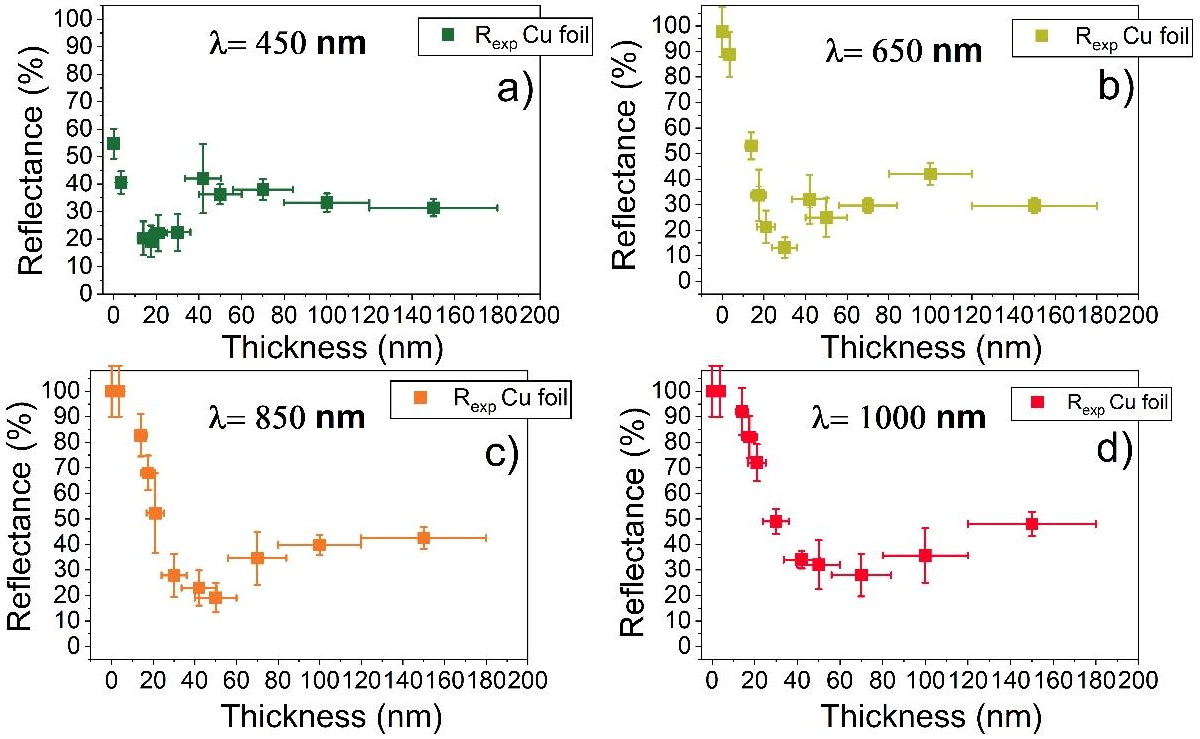

Figure 4.16: Experimental reflectance versus the a-C film thickness at constant wavelengths: a) 450, b) 650, c) 850, and d) 1000 nm)

4.3.5.1. The Amorphous carbon Model

The next step is to exploit the model detailed in appendix 4A the R_{th} is calculated using a plane wave propagation through a multilayer system. The initial trial of the refractive indexes for the a-C films were of pure amorphous film. The first proposed refractive index is from amorphous carbon films. The data used in the calculation is from Wyon *et al.* [28], and for copper refractive index data is from Johnson *et al.* [263], displayed in Table 4.2.

Table 4.2: Copper complex refractive index from [263] *and a-C from* [264] *and* [28]

Wavelength (nm)	Copper		a-C			
	Ref. [263]		Ref. [264]		**Ref.** [28] [XXI]	
	n_r	n_i	n_r	n_i	$\boldsymbol{n_r}$	$\boldsymbol{n_i}$
450	1.24	2.39	1.79	0.68	**2.25**	**0.75**
650	0.24	3.62	1.87	0.79	**2.4**	**0.4**
850	0.27	5.41	1.95	0.8	**2.5**	**0.5**
1000	0.32	6.54	2.05	0.93	**2.3**	**0.6**

Two samples were chosen to demonstrate that the proposed refractive indexes do not fit the experimental data. The Figure 4.17 displays the results for λ=1000 nm and λ=450 nm. Generally lower compared to the crystalline samples. This trend corroborates the studies of Born *et al.* [265] partially transparent ultra-thin coating over a reflecting substrate can act as an absorbing coating. In this case, due to the film's design, the reflectance is suppressed via destructive interferences and not losses [239,266]. In general, amorphous films do not corroborate other films' properties reported in the literature. These films are hard to reproduce the disordered bonds influence the resistivity and optical properties [28,91,267].

[XXI] Values used in the theoretical calculation

For a film without losses, the theoretical thickness at the minimum point (Mz) is expressed as: $Mz = \lambda / 4n_{r2}$, where n_{r2} is the refractive index of the second layer (in this case a-C) in nm. The minimum demonstrated in Figure 4.17 shows that the experimental data MR_{exp} does not match *Mz* thicknesses. The reflectance reaches theoretically lower values for pure amorphous carbon due to the lower value of n_i as indicated in Table 4.2 [265]. If the film is completely lossless and the copper, a perfect conductor *Mz* point is reached. The difference in the reflectance of MR_{exp} and Mz is due to losses to the a-C film indicating that n_i of a-C film is higher.

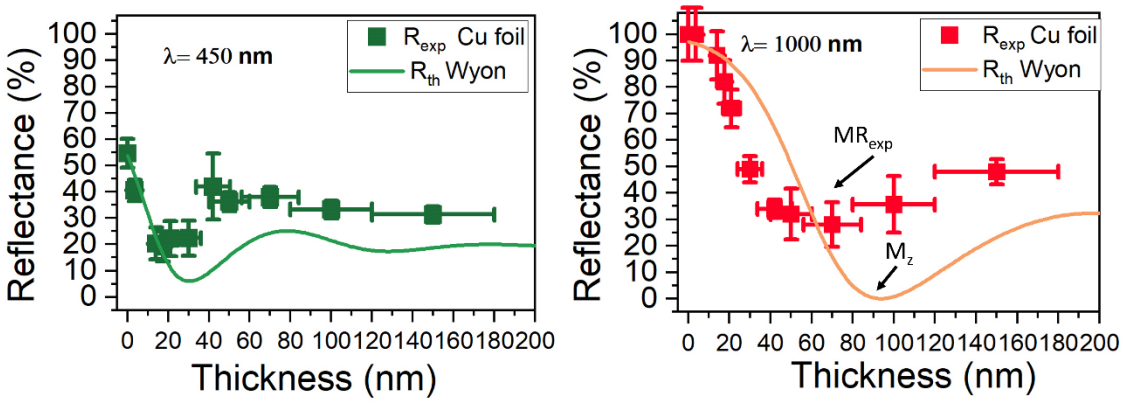

Figure 4.17:Comparison of the experimental points and the theoretical reflectance using typical amorphous carbon films and copper refractive index from [28,263].

For amorphous carbon films n_i show values below 1, for example, n_i can reach 0.68 at λ= 450 nm [258]. For transparent films, the reflectance is low due to destructive interferences. Kats *et al.* [239] reported that absorption could be achieved in a layer through attenuation or dissipation of the light with ultra-thin thicknesses. The authors reported a metallic back reflector with a thin dielectric spacer on top [234,239]. Analogous to this work, the metallic back reflector is the Cu foils and, the *dielectric* is the a-C. Once the samples present losses either to the film or to the copper, the film is now analyzed as a lossy film. The losses are an integral part of the design, by combining non-trivial interface phase shifts, the phase accumulated through propagation and the attenuation of the wave as it propagates through the lossy medium. Thus, the reflectance reduction of a-C over copper takes place because of losses and destructive interferences[268].

The loss comes from the excitation of bonded electron oscillations in the amorphous film covering a multitude of states. The maximum optical absorption is associated with the electron density in which the state is located [269–271]. These observations corroborate Raman demonstrated in Chapter 3 in the section 3.3.1 where the films present nanocrystalline graphite clusters in the amorphous matrix.

4.3.5.2. The Duality Amorphous Carbon Graphite

The used n_r and n_i fitting the experimental data is from Kwiecinska *et al.* [272] displayed in Table 4.3 with similar data from other authors. If one compares the refractive indexes from this and the previous section, the main difference is n_i that is higher for Kwiecinska *et al.* Meanwhile, n_r is comparable to the amorphous index shown in Table 4.2. So, n_r is comparable to amorphous carbon while n_i is analogous to graphite [258].

Table 4.3: Complex refractive index of copper and, graphite from several references.

Wavelength (nm)	Copper		Graphite					
	Ref. [263]		**Ref.** [272][XXII]		Ref. [273]		Ref. [274]	
	n_r	n_i	$\boldsymbol{n_r}$	$\boldsymbol{n_i}$	n_r	n_i	n_r	n_i
450	1.24	2.39	**2.45**	**1.45**	2.61	1.30	2.64	1.28
650	0.24	3.62	**2.5**	**1.6**	2.85	1.61	2.96	1.81
850	0.27	5.41	**2.8**	**1.65**	3.07	1.81	3.1	1.9
1000	0.32	6.54	**2.9***	**1.8***	3.19	1.91	3.25	2.07

When using the complex refractive index of Kwiecinska *et al.* [272], the model is in good agreement with the experimental measurements. The theoretical minimum reflectance MR_{th} are in fair-to-good agreement with the MR_{exp} for all the selected wavelengths, as displayed in Figure 4.18 a–c. The intensity of MR[XXIII] match at 20% within the error bars margin. A slightly lower R_{exp} (18%) is observed at z = 31 nm, before the MR_{th} at 41 nm, at λ = 650 nm. For the near-IR wavelengths, λ = 850 nm, and λ = 1000 nm MR matches around $z \approx 55$ nm and 66 nm, respectively (Figure 4.19 c. – d.). All the MR is displayed in Table 4.4.

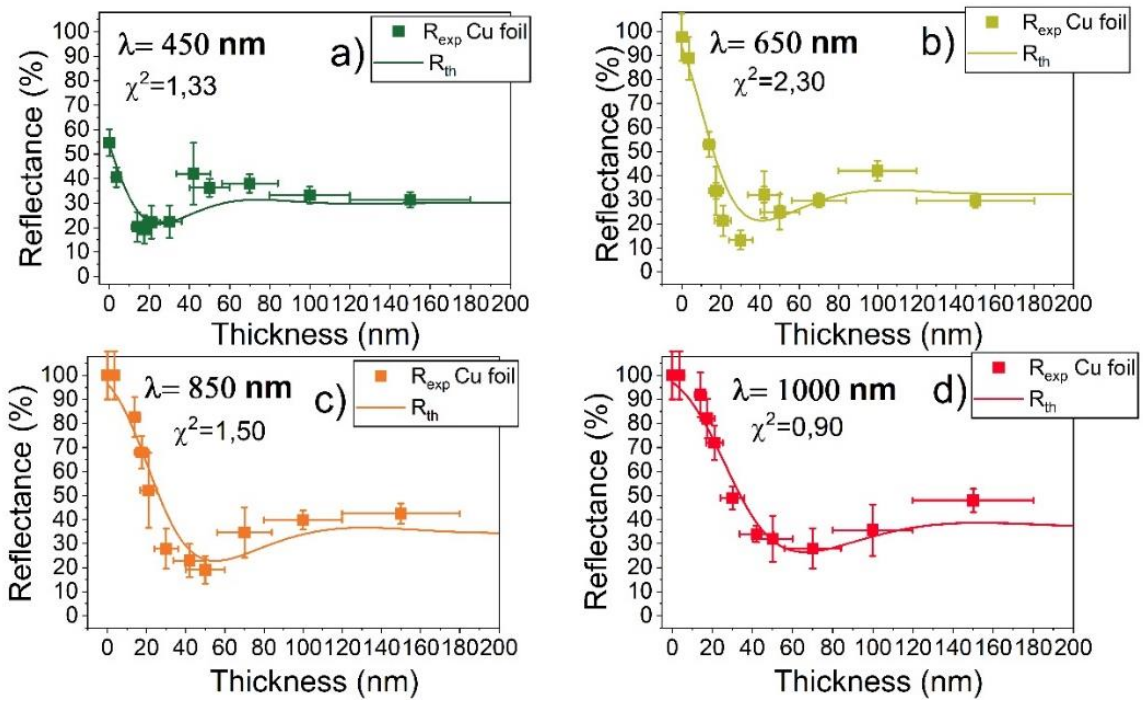

Figure 4.18: Comparison of copper foil's experimental (R_{exp}) and theoretical (R_{th}) reflectance given by Eq. (4A.25) versus the respective thickness at constant wavelengths: a) 450, b) 650, c) 850, and d) 1000 nm) (n_r, n_i calculated using the values reported by Kwiecinska et al. [272] *for graphite and Johnson et al.* [263] *for copper. χ^2 is calculated for a-C over copper foil samples.*

Thus, the a-C thickness at MR is in good agreement with the error bars margin for copper foils. Although they vary more at lower wavelengths as the χ^2 value indicates. When significant statistical data is obtained χ^2 distribution is around 1. The complete χ^2 calculation method is complete in appendix 4B. The best agreement between MR_{exp} and MR_{th} is found for λ = 1000 nm, the discrepancy goes <10%. The respective MR using the references in Table 4.3 is present in Table 4.4 demonstrate that MR_{th} is similar to MR_{exp} values for other references.

[XXII] Values used in the theoretical calculation
[XXIII] Referred to the theoretical and the experimental.

Table 4.4: a-C thickness at minimum experimental (MR_{exp}*) and theoretical (*MR_{th}*) reflection of graphite using different* n_i *and* n_r *from the literature.*

Wavelength (nm)	*a-C thickness (nm)*			
	MR_{exp}	MR_{th} from:		
		Ref. [272]	Ref.[273]	Ref. [274]
450	25	**25**	22	21
650	30	**41**	33	30
850	50	**55**	47	46
1000	65	**66**	57	55

Furthermore, the film's dual effect discussed in chapter 3 might cause extra losses or absorption. The film's duality influences the optical properties of this film, considering that the theoretical calculations using pure amorphous carbon complex refractive index do not adjust the experimental data [92]. The presence of nanocrystalline graphite (NC graphite) in the amorphous matrix for samples deposited close to the cathode (TSD=2 and 3 cm) is discussed in chapter 3 section 3.3 [9,216,251]. The absorption in a-C films involves mainly the π bands. The electrons come from 2p orbitals (one electron per atom) which make up the Highly Oriented Pyrolytic Graphite crystals. For glassy carbon[XXIV] considerably less than the one π electron per atom is involved in optical transitions. For graphite the transitions occur on either side of the planes of atoms. On the contrary, in glassy carbon, the graphite orientation between the atomic planes does not occur in the amorphous carbon structure the π electron participation reduces [264,275,276]. Consequently, William *et al.* [264] reported as reasonable to interpret the data for glassy carbon by analogy with those of graphite. According to Taft *et al.* [267] mechanically polished glassy carbon exhibits a very similar trend of graphite reflectance. The glassy carbon is a structure comparable to the a-C films deposited at TSD= 2 cm.

4.3.5.3. The Cu Substrate Roughness

The as-received copper foil surface roughness is ten times higher than the film thickness (R_a = 400 nm±50 nm); thus, it is compared to the Si/Cu films (R_a = 5 nm±2 nm). Figure 4.19[XXV] demonstrates *the a-C films deposited on Si/Cu films*, the previous results of copper foils compared to theoretical reflectance. This comparison clarifies if the substrate roughness affects the reflectance. Copper films present slightly higher reflectance than foils, although they present a similar reflectance evolution with the thickness. In this study, the roughness of the copper foils play a role.

The most remarkable reflectance difference between the a-C deposed over foils and film is in lower wavelengths such as λ= 450 and λ= 650 nm. On the contrary, this discrepancy vanishes for large wavelengths or thicker films. The a-C film thickness of 400 nm over Si/Cu films confirms that reflectance no longer decreases in any wavelength as displayed in Figure 4.19. The light penetration (d) *de*monstrate that light does not reach Cu after some nanometers, *d* is displayed in Table 4.5.

[XXIV] Glassy carbon is a form of hard amorphous carbon, with an extremely smooth surface. X-ray diffraction suggests that the structure planes are not aligned. Carbon Crystallite size can be in the film as small 'packets' with graphite orientation between the planes [264,275]

[XXV] The Figure 4.19 a–d. can be found in Appendix 4A in a larger size.

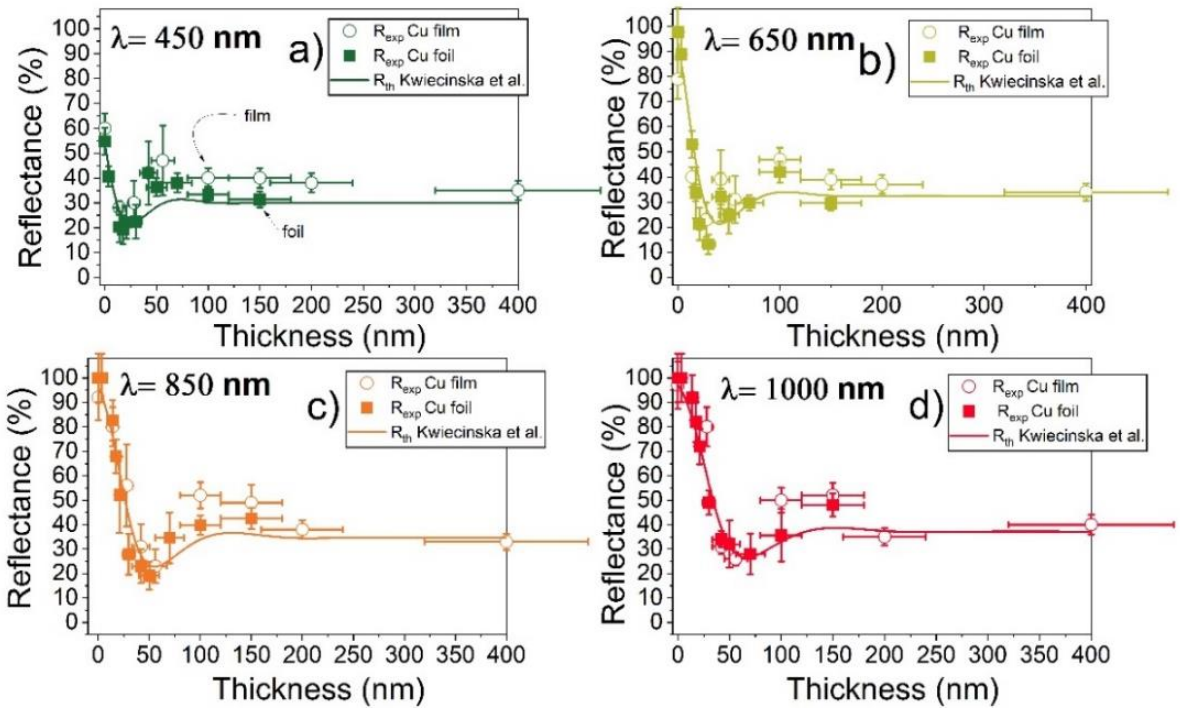

Figure 4.19: Cu foils and film reflectance (Rexp) comparison with the theoretical reflectance (R_{th}) given by Eq. (4A.25) versus their respective thickness at constant wavelengths: a) 450, b) 650, c) 850, and d) 1000 nm) (n_r, n_i calculated using the values reported by Kwiecinska et al. [272] *for graphite and Johnson et al.* [263] *for copper.*

The wavelength of light changes when it travels through different media. So, the speed of light (c) from the vacuum, in the amorphous carbon film changes to another velocity (v). Equation (4.1) indicates the dependence of wavelength (λ),frequency (f) and the velocity. One might consider that f is the same in any material so, the velocity and the wavelength (λ_i) change [277].

$$\lambda = \frac{c}{f} \; and \; \lambda_i = \frac{v}{f} \; so \; \frac{\lambda}{\lambda_i} = \frac{c}{v} = n_r \tag{4.1}$$

To understand how roughness can affect the light reaching the copper from the a-C layer it is important to know the characteristic wavelength (λ_i)in the film using equation (4.2):

$$\lambda_i = \frac{\lambda}{n_r} \tag{4.2}$$

Also, penetration of the light intensity in equation (4.3) is useful to estimate when using ultra-thin films:

$$d = \frac{\lambda}{4\pi n_i} \tag{4.3}$$

Indeed, the surface roughness is more perceived at lower wavelengths, where the copper's roughness R_a is bigger than λ_i. At larger wavelengths, the characteristic wavelength approaches the same magnitude of R_a as displayed in Table 4.5. Considering that the light is at normal incident, it approaches the theoretical model of flat interfaces. This corroborates that the differences between a-C over foil and over Si/Cu film becoming negligible for higher wavelengths as 1000 nm.

Table 4.5: Complex refraction index of graphite. The characteristic wavelength and the characteristic propagation length.

Wavelength (nm)	Graphite Ref. [272]			
	n_r	n_i	λ_i	d
450	2.45	1.45	183.7	24.6
650	2.5	1.6	260.0	32.3
850	2.8	1.65	303.6	41.0
1000	2.9*	1.8*	344.8	44.2

Ang *et al.* [278] demonstrated the effect of nanostructures either roughness or created on a surface. The light trapping drastically increases according to the trap size and the wavelength. Considering that the traps in this study are not optimized, multi-reflection in the traps causes a relative reflectance decrease or light scatter, eventually producing dispersion in the experimental reflectance.

More than the roughness, copper reflectance varies. After $\lambda \approx 580$ nm, Cu reflectance grows from 55% to 100% due to a great diminishing in n_i while n_r values increase [263]. On the contrary, for longer wavelengths ($\lambda \approx 850$ nm – IR) the Cu complex optical index stabilized [279,280]. The copper variation in reflectance can create dispersion in the visible range. Otherwise, at λ =1000 nm the reflectance of copper and foils differences are negligible.

4.4. Conclusions

Conclusions a-C:SS and a-C films present a reduction in the reflectance of copper substrates. Thus, the films are an excellent option to reduce reflectance in 3D copper printing. The stainless-steel addition in the amorphous matrix (a-C:SS) reduces around 10% more reflectance than a-C films. However, adding minimal quantities of other elements than Cu is preferable. Hence, the a-C film composed only of amorphous carbon and NC graphite is better suited to future applications in 3D metal printing.

Cu reflectance reduces 80% when covered with an ultra-thin a-C film. For sufficiently thin films, the waves can reach the substrate, reflecting on the substrate and the film. The design of ultra-thin films changes the optical path and the phase of one backward wave, resulting in destructive interferences. This effect results in a minimum reflectance point at specific ultra-thin a-C film. The reflectance reduction combines interferences and losses to the a-C films and copper. When the interferences are over, a-C's reflectance is constant at around 30% for thicker films than 150 nm. The best agreement of the theoretical results is at longer wavelengths.

On the contrary, Cu reflectance varies from 55 to 100% for shorter wavelengths around λ=580 nm. The roughness influence is apparent when comparing foils and Si/Cu films as substrates with different roughness. For 1000 nm, both substrates, foils, and film comparable the same reflectance, while for 450 nm, the Cu film shows higher reflectance at equivalent thicknesses. The roughness in the substrate can cause light to be scattered or trapped, resulting in dispersion. Thus, the multilayer calculation model can predict ultra-thin layers of a-C that cause interferences on Cu more accurately in the infrared or longer wavelengths.

The reflectance reduction using ultra-thin films is applicable in several areas, for example, optoelectronic devices. In addition, magnetron sputtering, a conventional fabrication technique, allows thin film scalable depositions.

Although, the complex refractive index for dual film characteristics needs further research. These results show that a-C and a-C:SS films can be an alternative strategy for anti-reflective coatings, such as copper or other reflective metals. Moreover, stainless steel addition to the amorphous films shows the possibility of decreasing both resistivity and reflectance.

CHAPTER V: The Welding of a-C Films over Copper Substrates

Chapter V summarizes the main results of graphite-like and the a-C films deposited by DCMS over copper powder and copper foils welding using an IR laser. The topography and cross-section of the welding are analyzed for several laser powers. The analysis is to minimize the carbon quantity and comprehend the behavior after welding.

Summary

Abbreviations Chapter V

a-C25	25 nm of amorphous carbon
EDS	Energy Dispersive X-Ray Spectroscopy
R_{exp}	Experimental Reflectance
G	Graphite spray
IR	Infrared
D	Laser spot diameter
T_i	Melting temperature of the element (i)
P	Power
ϕ	Power density
Cu MA	Pure copper metal additive
r_{Cu}	Radius of copper bead
r_{Cu+C}	Radius of copper bead + graphite film
R_{th}	Theoretical Reflectance
σ	Thermal conductivity
λ	Wavelength
wt.	Weight

5.1. Chapter Introduction

Cu fusion is challenging due to thermal conductivity, heat losses, and reflectance. The Cu thermal conductivity makes it solidifies faster. Furthermore, the rapid heat loss generates large local heat gradients in fused Cu [112,281]. Another characteristic is that Cu is one of the most reflective metals under infrared (IR) radiation, the same used in SLM lasers. In addition, the Cu reflectance depends on its state [58]. The solid-state reflectance is around 98% and can drastically decrease in the liquid state (melting), mainly around the green wavelength [82].

Several strategies to improve the poor absorption of copper in the IR range have developed, among them the use of alloys, oxides and carbon. The 3D printing using alloys such as Cr-Zr-Ti and Cu-Al-Ni resulted in higher relative density (99.74%) [282]. The oxidation darkens the Cu surface easily and cheaply enhances absorption. Other approaches for improving Cu IR absorption use different forms of carbon. Chen *et al.* [129] used a nanocomposite material as an absorber (99.8%wt. purity metal additive (MA)[XXVI] mixed with a polymer base transparent resin). Carbon nanoparticles included in the powder bed lead to a reduction in the power to melt Cu [113,129,130]. Inspired by the recent development of printable graphene conductor inks, the joint of a graphite-like layer also appears to be an easy alternative to manage Cu's fusion using IR energy [283,284].

This chapter demonstrates that thin and ultra-thin graphite-like coatings on the outermost surface of Cu substrates (powder/foil) efficiently reduce IR power for copper welding and melting in a single weld simulating the SLM process.

5.2. Methodology

5.2.1. Graphite – Spray on Cu Powder

The first set of samples consisted of a graphite-like spray-covered powder bed (composition 100% Cu and its native oxides, 45–106 µm diameter distribution supplied by Add Up Global Solutions) shown in Figure 5.1. The Cu powder was coated using a commercial carbon spray called GRAPHIT 33[XXVII]. The purpose of aerosol spray was to obtain an 'express' black layer to absorb laser energy without transporting the sample for long distances. One must consider that the laser facility didn't have any other process to deposit carbon. The test goal was to deposit carbon only on the surface of the beads exposed to the laser, as demonstrated in Figure 5.1b. Long transports would not preserve the thin layer on the upper part of the powder bed. The loose powder with carbon would move or roll before reaching the facility and the strategy of the deposition only on the upper surface would vanish.

The main spray drawbacks are that it is a liquid solution not only composed of graphite. The spray takes four hours to dry and contains only 5 wt.% graphite. The other part of the composition is hydrocarbons and alcohols as isopropanol.

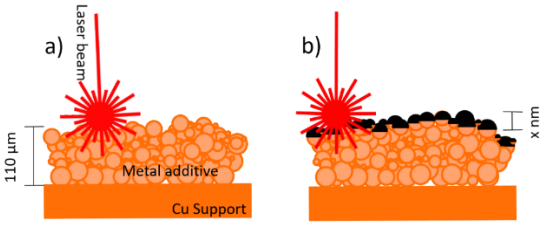

Figure 5.1 a) copper powder and b) Graphite spray over Cu powder welded at normal incidence.

[XXVI] It refers to metal powder used in 3D printing.
[XXVII] the aerosol details are in Appendix 5A.

The welded sample has three important parts consisting of graphite spray in the upper part, the Cu powder bed powder and the support plate where the powder was welded. In the laser facility, a powder bed (1 cm × 2 cm × 110 µm) was placed on a support. The sample was about 30 cm from the aerosol to obtain a homogeneous coat. Additional samples of Si and Cu substrates were also coated to investigate the graphite-like coating homogeneity and thickness. A thin coating of 3.5 ± 1.5 µm[XXVIII] was produced, according to the measurement on Si substrates. The reflectance of the graphite-like layer over the Cu is around 30%, using the same measurement method used for chapter 4 samples described in chapter 2 in the section 2.3.4.

Laser power was varied in the range of 600 W -2,000 W. The set of graphite-like spray-covered samples are called, '*G+ laser power*', their analogous welded samples without carbon '*Cu MA + laser power*'. All the laser powers used for these samples are listed in Table 5.1.

Table 5.1: Laser power used in the welding of graphite-like spray over copper foils.

Laser Power (W)
600, 800, 1000, 1200, 1500, 2000

Cross-sections are analyzed for the samples irradiated with laser powders of 600, 1200 W and 1500 W before and after the electroplating described in the section 2.3.2.

5.2.2. a-C films on Copper Foils

The second set of samples was prepared with optimized ultra-thin a-C film deposited by direct current magnetron sputtering DCMS on copper foils, to verify the efficiency of the welding process in lower thicknesses. Figure 5.2a shows the reflectance of a-C film over copper foil for λ=1000 nm, the same results obtained in chapter 4 in the section 4.3.5.2.

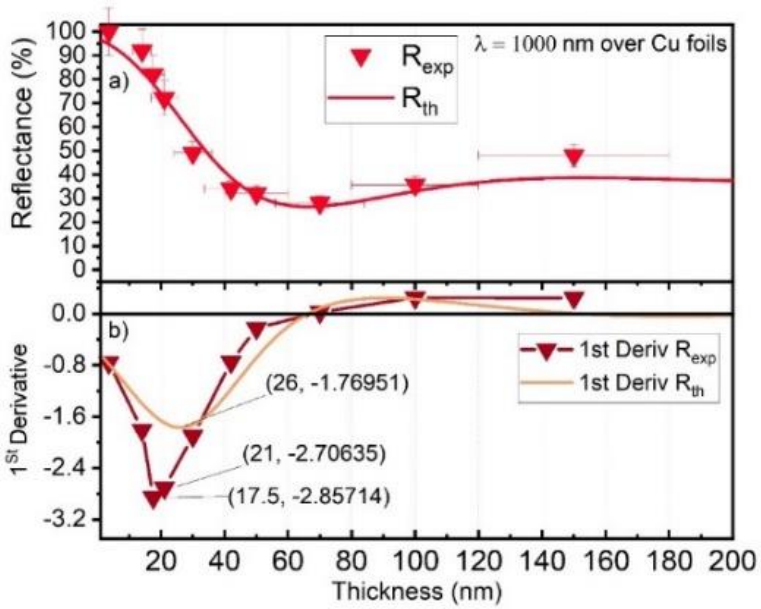

Figure 5.2: Theoretical and experimental a) reflectance results for a-C film over copper foils detailed in the section 4.3.5.2 and b) the first derivative result of a).

The derivation of the reflectance (experimental and theoretical) demonstrated what point the variation of the reflectance was greater in the least a-C thickness. Figure 5.2b shows that the higher variation of thickness is around 18–26 nm of a-C films the theoretical model corroborates the experimental points. Based on this result, the thickness deposited over copper foils is 20–25 nm.

[XXVIII] measured over Si samples.

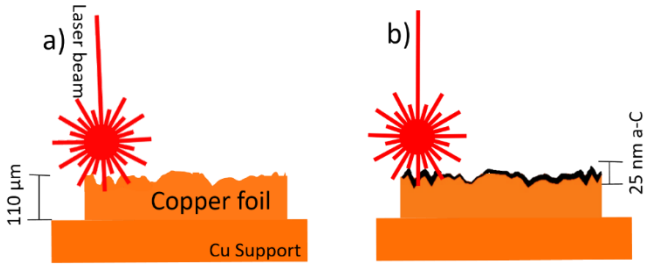

Figure 5.3: a-C film deposited by DCMS over copper foils welded at normal incidence.

The pure amorphous carbon thin film (a-C) was grown by (DCMS) as represented in Figure 5.3 a–b. The same a-C films described in Chapter 3 deposited from a target to the substrate distance of 2 cm were used. The reflectance of these samples is described in chapter 4 section 4.3.5.2. During copper foil welding a copper plate of 1 mm was used as base support. These samples are called '*a-C25+the laser power';* their analogous without films are referred to as '*foil+ laser power'*. The variable of this experiment was the laser power summarized in Table 5.2.

Table 5.2: Laser power used for the set of a-C film over copper foils

Laser Power (W)
600, 800, 1000, 1200, 2000

The laser was focused on the different samples and moved at a constant speed, mimicking a single track of the SLM process under an Ar protective atmosphere. The main laser parameters used in single tracks are summarized in Table 5.3. The surface power density Φ was calculated this parameter considers the spot diameter (D) of the laser in µm and the laser power (P) in Watts used in the welding as demonstrated equation (5.1).

$$\Phi = \frac{4P}{\pi D^2} \qquad (5.1)$$

The power density estimates better the energy input than only the laser power it considers the role of the laser spot, it describes how the laser power is distributed over a given area, Φ is in W/mm^2 [285].

Table 5.3: Laser main parameters.

Power range (W)	Spot (µm)	Scan speed (mm/s)	Focal length (mm)	Scan strategy	Powder temperature	Powder bed height (µm)	Shot Length (mm)
600 – 2,000	200 ±20	500	200	Single tracks	Room temperature	~100	5

5.2.3. a-C films Over a 3D Printed Object

The test of a-C films deposited by DCMS was done using a 3D printed object. The films were deposited on partially printed squares using SLM at Add Up Global Solutions company. Further 25 nm of a-C film was deposited at LPGP over the squares in the same conditions of chapter 3 in section 3.2 then the sample returned to the company to continue the SLM process. The schematic representation is in Figure 5.18.

5.3. Results and Discussions

5.3.1. Graphite Spray Over Cu Powder Results

Figure 5.4 a – b shows the powder bed and the welding tracks. In Figure 5.4a, one can see that the track is not continuous. As the laser power increased, more Cu drops were welded in the track for Cu-MA. MA-1500 still presented intermittent melting.

The evolution of the Cu drops demonstrated that the melted copper changed from spherical to elliptical Cu drops as the energy increased [286]. In the sample *MA-1200,* the melted Cu became more elongated, indicated by the orange dashed arrows. This elongation of the grains was also observed in the literature this effect is discussed below [287,288]. Figure 5.4b demonstrates the analogous samples coated with graphite-like spray. For the G-600, one can observe some intermittent melting or the balling effect. It happens when only part of the Cu powder is melted, forming intermittent balls of welded Cu. However, the track is generally continuous for higher energy, such as G-1200, G-1500 and G-2000 [286].

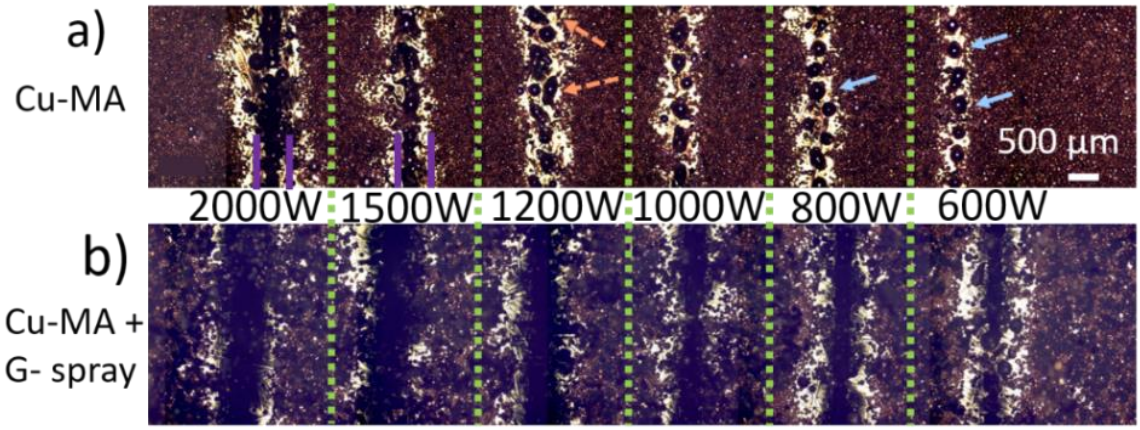

Figure 5.4: Optical images of the welding using several laser powers a) pure Cu metal additive (Cu-MA) and b) Copper metal additive covered with graphite spray. The tracks are with their respective powder bed. The dashed lines separate the tracks. The purple lines in a) indicated the continuous track. The arrows indicate the balling effect for spherical melted Cu (blue) and elongated (orange dashed). All images have the scale shown in the panel a).

The support plate around the balling effect is visible, indicating that the Cu powder of the previous uniform powder bed left the sides of the track. When the graphite is present, the support plate is not as visible, and the powder stays around the track, mainly for energy above MA-100(see Figure 5.4b). If the Cu powder does not absorb enough energy to melt, it flies and spatters (laser pressure, reflectance), generating the denudation effect or a lack of powder around the track [289]. The spatter reduction between balling and continuous-stable welding has already been observed on stainless steel and corroborates the penetration depth of laser welding. In this context, when the graphite layer is over the powder, the energy is sufficiently absorbed to melt a continuous track resulting in a minimal denudation effect as shown in Figure 5.4b [290].

The essential function of this experiment is to verify the effective powder welded in the support plate in the track [289,291]. The topography SEM images show welded Cu without the powder bed around and in Figure 5.5[XXIX].

[XXIX] Larger size Figure 5.5 can be found in appendix 5B.

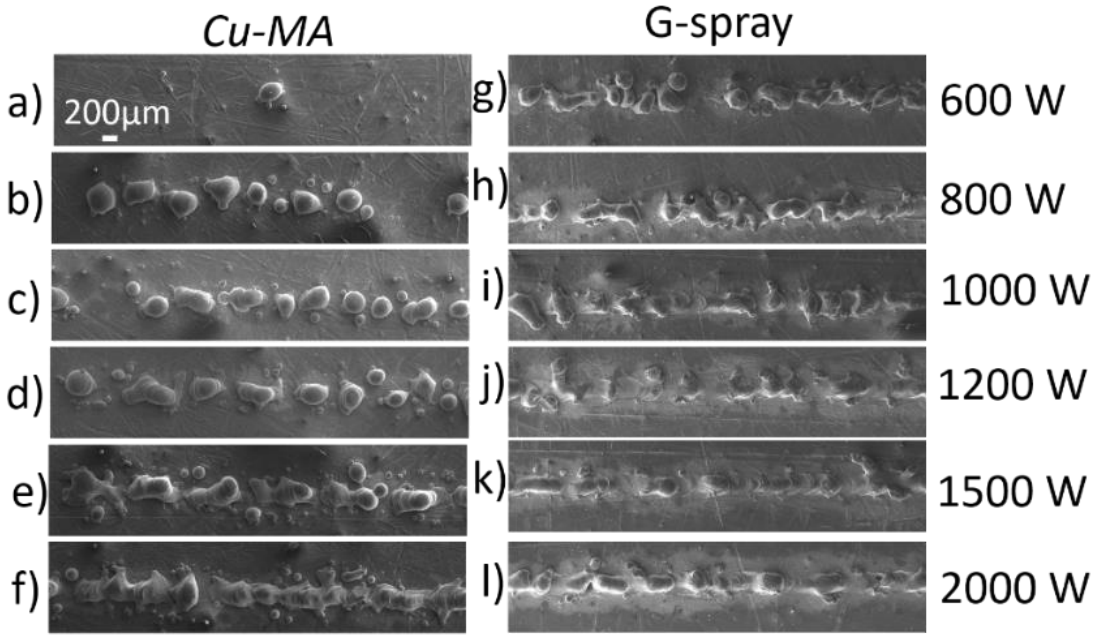

Figure 5.5: a) Topography SEM images of Cu – MA a–f) and covered with graphite spray (left) g-h) in the indicated powers in the right. All images have the scale displayed in a). This image can be found in appendix A.

The topography SEM images confirmed the balling effect from energies lower than 1500 W demonstrated in Figure 5.5 g-h for Cu-MA (left column). The evolution of the balling effect is observed from rare drops in Figure 5.5a to an almost continuous track in Figure 5.5f. This energy is not sufficient to obtain continuous joints. Some sparse grains and tiny grains called satellites are welded. The low absorption of the laser power gives rise to the balling characterized by highly coarsened balls possessing an interrupted dendritic structure on the surface layer [286]. The balling effect decreases as the energy increases, larger coarsened balls in the elongate shape of around 10 µm on the laser-sintered copper drops are caused by high scan speed [292]. The surface morphology found for Cu-MA(left column) could be due to incomplete wetting[xxx] and spreading of molten Cu droplets. The same morphology corroborates the results of tungsten powder [288]. Surface instability of single scan tracks like balling and irregular track width can lead to the formation of pores and deteriorate the sample quality [294]. The solidification time is short for Cu and tungsten with increasing temperatures. The Cu solidification is faster around its boiling temperature, resulting in larger balling tendencies than titanium, for example [288,293].

One can notice that the weld drastically improves when the graphite spray is on the sample (see Figure 5.5 g-l, the right column). The contrast around the track is modified for higher power and continuous welding is observed from G-1000 due to the higher energy absorption and fewer losses in reflectance (Figure 5.5c) [287,288]. The use of graphite results in continuous welding with eventual discontinuities at lower energies, such as 1000 W. Higher energy input improves the wetting and the quality of welds. On the contrary, satisfactory welding is only obtained at 2000 W for pure Cu use as a reference value for energy in this chapter (Cu-MA 2000) (Figure 5.5f). The power density was calculated using equation (5.1), the results are displayed in Table 5.4.

[xxx] the melted metal solidifies on a previously printed layer. It indicates the contact angle of the melting pool and the solid layer depends on the surface tension and thermal conductivity, among other parameters [288].

Table 5.4: Power density calculation for all the laser power used in this chapter using equation (5.1).

Power (W)	Power density (kW mm^{-2})
600	19.0
800	25.5
1000	31.8
1200	38.2
1500	47.7
2000	63.7

Three representative samples were chosen for the detail characterization, the G-600, G-1200 and G-1500, according to the reduction in the power density. Figure 5.6a – f. show the IR laser welding topography for 600, 1200 and 1500 W. One can notice that in general, for the three cases texture and form of the bead change when the Cu is graphite-like coated. Figure 5.6b, d and f present coarser and more coalesced grains than their analogous Cu-MA (Figure 5.6a, c and d). In the Cu-MA images one can notice several spatters (small melted Cu balling) around the main track that is not continuous [295].

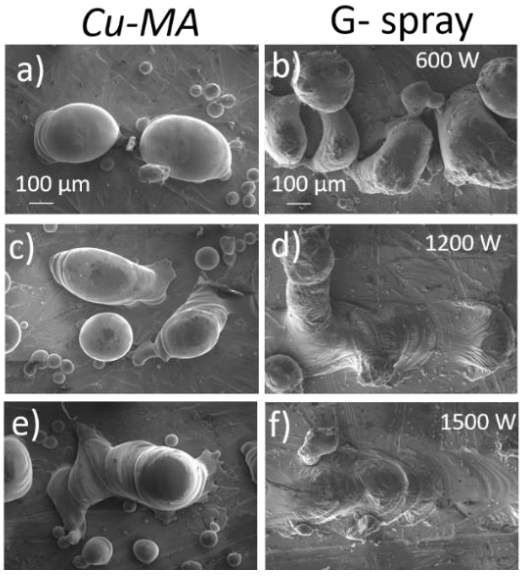

Figure 5.6: Topography SEM image of welding in three selected laser powers 600 W,1200 W and 1500 W; a), c), e) for Cu-Ref. and b), d), f) for samples covered with graphite spray. All the samples have the same scale of a) and b) samples.

The resulting shape of melted copper grains (or balling) indicates the melting pool shape during fusion since copper solidified fast. The solidification can lead to temperature gradients within the melt pools, resulting in balling effect [296]. The melting pool is a brief moment when Cu is in the liquid phase during laser fusion as detailed in Chapter I [297,298]. A fully continuous welding track is observed by adding the graphite-like coating (see G-1200 and G-1500 d and-f). The Cu powder grains were fully molten. Some instabilities can still be seen around the track due to the speed of the welding. The instabilities sizes may exceed the diameter of the laser spot, which triggers instability and distortion of the molten track [286]. The oval format of the melted sparse grains in Figure 5.6a – f. indicates a typical Cu melting pool shape [129].

5.3.1.1. The Copper Melting Pool using Graphite Spray.

In general, all the Cu pools presented an oval shape as in Figure 5.7a – b when using 1500 W over the copper plate covered by the graphite spray [296,299]. The copper melting pool is only perceived when the graphite spray is on the sample. The Cu plate reflects all the IR power, as shown in Figure 5.7c – e. The only signal of the welding of Cu plates is the color changing in Figure 5.7 d – e (dashed lines).

Figure 5.7a – b present superposed oval marks, only visible when the graphite spray covers the support plates. The oval format corroborates the marks of the image Figure 5.7f – h. The shape confirms the oval melting and solidification of the copper. Constantin *et al.* [122] reported a similar speed welding used in this thesis, around 400 mm/s using an IR laser YB:YAG (spot of 70 µm and 400 W power) on the spherical powder of average of 45 µm. The Cu microstructure is very similar to the one reported in this work. Also, when the temperature is around the Cu fusion point, the melting pool achieves the necessary viscosity, resulting in a stable molten pool [122]. Very similar structures of Figure 5.7g – h are reported by Qu *et al.* [300]. Figure 5.7h irregular shapes are attributed to either speed or excessive laser power when a graphite layer covers the Cu plate. Irregular shapes tend to present less dense welding [300].

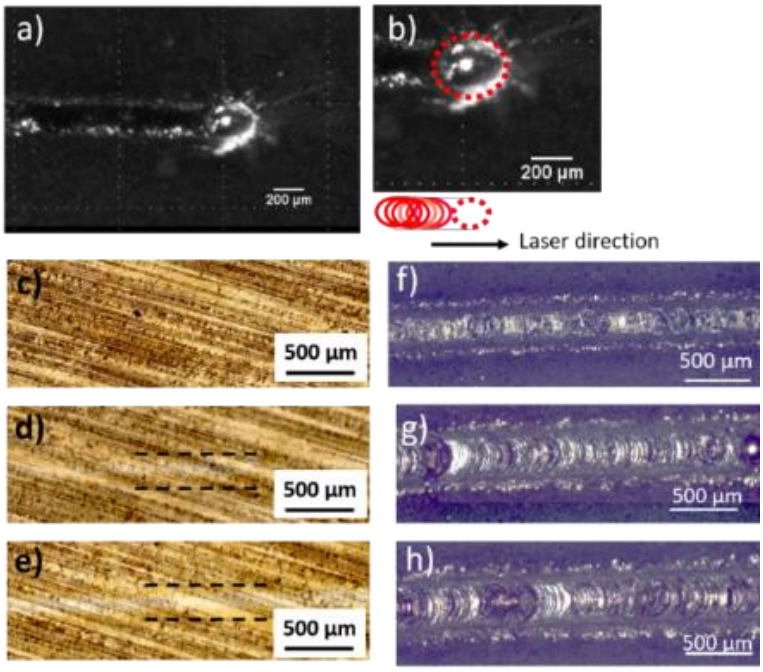

Figure 5.7: Copper liquid pool format a) video frame demonstrates the pool shape during welding employing 1500 W; b) schematic representation of the oval melting pool. c),d) and e) show pure copper and f), g), and h) the Cu plate coated with spray at 600 W,1200 W and 1500 W respectively.

The next analyses observe the cross-sections analogous to the Figure 5.1, i.e. copper support, powder and graphite spray.

5.3.1.2. Cu Powder Coated with Graphite Spray Cross-Section

Pure Cu welding tracks are shown in Figure 5.9 a-c. It was not possible to observe the bead's cross-section welded with laser powers up to 1000 W. This is attributed to the low energy input to weld the powder, or to the impact of the metallography preparation. So Figure 5.8 a-c shows the cross-sections of samples above 1000 W. Figure 5.8a presents irregular borders for the cross-section of Cu-MA 1200.

Figure 5.8b-c shows that when the power increases, the cross-section becomes more regular. The laser power requires continuous welding for pure Cu powder is 2000 W (~ 64 kW mm^{-2}) for this work weld configuration. The Cu-MA 2000 is shown in Figure 5.8c

[120,122,123]. The welding cross-sections show that in the track center powder is correctly joined to the plate (green dotted line), but the edges show welding failure (red dotted lines in Figure 5.8 a–c.

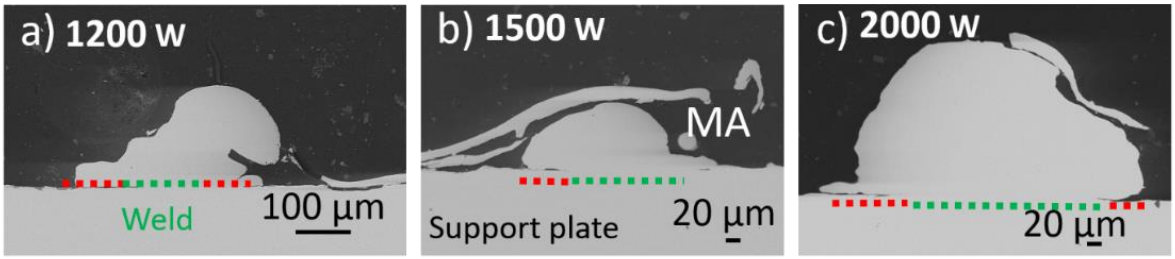

Figure 5.8: Pure Cu powder cross-section welded bead SEM backscattered images for: a) Cu MA 1200 and b) Cu MA 1500 and c) Cu MA 2000. The dotted line under the bead shows the welding zone in green and the zones not connected to the plate are shown in red. The samples presented were treated with metallography standard procedures until grit foil 2000 (SiC).

The Cu powder covered with graphite cross-section is displayed in Figure 5.9 a–c. Figure 5.9a shows minor cracks, pointed by the arrows(G-600). The Figure 5.9b-c do not present discontinuities in the welding joints. However, they presented a detachment in the upper part of the cross-section grain. This effect is also observed for pure copper. The backscattered images in Figure 5.9 do not show any differences in contrast, indicating the presence of one element. This result suggests that graphite does not appear in single tracks' cross-sections, since they are comparable to pure Cu in Figure 5.8.

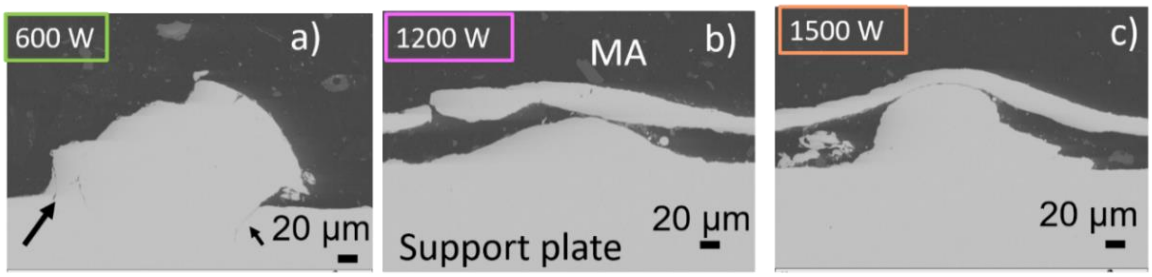

Figure 5.9: Cu powder coated with graphite-spray cross-section SEM backscattered images for a) G-600 and b) G-1200 and c) G-1500 until metallography standard procedures grit foil 2000 (SiC). The arrows indicate minor cracks in a).

The cross-section in Figure 5.10 a–c presents the same tracks as Figure 5.9 after the electroplating procedure. The metallography process can affect the edges of the cross-sections. The copper is a hard metal to work in metallography since it deforms easily [301]. The discussion is limited to the grain joints. Crystallography provides a better understanding of cross-sections in welding using graphite-like film. The interface Cu powder/plate did not present cracks, although some pores were detected in the upper part of the weld. The number of pores decreased for G-1200 and increased to G-1500. This result indicates that higher power is not guaranteed to reduce pores when using graphite-like spray.

Figure 5.10 a–c shows that carbon did not precipitate after fusion [302]. The grain boundaries did not present precipitation (dark point, particles, dendrite oxides or carbides) in Figure 5.10. The result was a homogeneous phase for welded Cu powder covered with graphite-like layer only in the parts exposed to the laser, this is discussed later. In the literature, carbon nanoparticles added to the Cu matrix agglomerate and separate from the Cu matrix in specific structures during fusion [302].

Globally, the shape of G-1200 is more regular than Cu-MA-1200. The elongated grains in the base turn into classical equiaxial grains in the upper part, parallel to the build direction,

due to rapid solidification [303,304]. The same happens in SLM in multitrack since the rate of heat conduction is higher in the previously solidified layers than in the one being melted [305,306].

The depth of the melt pool of graphite-like spray over copper powder is around 12 ± 0.5 and 22 ± 0.7 µm and 40 µm±1 µm in the deepest part of G-600 and G-1200 and G-1500 respectively, as indicated in Figure 5.10. The fusion depth is lower than the conventional depths of Cu in SLM due to the energy range. The pure melt pool depth of copper is approximately in the range of 50 µm to 100 µm. This range sufficiently melts the previous layer (layer superposition in SLM) by employing a larger IR laser energy density such as 407 kW mm^{-2} (spot= 25 nm, laser power 200 W) [300]. Ansari *et al.* [307] reported for Ti_6Al_4V depths of 68 µm in higher energies. In the frame of a multitrack SLM process, G-1200 exhibits a lower wetting angle, which is supposed to be more adapted to the SLM global process.

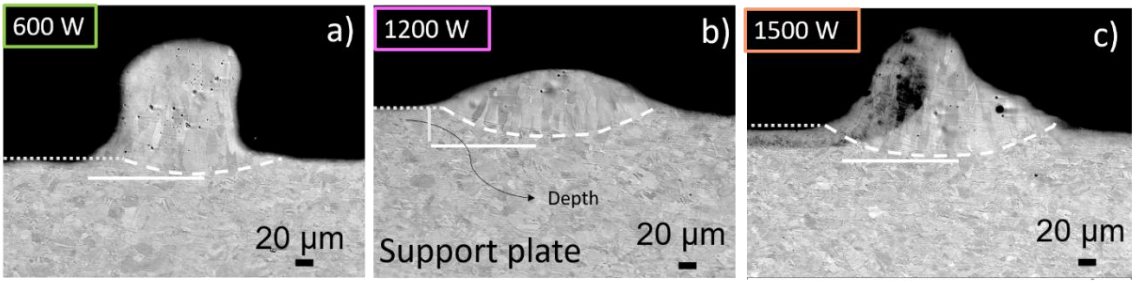

Figure 5.10: Graphite-spray coated Cu powder cross-section SEM backscattered images for a), G-600 and b) G-1200 and c) G-1500 the crystallography grains are revealed (electroplating). The dashed lines indicate the fusion depth. The grain shape is modified due to the metallography process.

The inverse pole figure (IPF) shows the direction of the crystal structure in Figure 5.11 a – c. The IPF demonstrates that the crystallography grain junctions between the welded powder and the support plate at the *junction zone*. Here the crystallography grains in the support plate are smaller than the welded bead. After melting, a microstructural change along the vertical axis of the bead was observed due to thermal gradients but not necessarily in the crystal direction. The grain fusion indicates good welding at the junction zone without cracks or pores, even for the lower power case, G-600. This result is attributed to the lower part of the powder bed that preserved the copper characteristics, i.e. it did not contain carbon so the junction Cu-Cu is conserved. The grain colors in samples G-1200 grain presented blue hues indicating orientation 111, while the ones in G-1500 presented orientation 101 (green).

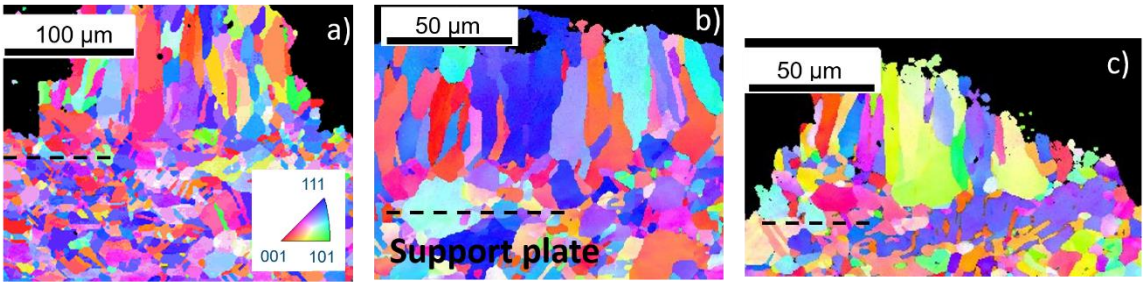

Figure 5.11: Inverse Pole Figure (IPF) demonstrates the crystallography orientation of the grains: a) G-600 and b) G-1200 and c) G-1500 respectively. The reference color is common for all images. The dashed lines indicate the approximative limit between the powder and the support.

By using this method only, the upper part of the Cu powder is covered by graphite, considerably reducing the graphite-like quantity in a single track.

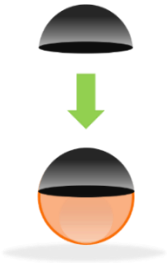

Figure 5.12: Graphite-like layer over a Cu beads schematic representation.

The graphite-like is only present on the surface exposed to the laser. The lower part of the powder preserved the pure Cu characteristics. The edge where the carbon film's end and the copper start were not delimited, but it is represented in Figure 5.12.

For 3D printing pure forms of carbon are preferable without liquid solutions. The graphite-like spray solution needs further improvements. The actual deposition tests were done using direct current magnetron sputtering. For future depositions, the recommended process is the cathodic arc deposition that fits better 3D printing. Both the deposition and the 3D printing process are done at the same pressure range, and the faster deposition rate of the cathodic arc can replace the GRAPHITE 33 spray [308].

5.3.2. a-C film Results on Copper Foils

Amorphous carbon deposited by magnetron sputtering was used on copper foils deposited at TSD = 2 (see section 3.2) to understand the absorption effect of the minimal films. We analyzed ultra-thin amorphous carbon films (25 nm) on Cu during welding. The thinnest layer implies the lowest deposition time and the higher reflectance reduction demonstrated in Chapter 4 and section 5.2.2.

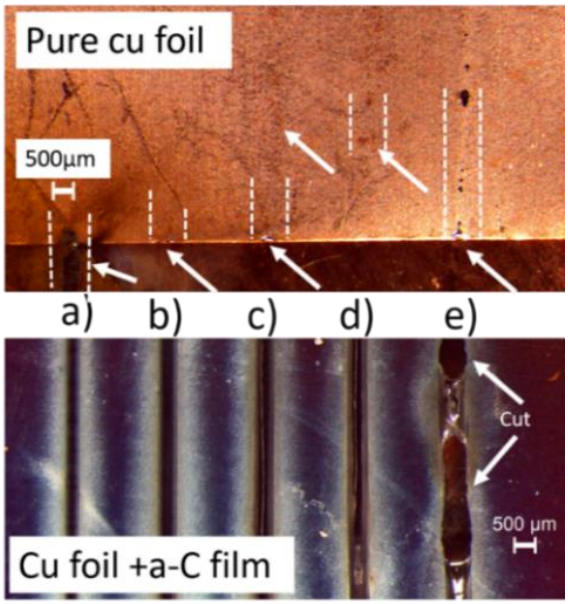

Figure 5.13: Pure copper foil and copper foil coated with 25 nm a-C film both welded at a) 600 W, b) 800 W, c) 1000 W, d)1200 W, and e)2000 W. Dashed lines indicate where the foil was marked by the laser. In Cu foil + a-C film, arrows indicate where the foil was cut by the laser.

The difference between the pure copper foil (top image) and the one covered with 25 nm a-C (bottom image) in Figure 5.13 a–e. The optical images of pure copper foils did not reveal the welding track position. The foils showed minor melting at the edges, and minimal oxidation in the laser track (indicated by the arrows) shown in the top image of Figure 5.13.

On the contrary, the presence of a-C films shows all the welding positions. In general, the color of the sample is tawny brown. However, the color around the track changed to a lighter

hue. The track thickness increases with the welding power. The arrows indicate where the foil was cut using higher laser power. SEM images confirm these results as indicated by the arrows and dashed lines in Figure 5.14a – d. The oxidation of Cu foils is cleared mainly for 2000 W (left column of Figure 5.14 d).

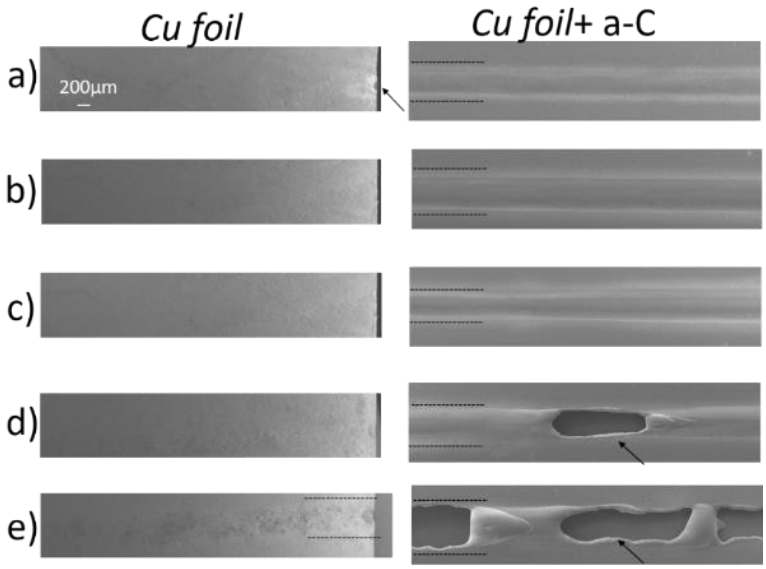

Figure 5.14: a) Topography SEM images of Cu foil (right) and covered with a-C films (left) using a) 600 W, b) 800 W, c) 1000 W, d) 1200 W e) 2000 W. All images have the same scale indicate in a). This image is also in appendix B.

For a-C25-1200 and a-C25-2000, the laser cut the Cu as indicated by the arrows in Figure 5.14d-e (right column). The remaining regions were affected by the laser, either melted or bent. The copper of the substrate melted at some points, forming protruded copper droplets. The foil was not rigidly fixed on the plate, so it moved during laser cutting due to laser power or recoil vapors.

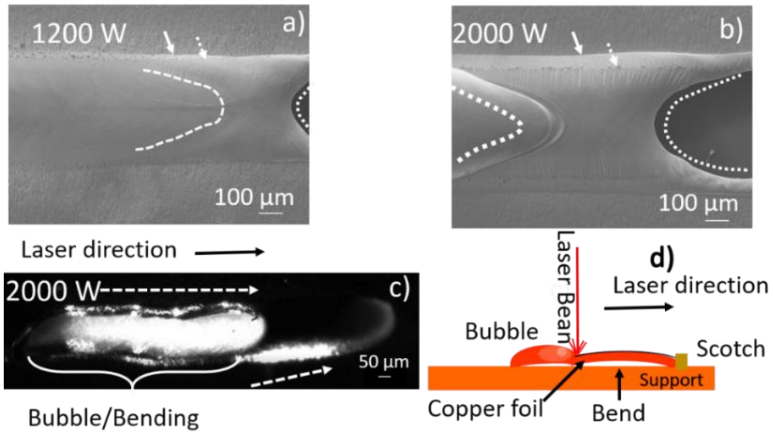

Figure 5.15: Topography SEM image of welding in a) 1200 and b) 2000 W, c) recording frame of the welding video showing a bubble formed during the process using 2000 W the arrows indicate the laser directions. In a) and b) the arrows indicate the striped line in the sides and, the dashed lines indicate the melting pool shape. The dashed arrow indicated the direction of the laser.

One can see an incomplete cut due to recoil vapors and fast heat diffusion in Figure 5.15 a – b. [115]. The power density used in this study was low, although it was sufficient to cause striations in the remaining Cu parts. Figure 5.15 a-b indicate stripes with different contrast and surface texture along the welding borders (between the welding and the film). The stripe's thickness increases from a-C25-1200 to a-C25-2000, indicated by the arrows in Figure 5.15 a – b. The upper part of the stripe striations appeared from the borders to the welding center, mainly

in the a-C25-2000 (Figure 5.15 b). The laser marks in the copper tend to be oval to turn into a triangular shape to a-C25-1200 to a-C25 -2000 (dashed lines). The cut format confirmed that the melting pool was oval and corroborated the literature shape [300]. The recoil vapor pressure occurs when metal evaporates, and the foil bends, creating a bump confirmed by the video frame in Figure 5.15c the edges are affected differently, resulting in the stripes. The laser causes the movement of the foil during laser welding [309]. In high-speed laser processes that result in cutting, the molten material quantity increases per unit of time. The high speed/high energy combination induces oscillations in the melting pool, resulting in spatial distortions [290]. The stripes and bending are attributed to the oscillations [310]. Laser cut surface finishing depends on the pressure of assisting gas, cutting speed, laser operation mode, and spot overlap [311,312]. Such a low power density as in Table 5.4 was not found in the literature for copper cutting process by laser or any copper melting process involving IR laser [72,233]. In general, energies in the order of hundreds of kW mm^{-2} are involved in the process[122,253,300,313,314].

5.3.2.1. a-C Laser Removal

In Figure 5.16 a–b, EDS spectrum and SEM images are shown to qualitatively verify any remaining a-C content after single-track welding. The cross indicates the position of the EDS in the images. The laser powers chosen for this comparison are 600 W and 1200 W. The EDS of a-C25-600 reveals that the processes significantly removed the a-C from the welding track compared to the *Reference a-C film* (not welded). The relative intensity of the *carbon peak* decreases while the *Cu* increases (counts y-axis). The higher energy density used in the sample C25-1200 resulted in a minimal *carbon peak* intensity(lower than 100 counts) and the highest intensity value of the C*u peak.* This comparison is relative to the other two samples, C25-600, and the *Reference a-C film*.

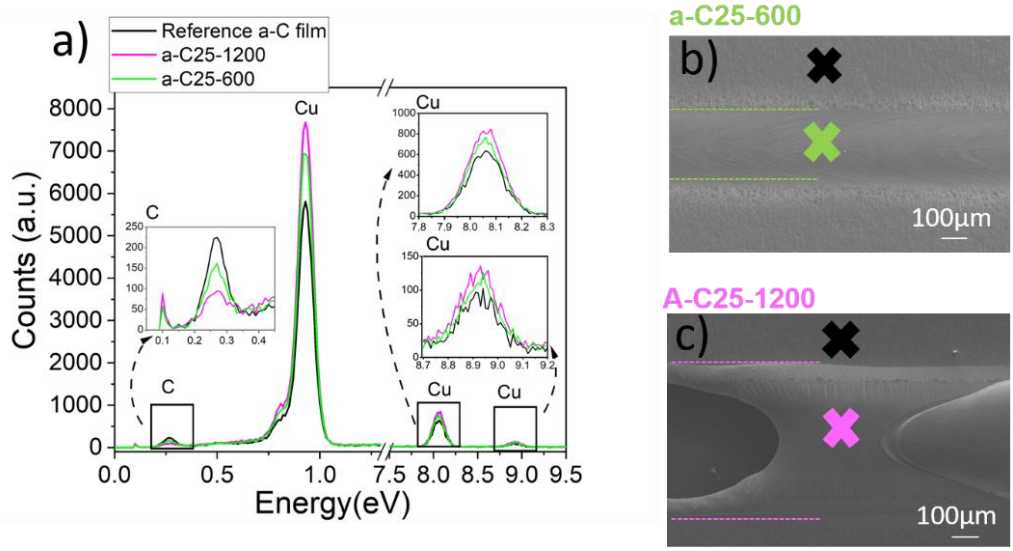

Figure 5.16: a) EDS of the 25 nm a-C ultra-thin film deposited over copper foil and the welding at b) 600 W and c)1200 W. The color of the crosses in panels b) and c) indicates the corresponding place of the analysis shown in a).

a-C coating absorbs more laser photons, as shown in chapter 4 and evaporates the underlying copper. For these conditions (1200 W), the laser can remove up to 110 µm of Cu, the so-called laser cutting as discussed in the section 5.3.2. As mentioned in the introduction, Cu reflects around 98% of IR rays, challenging processes such as SLM, or even for laser cutting. The integrating sphere done at PIMM laboratories demonstrated that the a-C layer improves laser absorption over Cu substrates. Only 25 nm a-C films absorb and transmit around 40% more light compared to pure Cu (0–5 % maximum IR absorption). The extra absorption when a-C films are on track results in less energy loss by reflection. This loss can reach 100% at λ= 1000 nm as indicated in Figure 5.17.

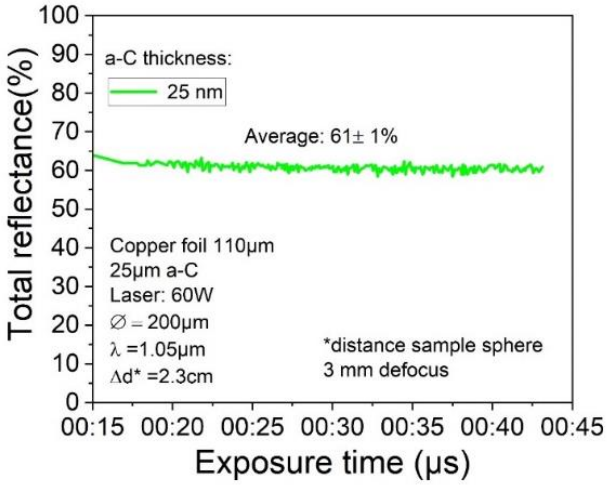

Figure 5.17: Total reflectance of 25 nm a-C film over copper foil measured using an integrating sphere and the Trumpf laser at PIMM laboratories.

Previous optical analysis of the same type of film using an integrating sphere at a spectrometer UV-Visible confirms this study's results in chapter 4 [258].

5.3.2.2. Amount of a-C films over Copper

An important point to SLM is to add the minimum quantities of material in the copper. Thus, the percentage weight of graphite added in Cu powder bed was calculated using classical volume formulas. The track is considered a rectangle, the a-C film hollow-hemispheres which the volume is calculated using equation (4.2)

$$V = \frac{2}{3}\pi(r_{Cu}^3 - r_{Cu+C}^3) \qquad (4.2)$$

Where the final width of the hemisphere is the carbon film layer thickness. The graphite density was used 2.26 g/cm^3 for the film. A Cu powder bed of an average of 55 µm and dimensions: 200 µm × 5 mm ×110 µm was considered. The copper density used was 9 g/cm^3 [58,274]. The mass of graphite in one bead was calculated. The number of grains in a track was also estimated using the volume of one bead of 55 µm. The mass of the one graphite hemisphere (volume × density) was multiplied by the total grains in a powder bed so the mass of carbon was obtained.

Around 1.6×10^{-6} % wt. is added to the track considering pure graphite density as continuous hollow hemispheres of 3.5 µm thickness. Since a maximum of 5% of this layer is graphite (see the composition of GRAPHITE 33 in appendix 5A), this value is reduced to 8×10^{-8} % wt. One might consider other impurities such as isopropanol and hydrocarbons (50–75 % of the spray composition). If 25 nm of graphite were inserted in this configuration, the value is 1×10^{-8}% wt.

The same calculation was done for copper foils and a-C films considering the track as a rectangle. When a massive a-C layer of dimension 200 µm × 5 mm × 25 nm is inserted over the same previous track volume of copper (200 µm ×5 mm ×110 µm). The a-C density found in chapter 3 for TSD = 2 cm around 1.5 g/cm^3. The a-C quantity result is the result is 4×10^{-3} % wt. The carbon peak is already minimal in the EDS of the *Reference a-C film* when compared to Cu, the tendency is that less than the initial carbon concentration stays in the samples after the welding for 1200 W (see Figure 5.16).

The mechanism of a-C absorption has to be considered to reach the necessary fusion temperature in lower laser powers. Pure carbon evaporates at around 3550 °C, copper evaporates at around 2595 °C. Some forms of carbon have pressure vapors at temperatures of

2400 °C [315]. One can speculate that when 40% extra laser power is absorbed, providing sufficient energy to the graphite-like film.

Jadhav *et al.* [130] suggest that carbon from the copper powder reacts with oxygen leaving the welding zone in any stable form of gas, such as CO_2 or CO in gas format. The formation of carbon dioxide/monoxide (gas) is favored when the temperature of the system containing Cu, O, and C elements exceed 150 °C [316]. In the literature, the authors observed a lower amount of carbon and oxygen after SLM compared to the corresponding powder before the printing process [317]. These results corroborate this thesis observation Other factors are the bouncing mechanism in the a-C film discussed in chapter 4 and that minimal deposition only in the laser exposed part of powder grains or foil are crucial for the energy absorption.

Cu evaporates when energy is in excess, a very common process to find copper on the fusion chamber's wall, the main objective is to melt Cu [258,303]. Other metals are largely studied in 3D printing as Ti_6Al_4V due to the vapors that condensate on the focal lens of laser beam processes, resulting in building failure [318]. In the copper case, more than vapors, the high energy is also a problem to the lens lifetime, pushing the development of this component [319]. It is common in both processes, SLM and EPBF, to overuse the source power (laser and e-beam) such as part of the Cu evaporates as discussed before increasing local *vapor pressure*. The striation and the cut in the foil confirming that G-1200 W (Figure 5.16) reaches the necessary energy to vaporize copper and remove a-C film/On the contrary, the necessary energy to cause striations on pure copper are far higher. The power can be reduced by at least a factor of 2 when a graphite-like layer is present to cut copper foils [309]. In general, the extra power in SLM is necessary to overcome challenging copper features when using lasers. The high conduction leads to heat losses and fast solidification. The high reflection rate in IR range resulting in poor energy absorption. These features create several drawbacks such as vapor clouds, droplets over the Cu melt pool during fusion influencing the quality of the final properties of the printed object [120,303]. However, the details of this mechanism are yet to be studied.

5.3.2.3. SLM of a-C Copper Preliminary Results

A multilayered system using SLM is present in Figure 5.18 a-c. The diagonal line of squares in Figure 5.18a was printed on a Cu plate. Figure 5.18b demonstrates the part recovered with 25 nm of a-C film deposited by DCMS. One can notice the color of the sample change to blue and tawny brown hues, the same colors as the samples analyzed in section 4.3.2. However, in Figure 5.18c, when another powder layer was welded over the a-C films using the SLM process, the squares presented their characteristic bright Cu color again.

The preliminary results showed that the copper powder is welded over a-C films indicating good adhesion to the previous layers. Also, the square presented suitable shapes.

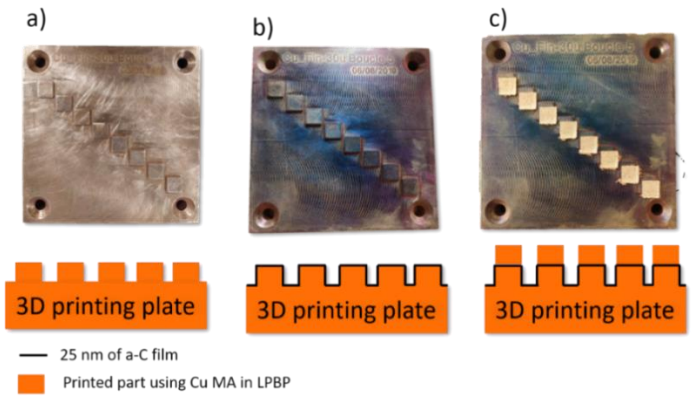

Figure 5.18: a) Sequence of printed squares in a printing plate using SLM process b) deposition of 25 nm of a-C film and c) continuation of the printing process over the a-C film.

5.4. Conclusions

Good welding is achieved by reducing up to 70% density power of an IR laser when graphite-like films are deposited over Cu substrates. Therefore a continuous track is obtained for low laser power. The presence of graphite reduces the drawbacks of the higher energy needed to melt Cu, such as the denudation and balling effect. The cross-section analysis was only possible for pure Cu powder for laser power higher than 1000 W. On the contrary, all cross-sections of the set were examined using graphite-like film starting at 600 W. The coatings are deposited on one side of the powder beads preserving the character of the Cu-Cu junctions in the support and, eventually, the energy transference to the support. The cross-section of the fusion Cu powder-support plate did not show cracks or pores when using graphite films. The cross-section reveals elongated columnar grains turning in equiaxial on the top due to thermic gradients when graphite is present. G-1200 presents a better wetting angle for a future application in the multitrack SLM process using 40% less IR laser power, as the previous results indicate.

Further, negligible carbon residue remains after welding for ultra-thin a-C film 25 nm. When employing 1200 W, the a-C film did not segregate on the Cu matrix and tended to leave the track in CO or CO_2 for the single-track laser weld. The results indicate a good energy transfer from a-C to Cu, even for the ultra-thin case. Indeed, the addition of graphite-like coatings over the Cu decreases the required IR laser power for continuous quality welding using powder from 2000 W down to only 600 W. The ultra-thin a-C on Cu can be further extended to other energy absorption purposes like lightweight, flexible electronic devices. The deposition process (direct current magnetron sputtering) is scalable to large-area coatings and is effective for laser processes. The graphite spray is efficient in absorbing the IR laser. However, it presents impurities, and the spray is a liquid solution. Thus the use of plasma deposition is recommended, such as magnetron sputtering deposition or cathodic arc discharges to thin film deposition are an excellent alternative since the pressure range of the deposition and the printing machine are the same around the atmospheric pressure.

CHAPTER VI: Cu Powder Under a Voltage

In this chapter, physical phenomena involving conduction in granular materials are discussed. Due to the complexity of the mechanisms, they have not yet been completely elucidated. The current flow mechanisms through the *copper powder* are crucial for the control of superficial *charging and sintering* in the printing manufacturing process. The understanding of powder electrical properties can be used to avoid several drawbacks, including charging and the smoke effects in the EB-PBF process.

Summary

Abbreviation Chapter VI

R	Calibrated Resistance
I	Current
DFT	Discrete Fourier Transform
E_0	Electric field
V (r)	Electron potential energy
FFT	Fast Fourier Transform
Hz	Hertz (frequency)
V_1	Input voltage
k Ω	Kilo ohms
LPBF	Laser Powder Bed Fusion
MA	Metal additive
V_2	Output voltage
V_{pp}	Peak-to-peak
V_3	Powder voltage
E	Total energy

6.1 Chapter Introduction

Granular materials, specifically oxidized metal powder, generally have a much lower electrical conductivity than metal bulk [320]. Contrary to a piece of metal, the powder conduction depends on several factors on the nanoscale and micro-scale [136,320]. The micro-scale includes the state of compaction, grain distribution, and contact among grains. The nanoscale can consist of the oxide layers and other Wan der Waal forces discussed later in this chapter [133,136]. Furthermore, the packing density and the thermal and mechanical properties of a layer are crucial to the excellent achievement of a printed part [74,321,322]. It remains critical to characterize the electrical properties of the Cu powder since they ultimately determine the layer properties in 3D metal printing mainly but not exclusive in EB-PBF due to the charges' evacuation mechanism.

Édouard Branly was one of the first scientists to measure granular resistivity in 1980 [192,323]. Branly studied the resistivity of different fine materials. He observed that the resistivity of metallic powder changed instantaneously when induced waves by a Ruhmkorff coil passed through the powder inside a glass tube. He used several metals like Fe (iron dust), Al, and Cu. Branly observed the same effect even the inductor (Ruhmkorff coil) was 20 m away in the other room [324]. The conclusion was that waves could travel in the air to a receptor revolutionizing his time. At first, the Cu powder presents an insulator condition due to poor contacts; when an external disturbance happens as an applied current, the resistance values vary considerably [192]. This effect is the transition from an insulator to a conductor of oxide granular powders [184].

According to Dorbolo *et al.* [137], external disturbances enhance or create contacts among the grains, the external disturbance can be an electromagnetic wave or electric current. Other mechanisms of the transition effect are electrostatic charges and micro-sparks [325]. The transition from insulator to conductor exhibits non-linear behavior attributed to the oxide layer [320]. One of the explanations agreed upon among authors is micro sintering [184,326–329]. The resistivity transition is due to the temperature of micro-contact. The micro-contacts are due to the grain's roughness; they change their temperature when the current passes through the connections. The grains start to soften if enough current reaches the micro-contact fusion point [330,331]. If the current keeps increasing, local damage due to Joule heating, micro-sparks, or breakdown events destroy the oxide layer, subsequent melting and finally soldering of one grain into another [137,332]. The soldered grain and the oxide removal lead to a growing network of conducting channels, following Ohm's law [320,333].

Two states are possible when conducting channels are in the powder. If the grains are sintered the paths are permanent, the resistivity of the powder is lower than its initial state without conductive paths. Irreversible micro-sintering or micro-welding is a strategy to increase the grains conduction network to the best progress E-PBF, avoiding drawbacks such as the smoke effect, powder charging, and repulsion due to the better charge flow [334,335]. However, this way to improve the power conductivity critically affects the recyclability of the powder. On the contrary, the transition is reversible if the temperature is not enough to melt grains together, so the grains can return to their insulator state if the applied current is off [184]. The current flows in a powder bed used in 3D metal printing have not been completely elucidated [320,335]. This chapter shows empirically analyzes the currents flow in Cu powder, the transition from an insulator to a conductor for two of the grain size distribution.

6.2 Methodology

The experiments were done using two distributions of copper powder and its native oxides in the circuit described in Figure 6.1a. The first granulometry particle 45 µm-106 µm

averaged at 61 µm supplied by Add Up metal solutions. The second granulometry particle is 15 µm-52 µm averaged 32 µm supplied by UTBM-ICB. A desiccator under primary vacuum preserved the powder oxidation.

The circuit used in this work is demonstrated in Figure 6.1a. The experimental data collected from this experiment was the voltage at two terminals in the circuit. The arbitrary wave generator is configured to generate a triangle pulse detailed below. The probe V_1 measures the values delivered at the terminal of the DC power coupled to the generator. The probe V_2 recorded the voltage at a calibrated resistance R terminal. So, the difference between V_1 and V_2 is called V_3 is assumed to be the voltage in the metallic powder indicated in Figure 6.1a. From equation (6.1), the current of the circuit (I) is calculated using V_2 and the calibrated resistance R. The chosen resistances are 470 and 330k ohms generating a maximum current of 140 mA and 0.20 mA, respectively. The current varies by a factor of 600, the same magnitude as the resistance factor.

$$I = \frac{V_2}{R} \tag{6.1}$$

Figure 6.1b shows the metallic powder support or the cohéreur as it is referred to in Chapter 2. Two electrodes are screws of M10 thread. The electrodes were employed to adjust the crucible height and the vertical contacts on the powder surface. The upper electrode is responsible for the input voltage. The crucible is a plastic cylinder threaded in the lower electrode so the recipient height is adjusted depending on the number of turns in the lower screw. Two plastic aligners were used to center the M10 electrodes.

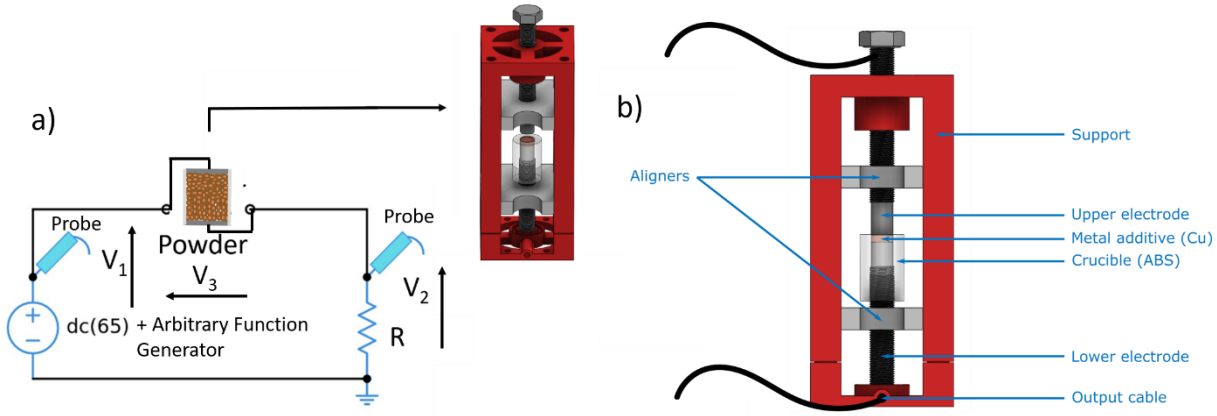

Figure 6.1: a) Schematic representation of the circuit used in the measurements, V_1 values correspond to the power supply terminal coupled with the generator. V_2 values correspond to the resistance R terminal, and V_3 is the voltage in the red support. b) The 'Cu powder support' or the cohéreur contains two M10 screws or the electrodes (up and low), the crucible or powder recipient, and aligners to centralize the electrodes.

The crucible of 10 mm diameter was unscrewed from the lower axis until the desired height of 5 mm, equivalent to around three turns counter-clockwise. This distance was kept constant in all sequences, the crucible volume is 393 mm^3. The metallic powder was mixed in its original container to obtain a representative sample of the particle's distribution. Later, the crucible is homogeneously filled resulting in a powder column of 5 mm. The crucible edges were carefully cleaned using a paintbrush, so the upper electrode touches only the powder inside the crucible as indicated in Figure 6.2. The Cu powder did not contain any agglomerates before the tests. The upper electrode was lowered until the *touching point* demonstrated in Figure 6.2. After the *touching point*, the compression is measured as the height between the crucible top edge and the bottom of the electrode.

The upper electrode is immersed in the powder as shown in Figure 6.2. The upper electrode compacts the powder. The compaction role is to obtain stable contacts, so the bare minimum was used in this chapter results, around 0.23 mm, 15% of one electrode turn below the touching point. However, other compressions were tested depending on the powder granulometry cited above. The maximum powder compression was 1.96 mm (1.25 extra turns after the touching point). The electrode and crucible adjustments are manual. The compressions used in the pulses sequence are described in the sections 6.3.1 and 6.3.2. Each sequence employed a new metallic powder.

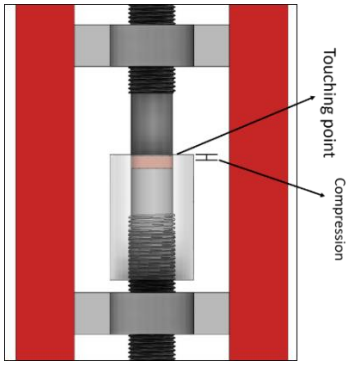

Figure 6.2: a) Schematic representation of the Cu powder support. The touching point is where the upper electrode only touches the powder surface, the compression is quantified in the Cu powder the distance between the upper crucible border and the electrode's bottom when the upper electrode is immersed.

The parameters of the pulse are constant in all sequences called the *Standard Pulse*. The triangle pulse is generated using the function 'frequency-shift keying (FKS)' of the Arbitrary Waveform Generator. The peak-to-peak voltage (V_{pp}) is +10 V, the final voltage was a triangle of +65 V±2 V due to the amplification of the coupled DC power as demonstrated in Figure 6.3. The voltage of the pulse was constant and unipolar positive applied directly in the metallic powder. The pulses were manually started in an interval of 15s±2 s between each pulse.

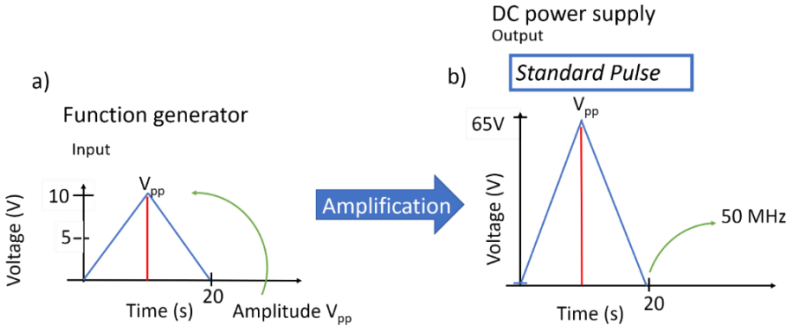

Figure 6.3: Schematic representation of the standard pulse. a) The function generator input parameters, b) the final pulse after amplification using a DC power supply.

Four sequences are presented in the Results and Discussions section, for each condition shows a sequence of representative pulses. Each sequence is referred to by a number summarized in Table 6.1.

Table 6.1: The resistance and the powder distribution size are demonstrated for each sequence in the circuit of Figure 6.1.

Sequence	1	2	3	4
Cu powder Ø (µm)	45-106	45-106	15-54	15-54
Resistance R (Ω)	470	330K	470	330K

6.2.1 Signal Filters

The raw and filtered peaks are shown in Figure 6.4 a–b. The raw signal obtained V_1 and V_2 in the circuit demonstrated in Figure 6.1a was filtered using a Fast Fourier transform (FFT). The numerical signal of the generator is treated using a low pass filter of 5 Hz to avoid high frequency noise. The smoothing treatment in V_3 and the current (I) was chosen to avoid distortions and misinterpretation of spikes. The raw and treated peaks are shown in Figure 6.4b.

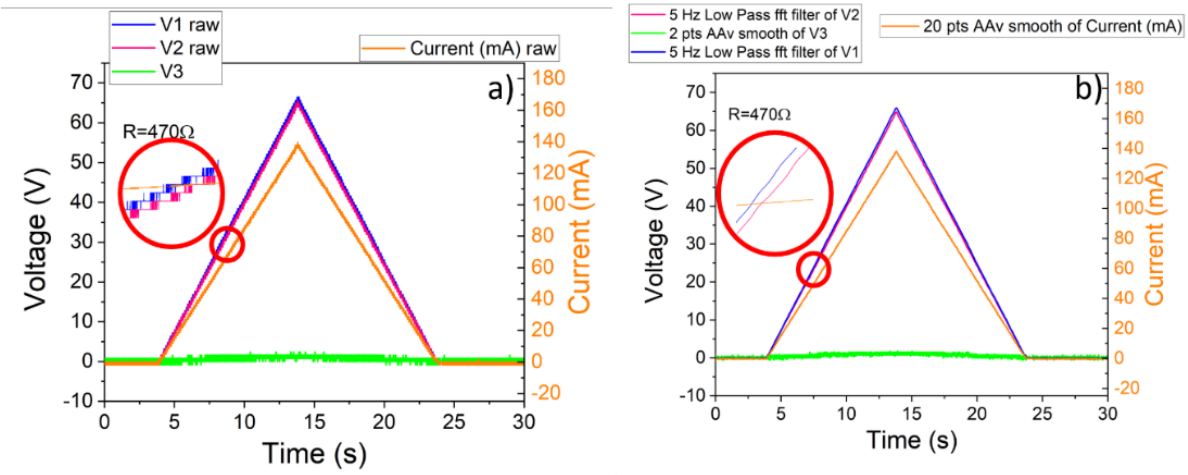

Figure 6.4: Demonstrative pulses without Cu powder in the system; a) the raw data and b) the treated data as presented in the results section. The zoom in the inset shows the raw and filtered peak.

6.2.2 Procedure to Find the Residual Reference of the System

The residual resistance measurements were done without powder in the circuit. This measure avoided misleading interpretation of an eventual residual effect coming from another component. No particular effect happened without Cu powder in the system (Figure 6.4 a–b). The reference test used 470 Ω and 330k Ω) applying the standard pulse. In this experiment, the systematic error is around 2%.

6.3 Results and Discussions

All the following results are obtained in the presence of powder between the electrodes. The results are displayed according to the Cu powder distribution. The first set of results here is for the 45–106 µm (sequences 1–2), followed by the second set for 15–52 µm (sequences 3–4). This section is dived in results and discussions.

6.3.1 Sequences 1–2

Sequences 1–2 show the behavior of the Cu powder in a series of pulses using different currents. [133,134]. After several tests, the best compression to guarantee that the electrodes are in contact with the powder is when the upper electrode is immersed 0.23 mm in the Cu powder. This represents around 5% of the crucible's total volume (15% of extra upper electrode turn after the touching point). In this case, the assumption is that the upper electrode did not compress the powder. Sequences 1 and 2 used this 'standard' condition of compression in all pulses.

A general view of the sequences 1 and 2 using different currents is demonstrated in Figure 6.5 a–b. One can notice the evolution of the current in the Cu powder. When V_1 is triggered, the system behaves similarly to an insulator (the current (*I*) and V_2 are both zero). The metal additive system[XXXI] did not conduct immediately, so the voltage in the Cu powder V_3 increased. The threshold point indicated by the star triggers the transition effect characterized

[XXXI] By MA system one might consider the MA the spaces among the grains air oxides, etc. ;

by a current jump. One can observe that in the threshold the *current I and* V_3 *varies*. Once the charges find a conductive path among the grains, the transitional effect occurs and V_3 drops [184,320]. Once the system stopped acting like as an insulator, the current passed through the Cu powder during the whole pulse time following Ohm's law. The powder conducted during the hole pulse in the last two pulses of Figure 6.5 a.

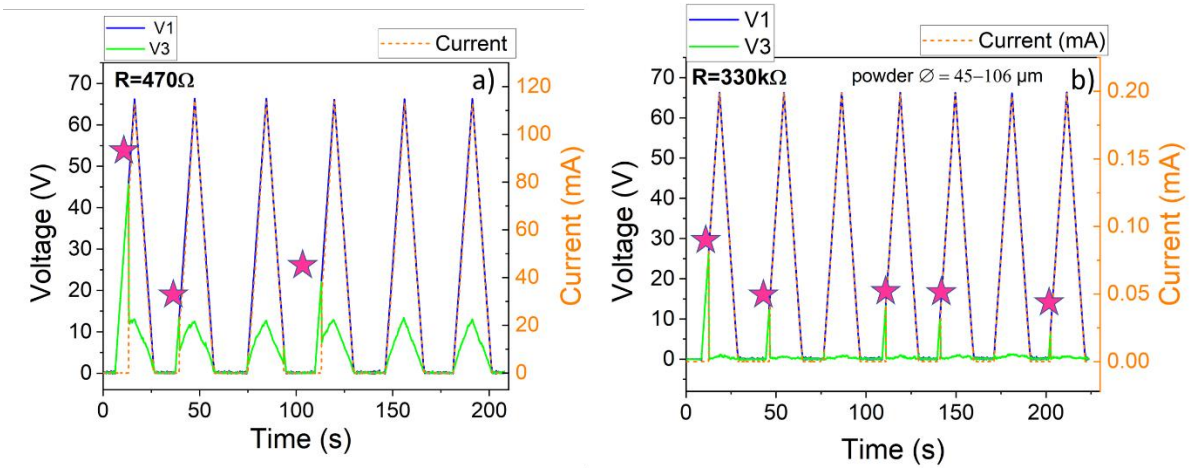

Figure 6.5: The complete sequence of pulses a) using the resistance of 470 ohms resulting in a maximum current of 120 mA (sequence 1) and b) using the resistance of 330k resulting in a maximum current of 0.20 mA (sequence 2). The experimental input voltage V_1 and V_3 are comparable on the left y-axis. The current (dashed orange) is reported on the right y-axis. The stars indicate current flow jumps.

The powder acts as an insulator at the beginning of the pulse. Although, if pulses are applied in a row, the insulator character is reduced and extinguished. Several stars indicate the recurrence of the insulator state in the sequences of Figure 6.5 a–b. After several pulses, the system preserved a conductive path and the current flowed from the beginning of the pulse, in the case of the last two pulses in Figure 6.5a. On the contrary, in Sequence 2, the transition effect happened more times, as indicated by the stars in Figure 6.5b. The stability of the current paths between sequences 1 and 2 was different due to the recurrence of the insulator character. Higher currents increase heat in the powder contacts by the Joule effect detailed in the discussions section [332]. The insulator effect was generally more pronounced in the first peak than in the last one [336]. The first peak of both sequences was analyzed in detail.

The zoom of the first peak of Figure 6.5a using a higher current is displayed in Figure 6.6 a–b. The peak was divided in three zones. At the beginning of the pulse V_3 follows V_1, indicating that current is not passing through the Cu powder, the zone I. When the *transitional effect* happens in zone II, the current jumps from 0 mA to around 68 mA a brief moment indicated by the star. At this point, V_3 drops because the current can flow. After, the Cu powder conducts during the remaining pulse period, following Ohm's law, Zone III.

Though due to the transition from an insulator to conductor hysteresis is observed between the voltage increasing and decreasing in the triangle pulse shown in Figure 6.6b. One can notice that the vertical arrow in Zone II indicates the current jump. The first points after the jump (voltage up) indicated lower current compared to the voltage down. The specific duration of each zone represented on the x-axis of Figure 6.6a is hard to determine since it is a sensitive parameter. It is highly dependent on the compression, a little variation in the compression can alter the duration of all three zones. Zone II is the border between Zone I (insulator) and zone III (conductor).

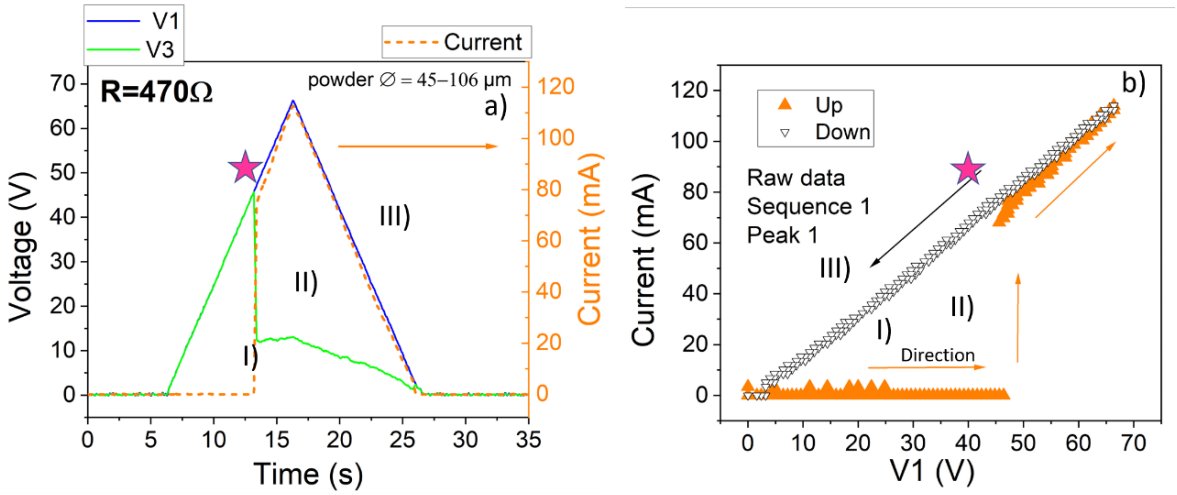

Figure 6.6: The first pulse of sequence 1 using R= 470 Ω is analyzed. The star in a) indicates the transition effect. The experimental inputs V_1 and V_3 are comparable on the left y-axis. The current (orange dashed line) is reported on the right y-axis as indicated by the arrow. b) Representation of hysteresis in the current (mA) when the input voltage (V_1) is increasing (up) and decreasing (down).

For the sequence 2, the pulse was analyzed using a resistance R of 330 k Ω in the circuit, representing the lower current (0.2 mA) in Figure 6.7a–b. For the 54 µm-106 µm the current reduction indicates a similar transition as the one observed in higher current in Figure 6.6a. The hysteresis of this transition was smaller than for bigger currents despite this observation is not determinant for all lower current cases. The current jump went from 0 mA to 0.08 mA.

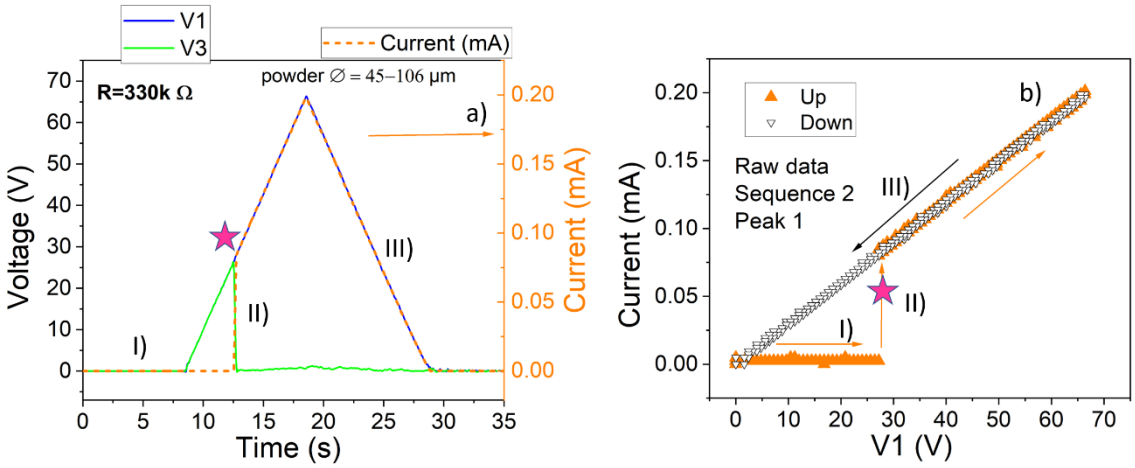

Figure 6.7: a) The first pulse of sequence 2 using R= 330k Ω is detailed. The star in a) indicates the threshold. The experimental input V_1 and V_3 are comparable on the left y-axis. The current (orange dashed line) is reported on the right y-axis as indicated by the arrow. b) Representation of hysteresis in the current (mA) when the input voltage (V_1) is increasing (up) and decreasing (down). The arrows represent the path direction.

6.3.2 Sequences 3–4

Sequences 3 and 4 use a lower powder distribution of15–52 µm with an average diameter of 32 µm. The size is the main difference from the previous sequences. Nowadays SLM process uses this Cu powder distribution. The printed objects have a more refined surface finish and better mechanical properties using this distribution [282,337]. The 15–52 µm distribution, also called *the lower distribution* tends to form more agglomerates than the bigger distributions shown in Figure 6.8a.

The as-received Cu powder represented by state (I) presented agglomerates. On the contrary the bigger distribution did not present any before the pulses. The distribution15-52 µm

was sieved using a mesh of 110 µm. The resulted powder without macro-scale agglomerates is shown in state (II). All the Cu powder samples submitted to sequences 3 and 4 did not present macro agglomerates. Nevertheless, the agglomerates were re-formed after the pulses, as demonstrated for one representative sample in Figure 6.8b.

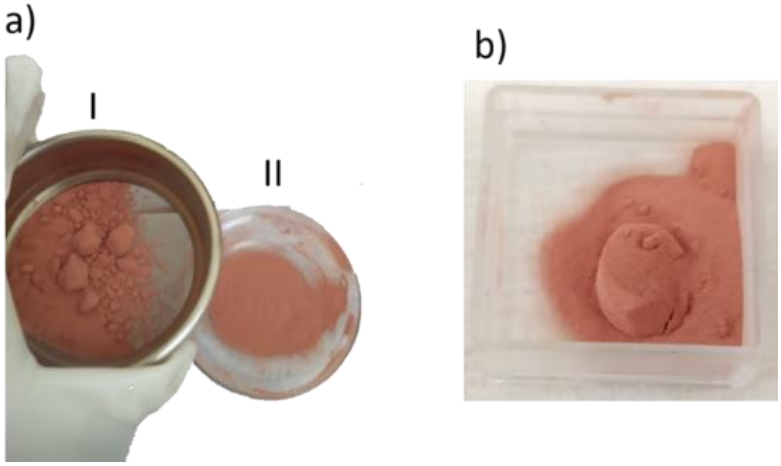

Figure 6.8: a) Cu powder distribution of 15–52 µm as received demonstrated at I). The powder of state I sieved in a mesh of 110 µm to unpack the agglomerates at ii). b) Sample of sequence 3 after the pulse sequence with re-formed agglomerated powder.

The basic difference of smaller distributions is the influence of forces among the grain. This type of Cu powder is much more sensitive to the compression, it tends to agglomerate. For small distributions, the inter-particle force becomes more important than the gravity [128]. The powder mass is not sufficient to overpass this cohesion. The magnitude of the Van der Waals force (attraction between the particles in a certain distance), electrostatic charges, and capillary (forces due to the presence of a liquid) or event friction between the beads has more influence in smaller distribution [136,322,338]. Due to this agglomeration effect, the compressions varied to find the transition effect. For this configuration the transition was not systematic as for bigger currents. The upper screw is immersed into the powder from 0.23 mm to 1.96 mm (15–125% extra turn after the touching point). The compression range of lower distribution is discussed separately for each sequence.

The general aspect of the sequences 3–4 is shown in Figure 6.9a–b. The transition effect was not as easily triggered using smaller powder. On the one hand, for sequences 1 and 2 the transition effect appeared systematically in the first or second pulses with negligible compression. On the other hand, different phenomena occurred in the same compression range tested for sequences 3 and 4. The peaks are identified by a letter to understand better the effects in each peak.

In sequence 3, the transition effect required more compressions than sequences 1-2. The range of compressions is 0.23-0.4 mm of the upper electrode inside the powder. Specifically, the compression for sequence 3 was around 0.4 mm below the touching point around the double distance of sequences 1-2. In Figure 6.9a, the current presented a different pattern, a tiny current passed. The peaks b, c and, d showed that the threshold (star) in the system decreased along the pulse sequence corroborating the previous results. Last, the peak conducted current during the whole pulse period.

In sequence 4 the pulses have different compressions. This configuration demonstrated that a minor variation in the compression changed the current flow as indicated in Figure 6.9b. The sequence started at the upper electrode immersed 0.23 mm in the powder, in the case of peak f then it varied. The compression reduced to less than 0.23 mm for peak g-h, and increased for peaks i-j, (> 0.23 mm). The variation in each peak was at most ±10%. In this set the first

observation was conduction. The insulator effect did not appear at comparable compressions than the ones used for bigger powders. Two behaviors were observed, in the first the Cu powder conducted straight as in peak f. In the second, it acted as an insulator during the whole pulse period as in peak g–h.

Contrary to the other sequences, the transition effect demonstrated in peak i was difficult to obtain. The transition occurs at a more precise compression for this configuration, the system did not contain the fine adjustment to quantify the compression. The powder compression was manually done using an M10 screw. The compressions for this sequence were hard to specify due to its extreme influence, mainly in lower current.

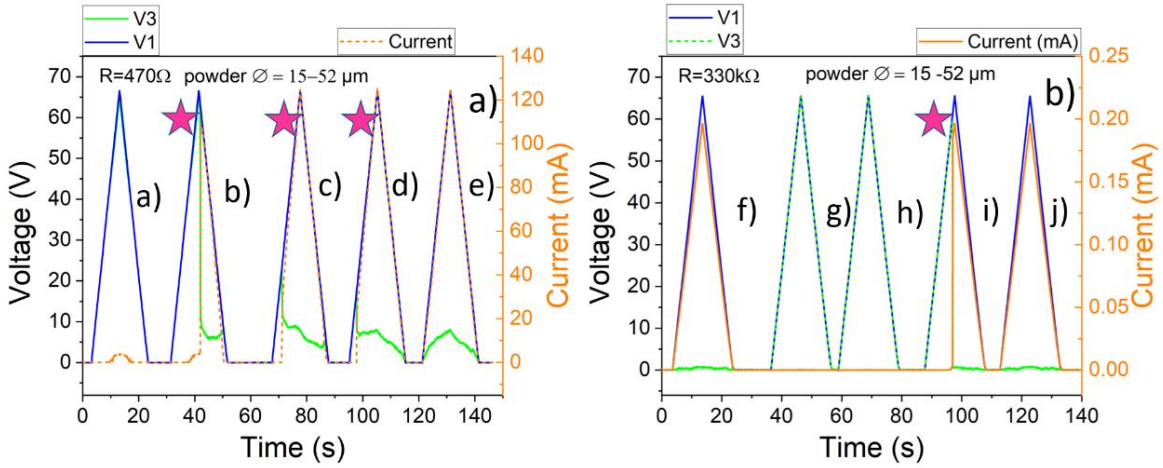

Figure 6.9: Integral sequence of pulses a) Sequence 3 compressed at 0.4 mm down the surface of the powder and b) Sequence 4 that present different compression for each peak (around 0.23 mm below the touching point). The experimental input V_1 and V_3 are comparable on the left y-axis. The current (orange) is reported on the right y-axis as indicated. The stars indicate current flow jumps.

Figure 6.10 a – b. zooms the peaks a-b of Figure 6.9a. In this sequence two different current flows were observed.

Current barely circulated in Figure 6.10a (indicated by the arrows) when the voltage V_1 is maximal, V_3 is slightly lower than V_1 (green arrow) confirming a small disturbance in the current. This effect was only observed for the lower size distribution, referred to as the *intermediary state*[XXXII] (Figure 6.10 a). For very small compressions such as 0.23 mm, the *intermediary state* could last for many peak sequences similar to *Sequence 3* without other effects. This effect is attributed to the inter-particle forces of the cohesive powders [322,338]. The *intermediary state* in this distribution appeared before the abrupt change in the current flow as in the second peak in Figure 6.10b. The intermediary effect was observed for all compressions of this study (0.23 mm to 1.96 mm) employing higher currents [128]. The Joule heating was pronounced in peaks b, c, d and, e. In the second peak, the current started to growth (dashed arrow) right before the transitional effect (the star) then V_3 dropped. The two first peaks of this sequence indicated different contributions to the charges flow of the small powders. The first indicates the presence of electrostatic and cohesive forces cited above [339,340]. The second suggests the presence of Joule heating effect in the grains the Joule effect facilitates the current flow and increases with the pulses [341,342]. The peaks of sequence 3 are repeatable around 0.23 mm -0.4 mm compression.

[XXXII] an intermediate, transitional, or midway state.

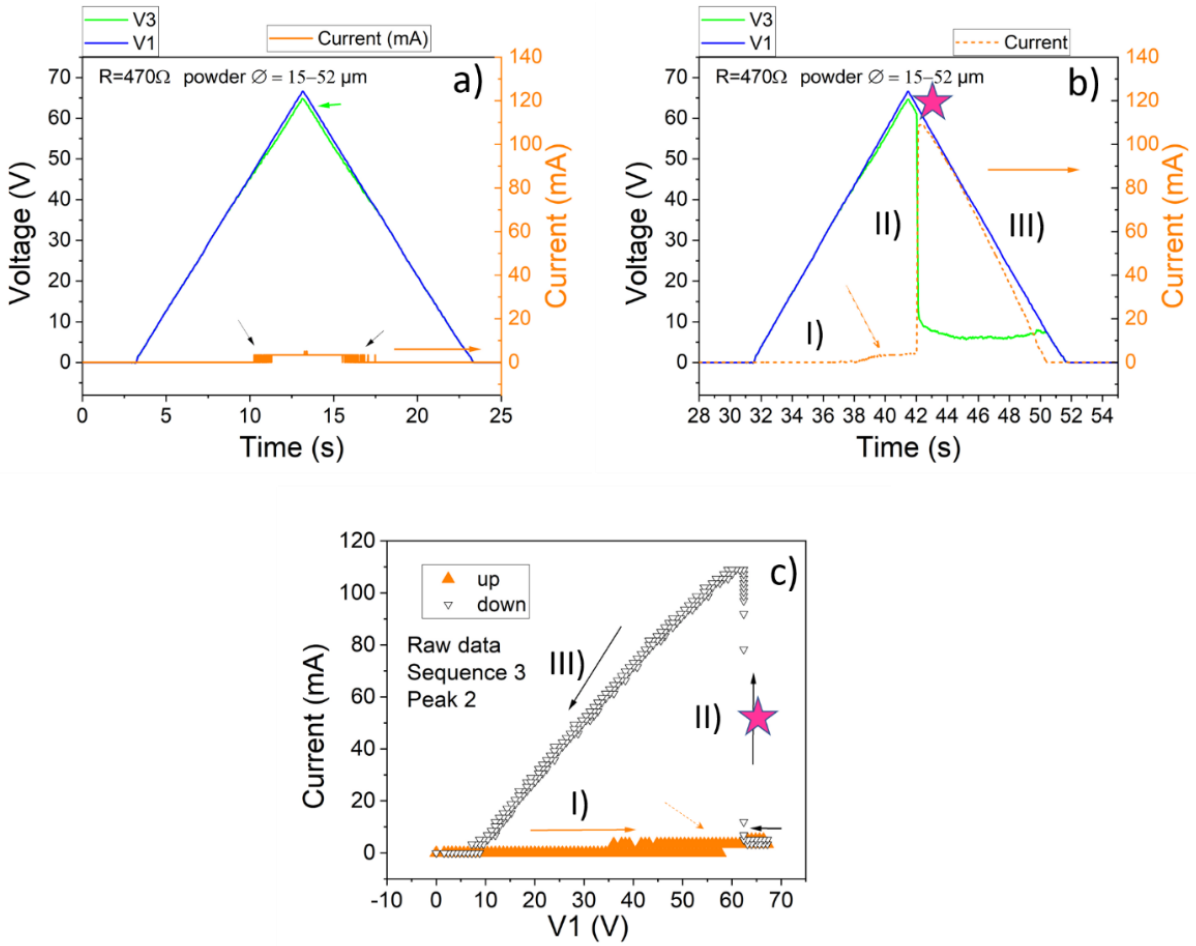

Figure 6.10: Pulses of 15 µm -52 µm pulse a) disturbance in the current flow in the first peak of the sequence 3, the intermediary state, the arrows signalize the current and V_3 disturbances, b) abrupt threshold in the current flow in the second peak located by the star. The experimental input V_1 and V_3 are comparable to the left y-axis. The current (orange) is reported on the right y-axis as indicated by the arrow. c) Representation of the current (mA) when the input voltage (V_1) is increasing (up) and decreasing (down) for the peak in b) the three zones I), II) and III) are comparative for peal b and c), the arrow represents the path direction.

The hysteresis is present in Figure 6.10c represents the peak of Figure 6.10b. The current flow started when the voltage was decreasing. The threshold where the transition effect occurred varied considerably in this configuration. The dashed arrow indicates a slight increase in the current before the transitional effect.

In Sequence 4, the peak f is examined. The peak in Figure 6.11a did not present hysteresis as shown in Figure 6.11b, the current flowed during the entire peak period, characteristic of long-lasting conductor state. The current started to flow since the very beginning of the pulse following Ohm's law. This indicated that the powder only presented its conductor behavior. The current flow through paths in a granular media as powders, thus the crucible full of powder could have insulated areas. One can speculate that the resistivity varies according to the regions within the powder. The conductive path resistivity is lower (percolation) than in other areas presenting an insulated characteristic [343].

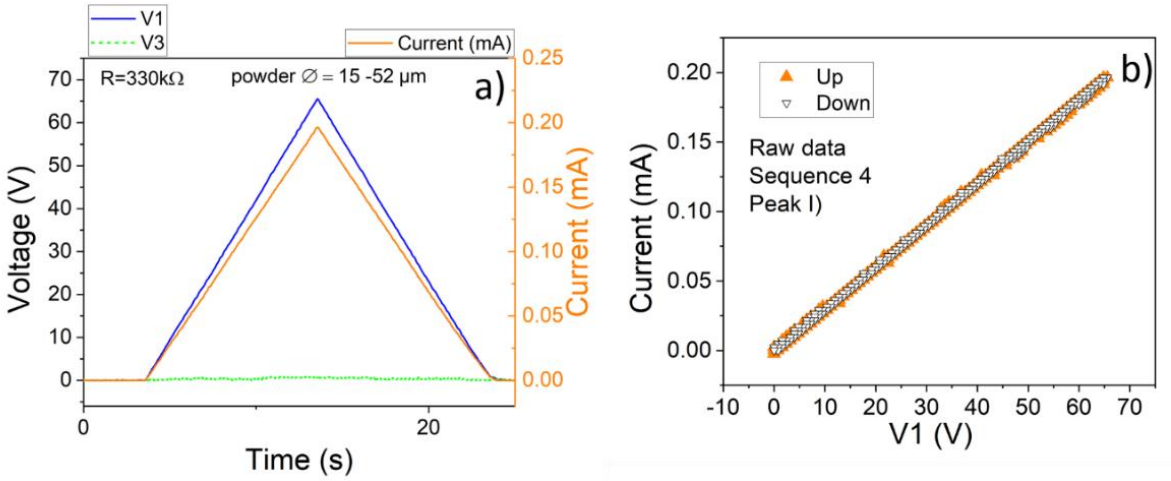

Figure 6.11: a) Zoom in the first pulse of Sequence 4 demonstrates the current flow during the entire peak. The experimental input V_1 and V_3 are comparable to the left y-axis. The current (orange) is reported on the right y-axis as indicated by the arrow. b) Representation of the current (mA) when the input voltage (V_1)is increasing (up) and decreasing (down, the arrows represent the path direction.

The diagram in Figure 6.12 a–d. summarizes the observed effect for both distributions used in this work. The intermediary state and the transition effect are identified in 0.23–1.96 mm compressions. It is important to mention that if the compression is too small (0.23 mm), the insulator character of the powder is persistent; the transition effect is hard to obtain. On the contrary, the powder conducts straight if the compression is more significant. The straight conduction confirms that the transitional effect happens only in a specific range of the compression depending on the powder distribution [184]

Figure 6.12a shows lower distribution 15–52 µm submitted to higher currents. The distribution presented the intermediary and the transitional states. The transition state appeared in higher compressions as 0.4 mm. At lower currents 15–52 µm distribution, the transitional effect happened in a narrow compression zone as shown in Figure 6.12b. The lower powder only presented the transitional effect on precise compression. The transitional effect occurred in very low compressions. The results indicate whether the powder conducted or demonstrated an insulator characteristic. The fact that transitional effect became rare is attributed to the inter-particle forces and the fewer spaces of smaller distribution [136]. The quantitative values for compression of lower powder are not clarified yet. Instead, for larger distributions 45–106 µm, the transition effect systematically appeared in all tested configurations. For the larger distribution, the reproducibility of results is excellent for both currents shown Figure 6.12 c-d. In a larger current, the powder maintained the conductor aspect longer than for lower currents due to Joule heating and stability in the current paths [344]. A remarkable finding of this study is the absence of any trace of sintering or permanent bonding between the powder grains, during the pulses.

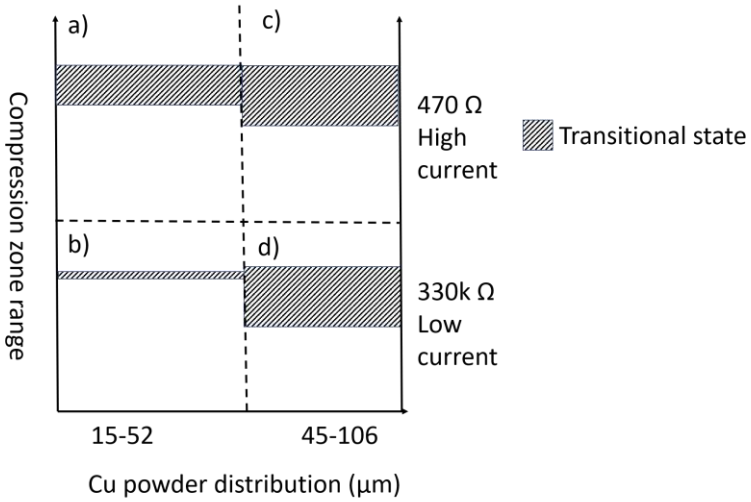

Figure 6.12: Diagram representing the observed transition zone of the Cu powder distribution as a function of the compression zone range.

6.3.3 Discussions

This discussion is based on the empirical tests done in the two powder distributions in low compression. A conductive path in the powder between the electrodes was not guaranteed due to the negligible compressions generating the insulator effect. The movement of the charges (current) can be attributed to dipoles, among other effects such as micro-contact among the beads [184,345]. The Joule heating and *electrostatic charge influence the transition effect.* Charges can be created around grains or in the oxide layer due to the input voltage. The peripherical charges can attract a new grain or improve contacts depending on the grain's characteristics such as weight and the oxide layer thickness [346,347]. Figure 6.13 a–b represents schematic spherical grains. The grain I positively charged induces negative charges in grain II, creating *dipoles*. One of these dipoles can produce a displacement of an electron in an adjacent atom, which induces another dipole that is then weakly attracted or bonded to the grains [348]. Usually, these secondary *bonds* fluctuate, similarly to the cohesive forces. An electric field modifies both the secondary bonds and the cohesive forces [349–351].

The charges on the surface of the grain can create a multitude of dipoles and eventually a force between them, as indicated in Figure 6.13b [352]. Kurata *et al.* [353] observed multi-poles in an isolated nanoparticle of silver irradiated by electrons. The direction of the radiation is crucial to the multi-poles force [354,355]. Noguez *et al.* [356] demonstrated the effect of two electric fields direction for 1D chain silver nanoparticles from the extreme loosen to the close-packed limits. More multipolar interactions are present in closed pack powders. An external field parallel to the chain induces multi-poles in each sphere, with an axis of symmetry parallel to the chain. When a transverse field is applied to the chain, they fluctuate in magnitude and phase, multipolar effects are similar but less pronounced in the transverse configuration [353,356].

The polarization phenomenon is supposed to be reproduced in the ripple effect, so one can observe the *transition effect.* The effect seen in all sequences of this work is comparable to the so-called *Branly effect* [192]. According to Branly, the responsible for the transition effect is the contact among the grains. Branly *et al*. tested two configurations of isolated and heavy spheres. Branly and Lodge [324] covered the grains in paraffin, wax, and resin, and in each experimental condition, the Branly's effect persisted [187]. They did not demonstrate the role of the dielectric [324,357]. It is worth mentioning that the movement of the spheres during the effect could not be clarified. Branly discarded movement among the beads by the use of heavy spheres. The smaller powder distribution used in this work presents the grains <15 μm diameter,

their weight is negligible, and the powder is cohesive. The agglomerates observed in this distribution before and after the pulse sequence prove that attraction among the spheres is important and stronger than gravity [128,338].

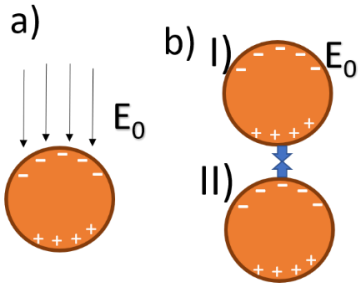

Figure 6.13: a) Representation of the surface charges polarization of one grain under the influence of an electric field; b) two grains submitted to an electric field. State I show the charges in the grain surface attracting the grain II. The charges or multi-poles opposing the electric field create attraction forces between the two spheres. Adapted from [350,351].

The lower distribution agglomerates are much easier than the larger distribution. The agglomeration effect in small powders is due to the different forces involved in the natural attraction tendency. The gravity forces have a substantial impact on very light powder, the cohesive forces, and compactness due to the physical size of the particles [128,322]. Ali *et al.* [358] correlated the particle size and the compaction of a powder bed in SLM processes. The smaller Cu powder compacted around 15% more than the bigger distributions due to Van der Waals, Coulomb, friction, and gravitational effects that influence the distribution of cohesive powders [321].

In sequence 3 an intermediary state where the transition effect did not occur but a disturbance in the current was detected. The copper density inside the crucible varies due to compactness, resulting in fewer free spaces among the grains for the low distribution [358,359]. The current flows better when micro-contacts are established due to compactness[360]. External compaction is a very sensitive parameter that creates current paths of different nature between the electrodes, reducing the probability of the transition effect. The direct bypass or straight conduction is also attributed to compactness and better micro-contact quality. The extra-natural cohesive forces create the intermediary state. The particles create agglomerates and anisotropy in the powder with minimal compressions [338].

The idea of disorder and heterogeneity governing the behavior of granular packing is not recent. One can assume that the current percolates through the grains in powder media. The percolation causes the temperature to be different between the zones crossed by the current and the ones still isolated. Thus, Joule heating should continue the ripple effect on the preferential current path chain and intensify the thermal stress in the powder in localized areas [128,343]. The dependence of the electrical resistance and the stress are reported in [361,362]. Creyssels *et al.* [345] have demonstrated that the current path is inhomogeneous in 2D hexagonal media for 8 mm stainless-steel beads as demonstrated in Figure 6.14 a–c. In this study, the vertical electric field is applied to the base of the hexagon couples' particles when the current flow occurs. They reported that the stability of the current path increases at high currents. In Figure 6.14a one can see that the smaller current spread through different paths.

On the contrary, a higher current circulates in the same grain chain, as shown in Figure 6.14c [361,363]. The higher current creates a stable conduction path, supporting that sequences 1 and 3 reach the steady state earlier than the low current sequences. Also, since the voltage is input through the pulses, the path becomes more stable along a sequence, decreasing the insulator character. The first pulse presents the stronger insulator character, and the steady

state is achieved in the last pulses. The transition effect or the current jump happens suddenly, reinforcing the idea of percolation [364,365].

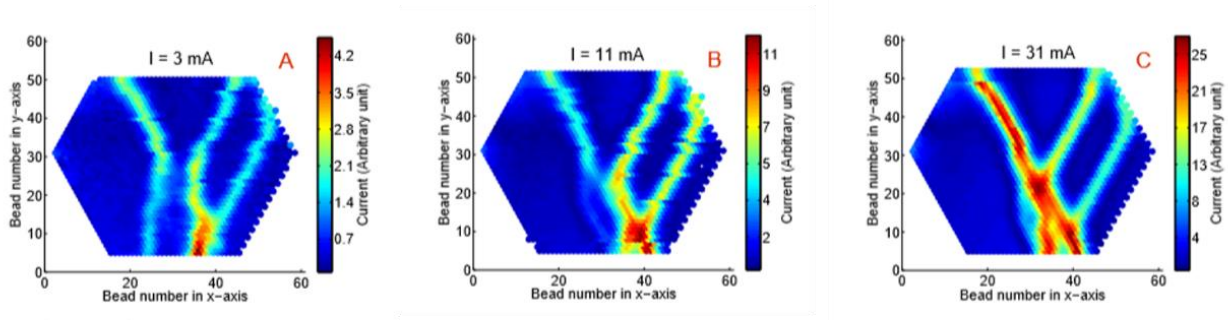

Figure 6.14: Current path in 2D hexagonal packing of stainless-steel beads. The applied voltage increases from the base (x=0) to the top. Isotropic stress is created by using 20 N force on each upper face. a) maximum current of 3 mA b) 11 mA, and c) 31 mA. Adapted from [345]

In 1997 IR imaging of one grain layer showed a heating effect in the conduction path [333]. Later it was demonstrated that the current flow in a small cross-section of contact between two grains, since the cross-section is small and the current flow only in this area resulting in temperature raises at this point. If enough current passes through the contact, the micro-contacts reach the sintering state as stated detailed in the introduction [184,332]. In this work, the conductive paths are destroyed with a strike or vibrations, which means that sintering did not happen in this case. Once the current paths are established and the powder becomes a conductor, they follow Ohm's law.

The three zones represented by I) the insulator, II) the current jump, and III) the conductive aspect of the powder. The three zones result in current hysteresis. At first, no current passes through the system due to poor contact and spacing among the grains, the zone I). The transitional effect II) indicated by the star happens in a brief moment of change induction in the beads, indicating that the current percolates through the grains. Lastly, in Zone III, the current paths follow Ohm's law. This effect results in hysteresis during the pulse ramps (up and down).

This work could not rule out the motion of spheres, polarization, and static charges. The probability of sparks between spheres is low due to the relatively low voltage and currents used. The role of the Cu oxide layer around the grains was not determined. However, oxides increase the resistivity of granular media, making conductive paths creation difficult [320]. More about polarized spheres and mechanisms of how the charges can become mobile can be found elsewhere [351,366].

6.4 Conclusions

Metallic spheres or powders present a transitional effect on electrical properties under the influence of an electric field or a current. The electric field induces charges on the sphere's surface, and the charges create multi-poles. These multi-poles can attract or induce charges in a second sphere under the influence of the initial multi-poles. This effect generates a ripple effect to create a path to the current flow. The Joule effect creates temperature differences and stress, possibly governing the ripple effect. The paths are likely to be heterogeneous since the current flows in grains through percolation. The stability of the paths improves in higher current. For some powders, the current flows abruptly. The effect is similar to the Branly effect, where the metallic grains change their conduction due to an electromagnetic field, the transition insulator to a conductor.

The current input and the powder distribution influence the charges flow. The lower distribution powder tendency is not to present the current flow transitional effect. Three

possibilities are observed in the current flow: no current at all, the intermediary state, and perfect current flow. This is attributed to the cohesive forces in this powder type that tend to naturally agglomerate. The smaller powder function is to fill gaps among the beads creating a path that conducts more or less depending on the micro-contact. The transitional effect still happens when the current is higher.

On the contrary, the current flow jump is present in all set-ups for larger powder diameters. The effect of several variables could not be set in current flow, as the motion of spheres such as polarization, static charges, and the dielectric (oxide) role. Although, this is a motivating work to control the charges of powder bed and reduces undesirable effects such as the smoke or the agglomeration of the powder. The control of charges in micro and nanoparticle is applicable in several areas, including EB-PBF, since the materials and components are getting more into the nanoscale.

General Conclusions

This thesis has demonstrated that ultra-thin amorphous carbon film (a-C) deposited by direct current magnetron sputtering reduces the necessary energy to melt copper in laser 3D metal printing processes. Findings from different disciplines help associate the film's thickness, the intrinsic optical, and electrical properties to the photon absorption. The work carried out in this thesis reveals that carbon is an adequate element to be combined with copper (Cu). The thickness of the film and minor deposition area are the main parameters to reduce light radiation from a metallic substrate without affecting its properties. The properties of the 3D printed object are fundamental to their later application.

Two films were optimized to reduce reflectance the a-C and the amorphous carbon stainless steel films (a-C: SS). The properties were observed for films deposited in the ballistic regime of the plasma when using direct current magnetron sputtering. The plasma species densify the film resulting in smooth morphology and lower resistivity. To achieve the ballistic deposition, the films were deposited at smaller distances from the cathode, lower than the mean free path, around 4 cm for this deposition. In addition, these films present a fast deposition rate since the plasma is less scattered than in higher distances, an essential parameter for fast industrial applications. The a-C films show crystalline graphite structure in the amorphous matrix. The a-C: SS films contain 50% of stainless-steel metals, mainly Fe, with traces of Ni and Cr and 50% dual carbon similar to the a-C. The insertion of metals, such as Fr, Cr, and Ni, into the amorphous matrix results in reflectance and resistivity reduction. Compared to pure carbon films, the addition of stainless-steel reduced reflectance by about 10% more and the resistivity of up to two orders of magnitude. However, the minimal addition of different elements is preferred to preserve copper properties.

The energy laser reduction is connected to the Cu powder reflectance. Preliminary results of a-C over Cu spheres indicate a variation of around 17% using 25 nm. The reduction can reach up to 50% when deposited over foils using the same 25 nm in the range of the commercial infrared laser used in 3D printing. In addition, the ultra-thin a-C films tailor the reduction by the presence of interference phenomena and losses. The ultra-thin film causes destructive interference as a function of the wavelength, which results in minimal reflectance. Hence, thick a-C films are not recommended to reduce reflectance effectively. Multilayer calculations confirmed that the ultra-thin films reduce the reflectance by interference and losses due to the duality of the films. The parameters that can influence the reflectance reduction are the copper roughness and the Cu absorption in lower wavelengths. The substrate roughness can affect the reflectance mainly in the near-ultraviolet visible spectra when the characteristic wavelength in the media is shorter than the roughness dimensions (R_a). The Cu absorption resulting in its red color also varies in the range of λ=580 nm, influencing the final reflectance.

Two configurations ensure the success of the effect of lower energies in the copper substrates coated with a-C film. In the first configuration, the laser during welding removes a-C ultra-thin films. Surprisingly, low power of 1200 W cut foils coated with 25 nm of a-C films. Preliminary results indicate that the laser beam removes the a-C film in the laser track. On the contrary, the maximum laser power available only presents a few marks in foils without a-C film. The second configuration employed a prototype spray to produce thick graphite-like layers of about 3.5 µm. This technique was used to guarantee that only the exposed powder was covered. This method was the only one to deposit carbon in the laser facility since the transport powder with a-C films only in one hemisphere is not developed. When graphite-like layers are in the powder hemisphere exposed to the laser, the powder melted at around 1200 W or a density power of 38.2 kW mm^{-2} instead of 2000 W, i.e. 64 kW mm^{-2}. The copper powder presents a good welding joint over the plate. The weld cross-section revealed that the melted powder merged with the support. The crystallography grains in the welding show elongated grains turn into classical

equiaxial grains in the upper part due to rapid solidification improving wettability. Even for thicker graphite-like coatings, the influence of the film could not be observed in the welding bulk. The best compromise between reflectance reduction and the minimal a-C thickness is about 25 nm deposited only in substrate exposed to the laser. 25 nm a-C thickness did not influence the Cu properties in laser printing processes. The laser potentially removes ultra-thin layers of amorphous carbon. An optimized structure film thickness over copper substrates leads to a 40% reduction in the necessary energy to obtain quality welding in the future application using Cu in the SLM process.

Lastly, understanding copper electrical properties is crucial to avoid drawbacks in the process, mainly using electrons as a power source to obtain quality conduction in the final 3D object. The effects of a current flowing in different pure Cu powder distributions revealed powder electrical properties' dependence on several factors, mainly compression. The powder exhibited an insulating-to-conductive transition effect, similar to the one observed by Edouard Branly in 1888. The insulator character of a powder media appears when the current does not percolate between two electrodes due to poor contact among the grains. The transition effect depends on powder compression. The transition insulator-to-conductive can be attributed to charge induction in a spherical powder surface, the Joule effect between the grains and micro sparks that eventually remove Cu oxides, improving the contacts between the spheres. The smaller distribution is much more sensitive to compression, and it does not tend to present the transition effect as the bigger distribution. Instead, smaller grains demonstrate the effects of the extra inter-particle forces, resulting in minimal or null current flow. The small distribution conducts straight in minor compression variation while the bigger grain presents the transition effect. In general, once the current flows higher currents create more stable paths, the conductor aspect of the powder lasting longer than lower electric currents. The transition insulator-to-conductive observed in this study is reversible, demonstrating that the powder grains were not sintered together but created temporary conductive paths following Ohm’s law. Understanding the current flow in powder is essential to improve the spreadability and charges evacuation in the 3D printing, mainly in the electron beam powder bed fusion processes using powder as feedstock.

The results summarized above can impact the 3D printing process’s energetic efficiency and powder charge control. The a-C thin film over a reflective substrate is an eco-friendly material that can develop other energetic applications on a large scale. Understanding the electrical properties of the powder can lead to easy management of charging accumulation and agglomerates in powder media.

Perspectives

The results presented in this thesis are promising and encourage further investigation. Moreover, there are still some unanswered questions in the discussion of some results, which require additional work to fully understand them. The following are perspectives for continuing this work:

To investigate the behavior of carbon and copper multilayers on laboratory and industrial scales. The behavior of the carbon layer after welding requires in-depth investigation. Understanding the thermal processes in both materials is motivated by the annealing of the multilayer sample. The composition and cross-section of the annealed multilayered sample also require further investigation. HiPIMS will be used to deposit copper and carbon, and the results will be compared to those of DC films. To fully comprehend the dual effects of the graphite-like and amorphous films observed in the films, additional characterization and depositions are required.

The reflectance of copper foils using the prototype spray should be compared to a-C films. The graphite spray used in this work needs further improvements to be applied in a 3D printing process. The other methods to deposit films in the atmospheric pressure in 3D printing machines need to be explored, for example, the electric arc deposition process.

The welding of copper foils with a-C films showed promising results. However, more research is required to comprehend the deposition of a-C films over copper metal additives. A model of magnetron sputtering deposits over the spheres is necessary to study the deposition only in one hemisphere of the grains and complete the reflectance studies. The transport of powder samples must be developed to ensure the success of the strategy of depositing carbon only in one hemisphere of the metal additive grains. An ultra-thin carbon film (<10 nm) applied over copper should be subjected to other laser wavelengths, such as green lasers, to avoid extra absorption of the laser when the copper is in a liquid form. The effects of interference phenomena on spherical substrates require investigation.

The current flow in the powder is a preliminary study. There are essential aspects that require attention, including improving the system used for fine-tuning compression and current input and output measurements; understanding the mechanism that controls the insulator-to-conductor transition effect; studying charge detrapping mechanisms; describing the role of oxides, static charges, polarization, and possible granular medium motion in a current flow; subjecting the powder to different pulses formats (square and negative); and understanding the role of the agglomerated. Use powder coated with carbon to pursue the current flow studies.

Appendices

Author's Publications and awards

Award:

Bernhard Gross Award - XVIII Brazil MRS meeting Best oral contribution of the Symposium U, Carbon based materials and devices - Low resistivity a-C:Fe thin films applied as anti-reflective coating on copper substrates -, 2019

Published paper in international reviews:

Â.E. Crespi, C. Ballage, M.C. Hugon, J. Robert, D. Lundin, I. Vickridge, J. Alvarez, T. Minea, Low resistivity amorphous carbon-based thin films employed as anti-reflective coatings on copper, Thin Solid Films. 712 (2020) 138319. https://doi.org/10.1016/j.tsf.2020.138319.

Â.E. Crespi, C. Ballage, M.-C. Hugon, J. Robert, T. Minea, The Role of Amorphous Nanocrystalline Carbon Films in Interference on Flexible Copper Foils, ACS Appl. Electron. Mater. 4 (2022) 576–584. https://doi.org/10.1021/acsaelm.1c00520.

Patents:

Gilles Walrand, Tiberiu Minea, and Albin Effernelli **Crespi A.E;** submitted in June 2021.

Walrand, G. Minea T., Ballage C., and Effernelli A., **Crespi A.E.** submitted in June 2021.Classified Patents until 2023

Conferences:

ICMCTF 2021- Interference signal induced by ultra-thin amorphous carbon films over flexible copper foils demonstrated by electromagnetic boundaries calculations (Virtual meeting) Authors: Ângela Crespi, Charles Ballage, Marie Christine Hugon, Jacques Robert, Daniel Lundin, Tiberiu Minea.

XV MRS meeting Brazil, Low resistivity a-C:Fe thin films applied as anti-reflective coating on copper substrates. 2019. (Meeting) Authors: Ângela Crespi, Charles Ballage, Marie Christine Hugon, Daniel Lundin, Jacques Robert, Tiberiu Minea.

Escampig (2020 postponed 2022) Effect of the target to-substrate-distance on a-C and a-C:Fe deposited by magnetron sputtering- applied to optics. Authors: Ângela Crespi, Marie Christine Hugon, Jacque Roberts, Daniel Lundin, Charles Ballage, Tiberiu Minea.

Résumé en Français

Le développement rapide de la technologie d'impression 3D pour les objets métalliques exige l'optimisation de l'énergie du faisceau laser ou d'électrons pendant les processus de fabrication. La fusion laser sur lit de poudre (ou en anglais Laser Powder Bed Fusion (L-PBF)) ou la fusion sélective par laser (Selective Laser Melting (SLM)) utilise une poudre métallique pour former un objet 3D. La poudre est déposée en couches et fondue à l'aide d'un laser. Les différentes couches métalliques sont fusionnées ou frittées successivement pour former le futur objet. Dans le cas du cuivre, une grande quantité d'énergie est généralement impliquée dans le processus de fusion en raison des propriétés physiques uniques de ce métal. Le cuivre a une température de fusion élevée (T_{Cu} = 1083 °C) et une conductivité thermique également élevée (σ_{Cu} ~ 398 W/m K). Ces propriétés entrainent à une solidification rapide et des gradients thermiques locaux importants dans le bain de fusion. De plus, le Cu reflète davantage le rayonnement IR que la plupart des métaux. Au-dessus de λ = 580 nm, il reflète presque 100% de la lumière incidente. Par conséquent, la fusion de Cu de haute qualité pendant le SLM nécessite une gestion différente de l'énergie laser. La faible absorption du Cu nécessite donc un laser de forte intensité pour pénétrer suffisamment le matériau, garantissant ainsi une pièce finale de qualité.

L'ajout d'autres éléments à la matrice de Cu est une excellente stratégie alternative, malgré les récentes améliorations de la qualité des pièces finales fabriquées à partir de Cu pur. L'ajout d'un élément supplémentaire a pour but de modifier les propriétés physiques et métallurgiques du Cu. L'ajout d'autres éléments peut améliorer les propriétés mécaniques et chimiques de la matrice de Cu, mais il réduit généralement la conductivité électrique. Un exemple est le phosphore, que l'on trouve comme impureté dans le Cu. Le phosphore forme des oxydes de phosphore, qui provoquent des défauts de soudure et une réduction de la conductivité. L'ajout des couches minces de carbone amorphe (a-C), pures ou composées comme le carbone amorphe composé avec l'acier inoxydable (a-C:SS), sur la surface du lit de poudre exposée au laser, a un effet positif. Cette déposition réduit l'insertion de carbone à des quantités minimales , négligeables par rapport à la quantité de cuivre. Le principal défi est d'améliorer l'absorption pendant le L-PBF sans affecter négativement les propriétés de conduction du futur objet en Cu.

Les matériaux granulaires, en particulier la poudre métallique oxydée, ont généralement une conductivité électrique beaucoup plus faible que le même métal en volume. Contrairement à une pièce de métal, la conduction de la poudre dépend de plusieurs facteurs à l'échelle nanométrique et microéconomique. La micro-échelle comprend l'état de compaction, la distribution des grains et le contact entre les grains. L'échelle nanométrique peut être constituée des couches d'oxyde et d'autres forces de Wan der Waal. De plus, la densité de tassement et les propriétés thermiques et mécaniques d'une couche sont cruciales pour l'excellente réalisation d'une pièce imprimée. Il reste essentiel de caractériser les propriétés électriques de la poudre de Cu, car elles déterminent en fin de compte les propriétés de la couche dans l'impression 3D de métaux principalement, mais non uniquement quand on utilise la fusion par faisceau d'électrons de lit de poudre ou en anglais (Electron beam powder bed fusion (EB-PBF). Un défi majeur a été de comprendre comment contrôler les charges électriques dans la poudre métallique utilisée comme matière première dans un processus d'impression 3D. Comprendre comment un flux de courant influence les effets de charge pour améliorer la qualité générale du processus. Un autre problème est celui du Cu sous forme de poudre. Sous cette forme, la conduction du Cu et l'évacuation des charges électriques sont brusquement modifiées notamment lors de l'utilisation d'électrons pour fondre la poudre.

Les objectifs de la présente thèse sont les suivants :

1) explorer les propriétés physiques, électriques et optiques des films minces de a-C:SS et a-C composés déposés par pulvérisation cathodique magnétron à courant direct en fonction de la distance cible-substrat ;

2) identifier les phénomènes fondamentaux impliqués dans la réduction de la réflectance du Cu lorsque des films à base de carbone sont ajoutés ;

3) déterminer le rôle des phénomènes d'interférence pour le système films ultraminces de a-C /substrat de Cu et décrire théoriquement les phénomènes d'interférence pour un système à double interface vide/a-C/Cu dans la gamme de longueurs d'onde étudiées;

4) optimiser l'épaisseur d'une couche ultramince à base de carbone à la surface de la poudre de Cu afin de réduire substantiellement la puissance laser nécessaire pour faire fondre le Cu ;

5) étudier le flux de courant et ses effets sur la poudre de Cu métallique qui sont analogues au comportement de la poudre dans le processus de fusion EB-PBF.

Deux films ont été déposés : des films de carbone amorphe a-C et des films composés a-C:SS (carbone métal amorphe). Pour l'incorporation de métal dans le film de carbone amorphe nous avons utilisé un anneau d'acier inoxydable pendant le dépôt, le film résultant est alors composé de 50% de métaux provenant de l'acier inoxydable comme Fe, Ni et Cr et 50% de carbone.

La variable du dépôt est la distance entre la cible et le substrat, la distance a varié entre 2,3,5, et 10 cm. La variation de la distance change le régime du plasma pendant le dépôt. Pour la plus grande distance (10 cm), les espèces du plasma sont thermalisées, les espèces présentent approximativement la même énergie à cause de collisions. Le libre parcours moyen des espèces dans l'enceinte de dépôt est de 4 cm pour une pression de 0.5Pa. Au contraire, pour les distances faibles (<4 cm) les espèces du plasma sont en régime balistique. En général, les deux films a-C et a-C:SS présentent une évolution très similaire en fonction de la distance entre la cible et le substrat pour les propriétés suivantes : la morphologie superficielle, l'hybridation du carbone et les propriétés électriques. En général, tous les films sont composés de carbone amorphe confirmé par l'analyse de diffraction de rayon X (DRX), la morphologie est affectée par la distance entre la cible et le substrat. La morphologie passe de grains compacts à des grains réguliers discernables lorsque la distance de dépôt augmente. La densité diminue également en augmentant la distance de dépôt. L'association d'une faible densité et d'une morphologie granuleuse entraine l'augmentation de la résistivité. Les différentes analyses des échantillons montrent que les meilleures propriétés en termes de densité et de morphologie sont atteintes pour les distances cible-substrat les plus faibles c'est-à-dire lorsqu'on se situe en régime balistique. Ainsi le film déposé à 2 cm a été choisi pour l'analyse de la réflectance.

La réflectance des substrats de cuivre recouverts de ces différents films a été mesurée à l'aide d'un spectromètre optique. Les films amorphes peuvent réduire la réflectance du substrat de cuivre jusqu'à 80% dans la gamme du laser infrarouge commercial utilisé pour l'impression 3D. Le film a-C:SS réduit davantage la réflectance et présente une meilleure conduction. Cependant, pour l'impression 3D, l'ajout d'un matériau est préférable à plusieurs, d'où le choix des films d'a-C. Plusieurs épaisseurs de film d'a-C ont été testées sur des substrats de cuivre. L'évolution de la réflectance en fonction de l'épaisseur du film d'a-C a démontré que les films ultraminces (< 100 nm) réduisent davantage la réflectance à cause des phénomènes d'interférence. La présence d'interférences a été confirmée par un calcul théorique de la réflectance. Ce calcul considère une onde plane qui « voyage » dans un système multicouche (vide/carbone/cuivre), les interfaces ont été considérées sans rugosité. Les films d'a-C de cette étude ont présenté une absorption plus importante que les films amorphes de la littérature, cela pourrait indiquer que les films de cette étude sont une combinaison de carbone amorphe et de nano-clusters de graphite. Cette hypothèse a été confirmée par spectroscopie Raman. La présence des interférences et pertes dans le film a conduit à réduire l'apport énergétique du laser de 40 % tout en conservant une soudure de qualité.

L’impression 3D de métal en utilisant un lit de poudre déposée couche par couche utilise principalement deux technologies : le laser et les faisceaux d’électrons pour apporter l’énergie nécessaire à faire fondre le cuivre. Le plus discuté dans ce manuscrit est l’utilisation du laser qui implique des mécanismes d’absorption de la lumière. Dans le cadre d’un faisceau d’électrons comme source d'énergie, les mécanismes changent, les charges et la conductivité de la poudre de cuivre deviennent essentielles. La compréhension des mécanismes de conduction électrique d’une poudre est primordiale. Pour mieux comprendre l’évacuation de charges dans un milieu granulaire, deux distributions de poudre ont été soumises à deux intensités de courant 120 mA et 0.2 mA. Les deux distributions de tailles de grains ont révélé une transition de l'état isolant à l'état conducteur pour les deux intensités de courant pour des compressions spécifiques de la poudre de cuivre. On peut supposer que la transition dépend des charges électrostatiques, de l'effet de chauffage des micro-contacts et de la taille des grains. Pour une taille de grain comprise entre 52µm-106µm, la transition isolant-conducteur est reproductible et systématiquement observée. Par contre, la distribution de grain plus petit entre 15 µm -45 µm parcourut par de faibles courants (< 0.20 mA) présents autres comportement, ou la poudre conduite, ou la poudre se comporte comme un isolant pour des variations de compressions minimes. La transition isolant-conducteur se produit dans une gamme très étroite de compression.

Appendix 2A: Vacuum installation diagram

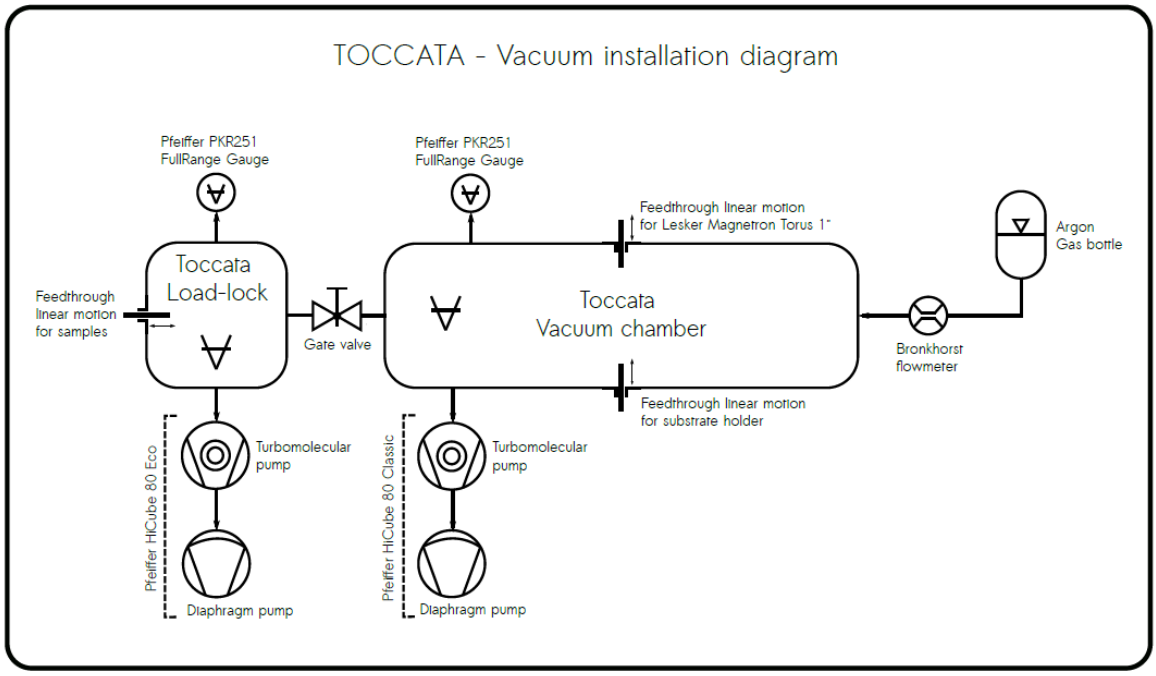

Appendix 4A: Multilayer Calculations.

The vectors $\vec{E}$ and $\vec{B}$ denote the electric field and magnetic field induction. The propagation sign and media are referred to as indices of the equations along the calculations. The index refers to the medium, one (1) refers to the vacuum, two (2) represents the amorphous nanocrystalline carbon coating layer and, three (3) refers to the copper foil as shown in Figure 4A.1[367,368].

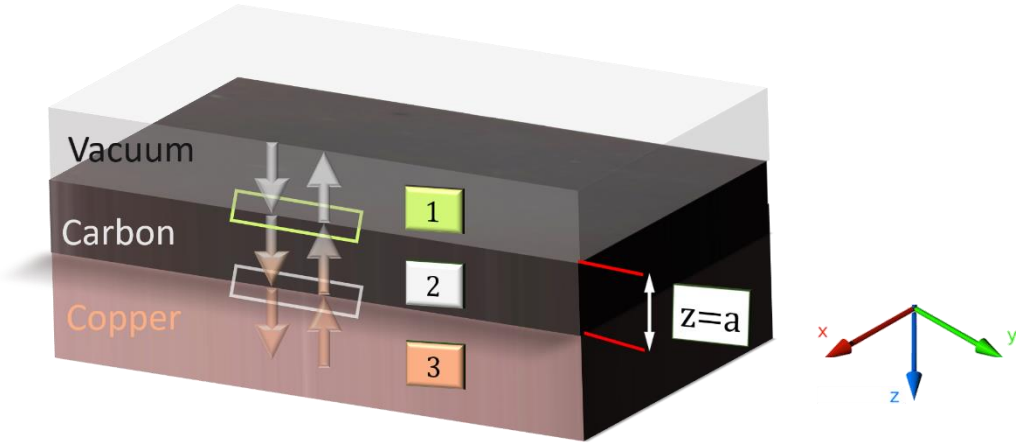

Figure 4A.1: Cross-section of the three media used in these calculations: (1) vacuum, (2) amorphous carbon and (3) copper. The tangential field component of the light (electromagnetic wave) is assumed to be continuous through the boundary. The arrows schematically represent the propagation (in the sense of the arrow), and the sign is done by the referential (in the right. Colors and sizes are merely illustrative.

Relationship between frequency, complex index, wavelengths, and attenuation:

If we consider $\lambda = \frac{c}{f}$ where "c" is the speed of light, "f" frequency and, the refraction complex index "N" is:

$$N = (n_{r\alpha} - i n_{i\alpha}) \quad (4A.1)$$

the attenuation can be correlated as follows

$$\overline{k_\alpha} = k_{r\alpha} - i k_{i\alpha} = \frac{2\pi f}{c}(n_{r\alpha} - i n_{\alpha i}) \quad (4A.2)$$

Where:

(α) is generalization the three media (1) for vacuum, (2) for the a-C film and (3) for the Cu foil.

$\overline{k_\alpha}$= complex wave vector;

$n_{r\alpha}$=real part of the refractive index;

$n_{i\alpha}$=the imaginary part of the (extinction coefficient);

t= time

Expression for electromagnetic fields propagating at normal incidence:

The two components of the total wave decomposed into plane waves are distinguished by their direction of propagation. For each of these components, the expression relating the

magnetic part of the electric part of the electromagnetic field is deduced from the expression of fields in complex representation-$\vec{E}_{\alpha(z,t)}$ and $\vec{B}_{\alpha(z,t)}$

One might consider Maxwell -Faraday equation:

$$\vec{\nabla} \wedge \vec{\mathrm{E}} = -\frac{\partial \vec{B}_\alpha}{\partial \mathrm{t}} \qquad \textbf{(}4\mathrm{A}.3\textbf{)}$$

Assuming that ĵ is a unitary vector to describe$\vec{\boldsymbol{E}}_{\boldsymbol{\alpha}}$ polarization**,**

$$\vec{E}_{\alpha(z,t)} = \hat{\jmath}\left\{\bar{E}_\alpha e^{\left[i2\pi f t_{(\alpha)} - i\overline{k_\alpha} z\right]} + \bar{B}_\alpha\, e^{\left[i\cdot 2\pi f t + i\vec{k}_{(\alpha)} z\right]}\right\} \qquad (4\mathrm{A}.4)$$

Also, $\overrightarrow{\nabla_e} i^{\vec{k}\vec{r}} = i\vec{k}e^{i\vec{k}\vec{r}}$ and $\vec{k} = k\vec{z}$ where $\vec{z}$ and $\vec{r}$ are unitary vectors, the complex magnetic field is:

$$\vec{B}_{\alpha(z,t)} = \frac{(\hat{\jmath}\wedge\hat{z})}{2\pi f}\left\{\overline{k_\alpha}\bar{E}_\alpha e^{\left[i2\pi f t_{(\alpha)} - i\overline{k_\alpha} z\right]} - \overline{k_\alpha}\bar{B}_\alpha\, e^{\left[i\cdot 2\pi f t + i\overline{k_\alpha} z\right]}\right\} \qquad (4\mathrm{A}.5)$$

These expressions allow one to write the continuity conditions of the fields -$\vec{\boldsymbol{E}}_{\boldsymbol{\alpha}}and\overrightarrow{\boldsymbol{B}_{\boldsymbol{\alpha}}}$ at the interfaces between the media and to infer the relationships.

Discrimination of the interfaces: (α=1) for vacuum (α=2) for the second absorbing medium (a-C) and (α=3) third absorbing medium Cu.

The interface between vacuum (α=1) and the second medium (α=2) is located in z = 0. The interface between the second medium (α=2) and the third medium (α=3) is located z>a that imposes $\bar{\mathrm{B}}_3 = 0$. We normalize the amplitudes with respect to the incident wave in the vacuum $\overrightarrow{\boldsymbol{E}_{\mathbf{1}}} = \boldsymbol{E}_{\mathbf{0}}$.

$$\vec{E}_1 = \hat{\jmath}\{\overline{B_1} + E_0\} = \hat{\jmath}\{\overline{E_2} + \bar{B}_2\}. = \vec{E}_2 \qquad (4\mathrm{A}.6)$$

While for magnetic field

$$\vec{B}_1 = \frac{(\hat{\jmath}\wedge\hat{z})}{2\pi f}\left[+k_0\, E_0 - k_0\bar{B}_1\right] = \frac{(\hat{\jmath}\wedge\hat{z})}{2\pi f}\left[+\bar{k}_2\,\bar{E}_2 - \bar{k}_2\bar{B}_2\right] = \vec{B}_2. \qquad (4\mathrm{A}.7)$$

By solving the equation system of 4A.6 and 4A.7 the obtained result is:

$$E_0 + \bar{B}_1 = \bar{E}_2 + \bar{B}_2. \qquad (4\mathrm{A}.8)$$

$$E_0 - \bar{B}_1 = \frac{\bar{k}_2}{k_0}\,\bar{E}_2 - \bar{B}_2. \qquad (4\mathrm{A}.9)$$

The interface (1-2) is analogous to interface (2-3) when (z =a), considering the following particular case: the third medium is supposed to have infinite extension in the direction z ≫ a, which amounts to imposing $\bar{\mathrm{E}}_3$=0 and $\bar{\mathrm{B}}_3$=0. So, equation 4.A10 is obtained:

$$\bar{E}_2 e^{\left(-i\bar{k}_{(2)}a\right)} + \bar{B}_2 e^{i\bar{k}_{(2)}a} = \bar{E}_3 e^{\left(-i\bar{k}_{(3)}a\right)} \qquad (4\mathrm{A}.10)$$

While;

$$\left[+\bar{k}_2\bar{E}_2 e^{(-i\bar{k}_2 a)} - \bar{k}_2\bar{B}_2 e^{(i\bar{k}_2 a)}\right] = \left[\overline{+k_3}\bar{E}_3 e^{(-i\bar{k}_3 a)}\right] \qquad (4\mathrm{A}.11)$$

The amplitude relation:

$$\bar{k}_3\left[\bar{E}_2 e^{(-i(\bar{k}_2 - \bar{k}_3)a)} + \bar{B}_2 e^{(i(\bar{k}_2 + \bar{k}_3)a)}\right] = \bar{k}_3\bar{E}_3 \qquad (4\mathrm{A}.12)$$

$$+\bar{k}_2\left[\bar{E}_2 e^{(-i(\bar{k}_2 - \bar{k}_3)a)} - \bar{B}_2 e^{(i(\bar{k}_2 + \bar{k}_3)a)}\right] = \bar{k}_3\bar{E}_3 \qquad (4\mathrm{A}.13)$$

$$\bar{E}_2\left(\bar{k}_2-\bar{k}_3\right)e^{(-i(\bar{k}_2-\bar{k}_3)a)}=\bar{B}_2\left(\bar{k}_2+\bar{k}_3\right)e^{(i(\bar{k}_2+\bar{k}_3)a)} \quad (4A.14)$$

Then the relations of $\bar{E}_2$ and $\bar{B}_2$

$$\bar{B}_2=\bar{E}_2\frac{(\bar{k}_2-\bar{k}_3)}{(\bar{k}_2+\bar{k}_3)}e^{(-i2\bar{k}_2a)} \quad (4A.15)$$

$$\bar{E}_3=\bar{E}_2\frac{2\bar{k}_2}{(\bar{k}_2+\bar{k}_3)}e^{(-i(\bar{k}_2-\bar{k}_3)a)} \quad (4A.16)$$

$$E_0+\bar{B}_1=\bar{E}_2\left[1-\frac{(\bar{k}_2-\bar{k}_3)}{(\bar{k}_2+k_3)}e^{(-i2\bar{k}_2a)}\right] \quad (4A.17)$$

$$k_0(E_0-\bar{B}_1)=\bar{E}_2\bar{k}_2\left[1-\frac{(\bar{k}_2-\bar{k}_3)}{(\bar{k}_2+\bar{k}_3)}e^{(-i2\bar{k}_2a)}\right] \quad (4A.18)$$

The equation 4.A19 allows finding the relation between E_0 and $\bar{B}_1$:

$$\frac{E_0+\bar{B}_1}{k_0\left[1+\frac{(\bar{k}_2-\bar{k}_3)}{(\bar{k}_2+\bar{k}_3)}e^{(-i2\bar{k}_2a)}\right]}=\frac{(E_0-\bar{B}_1)}{\bar{k}_2\left[1-\frac{(\bar{k}_2-\bar{k}_3)}{(\bar{k}_2+\bar{k}_3)}e^{(-i2\bar{k}_2a)}\right]} \quad (4A.19)$$

From the equation 4.A18 and 4.A19:

$$\begin{bmatrix}1+\frac{(\bar{k}_2-\bar{k}_3)}{(\bar{k}_2+\bar{k}_3)}e^{(-i2\bar{k}_2a)}\\ 1-\frac{(\bar{k}_2-\bar{k}_3)}{(\bar{k}_2+\bar{k}_3)}e^{(-i2\bar{k}_2a)}\end{bmatrix}=\begin{matrix}\frac{2e^{(-i\bar{k}_2a)}}{(\bar{k}_2+\bar{k}_3)}\left[\bar{k}_2\cos\left(\bar{k}_2a\right)+\imath\bar{k}_3\sin\left(\bar{k}_2a\right)\right]\\ \frac{2e^{(-i\bar{k}_2a)}}{(\bar{k}_2+\bar{k}_3)}\left[\imath\bar{k}_2\sin\left(\bar{k}_2a\right)+\imath\bar{k}_3\cos\left(\bar{k}_2a\right)\right]\end{matrix} \quad (4A.20)$$

Finally, the simplified relation of E_0 and $\bar{B}_1$:

$$\bar{B}_1=E_0\left(\frac{\bar{k}_2(k_0-\bar{k}_3)\cos(\bar{k}_2a)+i\left(k_0\bar{k}_3-\bar{k}_2{}^2\right)\sin(\bar{k}_2a)}{\bar{k}_2(k_0+\bar{k}_3)\cos(\bar{k}_2a)+i\left(k_0\bar{k}_3+\bar{k}_2{}^2\right)\sin(\bar{k}_2a)}\right) \quad (4A.21)$$

From these relations it can be obtained at the reflectance:

$$R=\left|\frac{\bar{B}_2}{\bar{E}_2}\right|^2 \quad (4A.22)$$

The reflectance as a function of the thickness (z):

$$R(a)=\left|\frac{\bar{k}_2(k_0-\bar{k}_3)\cos(\bar{k}_2a)+i\left(k_0\bar{k}_3-\bar{k}_2{}^2\right)\sin(\bar{k}_2a)}{\bar{k}_2(k_0-\bar{k}_3)\cos(\bar{k}_2a)+i\left(k_0\bar{k}_3+\bar{k}_2{}^2\right)\sin(\bar{k}_2a)}\right|^2 \quad (4A.23)$$

When z=0 the known reflection formula between the vacuum and an infinite medium of complex indices

$$R(0)=\left|\frac{k_0-\bar{k}_3}{k_0+\bar{k}_3}\right|^2 \quad (4A.24)$$

Equation 4.A25 represented the so-called R_{th}, a function of the relative contribution of the thickness (z) of media 2, the a-C by the renormalization of equation 4.A23 and 4.A1:24

$$R_{th}(a)=\frac{R(z)}{R(0)}=\left|\frac{k_0+\bar{k}_3}{k_0-\bar{k}_3}\right|^2\left|\frac{\bar{k}_2(k_0-\bar{k}_3)\cos(\bar{k}_2a)+i\left(k_0\bar{k}_3-\bar{k}_2{}^2\right)\sin(\bar{k}_2a)}{\bar{k}_2(k_0+\bar{k}_3)\cos(\bar{k}_2a)+i\left(k_0\bar{k}_3+\bar{k}_2{}^2\right)\sin(\bar{k}_2a)}\right|^2 \quad (4A.25)$$

Appendix 4B: Probability Density Function -χ^2

The χ^2 probability density function (PDF) can be interpreted as providing a relative likelihood that the theoretical value would equal the experimental sample value. Figure 4B.1 shows the PDF versus χ^2 for the reflectance ratio analysis at several wavelengths. The values are also displayed in Figure 4.18.

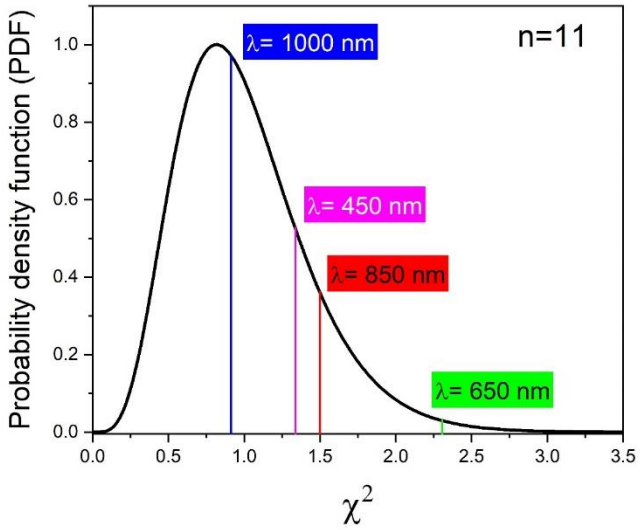

Figure 4B.1: χ^2 distribution with 11 degrees of freedom are the copper foils samples. The four wavelengths used in the model calculations for reflectance ratio are indicated in the distribution.

The χ^2 was calculated by the equation below:

$$\chi^2 = \frac{1}{n}\sum_i^n \frac{(E_i - T_i)^2}{\Delta_z {E_i}^2 + \Delta_m {E_i}^2} \qquad (1)$$

where E_i is the experimental data at point i, T_i is the corresponding theoretical data, n is the number of samples and $\Delta_m E_i$ is the measurement uncertainties on the intensity (vertical error bars shown in Figure 4.14 from the main manuscript). The uncertainty of the intensity, $\Delta_z E_i$, due to the experimental uncertainty on the thickness Δz_i (horizontal error bars of Figure 4.14 is estimated using the slope of the theoretical curve at point *i*:

$$\Delta_z E_i = \frac{\partial T_i}{\partial z}\,\Delta z_i \qquad (2)$$

In this study, the experimental and theoretical curves are normalized independently, thus the number of degrees of liberty is simply the number of samples.

The uncertainties on measurement and thickness are considered as independent, thus they sum as squares at the denominator of (1). When χ^2 is around 1, good significant statistical data is obtained. Here, the χ^2 obtained for wavelengths 450, 850 and 1000 nm are clearly in the bulk of the distribution, indicating a good agreement between experiment and theory. Only the χ^2 for λ = 650 nm lies at the limit of the distribution (the Pearson *p*-value is 0.007).

Appendix 4C: Powder Reflectance Comparison

Comparison of the powder reflectance done at the Laboratoire de Physique des Gases et de Plasma (LPGP) equipment a Spectralon SRS99 PerkinElmer Lambda 35 UV-Vis spectrometer from 400 to 1000 nm (a bandwidth of 2 nm) and a PerkinElmer Lambda 950 until λ=2000 nm at the Laboratoire de Génie Electrique et Electronique de Paris (GeePs). The sample of 150 nm a-C was chosen for comparison.

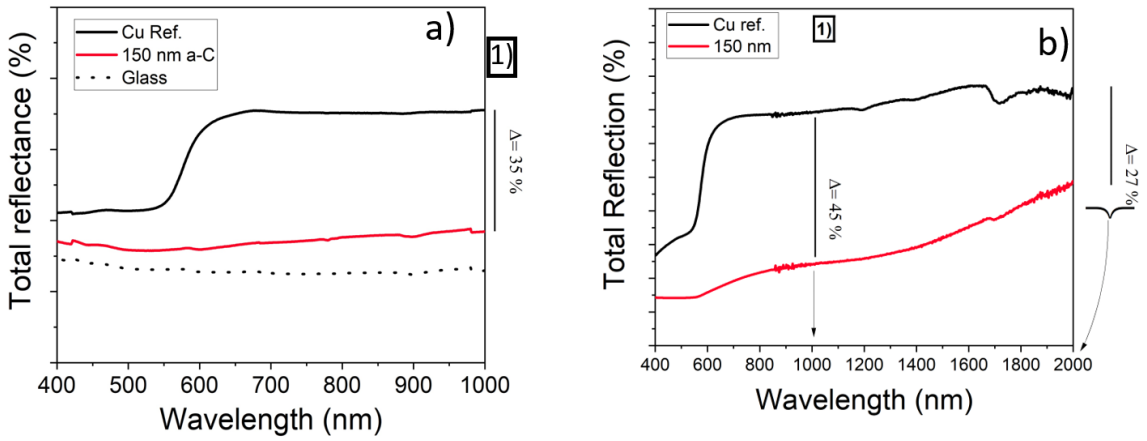

Figure 4C.1: Total reflectance of a) the spectrum until λ= 1000 nm done at the laboratory LPGP and b) spectrum until λ= 2000 nm done at the laboratory GeePs

In Figure 4C.1a, the samples presents 35 % variation while in Figure 4C.1b. the same sample variated 45% position (1). The found difference is attributed equipment calibration, the zone that the reflectance in the metal additive and eventually the glass in front of the sample [278]. The tendency is very similar for both measurements.

Appendix 4D: The Large Size of the Figure 4.19

The image 4.19 is here in larger size to facilitate the analysis

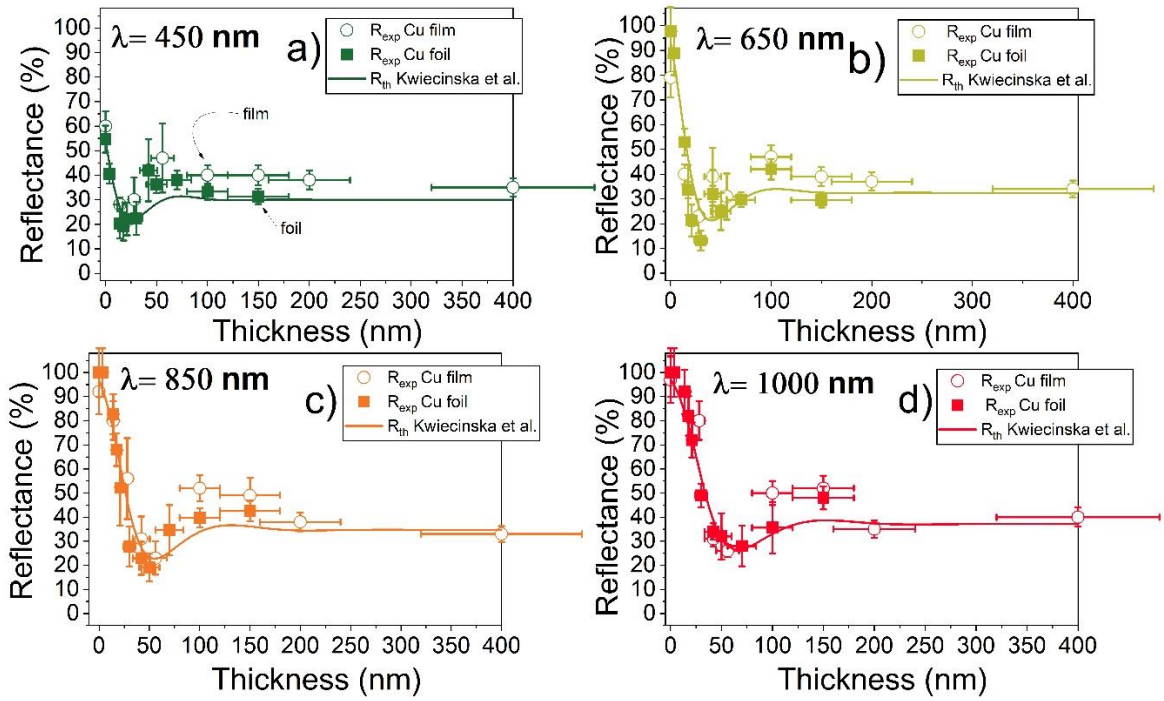

Figure 4D.1: Comparison of experimental (R_{exp}) of Cu foils and film and theoretical (R_{th}) reflectance given by Eq. (4A.25) versus the film of a-C films thickness at constant wavelengths: a) 450, b) 650, c) 850, and d) 1000 nm) (n_r, n_i calculated using the values reported by Kwiecinska et al. [272] *for graphite and Johnson et al.*[263]. χ^2 *is calculated for a-C over copper foil samples.*

Appendix 5A : Graphite 33 Composition

Table 5A.1: Composition of graphite 33 spray:

Ingredient	(%) of composition
1-3 butadiene 0.1%	50-75
Propan-2-ol	25-50
Graphite	1-5

More about graphite 33 in [369]

Appendix 5B : Images 5.6 and 5.7

The images are here present in larger size to facilitate the analysis.

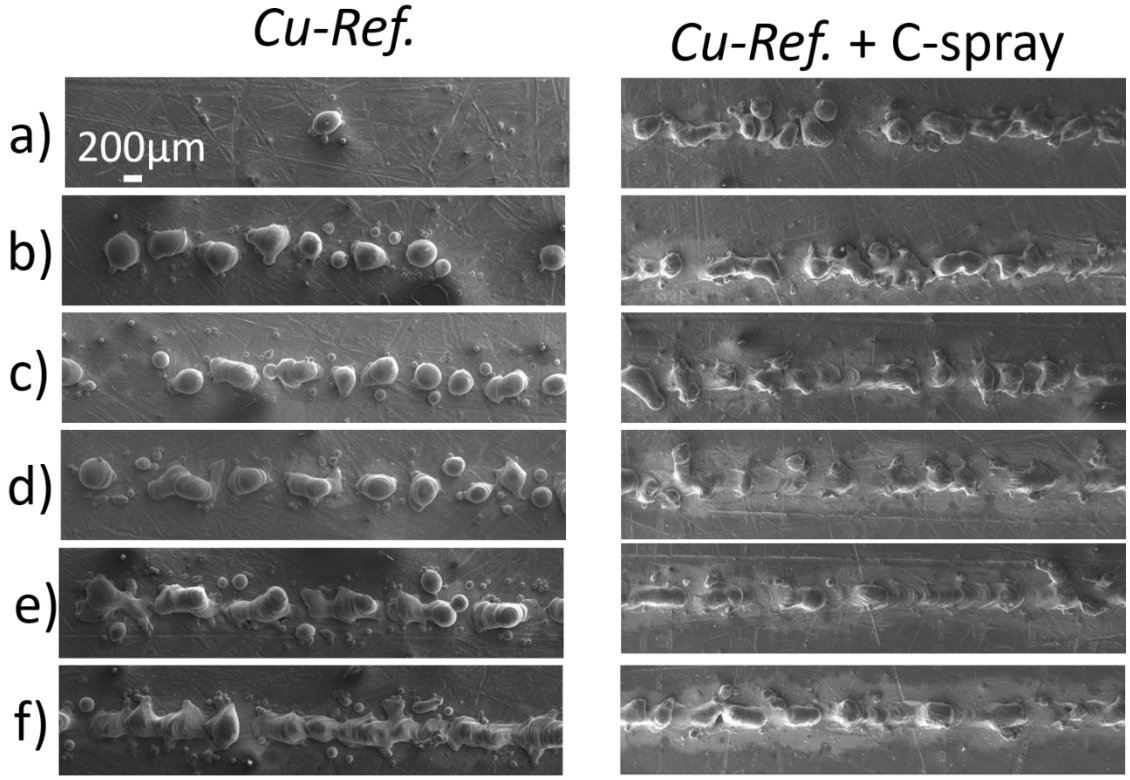

Image 5.15 in larger size

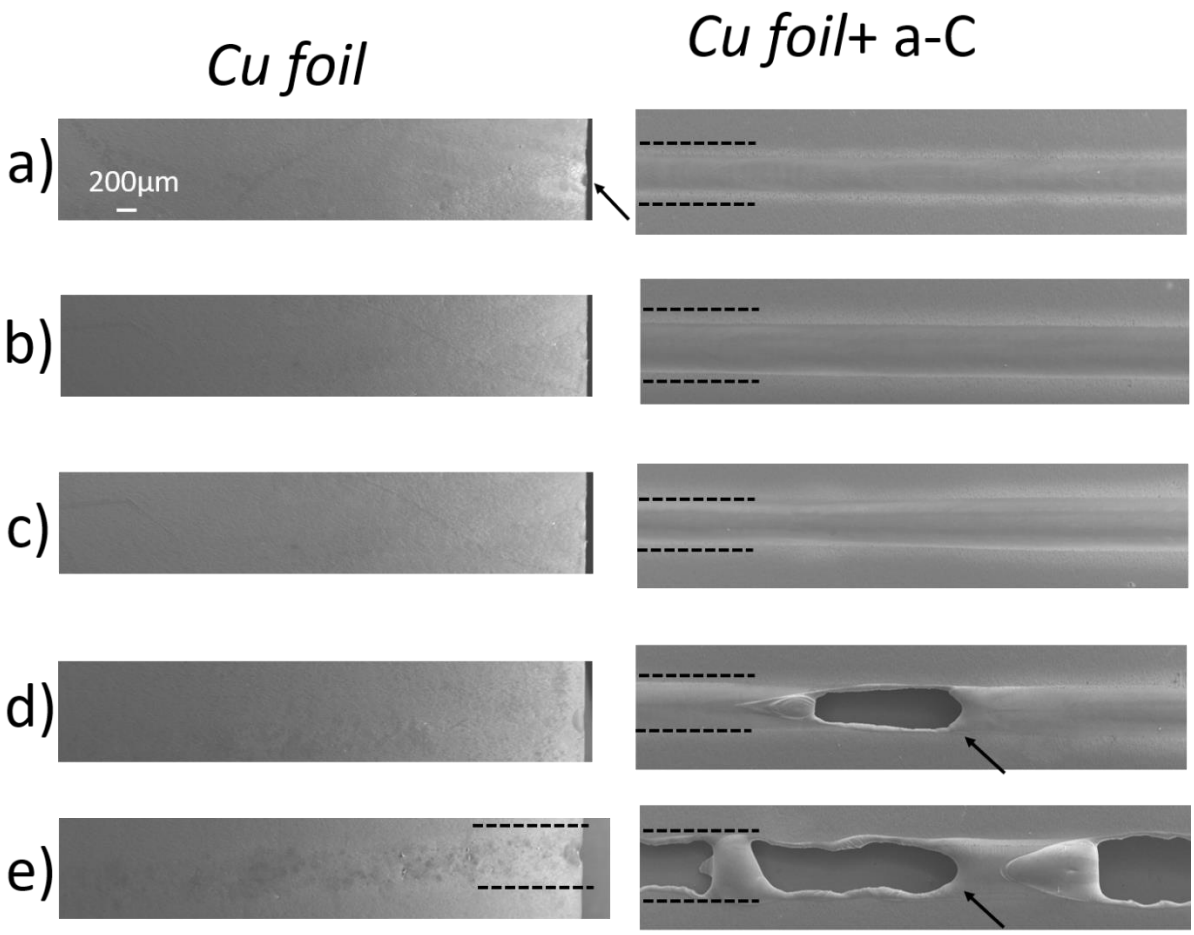

References

[1] H.S. Nalwa, Handbook of Thin Films, Elsevier, 2001.

[2] H. Tabata, K. Kumazawa, M. Funakawa, J. Takimoto, M. Akimoto, Microstructures and Optical Properties of Scales of Butterfly Wings, Opt. Rev. 3 (1996) 139–145. https://doi.org/10.1007/s10043-996-0139-x.

[3] M. Vannoni, A. Sordini, R. Gabrieli, M. Melozzi, G. Molesini, Measuring the thickness of soap bubbles with phase-shift interferometry, Opt. Express. 21 (2013) 19657. https://doi.org/10.1364/OE.21.019657.

[4] J.E. Greene, Review Article: Tracing the recorded history of thin-film sputter deposition: From the 1800s to 2017, J. Vac. Sci. Technol. A Vacuum, Surfaces, Film. 35 (2017) 05C204. https://doi.org/10.1116/1.4998940.

[5] D.M. Mattox, Deposition Processes, in: Found. Vac. Coat. Technol., Springer Berlin Heidelberg, Berlin, Heidelberg, 2003: pp. 11–33. https://doi.org/10.1007/978-3-662-10329-6_7.

[6] A.W. Wright, On a new process for the electrical deposition of metals, and for constructing metal-covered glass specula, J. Franklin Inst. 104 (1877) 242–251. https://doi.org/10.1016/0016-0032(77)90348-9.

[7] K.F. Jensen, W. Kern, J.L. Vossen, Thin Film Processes, Elsevier, 1991. https://doi.org/10.1016/C2009-0-22311-7.

[8] K. Seshan, D. Schepis, Handbook of thin film deposition, William Andrew, 2018.

[9] L. Marcinauskas, V. Dovydaitis, A. Iljinas, M. Andrulevičius, Structural and optical properties of doped amorphous carbon films deposited by magnetron sputtering, Thin Solid Films. 681 (2019) 15–22. https://doi.org/10.1016/j.tsf.2019.04.055.

[10] C. Adelhelm, M. Balden, M. Rinke, M. Stueber, Influence of doping (Ti, V, Zr, W) and annealing on the sp2 carbon structure of amorphous carbon films, J. Appl. Phys. 105 (2009) 033522. https://doi.org/10.1063/1.3075843.

[11] S.J. Bull, A.M. Jones, Multilayer coatings for improved performance, Surf. Coatings Technol. 78 (1996) 173–184. https://doi.org/10.1016/0257-8972(94)02407-3.

[12] H.K. Raut, V.A. Ganesh, A.S. Nair, S. Ramakrishna, Anti-reflective coatings: A critical, in-depth review, Energy Environ. Sci. 4 (2011) 3779. https://doi.org/10.1039/c1ee01297e.

[13] G.P. dos Santos Cavalcante, D.A. Rogers, A.J. Giarola, Analysis of electromagnetic wave propagation in multilayered media using dyadic Green's functions, Radio Sci. 17 (1982) 503–508. https://doi.org/10.1029/RS017i003p00503.

[14] S.K. Pankaj, K.M. Keener, Cold plasma: background, applications and current trends, Curr. Opin. Food Sci. 16 (2017) 49–52. https://doi.org/10.1016/j.cofs.2017.07.008.

[15] H. Zhang, Ultrathin Two-Dimensional Nanomaterials, ACS Nano. 9 (2015) 9451–9469. https://doi.org/10.1021/acsnano.5b05040.

[16] Y. Huang, J. Wu, K.C. Hwang, Thickness of graphene and single-wall carbon nanotubes, Phys. Rev. B. 74 (2006) 245413. https://doi.org/10.1103/PhysRevB.74.245413.

[17] Y. Kopelevich, P. Esquinazi, Graphene Physics in Graphite, Adv. Mater. 19 (2007)

4559–4563. https://doi.org/10.1002/adma.200702051.

[18] B. Schultrich, Structure of Amorphous Carbon, in: Tetrahedrally Bond. Amorph. Carbon Film. I, 2018: pp. 195–272. https://doi.org/10.1007/978-3-662-55927-7_6.

[19] I. Chambouleyron, J.M. Martinez, Optical properties of dielectric and semiconductor thin films, in: Handb. Thin Film., Elsevier, 2002: pp. 593–622. https://doi.org/10.1016/B978-012512908-4/50048-5.

[20] J.C. Angus, P. Koidl, S. Domitz, Carbon Thin Films, in: Plasma Depos. Thin Film., CRC Press, 2018: pp. 89–127. https://doi.org/10.1201/9781351075817-4.

[21] X. Jia, N. Huang, Y. Guo, L. Liu, P. Li, Z. Zhai, B. Yang, Z. Yuan, D. Shi, X. Jiang, … Z.Z.-J. of M., U. 2018, Growth behavior of CVD diamond films with enhanced electron field emission properties over a wide range of experimental parameters, J. Mater. Sci. Technol. 34 (2018) 2398–2406. https://doi.org/10.1016/j.jmst.2018.04.021.

[22] P. Bernier, S. Lefrant, Le Carbone Dans Tous Ses Etats, Taylor & Francis, 1997.

[23] D.P. Carmona F., Physical Properties of Noncrystalline Carbons, in: T.L.R.R. P; (Ed.), Chem. Phys. Carbon Vol. 17 A Ser. Adv., 1981: p. 89.

[24] P. Delhaès, Le polymorphisme des solides carbones, in: Carbone Dans Tout Ses Etats, Taylor & Francis, 1997: p. 69.

[25] P. Bernier, S. Lefrant, Le carbone element fondamental pour la recherche et ses applications, in: Le Carbone Dans Tous Ses Etats, Taylor & Francis, 1997: pp. 1–28.

[26] B. Schultrich, Structure of Amorphous Carbon, in: Tetrahedrally Bond. Amorph. Carbon Film. I, Berlin, Heidelberg, 2018: pp. 195–272. https://doi.org/10.1007/978-3-662-55927-7_6.

[27] J. Schwan, S. Ulrich, H. Roth, H. Ehrhardt, S.R.P.P. Silva, J. Robertson, R. Samlenski, R. Brenn, Tetrahedral amorphous carbon films prepared by magnetron sputtering and dc ion plating, J. Appl. Phys. 79 (1996) 1416–1422. https://doi.org/10.1063/1.360979.

[28] C. Wyon, R. Gillet, L. Lombard, Properties of amorphous carbon films produced by magnetron sputtering, Thin Solid Films. 122 (1984) 203–216. https://doi.org/10.1016/0040-6090(84)90048-8.

[29] J. Robertson, Diamond-like amorphous carbon, Mater. Sci. Eng. R Reports. 37 (2002) 129–281. https://doi.org/10.1016/S0927-796X(02)00005-0.

[30] J. Bohlmark, M. Lattemann, J.T. Gudmundsson, A.P. Ehiasarian, Y. Aranda Gonzalvo, N. Brenning, U. Helmersson, The ion energy distributions and ion flux composition from a high power impulse magnetron sputtering discharge, Thin Solid Films. 515 (2006) 1522–1526. https://doi.org/10.1016/j.tsf.2006.04.051.

[31] M.A. Lieberman, A.J. Lichtenberg, Atomic collisions, in: Princ. Plasma Discharges Mater. Process., Wiley, 2005: pp. 43–63.

[32] M.A. Lieberman, A.J. Lichtenberg, Direct Current (DC) Discharges, in: Princ. Plasma Discharges Mater. Process., Wiley, 2005: pp. 535–555.

[33] B.N. Chapman, Plasma, in: Glow Disch. Process., Wiley, 1980: pp. 49–69.

[34] B.N. Chapman, Gas phase collision problem, in: Glow Disch. Process., Wiley, 1980: p. 22.

[35] A. V Phelps, C.H. Greene, J.P. Burke, Collision cross sections for argon atoms with argon atoms for energies from 0.01 eV to 10 keV, J. Phys. B At. Mol. Opt. Phys. 33 (2000) 2965–2981. https://doi.org/10.1088/0953-4075/33/16/303.

[36] D. Lundin, M. Čada, Z. Hubička, Ionization of sputtered Ti, Al, and C coupled with plasma characterization in HiPIMS, Plasma Sources Sci. Technol. 24 (2015) 035018. https://doi.org/10.1088/0963-0252/24/3/035018.

[37] A.G. McNamara, Rocket measurements of plasma densities and temperatures in visual aurora, Can. J. Phys. 47 (1969) 1913–1927. https://doi.org/10.1139/p69-242.

[38] V.D. Kuznetsov, Space research of the Sun, Physics-Uspekhi. 53 (2010) 947–954. https://doi.org/10.3367/UFNe.0180.201009i.0988.

[39] J.E. Greene, Thin Film Nucleation, Growth, and Microstructural Evolution, in: Handb. Depos. Technol. Film. Coatings, Elsevier, 2010: pp. 554–620. https://doi.org/10.1016/B978-0-8155-2031-3.00012-0.

[40] M. Ohring, Gas Impingement On Surfaces, in: Mater. Sci. Thin Film., Elsevier, 2001: pp. 61–63.

[41] G. Abadias, L. Simonot, J.J. Colin, A. Michel, S. Camelio, D. Babonneau, Volmer-Weber growth stages of polycrystalline metal films probed by in situ and real-time optical diagnostics, Appl. Phys. Lett. 107 (2015) 183105. https://doi.org/10.1063/1.4935034.

[42] Y. Lifshitz, S.R. Kasi, J.W. Rabalais, Subplantation model for film growth from hyperthermal species: Application to diamond, Phys. Rev. Lett. 62 (1989) 1290–1293. https://doi.org/10.1103/PhysRevLett.62.1290.

[43] J.A. Floro, S.J. Hearne, J.A. Hunter, P. Kotula, E. Chason, S.C. Seel, C. V. Thompson, The dynamic competition between stress generation and relaxation mechanisms during coalescence of Volmer–Weber thin films, J. Appl. Phys. 89 (2001) 4886–4897. https://doi.org/10.1063/1.1352563.

[44] B. Schultrich, Growth of ta-C Films, in: 2018: pp. 299–370. https://doi.org/10.1007/978-3-662-55927-7_8.

[45] Y. Lifshitz, C.D. Roux, K. Boyd, W. Eckstein, J.W. Rabalais, Analysis of carbon film growth from low energy ion beams using dynamic trajectory simulations and Auger electron spectroscopy, Nucl. Instruments Methods Phys. Res. Sect. B Beam Interact. with Mater. Atoms. 83 (1993) 351–356. https://doi.org/10.1016/0168-583X(93)95855-Y.

[46] M.P.A.T. Bakai, A.S. Fateev, Topology, properties and thermodynamics of amorphous carbon, in: V.G. Milani,P. Ralchenko (Ed.), Nanostructured Carbon Adv. Appl., Springer Science & Business Media, 2001: pp. 185–193.

[47] Z. Marinkovic, R.R.- Carbon, U. 1976, Preparation and properties of sputtered “glassy” carbon films, Carbon N. Y. 14 (1976) 329–331.

[48] K. Kohary, S. Kugler, Growth of amorphous carbon: Low-energy molecular dynamics simulation of atomic bombardment, Phys. Rev. B. 63 (2001) 193404. https://doi.org/10.1103/PhysRevB.63.193404.

[49] N.C. Cooper, M.S. Fagan, C.M. Goringe, N.A. Marks, D.R. McKenzie, Surface structure and sputtering in amorphous carbon thin films: a tight-binding study of film deposition, J. Phys. Condens. Matter. 14 (2002) 723–730. https://doi.org/10.1088/0953-

8984/14/4/307.

[50] J. Robertson, Structural models of a-C and a-C: H, Diam. Relat. Mater. 4 (1995) 297–301.

[51] P.K. Chu, L. Li, Characterization of amorphous and nanocrystalline carbon films, Mater. Chem. Phys. 96 (2006) 253–277. https://doi.org/10.1016/j.matchemphys.2005.07.048.

[52] J.S. Chen, S.P. Lau, B.K. Tay, G.Y. Chen, Z. Sun, Y.Y. Tan, G. Tan, J.W. Chai, Surface energy of amorphous carbon films containing iron, J. Appl. Phys. 89 (2001) 7814–7819. https://doi.org/10.1063/1.1375808.

[53] J.S. Chen, S.P. Lau, Z. Sun, G.Y. Chen, Y.J. Li, B.K. Tay, J.W. Chai, Metal-containing amorphous carbon films for hydrophobic application, Thin Solid Films. 398–399 (2001) 110–115. https://doi.org/10.1016/S0040-6090(01)01455-9.

[54] J.A. Thornton, The microstructure of sputter-deposited coatings, J. Vac. Sci. Technol. A Vacuum, Surfaces, Film. 4 (1986) 3059–3065. https://doi.org/10.1116/1.573628.

[55] J.A. Thornton, Influence of apparatus geometry and deposition conditions on the structure and topography of thick sputtered coatings, J. Vac. Sci. Technol. 11 (1974) 666–670. https://doi.org/10.1116/1.1312732.

[56] A. Anders, A structure zone diagram including plasma-based deposition and ion etching, Thin Solid Films. 518 (2010) 4087–4090. https://doi.org/10.1016/j.tsf.2009.10.145.

[57] Y. Lifshitz, Hydrogen-free amorphous carbon films: correlation between growth conditions and properties, Diam. Relat. Mater. 5 (1996) 388–400. https://doi.org/10.1016/0925-9635(95)00445-9.

[58] J.R. Davis, Introduction and Overview, in: Copp. Copp. Alloy., ASM international, 2001: pp. 3–8.

[59] A.A. Cortes, J.M. Zuñiga, The use of copper to help prevent transmission of SARS-coronavirus and influenza viruses. A general review, Diagn. Microbiol. Infect. Dis. 98 (2020) 115176. https://doi.org/10.1016/j.diagmicrobio.2020.115176.

[60] C.R. Hammond, The elements, in: Handb. Chem. Phys., CRC press., 2000: pp. 4–10.

[61] Chilean Copper Commission, Cochilco, annual. Yearbook: copper and other mineral statistics, (n.d.) 142. https://www.cochilco.cl/Lists/Anuario/Attachments/24/Ae2021b.pdf.

[62] J.E. Tilton, G. Lagos, Assessing the long-run availability of copper, Resour. Policy. 32 (2007) 19–23. https://doi.org/10.1016/j.resourpol.2007.04.001.

[63] B.-E. Kim, T. Nevitt, D.J. Thiele, Mechanisms for copper acquisition, distribution and regulation, Nat. Chem. Biol. 4 (2008) 176–185. https://doi.org/10.1038/nchembio.72.

[64] D. Edelstein, J. Heidenreich, R. Goldblatt, W. Cote, C. Uzoh, N. Lustig, P. Roper, T. McDevitt, W. Motsiff, A. Simon, J. Dukovic, R. Wachnik, H. Rathore, R. Schulz, L. Su, S. Luce, J. Slattery, Full copper wiring in a sub-0.25 μm CMOS ULSI technology, in: Int. Electron Devices Meet. IEDM Tech. Dig., IEEE, n.d.: pp. 773–776. https://doi.org/10.1109/IEDM.1997.650496.

[65] F. Cemin, D. Lundin, D. Cammilleri, T. Maroutian, P. Lecoeur, T. Minea, Low electrical resistivity in thin and ultrathin copper layers grown by high power impulse magnetron sputtering, J. Vac. Sci. Technol. A Vacuum, Surfaces, Film. 34 (2016) 051506. https://doi.org/10.1116/1.4959555.

[66] F. Cemin, G. Abadias, T. Minea, C. Furgeaud, F. Brisset, D. Solas, D. Lundin, Benefits of energetic ion bombardment for tailoring stress and microstructural evolution during growth of Cu thin films, Acta Mater. 141 (2017) 120–130.

[67] S.J. Kim, S. Kim, J. Lee, Y. Jo, Y. Seo, M. Lee, Y. Lee, C.R. Cho, J. Kim, M. Cheon, J. Hwang, Y.I. Kim, Y. Kim, Y. Kim, A. Soon, M. Choi, W.S. Choi, S. Jeong, Y.H. Lee, Color of Copper/Copper Oxide, Adv. Mater. 33 (2021) 2007345. https://doi.org/10.1002/adma.202007345.

[68] R. Rosenberg, D.C. Edelstein, C.-K. Hu, K.P. Rodbell, Copper Metallization for High Performance Silicon Technology, Annu. Rev. Mater. Sci. 30 (2000) 229–262. https://doi.org/10.1146/annurev.matsci.30.1.229.

[69] L. Zaraska, G.D. Sulka, M. Jaskuła, Fabrication of free-standing copper foils covered with highly-ordered copper nanowire arrays, Appl. Surf. Sci. 258 (2012) 7781–7786. https://doi.org/10.1016/j.apsusc.2012.04.148.

[70] A. Simar, S. Godet, T.R. Watkins, Highlights of the special issue on metal additive manufacturing, Mater. Charact. 143 (2018) 1–4. https://doi.org/10.1016/j.matchar.2018.06.013.

[71] T. DebRoy, H.L. Wei, J.S. Zuback, T. Mukherjee, J.W. Elmer, J.O. Milewski, A.M. Beese, A. Wilson-Heid, A. De, W. Zhang, Additive manufacturing of metallic components – Process, structure and properties, Prog. Mater. Sci. 92 (2018) 112–224. https://doi.org/10.1016/j.pmatsci.2017.10.001.

[72] Q. Jiang, P. Zhang, Z. Yu, H. Shi, D. Wu, H. Yan, X. Ye, Q. Lu, Y. Tian, A Review on Additive Manufacturing of Pure Copper, Coatings. 11 (2021) 740. https://doi.org/10.3390/coatings11060740.

[73] B. Vayre, F. Vignat, F. Villeneuve, Metallic additive manufacturing: state-of-the-art review and prospects, Mech. Ind. 13 (2012) 89–96. https://doi.org/10.1051/meca/2012003.

[74] R.J. Hebert, Viewpoint: metallurgical aspects of powder bed metal additive manufacturing, J. Mater. Sci. 51 (2016) 1165–1175. https://doi.org/10.1007/s10853-015-9479-x.

[75] G.S. Upadhyaya, Metal powder production, in: Powder Metall. Technol., Cambridge Int Science Publishing, 1997: pp. 4–17.

[76] K. Jahns, R. Bappert, P. Böhlke, U. Krupp, Additive manufacturing of CuCr1Zr by development of a gas atomization and laser powder bed fusion routine, Int. J. Adv. Manuf. Technol. 107 (2020) 2151–2161. https://doi.org/10.1007/s00170-020-04941-7.

[77] G.S. Upadhyaya, Metal powder Characteristic, in: Powder Metall. Technol., Cambridge Int Science Publishing, 1997: pp. 18–30.

[78] Y. Ma, T.M. Evans, N. Philips, N. Cunningham, Numerical simulation of the effect of fine fraction on the flowability of powders in additive manufacturing, Powder Technol. 360 (2020) 608–621. https://doi.org/10.1016/j.powtec.2019.10.041.

[79] L.L. Wang, B.K. Tay, K.Y. See, Z. Sun, L.K. Tan, D. Lua, Electromagnetic interference shielding effectiveness of carbon-based materials prepared by screen printing, Carbon N. Y. 47 (2009) 1905–1910. https://doi.org/10.1016/j.carbon.2009.03.033.

[80] C. Rüffler, K. Gürs, Cutting and welding using a CO2 laser, Opt. Laser Technol. 4 (1972) 265–269. https://doi.org/10.1016/0030-3992(72)90027-8.

[81] M.I. Fathima, K.S.J. Wilson, Efficiency enhancement of silicon solar cell using effective interface face method in antireflective coating layers, Int. J. Mod. Phys. C. 31 (2020) 2050076. https://doi.org/10.1142/S012918312050076X.

[82] V.Y. Mendeleyev, V. V. Kachalov, A. V. Kurilovich, L.A. Dombrovsky, Abnormally strong decrease in reflectance of molten copper due to possible generation of levitating sub-micron melt droplets, Int. J. Heat Mass Transf. 113 (2017) 53–58. https://doi.org/10.1016/j.ijheatmasstransfer.2017.05.056.

[83] W.D. Callister, D.G. Rethwisch, Optical Properties, in: Mater. Sci. Eng., Wiley, 2011: pp. 746–760.

[84] W.C. Johnson, Transmission lines and networks, McGraw-Hill, 1963.

[85] B.C. Wadell, Transmission line design handbook, Artech House Microwave Library, 1991.

[86] W.M. Haynes, CRC Handbook of Chemistry and Physics, (1998) F88.

[87] J.K. Peter Atkins, Julio de Paula, The optical properties of solids, in: Atkins' Phys. Chem., Oxford University Press, USA, 2018: p. 679.

[88] S.N. Benchikh, Couches minces nanostructurées de carbone amorphe dopées ou alliées : Elaboration par ablation laser femtoseconde et Caractérisations. Matériaux., Université Jean Monnet, 2005.

[89] G.E. Jellison, F.A. Modine, Parameterization of the optical functions of amorphous materials in the interband region, Appl. Phys. Lett. 69 (1996) 371–373. https://doi.org/10.1063/1.118064.

[90] Q. Li, F. Wang, L. Zhang, Study of colors of diamond-like carbon films, Sci. China Physics, Mech. Astron. 56 (2013) 545–550. https://doi.org/10.1007/s11433-013-5002-z.

[91] M. Chhowalla, J. Robertson, C.W. Chen, S.R.P. Silva, C.A. Davis, G.A.J. Amaratunga, W.I. Milne, Influence of ion energy and substrate temperature on the optical and electronic properties of tetrahedral amorphous carbon (ta-C) films, J. Appl. Phys. 81 (1997) 139–145. https://doi.org/10.1063/1.364000.

[92] V.I. Ivanov-Omskii, A. V. Tolmatchev, S.G. Yastrebov, Optical properties of amorphous carbon films deposited by magnetron sputtering of graphite, Semiconductors. 35 (2001) 220–225. https://doi.org/10.1134/1.1349936.

[93] S. Logothetidis, Optical and electronic properties of amorphous carbon materials, Diam. Relat. Mater. 12 (2003) 141–150. https://doi.org/10.1016/S0925-9635(03)00015-3.

[94] S.M. Mominuzzaman, K.M. Krishna, T. Soga, T. Jimbo, M. Umeno, Optical Absorption and Electrical Conductivity of Amorphous Carbon Thin Films from Camphor: A Natural Source, Jpn. J. Appl. Phys. 38 (1999) 658–663. https://doi.org/10.1143/JJAP.38.658.

[95] Y.Y. Wang, S. Gupta, R.J. Nemanich, Role of thin Fe catalyst in the synthesis of double- and single-wall carbon nanotubes via microwave chemical vapor deposition, Appl. Phys. Lett. 85 (2004) 2601–2603. https://doi.org/10.1063/1.1796529.

[96] S.C. Ray, W.F. Pong, P. Papakonstantinou, Iron, nitrogen and silicon doped diamond like carbon (DLC) thin films: A comparative study, Thin Solid Films. 610 (2016) 42–47. https://doi.org/10.1016/j.tsf.2016.04.048.

[97] W.F. Hosford, Alloys: Copper, in: Encycl. Condens. Matter Phys., Elsevier, 2005: pp. 24–45. https://doi.org/10.1016/B0-12-369401-9/00533-7.

[98] Copper wire tables, 1914. https://archive.org/details/copperwiretables31unituoft/page/8/mode/2up.

[99] J.R. Davis, Applications, in: Alloy. Copp. Copp., ASM international, 2001: p. 154.

[100] Y.C. Cho, S. Lee, M. Ajmal, W.-K. Kim, C.R. Cho, S.-Y. Jeong, J.H. Park, S.E. Park, S. Park, H.-K. Pak, H.C. Kim, Copper Better than Silver: Electrical Resistivity of the Grain-Free Single-Crystal Copper Wire, Cryst. Growth Des. 10 (2010) 2780–2784. https://doi.org/10.1021/cg1003808.

[101] F. Chen, D. Gardner, Influence of line dimensions on the resistance of Cu interconnections, IEEE Electron Device Lett. 19 (1998) 508–510. https://doi.org/10.1109/55.735762.

[102] D. Josell, S.H. Brongersma, Z. Tőkei, Size-Dependent Resistivity in Nanoscale Interconnects, Annu. Rev. Mater. Res. 39 (2009) 231–254. https://doi.org/10.1146/annurev-matsci-082908-145415.

[103] R.A. Matula, Electrical resistivity of copper, gold, palladium, and silver, J. Phys. Chem. Ref. Data. 8 (1979) 1147–1298. https://doi.org/10.1063/1.555614.

[104] H.O. Pierson, Pyrolytic Graphite, in: Handb. Carbon, Graph. Diamonds Fullerenes, Elsevier, Oxford, 1993: pp. 141–165. https://doi.org/10.1016/B978-0-8155-1339-1.50012-8.

[105] J.Conard, Hydridation des orbitales du carbone et nature des liaisons, in: S. Bernier, Patrick; Lefrant (Ed.), Le Carbone Dans Tous Ses Etats, Taylor & Francis, 1997: pp. 250–255.

[106] S.M. Rossnagel, M.A. Russak, J.J. Cuomo, Pressure and plasma effects on the properties of magnetron sputtered carbon films, J. Vac. Sci. Technol. A Vacuum, Surfaces, Film. 5 (1987) 2150–2153. https://doi.org/10.1116/1.574941.

[107] E. Sandré, F. Cyrot-Lackmann, Formulations de Slater-koster pour les integrales de saut: dépendance avec la géométrie de coordination des atomes, in: P. Bernier (Ed.), Le Carbone Dans Tous Ses Etats, 1997: pp. 283–289.

[108] C. Corbella, G. Oncins, M.A. Gómez, M.C. Polo, E. Pascual, J. García-Céspedes, J.L. Andújar, E. Bertran, Structure of diamond-like carbon films containing transition metals deposited by reactive magnetron sputtering, Diam. Relat. Mater. 14 (2005) 1103–1107. https://doi.org/10.1016/j.diamond.2004.10.029.

[109] K.I. Schiffmann, M. Fryda, G. Goerigk, R. Lauer, P. Hinze, A. Bulack, Sizes and distances of metal clusters in Au-, Pt-, W- and Fe-containing diamond-like carbon hard coatings: a comparative study by small angle X-ray scattering, wide angle X-ray diffraction, transmission electron microscopy and scanning tunnelling microsco, Thin Solid Films. 347 (1999) 60–71. https://doi.org/10.1016/S0040-6090(98)01607-1.

[110] S. Craig, G.L. Harding, Composition, optical properties and degradation modes of Cu/(graded metal-carbon) solar selective surfaces, Thin Solid Films. 101 (1983) 97–113. https://doi.org/10.1016/0040-6090(83)90262-6.

[111] C.P. Klages, R. Memming, Microstructure and Physical Properties of Metal-Containing Hydrogenated Carbon Films, Mater. Sci. Forum. 52–53 (1991) 609–644. https://doi.org/10.4028/www.scientific.net/MSF.52-53.609.

[112] J.R. Davis, Copper and copper alloys, ASM international, 2001.

[113] S.T. Auwal, S. Ramesh, F. Yusof, S.M. Manladan, A review on laser beam welding of copper alloys, Int. J. Adv. Manuf. Technol. 96 (2018) 475–490. https://doi.org/10.1007/s00170-017-1566-5.

[114] Y. Tang, H.T. Loh, Y.S. Wong, J.Y.H. Fuh, L. Lu, X. Wang, Direct laser sintering of a copper-based alloy for creating three-dimensional metal parts, 140 (2003) 368–372. https://doi.org/10.1016/S0924-0136(03)00766-0.

[115] S. Engler, R. Ramsayer, R. Poprawe, Process Studies on Laser Welding of Copper with Brilliant Green and Infrared Lasers, Phys. Procedia. 12 (2011) 339–346. https://doi.org/10.1016/j.phpro.2011.03.142.

[116] M. Bonesso, P. Rebesan, C. Gennari, S. Mancin, R. Dima, A. Pepato, I. Calliari, Effect of Particle Size Distribution on Laser Powder Bed Fusion Manufacturability of Copper, BHM Berg- Und Hüttenmännische Monatshefte. 166 (2021) 256–262. https://doi.org/10.1007/s00501-021-01107-0.

[117] S.J. Raab, R. Guschlbauer, M.A. Lodes, C. Körner, Thermal and Electrical Conductivity of 99.9% Pure Copper Processed via Selective Electron Beam Melting, Adv. Eng. Mater. 18 (2016) 1661–1666. https://doi.org/10.1002/adem.201600078.

[118] P. Frigola, O. Harrysson, T. Horn, H. West, R. Aman, J. Rigsbee, D. Ramirez, F. Medina, R. Wicker, E. Rodriguez, Fabricating Copper components with Electron beam melting, Adv. Mater. Process. (2014) 20.

[119] S. Dadras, M.J. Torkamany, J. Sabbaghzadeh, Spectroscopic characterization of low-nickel copper welding with pulsed Nd:YAG laser, Opt. Lasers Eng. 46 (2008) 769–776. https://doi.org/10.1016/j.optlaseng.2008.04.023.

[120] T.I. El-Wardany, Y. She, V.N. Jagdale, J.K. Garofano, J.J. Liou, W.R. Schmidt, Challenges in Three-Dimensional Printing of High-Conductivity Copper, J. Electron. Packag. 140 (2018). https://doi.org/10.1115/1.4039974.

[121] R. Guschlbauer, S. Momeni, F. Osmanlic, C. Körner, Process development of 99.95% pure copper processed via selective electron beam melting and its mechanical and physical properties, Mater. Charact. 143 (2018) 163–170. https://doi.org/10.1016/j.matchar.2018.04.009.

[122] L. Constantin, Z. Wu, N. Li, L. Fan, J.-F. Silvain, Y.F. Lu, Laser 3D printing of complex copper structures, Addit. Manuf. 35 (2020) 101268. https://doi.org/10.1016/j.addma.2020.101268.

[123] M. Colopi, L. Caprio, A.G. Demir, B. Previtali, Selective laser melting of pure Cu with a 1 kW single mode fiber laser, Procedia CIRP. 74 (2018) 59–63. https://doi.org/10.1016/j.procir.2018.08.030.

[124] M.S. Zediker, R.D. Fritz, M.J. Finuf, J.M. Pelaprat, Stable keyhole welding of 1 mm thick copper with a 600 W blue laser system, J. Laser Appl. 31 (2019) 022404. https://doi.org/10.2351/1.5096092.

[125] K. Asano, M. Tsukamoto, Y. Funada, Y. Sakon, N. Abe, Y. Sato, R. Higashino, M. Sengoku, M. Yoshida, Copper film formation on metal surfaces with 100 W blue direct diode laser system, J. Laser Appl. 30 (2018) 032602. https://doi.org/10.2351/1.5040635.

[126] C. Rüttimann, U. Dürr, A. Moalem, M. Priehs, Reliable laser micro-welding of copper, in: B. Gu, G. Hennig, X. Xu, H. Niino (Eds.), 2011: p. 792007. https://doi.org/10.1117/12.875033.

[127] S. Pricking, R. Huber, K. Klausmann, E. Kaiser, C. Stolzenburg, A. Killi, High-power CW and long-pulse lasers in the green wavelength regime for copper welding, in: F. Dorsch, S. Kaierle (Eds.), 2016: p. 97410G. https://doi.org/10.1117/12.2213293.

[128] O. Molerus, Effect of interparticle cohesive forces on the flow behaviour of powders, Powder Technol. 20 (1978) 161–175. https://doi.org/10.1016/0032-5910(78)80045-X.

[129] H.-C. Chen, G. Bi, M.L.S. Nai, J. Wei, Enhanced welding efficiency in laser welding of highly reflective pure copper, J. Mater. Process. Technol. 216 (2015) 287–293. https://doi.org/10.1016/j.jmatprotec.2014.09.020.

[130] S. Jadhav, S. Dadbakhsh, J. Vleugels, J. Hofkens, P. Puyvelde, S. Yang, J. Kruth, J. Humbeeck, K. Vanmeensel, Influence of Carbon Nanoparticle Addition (and Impurities) on Selective Laser Melting of Pure Copper, Materials (Basel). 12 (2019) 2469. https://doi.org/10.3390/ma12152469.

[131] X. Wang, J. Liu, L. Yang, Y. He, Y. Wang, Nano-sized amorphous carbon covered surface formed by selective laser melting of ink-printed (SLM-IP) copper (Cu) nanoparticles (NPs), Appl. Surf. Sci. 448 (2018) 133–137. https://doi.org/10.1016/j.apsusc.2018.04.109.

[132] L. Wang, A. Yu, E. Li, H. Shen, Z. Zhou, Effects of spreader geometry on powder spreading process in powder bed additive manufacturing, Powder Technol. 384 (2021) 211–222. https://doi.org/10.1016/j.powtec.2021.02.022.

[133] C. Meier, R. Weissbach, J. Weinberg, W.A. Wall, A.J. Hart, Critical influences of particle size and adhesion on the powder layer uniformity in metal additive manufacturing, J. Mater. Process. Technol. 266 (2019) 484–501. https://doi.org/10.1016/j.jmatprotec.2018.10.037.

[134] S. Pratheesh Kumar, S. Elangovan, R. Mohanraj, J.R. Ramakrishna, Review on the evolution and technology of State-of-the-Art metal additive manufacturing processes, Mater. Today Proc. 46 (2021) 7907–7920. https://doi.org/10.1016/j.matpr.2021.02.567.

[135] A. Mussatto, R. Groarke, A. O'Neill, M.A. Obeidi, Y. Delaure, D. Brabazon, Influences of powder morphology and spreading parameters on the powder bed topography uniformity in powder bed fusion metal additive manufacturing, Addit. Manuf. 38 (2021) 101807. https://doi.org/10.1016/j.addma.2020.101807.

[136] C. Meier, R. Weissbach, J. Weinberg, W.A. Wall, A. John Hart, Modeling and characterization of cohesion in fine metal powders with a focus on additive manufacturing process simulations, Powder Technol. 343 (2019) 855–866. https://doi.org/10.1016/j.powtec.2018.11.072.

[137] S. Dorbolo, A. Merlen, M. Creyssels, N. Vandewalle, B. Castaing, E. Falcon, Effects of electromagnetic waves on the electrical properties of contacts between grains, Europhys. Lett. 79 (2007) 54001. https://doi.org/10.1209/0295-5075/79/54001.

[138] D. Lundin, The hipims process, Linköping University Electronic Press, 2010.

[139] B.N. Chapman, Glow discharge process: sputtering and plasma etching, Wiley, 1980.

[140] D.M. Sanders, Review of ion-based coating processes derived from the cathodic arc, J. Vac. Sci. Technol. A Vacuum, Surfaces, Film. 7 (1989) 2339–2345. https://doi.org/10.1116/1.575939.

[141] H.F. Winters, E. Kay, Gas incorporation into sputtered films, J. Appl. Phys. 38 (1967) 3928–3934. https://doi.org/10.1063/1.1709043.

[142] B. Chapman, Sputtering yield data, in: Glow Disch. Process. Sputtering Plasma Etch., Wiley, 1980: p. 380.

[143] N. Savvides, B. Window, Unbalanced magnetron ion-assisted deposition and property modification of thin films, J. Vac. Sci. Technol. A Vacuum, Surfaces, Film. 4 (2002) 504–508. https://doi.org/10.1116/1.573869.

[144] W.D. Sproul, P.J. Rudnik, M.E. Graham, S.L. Rohde, High rate reactive sputtering in an opposed cathode closed-field unbalanced magnetron sputtering system, Surf. Coatings Technol. 43–44 (1990) 270–278. https://doi.org/10.1016/0257-8972(90)90080-V.

[145] P.J. Kelly, R.D. Arnell, Magnetron sputtering: a review of recent developments and applications, Vacuum. 56 (2000) 159–172. https://doi.org/10.1016/S0042-207X(99)00189-X.

[146] X.Y. Zhang, L.F. Nie, C.H. Lin, Q. Wang, X.N. Li, C. Dong, J.P. Chu, Highly stable carbon-doped Cu films on barrierless Si, Appl. Surf. Sci. 257 (2010) 3636–3640. https://doi.org/10.1016/j.apsusc.2010.11.095.

[147] P.M. Martin, Handbook of deposition technologies for films and coatings: science, applications and technology, William Andrew, 2009.

[148] D. Dangoisse, D. Hennequin, V. Zehnlé, Principaux Lasers, in: Les Lasers, 3rd ed., Dunod, 2013: pp. 225–259.

[149] F.K. Kneubühl, M.W. Sigrist, Festkörperlaser (solid state laser), in: Laser, Springer-Verlag, 2008: pp. 355–388.

[150] J.S. Adolf Giesen, Thin-Disk lasers, in: High Power Laser Handb., McGraw-Hill Education, 2011.

[151] M. Larionov, Thin Disk Lasers, in: Encycl. Mod. Opt., Elsevier, 2018: pp. 407–414. https://doi.org/10.1016/B978-0-12-803581-8.09363-2.

[152] G. Zhu, Y. Qiu, Z. Wang, X. Zhu, C. Zhu, Analytical model of optical field distribution of thin disk laser with thermal-optical aberration gain medium, Opt. Laser Technol. 82 (2016) 134–138. https://doi.org/10.1016/j.optlastec.2016.03.002.

[153] A. Laskin, P. Kaiser, V. Laskin, A. Ostrun, Laser beam shaping for biomedical microscopy techniques, in: J. Popp, V. V. Tuchin, D.L. Matthews, F.S. Pavone (Eds.), 2016: p. 98872E. https://doi.org/10.1117/12.2217927.

[154] F.M.S.M.H. Dickey, Gaussian Bean Shape: Diffraction theory and design, in: Laser Beam Shap. Theory Tech., Marcel Dekker Inc., 2018.

[155] S. Zhang, G. Neil, M. Shinn, Single-element laser beam shaper for uniform flat-top profiles, Opt. Express. 11 (2003) 1942. https://doi.org/10.1364/OE.11.001942.

[156] R. Voelkel, K.J. Weible, Laser beam homogenizing: limitations and constraints, in: A. Duparré, R. Geyl (Eds.), 2008: p. 71020J. https://doi.org/10.1117/12.799400.

[157] M. Song, S.-P. Han, J. Park, H. Choi, S. Kim, T.T. Tran, H.D. Kim, M. Song, Flat-top supercontinuum generation via Gaussian pulse shaping, Opt. Express. 29 (2021) 12001. https://doi.org/10.1364/OE.421876.

[158] M. Brandt, The role of lasers in additivemanufacturing, in: Laser Addit. Manuf. Mater. Des. Technol. Appl., Woodhead Publishing, 2016: pp. 1–5.

[159] B. Nagarajan, Z. Hu, X. Song, W. Zhai, J. Wei, Development of Micro Selective Laser

Melting: The State of the Art and Future Perspectives, Engineering. 5 (2019) 702–720. https://doi.org/10.1016/j.eng.2019.07.002.

[160] AddUp, AddUp Manager™, (n.d.). https://addupsolutions.com/machines/pbf/pbf-software/ (accessed August 23, 2021).

[161] N. Shahrubudin, T.C. Lee, R. Ramlan, An Overview on 3D Printing Technology: Technological, Materials, and Applications, Procedia Manuf. 35 (2019) 1286–1296. https://doi.org/10.1016/j.promfg.2019.06.089.

[162] M. Geiger, M. Euringer, R. Neugebauer, F. Garreis, Lamellierte Aktiv-Werkzeugelemente in flexiblen Blechumformwerkzeugen, Blech, Rohre, Profile. 46 (1999) 34–37.

[163] C.Y. Yap, C.K. Chua, Z.L. Dong, Z.H. Liu, D.Q. Zhang, L.E. Loh, S.L. Sing, Review of selective laser melting: Materials and applications, Appl. Phys. Rev. 2 (2015) 041101. https://doi.org/10.1063/1.4935926.

[164] Y. Hagedorn, Laser additive manufacturing of ceramic components: materials, processes, and mechanisms, in: Addit. Manuf. Met., 2017: pp. 163–172.

[165] D.D. Gu, W. Meiners, K. Wissenbach, R. Poprawe, Laser additive manufacturing of metallic components: materials, processes and mechanisms, Int. Mater. Rev. 57 (2012) 133–164. https://doi.org/10.1179/1743280411Y.0000000014.

[166] F. Lemoisson, L. Froyen, Understanding and improving powder metallurgical processes, in: Fundam. Metall., Elsevier, 2005: pp. 471–502. https://doi.org/10.1533/9781845690946.2.471.

[167] S. Sun, M. Brandt, M. Easton, Powder bed fusion processes, in: Laser Addit. Manuf., Elsevier, 2017: pp. 55–77. https://doi.org/10.1016/B978-0-08-100433-3.00002-6.

[168] P. Yuan, D. Gu, Molten pool behaviour and its physical mechanism during selective laser melting of TiC/AlSi10Mg nanocomposites: simulation and experiments, J. Phys. D. Appl. Phys. 48 (2015) 035303. https://doi.org/10.1088/0022-3727/48/3/035303.

[169] A.J. Pinkerton, Laser direct metal deposition: theory and applications in manufacturing and maintenance, in: Adv. Laser Mater. Process., Elsevier, 2010: pp. 461–491. https://doi.org/10.1533/9781845699819.6.461.

[170] J.O. Milewski, Lasers, Electron Beams, Plasma Arcs, in: Addit. Manuf. Met., Springer International Publishing, Cham, 2017: pp. 85–99. https://doi.org/10.1007/978-3-319-58205-4.

[171] C. Körner, Additive manufacturing of metallic components by selective electron beam melting — a review, Int. Mater. Rev. 61 (2016) 361–377. https://doi.org/10.1080/09506608.2016.1176289.

[172] D. Agius, K. Kourousis, C. Wallbrink, A Review of the As-Built SLM Ti-6Al-4V Mechanical Properties towards Achieving Fatigue Resistant Designs, Metals (Basel). 8 (2018) 75. https://doi.org/10.3390/met8010075.

[173] E. Smith, G. Dent, Modern Raman Spectroscopy - A Practical Approach, John Wiley & Sons, Ltd, Chichester, UK, 2004. https://doi.org/10.1002/0470011831.

[174] W.L. Bragg, The diffraction of short electromagnetic waves by a crystal, (1929).

[175] P. Hariharan, Optical Interferometry, 2nd ed., Elsevier, 2003. https://doi.org/10.1016/B978-0-12-311630-7.X5000-X.

[176] D.C. Goldstein, J.I., Newbury, D.E., Michael, J.R., Ritchie, N.W.M., Scott, J.H.J., Joy, Backscattered Electrons, in: Scanning Electron Microsc. X-Ray Microanal., 2018: pp. 39–63.

[177] J.I. Goldstein, D.E. Newbury, J.R. Michael, N.W.M. Ritchie, J.H.J. Scott, D.C. Joy, Scanning Electron Microscopy and X-Ray Microanalysis, Springer New York, New York, NY, 2018. https://doi.org/10.1007/978-1-4939-6676-9.

[178] M.-A. Chu, Wei-Kan; Mayer, James; Nicolet, Backscattering Spectrometry, 1978.

[179] M.-A. Chu, Wei-Kan; Mayer, James; Nicolet, Influence of beam parameters, in: Backscattering Spectrom., 1978: pp. 185–221.

[180] S.H. Vollmer, Guidelines for Best Practices in Image Processing, Univ. Alabama Birmingham. (1999). https://ori.hhs.gov/education/products/RIandImages/guidelines/list.html (accessed June 23, 2021).

[181] I. Miccoli, F. Edler, H. Pfnür, C. Tegenkamp, The 100th anniversary of the four-point probe technique: the role of probe geometries in isotropic and anisotropic systems, J. Phys. Condens. Matter. 27 (2015) 223201. https://doi.org/10.1088/0953-8984/27/22/223201.

[182] H. Tompkins, E.A. Irene, Handbook of ellipsometry, William Andrew, 2005.

[183] B. Henderson, Optical Spectrometers, in: Handb. Opt. I Geom. Phys. Opt. Polariz. Light. Components Instruments, 3rd ed., McGraw-Hill, 2010: pp. 31.1-31.31.

[184] M. Creyssels, Quelques propriétés du transport électrique dans les milieux granulaires, 2006.

[185] J.A. Fleming, The principles of electric wave telegraphy, Longmans, Green, and Company, 1906.

[186] D.T. Emerson, The stage is set: Developments before 1900 leading to practical wireless communication, in: Globecom Meet. IEEE, San Antonio, TX, 2001. https://www.cv.nrao.edu/~demerson/ssetq.pdf.

[187] T. Tommasina, Sur un cohèreur très sensible, obtenu par le simple contact de deux charbons, C. r. Hebd. Séanc. Acad. Sci., Paris. 128 (1899) 1092–1095.

[188] T. Tommasina, Sulla sostituzione dell' azione magnetica all'azione meccanica del trembleur, per rompere direttamente le catene di limatura dei coherer, Nuovo Cim Nuovo Cim. 10 (1899) 283.

[189] K.E. Guthe, A. Trowbridge, On the Theory of the Coherer, Phys. Rev. (Series I). 11 (1900) 22–39. https://doi.org/10.1103/PhysRevSeriesI.11.22.

[190] T. Tommasina, Sulla natura e la causa del fenomeno dei coherer, Nuovo Cim Nuovo Cim. 10 (1899) 223–227.

[191] K.E. Guthe, On the Action of the Coherer, Phys. Rev. (Series I). 12 (1901) 245–253. https://doi.org/10.1103/PhysRevSeriesI.12.245.

[192] É. Branly, Variations de conductibilité sous diverses influences électriques, Paris - Gauthier-Villars - 1890. (1890) 785–787.

[193] J.I. Goldstein, D.E. Newbury, P. Echlin, D.C. Joy, C. Fiori, E. Lifshin, Electron-Beam-Specimen Interactions, in: Scanning Electron Microsc. X-Ray Microanal., Springer,

1981: pp. 53–122.

[194] B. Henderson, Optical Spectrometer - The Double-Beam Spectrophotometer, in: Handb. Opt. Vol. II Devices , Meas. , Prop., 2nd ed., 1995: p. 20.4.

[195] I. PerkinElmer, Lambda 25, 35, 45 User's Guide, (2000) 39.

[196] P. Groning, Cold plasmas, in: H.S. Nalwa (Ed.), Handb. Thin Film. -Deposition Process. Thin Film. V1, 2001: pp. 226–230.

[197] C. Benndorf, E. Boettger, M. Fryda, H.G. Haubold, C.-P. Klages, H. Köberle, Electrical conductivity and microstructure of metal containing a-C:H films, Synth. Met. 43 (1991) 4055–4058. https://doi.org/10.1016/0379-6779(91)91743-T.

[198] M. Grischke, K. Bewilogua, H. Dimigen, Preparation, Properties And Structure Of Metal Containing Amorphous Hydrogenated Carbon Films, Mater. Manuf. Process. 8 (1993) 407–417. https://doi.org/10.1080/10426919308934846.

[199] P. Tian, X. Zhang, Q.Z. Xue, Enhanced room-temperature positive magnetoresistance of a-C:Fe film, Carbon N. Y. 45 (2007) 1764–1768. https://doi.org/10.1016/j.carbon.2007.05.005.

[200] L.C. Costa, M. Valente, M.A. Sá, F. Henry, Electrical and magnetic properties of Polystyrene doped with Iron nanoparticles, Polym. Bull. 57 (2006) 881–887. https://doi.org/10.1007/s00289-006-0648-6.

[201] H. Kersten, H. Deutsch, H. Steffen, G.M.W. Kroesen, R. Hippler, The energy balance at substrate surfaces during plasma processing, Vacuum. 63 (2001) 385–431. https://doi.org/10.1016/S0042-207X(01)00350-5.

[202] D. Lundin, C. Vitelaru, L. de Poucques, N. Brenning, T. Minea, Ti–Ar scattering cross sections by direct comparison of Monte Carlo simulations and laser-induced fluorescence spectroscopy in magnetron discharges, J. Phys. D. Appl. Phys. 46 (2013) 175201. https://doi.org/10.1088/0022-3727/46/17/175201.

[203] M. Stepanova, S. Dew, Anisotropic energies of sputtered atoms under oblique ion incidence, Nucl. Instruments Methods Phys. Res. Sect. B Beam Interact. with Mater. Atoms. 215 (2004) 357–365. https://doi.org/10.1016/j.nimb.2003.09.013.

[204] A.A. Solovyev, K.V. Oskomov, A.S. Grenadyorov, P.D. Maloney, Preparation of nickel-containing conductive amorphous carbon films by magnetron sputtering with negative high-voltage pulsed substrate bias, Thin Solid Films. 650 (2018) 37–43. https://doi.org/10.1016/j.tsf.2018.02.013.

[205] C. Corbella, E. Pascual, G. Oncins, C. Canal, J.L. Andújar, E. Bertran, Composition and morphology of metal-containing diamond-like carbon films obtained by reactive magnetron sputtering, Thin Solid Films. 482 (2005) 293–298. https://doi.org/10.1016/j.tsf.2004.11.178.

[206] H.-Y. Cheng, W.-Y. Wu, J.-M. Ting, Microstructure and optical properties of chromium containing amorphous hydrogenated carbon thin films (a-C:H/Cr), Thin Solid Films. 517 (2009) 4724–4727. https://doi.org/10.1016/j.tsf.2009.03.095.

[207] J.S. Chen, S.P. Lau, G.Y. Chen, Z. Sun, Y.J. Li, B.K. Tay, J.W. Chai, Deposition of iron containing amorphous carbon films by filtered cathodic vacuum arc technique, Diam. Relat. Mater. 10 (2001) 2018–2023. https://doi.org/10.1016/S0925-9635(01)00474-5.

[208] D.R. Mckenzie, R.C. Mcphedran, N. Savvides, L.C. Botten, Properties and structure of

amorphous hydrogenated carbon films, Philos. Mag. B. 48 (1983) 341–364. https://doi.org/10.1080/13642818308246487.

[209] U. Geyer, U. von Hülsen, P. Thiyagarajan, Surface roughening and columnar growth of thin amorphous CuTi films, Appl. Phys. Lett. 70 (1997) 1691–1693. https://doi.org/10.1063/1.118671.

[210] B. Ghebouli, A. Layadi, A. Guittoum, L. Kerkache, M. Benkerri, A. Klimov, V. Preobrazhensky, P. Pernod, Electrical properties and Kerr effect study of evaporated Fe/Si and Fe/glass thin films, Eur. Phys. J. Appl. Phys. 48 (2009) 30503. https://doi.org/10.1051/epjap/2009183.

[211] S. Cusenza, P. Schaaf, Amorphous stainless steel coatings prepared by reactive magnetron-sputtering from austenitic stainless steel targets, Appl. Phys. A. 94 (2009) 139. https://doi.org/10.1007/s00339-008-4685-x.

[212] J.I. Goldstein, D.E. Newbury, J.R. Michael, N.W.M. Ritchie, J.H.J. Scott, D.C. Joy, X-Rays, in: J.I. Goldstein, D.E. Newbury, J.R. Michael, N.W.M. Ritchie, J.H.J. Scott, D.C. Joy (Eds.), Scanning Electron Microsc. X-Ray Microanal., Springer New York, New York, NY, 2018: pp. 39–63. https://doi.org/10.1007/978-1-4939-6676-9_4.

[213] J. Vetter, 60 years of DLC coatings: Historical highlights and technical review of cathodic arc processes to synthesize various DLC types, and their evolution for industrial applications, Surf. Coatings Technol. 257 (2014) 213–240. https://doi.org/10.1016/j.surfcoat.2014.08.017.

[214] J. Robertson, E.P. O'Reilly, Electronic and atomic structure of amorphous carbon, Phys. Rev. B. 35 (1987) 2946–2957. https://doi.org/10.1103/PhysRevB.35.2946.

[215] I. Bouabibsa, S. Lamri, A. Alhussein, T. Minea, F. Sanchette, Plasma investigations and deposition of Me-DLC (Me = Al, Ti or Nb) obtained by a magnetron sputtering-RFPECVD hybrid process, Surf. Coatings Technol. 354 (2018) 351–359. https://doi.org/10.1016/j.surfcoat.2018.09.033.

[216] A.C. Ferrari, J. Robertson, Interpretation of Raman spectra of disordered and amorphous carbon, Phys. Rev. B. 61 (2000) 14095–14107. https://doi.org/10.1103/PhysRevB.61.14095.

[217] J. Schwan, S. Ulrich, V. Batori, H. Ehrhardt, S.R.P. Silva, Raman spectroscopy on amorphous carbon films, J. Appl. Phys. 80 (1996) 440–447. https://doi.org/10.1063/1.362745.

[218] J. Robertson, Clustering and gap states in amorphous carbon, Philos. Mag. Lett. 57 (1988) 143–148. https://doi.org/10.1080/09500838808229624.

[219] A.C. Ferrari, Raman spectroscopy of graphene and graphite: Disorder, electron–phonon coupling, doping and nonadiabatic effects, Solid State Commun. 143 (2007) 47–57. https://doi.org/10.1016/j.ssc.2007.03.052.

[220] J. Fortner, J.S. Lannin, Radial distribution functions of amorphous silicon, Phys. Rev. B. 39 (1989) 5527–5530. https://doi.org/10.1103/PhysRevB.39.5527.

[221] A.C. Ferrari, J. Robertson, Raman spectroscopy of amorphous, nanostructured, diamond–like carbon, and nanodiamond, Philos. Trans. R. Soc. London. Ser. A Math. Phys. Eng. Sci. 362 (2004) 2477–2512. https://doi.org/10.1098/rsta.2004.1452.

[222] A.C. Ferrari, J. Robertson, Resonant Raman spectroscopy of disordered, amorphous, and diamondlike carbon, Phys. Rev. B. 64 (2001) 075414.

https://doi.org/10.1103/PhysRevB.64.075414.

[223] C. Baraniecki, P.H. Pinchbeck, F.B. Pickering, Some aspects of graphitization induced by iron and ferro-silicon additions, Carbon N. Y. 7 (1969) 58. https://doi.org/10.1016/0008-6223(69)90104-3.

[224] Z. Sun, W. Zhao, D. Kong, Microstructure and Mechanical Property of Magnetron Sputtering Deposited DLC Film, J. Wuhan Univ. Technol. Sci. Ed. 33 (2018) 579–584. https://doi.org/10.1007/s11595-018-1864-2.

[225] S. Flege, R. Hatada, A. Hanauer, W. Ensinger, T. Morimura, K. Baba, Preparation of Metal-Containing Diamond-Like Carbon Films by Magnetron Sputtering and Plasma Source Ion Implantation and Their Properties, Adv. Mater. Sci. Eng. 2017 (2017) 1–8. https://doi.org/10.1155/2017/9082164.

[226] Q. Wei, R.J. Narayan, J. Narayan, J. Sankar, A.K. Sharma, Improvement of wear resistance of pulsed laser deposited diamond-like carbon films through incorporation of metals, Mater. Sci. Eng. B. 53 (1998) 262–266. https://doi.org/10.1016/S0921-5107(98)00150-0.

[227] A. García-García, P.A. Algarabel, J.A. Pardo, Z. Arnold, J. Kamarad, Pressure dependence of the magneto-transport properties in Fe/MgO granular systems, J. Korean Phys. Soc. 62 (2013) 1458–1460. https://doi.org/10.3938/jkps.62.1458.

[228] A.L. Ėfros, Electric conduction of Impurity in Semiconductors. The Sphere problem, in: Phys. Geom. Disord. Percolation Theory, Imported Publication, 1986: pp. 147–161.

[229] Y. Catherine, P. Couderc, Electrical characteristics and growth kinetics in discharges used for plasma deposition of amorphous carbon, Thin Solid Films. 144 (1986) 265–280. https://doi.org/10.1016/0040-6090(86)90419-0.

[230] P.I. Vysikaylo, V.S. Mitin, E.E. Son, V. V Belyaev, Physical Alloying of Plasma Metallization Nanocomposite Coating by Allotropic Carbon Nanostructures—Part 1: Experimental Research, IEEE Trans. Plasma Sci. 46 (2018) 1775–1780. https://doi.org/10.1109/TPS.2018.2819138.

[231] C. Weissmantel, K. Bewilogua, K. Breuer, D. Dietrich, U. Ebersbach, H.-J. Erler, B. Rau, G. Reisse, Preparation and properties of hard i-C and i-BN coatings, Thin Solid Films. 96 (1982) 31–44. https://doi.org/10.1016/0040-6090(82)90210-3.

[232] Y. Pan, J. Zhou, G. Chen, Quantifying thermal transport in amorphous silicon using mean free path spectroscopy, Phys. Rev. B. 101 (2020) 144203. https://doi.org/10.1103/PhysRevB.101.144203.

[233] T.Q. Tran, A. Chinnappan, J.K.Y. Lee, N.H. Loc, L.T. Tran, G. Wang, V.V. Kumar, W.A.D.M. Jayathilaka, D. Ji, M. Doddamani, S. Ramakrishna, 3D Printing of Highly Pure Copper, Metals (Basel). 9 (2019) 756. https://doi.org/10.3390/met9070756.

[234] M.A. Kats, R. Blanchard, P. Genevet, F. Capasso, Nanometre optical coatings based on strong interference effects in highly absorbing media, Nat. Mater. 12 (2013) 20–24. https://doi.org/10.1038/nmat3443.

[235] C. Niu, Carbon nanotube transparent conducting films, MRS Bull. 36 (2011) 766–773. https://doi.org/10.1557/mrs.2011.213.

[236] T. Knych, G. Kiesiewicz, P. Kwasniewski, A. Mamala, B. Smyrak, A. Kawecki, Fabrication and Cold Drawing of Copper Covetic Nanostructured Carbon Composites/ Otrzymywanie Oraz Ciągnienia Kompozytów Miedzianych Typu Covetic O Strukturze

Nanometrycznej, Arch. Metall. Mater. 59 (2014) 1283–1286. https://doi.org/10.2478/amm-2014-0219.

[237] R.A. Isaacs, H. Zhu, C. Preston, A. Mansour, M. LeMieux, P.Y. Zavalij, H.M.I.I. Jaim, O. Rabin, L. Hu, L.G. Salamanca-Riba, Nanocarbon-copper thin film as transparent electrode, Appl. Phys. Lett. 106 (2015) 193108. https://doi.org/10.1063/1.4921263.

[238] B. Ma, U. Balachandran, J. Wang, J. Wen, T.H. Lee, S.E. Dorris, A.J. Rondinone, Structural hierarchy of nanocarbon in copper covetics, Appl. Phys. Lett. 113 (2018) 173102. https://doi.org/10.1063/1.5052622.

[239] M.A. Kats, F. Capasso, Optical absorbers based on strong interference in ultra-thin films, Laser Photon. Rev. 10 (2016) 735–749. https://doi.org/10.1002/lpor.201600098.

[240] M. Diem, T. Koschny, C.M. Soukoulis, Wide-angle perfect absorber/thermal emitter in the terahertz regime, Phys. Rev. B. 79 (2009) 033101. https://doi.org/10.1103/PhysRevB.79.033101.

[241] Z.H. Jiang, S. Yun, F. Toor, D.H. Werner, T.S. Mayer, Conformal Dual-Band Near-Perfectly Absorbing Mid-Infrared Metamaterial Coating, ACS Nano. 5 (2011) 4641–4647. https://doi.org/10.1021/nn2004603.

[242] B. Zhang, Y. Zhao, Q. Hao, B. Kiraly, I.-C. Khoo, S. Chen, T.J. Huang, Polarization-independent dual-band infrared perfect absorber based on a metal-dielectric-metal elliptical nanodisk array, Opt. Express. 19 (2011) 15221. https://doi.org/10.1364/OE.19.015221.

[243] N. Liu, M. Mesch, T. Weiss, M. Hentschel, H. Giessen, Infrared Perfect Absorber and Its Application As Plasmonic Sensor, Nano Lett. 10 (2010) 2342–2348. https://doi.org/10.1021/nl9041033.

[244] A. Tittl, P. Mai, R. Taubert, D. Dregely, N. Liu, H. Giessen, Palladium-Based Plasmonic Perfect Absorber in the Visible Wavelength Range and Its Application to Hydrogen Sensing, Nano Lett. 11 (2011) 4366–4369. https://doi.org/10.1021/nl202489g.

[245] Q. Hu, K.-T. Lin, H. Lin, Y. Zhang, B. Jia, Graphene Metapixels for Dynamically Switchable Structural Color, ACS Nano. 15 (2021) 8930–8939. https://doi.org/10.1021/acsnano.1c01570.

[246] R. Yu, V. Pruneri, F.J. García de Abajo, Active modulation of visible light with graphene-loaded ultrathin metal plasmonic antennas, Sci. Rep. 6 (2016) 32144. https://doi.org/10.1038/srep32144.

[247] D. Li, W.-Y. Lai, Y.-Z. Zhang, W. Huang, Printable Transparent Conductive Films for Flexible Electronics, Adv. Mater. 30 (2018) 1704738. https://doi.org/10.1002/adma.201704738.

[248] C. Feng, K. Liu, J.-S. Wu, L. Liu, J.-S. Cheng, Y. Zhang, Y. Sun, Q. Li, S. Fan, K. Jiang, Flexible, Stretchable, Transparent Conducting Films Made from Superaligned Carbon Nanotubes, Adv. Funct. Mater. 20 (2010) 885–891. https://doi.org/10.1002/adfm.200901960.

[249] S. Gupta, N.-H. Tai, Carbon materials and their composites for electromagnetic interference shielding effectiveness in X-band, Carbon N. Y. 152 (2019) 159–187. https://doi.org/10.1016/j.carbon.2019.06.002.

[250] Y. Homma, S. Tsunekawa, Planar Deposition of Aluminum by RF/DC Sputtering with RF Bias, J. Electrochem. Soc. 132 (1985) 1466–1472.

https://doi.org/10.1149/1.2114145.

[251] J. Robertson, The deposition mechanism of diamond-like a-C and a-C: H, Diam. Relat. Mater. 3 (1994) 361–368. https://doi.org/10.1016/0925-9635(94)90186-4.

[252] H. Miyaji, A. Pander, K. Takano, H. Kohno, A. Hatta, M. Nakajima, H. Furuta, Optical reflectance of patterned frost column-like CNT forest for metamaterial applications, Diam. Relat. Mater. 83 (2018) 196–203. https://doi.org/10.1016/j.diamond.2018.02.004.

[253] C. Silbernagel, L. Gargalis, I. Ashcroft, R. Hague, M. Galea, P. Dickens, Electrical resistivity of pure copper processed by medium-powered laser powder bed fusion additive manufacturing for use in electromagnetic applications, Addit. Manuf. 29 (2019) 100831. https://doi.org/10.1016/j.addma.2019.100831.

[254] D.E. Aspnes, The Accurate Determination of Optical Properties by Ellipsometry, in: Handb. Opt. Constants Solids, Elsevier, 1997: pp. 89–112. https://doi.org/10.1016/B978-012544415-6.50008-X.

[255] V.V. Atuchin, V.A. Kochubey, A.S. Kozhukhov, V.N. Kruchinin, L.D. Pokrovsky, I.S. Soldatenkov, I.B. Troitskaia, Microstructure and dispersive optical parameters of iron films deposited by the thermal evaporation method, Optik (Stuttg). 188 (2019) 120–125. https://doi.org/10.1016/j.ijleo.2019.04.122.

[256] P.K. Mehrotra, R. Hoffmann, Copper(I)-copper(I) interactions. Bonding relationships in d10-d10 systems, Inorg. Chem. 17 (1978) 2187–2189. https://doi.org/10.1021/ic50186a032.

[257] M. Bass, Handbook of Optics, Volume I: Geometrical and Physical Optics, Polarized Light, Components and Instruments, McGraw-Hill, 1996.

[258] Â.E. Crespi, C. Ballage, M.C. Hugon, J. Robert, D. Lundin, I. Vickridge, J. Alvarez, T. Minea, Low resistivity amorphous carbon-based thin films employed as anti-reflective coatings on copper, Thin Solid Films. 712 (2020) 138319. https://doi.org/10.1016/j.tsf.2020.138319.

[259] M. Abraham, Reflecting powder of metals - boundary conditions- Part 3, in: Class. Theory Eletr. Magn., 1932: pp. 191–196.

[260] M.F. Ubeid, M.M. Shabat, Reflection and transmission of electromagnetic waves by a multilayered solar cell containing organic materials, Opt. Quantum Electron. 51 (2019) 197. https://doi.org/10.1007/s11082-019-1860-6.

[261] J. Jackson, Boundary Conditions at Interfaces Between Different Media, in: Class. Electrodyn., 3rd ed., Jonh Wiley & Sons, 1998: pp. 16–19.

[262] Y. V Bludov, N.M.R. Peres, M.I. Vasilevskiy, Unusual reflection of electromagnetic radiation from a stack of graphene layers at oblique incidence, J. Opt. 15 (2013) 114004. https://doi.org/10.1088/2040-8978/15/11/114004.

[263] P.B. Johnson, R.W. Christy, Optical constants of the noble metals, Phys. Rev. B. 6 (1972) 4370–4379. https://doi.org/10.1103/PhysRevB.6.4370.

[264] M.W. Williams, E.T. Arakawa, Optical properties of glassy carbon from 0 to 82 eV, J. Appl. Phys. 43 (1972) 3460–3463. https://doi.org/10.1063/1.1661738.

[265] M. Born, E. Wolf, E. Hecht, Principles of Optics: Electromagnetic Theory of Propagation, Interference and Diffraction of Light, Phys. Today. 53 (2000) 77–78. https://doi.org/10.1063/1.1325200.

[266] R.H. Muller, Thickness Measurement of Transparent Thin Films on Metal Surfaces by Light Interference, J. Opt. Soc. Am. 54 (1964) 419. https://doi.org/10.1364/JOSA.54.000419.

[267] E.A. Taft, H.R. Philipp, Optical Properties of Graphite, Phys. Rev. 138 (1965) A197–A202. https://doi.org/10.1103/PhysRev.138.A197.

[268] Â.E. Crespi, C. Ballage, M.-C. Hugon, J. Robert, T. Minea, The Role of Amorphous Nanocrystalline Carbon Films in Interference on Flexible Copper Foils, ACS Appl. Electron. Mater. 4 (2022) 576–584. https://doi.org/10.1021/acsaelm.1c00520.

[269] D.L. Wood, J. Tauc, Weak Absorption Tails in Amorphous Semiconductors, Phys. Rev. B. 5 (1972) 3144–3151. https://doi.org/10.1103/PhysRevB.5.3144.

[270] Y.-H. Jia, P. Gong, S.-L. Li, W.-D. Ma, X.-Y. Fang, Y.-Y. Yang, M.-S. Cao, Effects of hydroxyl groups and hydrogen passivation on the structure, electrical and optical properties of silicon carbide nanowires, Phys. Lett. A. 384 (2020) 126106. https://doi.org/10.1016/j.physleta.2019.126106.

[271] Y.-Y. Yang, P. Gong, W.-D. Ma, R. Hao, X.-Y. Fang, Effects of substitution of group-V atoms for carbon or silicon atoms on optical properties of silicon carbide nanotubes*, Chinese Phys. B. 30 (2021) 067803. https://doi.org/10.1088/1674-1056/abdb1e.

[272] B. Kwiecinska, D.G. Murchison, E. Scott, Optical properties of graphite, J. Microsc. 109 (1977) 289–302. https://doi.org/10.1111/j.1365-2818.1977.tb01142.x.

[273] A.B. Djurišić, E.H. Li, Optical properties of graphite, J. Appl. Phys. 85 (1999) 7404–7410. https://doi.org/10.1063/1.369370.

[274] A. Borghesi, G. Guizzetti, Graphite (C), in: Handb. Opt. Constants Solids, Elsevier, 1997: pp. 449–460. https://doi.org/10.1016/B978-012544415-6.50060-1.

[275] J.C. Lewis, B. Redfern, F.C. Cowlard, Vitreous carbon as a crucible material for semiconductors, Solid. State. Electron. 6 (1963) 251–254. https://doi.org/10.1016/0038-1101(63)90081-9.

[276] J. Bauer, A. Schroer, R. Schwaiger, O. Kraft, Approaching theoretical strength in glassy carbon nanolattices, Nat. Mater. 15 (2016) 438–443. https://doi.org/10.1038/nmat4561.

[277] H. Fujiwara, Reflectance and transmittance, in: Spectrosc. Ellipsom. Princ. Appl., Wiley, 2007: pp. 40–41.

[278] L.K. Ang, Y.Y. Lau, R.M. Gilgenbach, H.L. Spindler, Analysis of laser absorption on a rough metal surface, Appl. Phys. Lett. 70 (1997) 696–698. https://doi.org/10.1063/1.118242.

[279] P. Hariharan, P. Hariharan, 11 - Macro- and Micro-Interferometry, in: P. Hariharan, P.B.T.-B. of I. (Second E. Hariharan (Eds.), Academic Press, Burlington, 2007: pp. 93–103. https://doi.org/https://doi.org/10.1016/B978-012373589-8/50013-4.

[280] H.E. Bennett, J.O. Porteus, Relation Between Surface Roughness and Specular Reflectance at Normal Incidence, J. Opt. Soc. Am. 51 (1961) 123. https://doi.org/10.1364/JOSA.51.000123.

[281] A. Heider, J. Sollinger, F. Abt, M. Boley, R. Weber, T. Graf, High-Speed X-Ray Analysis of Spatter Formation in Laser Welding of Copper, Phys. Procedia. 41 (2013) 112–118. https://doi.org/10.1016/j.phpro.2013.03.058.

[282] A. Popovich, V. Sufiiarov, I. Polozov, E. Borisov, D. Masaylo, A. Orlov, Microstructure

and mechanical properties of additive manufactured copper alloy, Mater. Lett. 179 (2016) 38–41. https://doi.org/10.1016/j.matlet.2016.05.064.

[283] A. Morvan, J.-L. Grosseau-Poussard, N. Caillault, F. Delange, S. Roure, P. Lepretre, J.-F. Silvain, Powder processing methodology for fabrication of Copper/Graphite composite materials with enhanced thermal properties, Compos. Part A Appl. Sci. Manuf. 124 (2019) 105474. https://doi.org/10.1016/j.compositesa.2019.105474.

[284] H. Ding, P. He, J. Yang, C. Liu, H. Zhao, B. Derby, Water-based highly conductive graphene inks for fully printed humidity sensors, J. Phys. D. Appl. Phys. 53 (2020) 455304. https://doi.org/10.1088/1361-6463/aba78a.

[285] A. Metel, M. Stebulyanin, S. Fedorov, A. Okunkova, Power Density Distribution for Laser Additive Manufacturing (SLM): Potential, Fundamentals and Advanced Applications, Technologies. 7 (2018) 5. https://doi.org/10.3390/technologies7010005.

[286] M. Boutaous, X. Liu, D.A. Siginer, S. Xin, Balling phenomenon in metallic laser based 3D printing process, Int. J. Therm. Sci. 167 (2021) 107011. https://doi.org/10.1016/j.ijthermalsci.2021.107011.

[287] S. Schiaffino, A.A. Sonin, Molten droplet deposition and solidification at low Weber numbers, Phys. Fluids. 9 (1997) 3172–3187. https://doi.org/10.1063/1.869434.

[288] X. Zhou, X. Liu, D. Zhang, Z. Shen, W. Liu, Balling phenomena in selective laser melted tungsten, J. Mater. Process. Technol. 222 (2015) 33–42. https://doi.org/10.1016/j.jmatprotec.2015.02.032.

[289] R. Fabbro, M. Dal, P. Peyre, F. Coste, M. Schneider, V. Gunenthiram, Analysis and possible estimation of keyhole depths evolution, using laser operating parameters and material properties, J. Laser Appl. 30 (2018) 032410. https://doi.org/10.2351/1.5040624.

[290] I. Yadroitsev, I. Smurov, Selective laser melting technology: From the single laser melted track stability to 3D parts of complex shape, Phys. Procedia. 5 (2010) 551–560. https://doi.org/10.1016/j.phpro.2010.08.083.

[291] K.N. Lankalapalli, J.F. Tu, M. Gartner, A model for estimating penetration depth of laser welding processes, J. Phys. D. Appl. Phys. 29 (1996) 1831–1841. https://doi.org/10.1088/0022-3727/29/7/018.

[292] D. Gu, Y. Shen, Balling phenomena in direct laser sintering of stainless steel powder: Metallurgical mechanisms and control methods, Mater. Des. 30 (2009) 2903–2910. https://doi.org/10.1016/j.matdes.2009.01.013.

[293] D. Gu, Y.-C. Hagedorn, W. Meiners, G. Meng, R.J.S. Batista, K. Wissenbach, R. Poprawe, Densification behavior, microstructure evolution, and wear performance of selective laser melting processed commercially pure titanium, Acta Mater. 60 (2012) 3849–3860. https://doi.org/10.1016/j.actamat.2012.04.006.

[294] X. Ren, H. Liu, F. Lu, L. Huang, X. Yi, Effects of processing parameters on the densification, microstructure and mechanical properties of pure tungsten fabricated by optimized selective laser melting: From single and multiple scan tracks to bulk parts, Int. J. Refract. Met. Hard Mater. 96 (2021) 105490. https://doi.org/10.1016/j.ijrmhm.2021.105490.

[295] M. Ahmed Obeidi, A. Mussatto, R. Groarke, R.K. Vijayaraghavan, A. Conway, F. Rossi Kaschel, E. McCarthy, O. Clarkin, R. O'Connor, D. Brabazon, Comprehensive assessment of spatter material generated during selective laser melting of stainless steel,

Mater. Today Commun. 25 (2020) 101294. https://doi.org/10.1016/j.mtcomm.2020.101294.

[296] S.D. Jadhav, S. Dadbakhsh, L. Goossens, J.-P. Kruth, J. Van Humbeeck, K. Vanmeensel, Influence of selective laser melting process parameters on texture evolution in pure copper, J. Mater. Process. Technol. 270 (2019) 47–58. https://doi.org/10.1016/j.jmatprotec.2019.02.022.

[297] V.Y. Belen'kii, V.M. Yazovskikh, Control of electron beam welding using plasma phenomena in the molten pool region, Weld. Int. 11 (1997) 554–556. https://doi.org/10.1080/09507119709452013.

[298] M. Boley, F. Abt, R. Weber, T. Graf, X-Ray and Optical Videography for 3D Measurement of Capillary and Melt Pool Geometry in Laser Welding, Phys. Procedia. 41 (2013) 488–495. https://doi.org/10.1016/j.phpro.2013.03.105.

[299] S. Kou, Weld Metal Solidification I: Grain Structure, in: Weld. Metall., Second Edi, 2002: pp. 170–198. https://doi.org/doi.org/10.1002/0471434027.ch7.

[300] S. Qu, J. Ding, J. Fu, M. Fu, B. Zhang, X. Song, High-precision laser powder bed fusion processing of pure copper, Addit. Manuf. 48 (2021) 102417. https://doi.org/10.1016/j.addma.2021.102417.

[301] E. Weidman, Electrolytic Polishing, in: ASM Handb. Metallogr. Microstruct., 2009: pp. 42–65.

[302] T.F. Ricksecker, R.E. Bower, Copper and Copper Alloys: Metallographic Techniques and Microstructures, in: ASM Handb. Metallogr. Microstruct., 2009: pp. 820–860.

[303] P.A. Lykov, E.V. Safonov, A.M. Akhmedianov, Selective Laser Melting of Copper, Mater. Sci. Forum. 843 (2016) 284–288. https://doi.org/10.4028/www.scientific.net/MSF.843.284.

[304] G. Demeneghi, B. Barnes, P. Gradl, J.R. Mayeur, K. Hazeli, Size effects on microstructure and mechanical properties of additively manufactured copper–chromium–niobium alloy, Mater. Sci. Eng. A. 820 (2021) 141511. https://doi.org/10.1016/j.msea.2021.141511.

[305] T. Vilaro, C. Colin, J.D. Bartout, L. Nazé, M. Sennour, Microstructural and mechanical approaches of the selective laser melting process applied to a nickel-base superalloy, Mater. Sci. Eng. A. 534 (2012) 446–451. https://doi.org/10.1016/j.msea.2011.11.092.

[306] L.N. Carter, C. Martin, P.J. Withers, M.M. Attallah, The influence of the laser scan strategy on grain structure and cracking behaviour in SLM powder-bed fabricated nickel superalloy, J. Alloys Compd. 615 (2014) 338–347. https://doi.org/10.1016/j.jallcom.2014.06.172.

[307] M.J. Ansari, D.-S. Nguyen, H.S. Park, Investigation of SLM Process in Terms of Temperature Distribution and Melting Pool Size: Modeling and Experimental Approaches, Materials (Basel). 12 (2019) 1272. https://doi.org/10.3390/ma12081272.

[308] D.M. Sanders, A. Anders, Review of cathodic arc deposition technology at the start of the new millennium, Surf. Coatings Technol. 133–134 (2000) 78–90. https://doi.org/10.1016/S0257-8972(00)00879-3.

[309] V. Semak, A. Matsunawa, The role of recoil pressure in energy balance during laser materials processing, J. Phys. D. Appl. Phys. 30 (1997) 2541–2552. https://doi.org/10.1088/0022-3727/30/18/008.

[310] A. Sharma, V. Yadava, Experimental analysis of Nd-YAG laser cutting of sheet materials – A review, Opt. Laser Technol. 98 (2018) 264–280. https://doi.org/10.1016/j.optlastec.2017.08.002.

[311] P. Di Pietro, Y.L. Yao, A new technique to characterize and predict laser cut striations, Int. J. Mach. Tools Manuf. 35 (1995) 993–1002. https://doi.org/10.1016/0890-6955(94)00063-P.

[312] B.-C. Kim, T.-H. Kim, Y. Jang, K.-H. Chung, Investigation of striation formation in thin stainless steel tube during pulsed Nd:YAG laser cutting process by numerical simulation, Metall. Mater. Trans. A. 32 (2001) 2623–2632. https://doi.org/10.1007/s11661-001-0052-7.

[313] C.R. Cunningham, J.M. Flynn, A. Shokrani, V. Dhokia, S.T. Newman, Invited review article: Strategies and processes for high quality wire arc additive manufacturing, Addit. Manuf. 22 (2018) 672–686. https://doi.org/10.1016/j.addma.2018.06.020.

[314] S.D. Jadhav, P.P. Dhekne, S. Dadbakhsh, J.-P. Kruth, J. Van Humbeeck, K. Vanmeensel, Surface Modified Copper Alloy Powder for Reliable Laser-based Additive Manufacturing, Addit. Manuf. 35 (2020) 101418. https://doi.org/10.1016/j.addma.2020.101418.

[315] F.P. Bundy, Pressure-temperature phase diagram of elemental carbon, Phys. A Stat. Mech. Its Appl. 156 (1989) 169–178. https://doi.org/10.1016/0378-4371(89)90115-5.

[316] M. Hasegawa, Ellingham Diagram, in: Treatise Process Metall., Elsevier, 2014: pp. 507–516. https://doi.org/10.1016/B978-0-08-096986-2.00032-1.

[317] P.J. Linstrom, Base de données standard de référence NIST numéro 69, (2018) Phase change data. https://doi.org/https://doi.org/10.18434/T4D303.

[318] B. Zhou, J. Zhou, H. Li, F. Lin, A study of the microstructures and mechanical properties of Ti6Al4V fabricated by SLM under vacuum, Mater. Sci. Eng. A. 724 (2018) 1–10. https://doi.org/10.1016/j.msea.2018.03.021.

[319] S. Kumar, S. Pityana, Laser-Based Additive Manufacturing of Metals, Adv. Mater. Res. 227 (2011) 92–95. https://doi.org/10.4028/www.scientific.net/AMR.227.92.

[320] S. Dorbolo, N. Vandewalle, The Branly Effect and Contacting Grains in a Packing, in: S.P. Hoogendoorn, S. Luding, P.H.L. Bovy, M. Schreckenberg, D.E. Wolf (Eds.), Traffic Granul. Flow ’03, Springer Berlin Heidelberg, Berlin, Heidelberg, 2005: pp. 521–524.

[321] J.H. Tan, W.L.E. Wong, K.W. Dalgarno, An overview of powder granulometry on feedstock and part performance in the selective laser melting process, Addit. Manuf. 18 (2017) 228–255. https://doi.org/10.1016/j.addma.2017.10.011.

[322] J. Visser, Van der Waals and other cohesive forces affecting powder fluidization, Powder Technol. 58 (1989) 1–10. https://doi.org/10.1016/0032-5910(89)80001-4.

[323] É. Branly, Radioconducteurs à billes métalliques, C. r. Hebd. Séanc. Acad. Sci., Paris. 128 (1899) 1089–1092.

[324] É. Branly, Résistance électrique au contact de deux disques d’un même métal, J. Phys. Théorique Appliquée. 8 (1899) 21–24. https://doi.org/10.1051/jphystap:01899008002100.

[325] L. Vanel, Etude experimentale de l’equilibre mecanique d’un milieu granulaire : exemples du silo et du tas de sable, Paris 6, 1999.

[326] S. Dorbolo, M. Ausloos, N. Vandewalle, Reexamination of the Branly effect, Phys. Rev. E. 67 (2003) 040302. https://doi.org/10.1103/PhysRevE.67.040302.

[327] É. Branly, Radioconducteurs a contact unique, CR Acad. Sci. Paris. 134 (1902) 347.

[328] W. Dai, D. Hanaor, Y. Gan, The effects of packing structure on the effective thermal conductivity of granular media: A grain scale investigation, Int. J. Therm. Sci. 142 (2019) 266–279. https://doi.org/10.1016/j.ijthermalsci.2019.04.028.

[329] E. Guyon, Disorders in granular matter, Phys. A Stat. Mech. Its Appl. 357 (2005) 150–158. https://doi.org/10.1016/j.physa.2005.05.055.

[330] R. Holm, Electric contacts: theory and application, Springer Science & Business Media, 2013.

[331] R.W. Wilson, The Contact Resistance and Mechanical Properties of Surface Films on Metals, Proc. Phys. Soc. Sect. B. 68 (1955) 625–641. https://doi.org/10.1088/0370-1301/68/9/307.

[332] P. Guyot, V. Rat, J.F. Coudert, F. Jay, A. Maître, N. Pradeilles, Does the Branly effect occur in spark plasma sintering?, J. Phys. D. Appl. Phys. 45 (2012) 92001. https://doi.org/10.1088/0022-3727/45/9/092001.

[333] D. Vandembroucq, A.C. Boccara, S. Roux, Breakdown Patterns in Branly's Coheror, J. Phys. III. 7 (1997) 303–310. https://doi.org/10.1051/jp3:1997123.

[334] J. Milberg, M. Sigl, Electron beam sintering of metal powder, Prod. Eng. 2 (2008) 117–122.

[335] C. Eschey, S. Lutzmann, M.F. Zaeh, Examination of the powder spreading effect in Electron Beam Melting (EBM), Solid Free. Fabr. Austin, TX, August. (2009) 3–5.

[336] A. Barrat, V. Loreto, Memory in aged granular media, Europhys. Lett. 53 (2001) 297–303. https://doi.org/10.1209/epl/i2001-00100-3.

[337] W. Chen, G. Yin, Z. Feng, X. Liao, Effect of Powder Feedstock on Microstructure and Mechanical Properties of the 316L Stainless Steel Fabricated by Selective Laser Melting, Metals (Basel). 8 (2018) 729. https://doi.org/10.3390/met8090729.

[338] O. Molerus, Theory of yield of cohesive powders, Powder Technol. 12 (1975) 259–275. https://doi.org/10.1016/0032-5910(75)85025-X.

[339] I.S. Aranson, D. Blair, V.A. Kalatsky, G.W. Crabtree, W.-K. Kwok, V.M. Vinokur, U. Welp, Electrostatically Driven Granular Media: Phase Transitions and Coarsening, Phys. Rev. Lett. 84 (2000) 3306–3309. https://doi.org/10.1103/PhysRevLett.84.3306.

[340] D.W. Howell, I.S. Aronson, G.W. Crabtree, Dynamics of electrostatically driven granular media: Effects of humidity, Phys. Rev. E. 63 (2001) 050301. https://doi.org/10.1103/PhysRevE.63.050301.

[341] P. Duquenne, A. Deltour, G. Lacoste, Application of inductive heating to granular media: temperature distribution in a granular bed, Int. J. Heat Mass Transf. 36 (1993) 2473–2477. https://doi.org/10.1016/S0017-9310(05)80130-9.

[342] P. Béquin, V. Tournat, Electrical conduction and Joule effect in one-dimensional chains of metallic beads: hysteresis under cycling DC currents and influence of electromagnetic pulses, Granul. Matter. 12 (2010) 375–385. https://doi.org/10.1007/s10035-010-0185-8.

[343] E. Falcon, B. Castaing, C. Laroche, "Turbulent" electrical transport in copper powders,

Europhys. Lett. 65 (2004) 186–192. https://doi.org/10.1209/epl/i2003-10071-9.

[344] M. Creyssels, C. Laroche, E. Falcon, B. Castaing, Pressure dependence of the electrical transport in granular materials, Eur. Phys. J. E. 40 (2017) 56. https://doi.org/10.1140/epje/i2017-11543-3.

[345] M. Creyssels, S. Dorbolo, A. Merlen, C. Laroche, B. Castaing, E. Falcon, Some aspects of electrical conduction in granular systems of various dimensions, Eur. Phys. J. E. 23 (2007) 255. https://doi.org/10.1140/epje/i2006-10186-9.

[346] C. Guerret-Piecourt, S. Bec, D. Treheux, Electrical charges and tribology of insulating materials, Comptes Rendus l'Académie Des Sci. - Ser. IV - Phys. 2 (2001) 761–774. https://doi.org/10.1016/S1296-2147(01)01218-5.

[347] M. Tokita, Method and system for automatic electrical sintering, US6383446B1, 2002.

[348] W.R.D. Callister Jr, 2.7 Atomic Structure and Interatomic Bonding, in: Fundam. Mater. Sci. Eng., 10th ed., Wiley, 2018: pp. 39–41.

[349] J. Lekner, Forces and torque on a pair of uncharged conducting spheres in an external electric field, J. Appl. Phys. 114 (2013) 224902. https://doi.org/10.1063/1.4845835.

[350] J. Lekner, Electrostatic force between two conducting spheres at constant potential difference, J. Appl. Phys. 111 (2012) 076102. https://doi.org/10.1063/1.3702438.

[351] J.D. Jackson, Eletrostatic- Multipoles of eletrostatic media,dieletrics, in: Class. Electrodyn., 3rd ed., John Wiley & Sons, Inc., 2007: pp. 145–169.

[352] D.J. Mitchell, B.W. Ninham, van der Waals Forces between Two Spheres, J. Chem. Phys. 56 (1972) 1117–1126. https://doi.org/10.1063/1.1677331.

[353] H. Kurata, Electronic State Analysis by Monochromated STEM-EELS, in: P.A. van A. Gennady Logvenov, Joachim Maier (Ed.), Jeol News, Vol 53, Jeol, 2018: p. 25. www.jeol.co.jp/en/applications/detail/1682.html.

[354] T. Okamoto, I. Yamaguchi, Field Enhancement by a Metallic Sphere on Dielectric Substrates, Opt. Rev. 6 (1999) 211–214. https://doi.org/10.1007/s10043-999-0211-4.

[355] Y. Fujiyoshi, T. Nemoto, H. Kurata, Studying substrate effects on localized surface plasmons in an individual silver nanoparticle using electron energy-loss spectroscopy, Ultramicroscopy. 175 (2017) 116–120. https://doi.org/10.1016/j.ultramic.2017.01.006.

[356] C. Noguez, Surface Plasmons on Metal Nanoparticles: The Influence of Shape and Physical Environment, J. Phys. Chem. C. 111 (2007) 3806–3819. https://doi.org/10.1021/jp066539m.

[357] T. Tommasina, Sur un curieux phénomène d'adhérence des limailles métalliques sous l'action du courant électrique, 1898.

[358] U. Ali, Y. Mahmoodkhani, S. Imani Shahabad, R. Esmaeilizadeh, F. Liravi, E. Sheydaeian, K.Y. Huang, E. Marzbanrad, M. Vlasea, E. Toyserkani, On the measurement of relative powder-bed compaction density in powder-bed additive manufacturing processes, Mater. Des. 155 (2018) 495–501. https://doi.org/10.1016/j.matdes.2018.06.030.

[359] I. Baesso, D. Karl, A. Spitzer, A. Gurlo, J. Günster, A. Zocca, Characterization of powder flow behavior for additive manufacturing, Addit. Manuf. 47 (2021) 102250. https://doi.org/10.1016/j.addma.2021.102250.

[360] A. Tkatchenko, Current Understanding of Van der Waals Effects in Realistic Materials, Adv. Funct. Mater. 25 (2015) 2054–2061. https://doi.org/10.1002/adfm.201403029.

[361] M. Creyssels, E. Falcon, B. Castaing, Experiment and theory of the electrical conductivity of a compressed granular metal, in: AIP Conf. Proc., American Institute of Physics, 2009: pp. 123–126.

[362] I.C. Kim, S. Torquato, Effective conductivity of suspensions of overlapping spheres, J. Appl. Phys. 71 (1992) 2727–2735. https://doi.org/10.1063/1.351046.

[363] E. Falcon, B. Castaing, M. Creyssels, Nonlinear electrical conductivity in a 1D granular medium, Eur. Phys. J. B-Condensed Matter Complex Syst. 38 (2004) 475–483.

[364] A.L. Efros, Physics and Geometry of Disorder Percolation Theory, Mir Publisher, Moscow, 1986.

[365] B.I. Shklovskiĭ, A.L. Éfros, Percolation theory and conductivity of strongly inhomogeneous media, Sov. Phys. Uspekhi. 18 (1975) 845–862. https://doi.org/10.1070/PU1975v018n11ABEH005233.

[366] G. Blaise, C. Le Gressus, Charge trapping-detrapping processes and related breakdown phenomena, RV Latham, (1994).

[367] P. Lorrain, D.R. Corson, Plane Electromagnetic Waves I Unform Waves in Free Space, in Nonconductors, and in Conductors, in: Lorrain, Paul Corson, Dale R, 2 nd, W. H. Freeman, 1970: p. 514.

[368] P. Lorrain, D.R. Corson, Guided waves III The planar optical waveguide A., in: Electromagn. Fields Waves, W. H. Freeman, 1970: pp. 648–655.

[369] Graphite 33 Safety Data Sheet, Regul. EC No 1907/2006 Art.31. (2020) 10. https://static.rapidonline.com/pdf/87-0695s_v2.pdf (accessed December 17, 2021).

[370] Merriam-Webster dictionary, Merriam-Webster's Coll. Dictionary, Elev. Ed. (n.d.). https://www.merriam-webster.com/dictionary/pump (accessed August 20, 2021).

[371] Polytec.com, Microscopes longue distance, (n.d.). https://www.polytec.com/fr/photonique-vision/produits/microscopes-longue-distance-telescopes-pour-lastronomie-questar/microscopes-longue-distance (accessed November 10, 2021).

[372] Pfeiffer Vaccum, Compact FullRange™ Gauge PKR 251 Operating instructions, Berlin, n.d.

If you reach this point:

L'expérience n'est jamais en défaut. Seul notre jugement qui attend d'elle des choses étrangères à son pouvoir.

Extrait des carnets de Leonardo Da Vinci